Understanding the Structure-Property Relationships in Selective Membranes for Desalination and Ion Separation

A Dissertation

Presented to

The faculty of the School of Engineering and Applied Science

University of Virginia

In partial fulfillment of

The requirements for the degree of

Doctor of Philosophy

By

Hongxi Luo

May 2021

APPROVAL SHEET

This

Dissertation

is submitted in partial fulfillment of the requirements for the degree of

Doctor of Philosophy

Author:

Hongxi Luo

This Dissertation has been read and approved by the examing committee:

Advisor: Geoffrey M. Geise

Committee Member: Gaurav Giri

Committee Member: Joshua J. Choi

Committee Member: Rachel A. Letteri

Committee Member: Lisa Colosi Peterson

Accepted for the School of Engineering and Applied Science:

Craig H. Benson, School of Engineering and Applied Science

May 2021

Acknowledgments:

This section is made to present my utmost gratitude for those who love me and support me. I, Hongxi Luo, value this section as the most important one in this dissertation.

First of all, I want to thank my family members. I spent most of my childhood with my great grandmother, Mrs. Xianxi Fu, and my grandparents, Mr. Chuandong Luo and Mrs. Guimei Jiang. My great grandmother, you perhaps never knew what science and engineering are, but you taught me the most important lesson in my lifetime, being an ethical person and trying to think what I could do for others. I really hope you could see me becoming the second Dr. Luo in the family, but I guess you would still be proud of me, as you always did. My grandparents, both of you just retired by the time I was born. You could have enjoyed the leisure, but instead you chose to take care of me. You spent a lot time showing me around my hometown, and probably have bought me every toy that I have asked for. The unconditional love I received from you in my childhood later becomes the strongest shield in my mind. When I became a primary school student, I moved back to live with my parents, Mr. Zhen Luo and Mrs. Yun Li. Both of you have sacrificed a lot in your self-development, to give me a stable and warm home for my growth. Both of you are very open-minded, and you respect each decision I made in my life and for my career. Eight years ago, I decided to study abroad and switched my major from chemistry to chemical engineering. Facing a new environment and a new major, I was never stressed, because I know you are always there for me and I know I am the son of two excellent chemical engineers. Thank you for everything you've done for me, and now it's my turn to take care of you. In 2014, I met my wife, Mrs. Fangwei Cheng, at the University of Missouri - Columbia. Ever since then, you became one of the most important parts of my life. I appreciated that you agreed to pursue a doctoral degree together with me, and it was your decision that allowed us to create a lot of warm memories at the University of Virginia. In the past five years, you always make your schedule flexible for me, and that is the major reason why I could always stay focused. During the darkest time of my Ph.D., you were always by my side trying to keep me strong. It was you who pulled me out of the desperation, and it was you who make me willing to trust the world again. Having you as my best friend, my excellent colleague, and my beloved wife is the utmost privilege I've ever had in my life.

Next, I want to thank the members of the Geise research group, Prof. Geoffrey Geise, Dr. Yuanyuan Ji, Dr. Kevin Chang, Ms. Saringi Agata, Mr. Patrick Mccormack, and Mr. Kevin Bahati. Geoff, you were the reason why I applied for UVA. In the past five years, you gave me a lot of guidance on doing research and a lot flexibility to explore the science I'm interested in. We have many fruitful discussions on research, and I benefitted a lot from them. I appreciate that you encouraged me to make decisions on my own such that I could become a better independent researcher. Yuanyuan, you were the only senior graduate student in the lab when I joined the Geise research group. You not only taught me the important technical skills but also shared your experience on being a successful graduate student with me. It's my fortune to learn from a senior student like you. Kevin (KC), you and I joined the lab in the same year, and we have accomplished a lot together. As a friend, you are trustworthy and you always have the patience to listen to me. As a colleague, you are reliable and you are willing to share your credits with me. I'm always grateful for having you in my graduate studies. Saringi and Patrick, thank you for including me as part of your own researches, as those experiences helped me gain better insights into my own researches. I also appreciate that both of you are always being supportive to me. Kevin (KB), you are the undergraduate research who I worked with for four years. Your passion on doing research also motivates me, and I want to thank you for your valuable contribution to my research throughout the four years.

Then, I'd like to thank my committee members, Dr. Gaurav Giri, Dr. Rachel Letteri, Dr. Lisa Colosi Peterson, and Dr. Joshua Choi. Gino, thank you for sharing your knowledge on MOFs with me and encouraging my collaborations with students in your lab, which is an important part of my graduate studies. Rachel, I appreciate the insights on polymer synthesis you offered me and I learnt a lot from our discussions. Lisa, thank you for guiding me through LCA and TEA, these skills opened up more pathways for my future career. As Fangwei's husband, I'm also grateful that you created a cheerful learning environment for her. Seeing her come back from work with a smile often illuminates my mind. Josh, you taught me thermodynamics and I benefited a lot from it later in my research. Thank all of you for your advice and help with my graduate study. It's an honor to work with talented and nice engineers like you, and your suggestions add a lot value to my dissertation.

Now, I want to thank my classmates (graduate class 2016), Dr. Kevin Gu, Ms. Xueying Zhao, Mr. Luke Huelsenbeck, Ms. Lucy Yoon, Ms. Katelyn Dagnall, Ms. Erica Hui, Ms. Naomi Miyake, Mr. Lucas Kimerer, Mr. Joey Roberts and Ms. Devanshi Gupta. Our class is the definitely the best class in this department. We are doing a decent job in research and teaching, and we even never lost a competition in the dessert cooking. But these are only the add-on values of this class, this class is great because of its inclusiveness. The inclusiveness of this class gives me a strong sense of belonging, which is rather important for an international student like me. Kevin, it's always a nice thing to see an undergraduate alumnus in graduate school. Your optimism about life and research motivates me, and I’m sure I would miss the regular Friday dinners we had back in the first year. Xueying, you are always a kind and generous friend and you always invite Fangwei and I to events and share your homemade dessert with us. I also really appreciate your support for Fangwei last year, when she came back to Charlottesville alone. Luke, you are a nice friend and a talented collaborator. My collaboration with you is an important part of my research from 2018 till now. I’m honored to be part of your research, and I’m grateful for the support you gave me during the hard times. Lucy, we had a lot of discussions throughout the entire five years, from courses to research and from work to life. As a collaborator, you are attentive and you could always catch what I missed. As a friend, you gave me a lot of help and I really appreciate it. Kate, Erica, Naomi and Lucas, all of you are my secret Santa (from 2016 to 2019) and I really love the gifts I received from you (different kinds of alcoholic drinks, a coffee cup with caffeine structure on it, a mortar used for grinding garlic and a set of wine glasses with my family name on it). Kate and Naomi, thank you for the delicious cheesecakes you made me on my birthdays and thank you for checking on me during the lockdown of Wuhan. Erica, thank you for your help when I needed to use equipment in your lab back in 2018 and I also appreciate your support during the COVID-19 outbreak. Lucas and Joey, I benefited a lot by learning some chromatography knowledge from you in the spring of 2019, and I really enjoyed the class events held at your apartment. Devanshi, thank you for offering me a lot of help in the lab during the weekends/holidays in the past 5 years, and thank you for asking me about my situation in Wuhan last year. I really hope our class could have another Chinese-style dinner together in the future (as we did in 2017 and 2019).

Further, I want to thank my collaborators, Dr. Qi Zhang, Dr. Jie Wang, Ms. Natalie Smith, Dr. Yutian Feng, Dr. Zan Gao, and Dr. Yunya Zhang. Not all my friends are my collaborators, but all my collaborators are my friends. Qi and Jie, both of you are excellent researchers and both of you are kind friends. In the past five years, you helped me figure out the solution to scientific problems many times, and you offered me a lot of excellent ideas without any reservation. If I could only pick one thing as ECUST’s contribution to my career and life, that would be assigning you both and me to the same class, Fine Chemical 111. Natalie, you are a talented and optimistic researcher and you offered a lot of help and support to my research last year. I’m rather grateful for what you have done, as those works would never be what they are now without your contributions. Yutian, you gave me a lot of suggestions when I was applying for graduate schools, and those suggestions made my path forward much less tortuous. I also appreciate your advice on how to balance between work and family and you support during the Wuhan lockdown. Zan and Yunya, thank you for showing me a field that I never knew in the past. Your diligence and attitude always motivate me to try my best and become a better researcher.

Abstract

Membrane-based desalination and ion separation processes have been developed to mitigate the stress on global water supply and to satisfy the needs for the emerging clean-energy production and storage field. To continue to meet the increasing demand, advanced and highly selective membranes are required to separate water and ions from seawater in cost-effective and energy-efficient manners. A general lack of fundamental structure-property relationships frustrates the development of these membranes. Advances in membrane synthesis enables precise functionalization of the membranes with task-specific functional groups (e.g., charged group for enhanced salt rejection) or fillers (e.g., size-selective fillers for ion separation), yet more research efforts are required to fully elucidate the role of these functional groups/fillers on the membrane water/salt transport properties. Several problems, important but often overlooked, naturally arise from the membrane functionalization. First, the mismatch of introduced functional group/filler hydrophilicity and the pristine membrane hydrophilicity would cause changes in the hydrated membrane water fraction, which eventually affects the membrane water/salt transport. Next, the introduced functional groups/fillers aimed to tailor the membrane water/salt sorption could possibly change the membrane water/salt diffusion as well, thus making the overall effects of the functional groups/ fillers on the membrane water/salt transport hard to predict. Finally, any functionalization on the membrane is associated with environmental and economic costs, so the membrane functionalization is only justified if the benefits of functionalization overcome such costs.

In this thesis, fundamental theories and basic models related to membrane small molecule transport, e.g., the free volume theory and the solution-diffusion model, were first introduced, to establish the theoretical frameworks for further discussion on desalination and ion separations. The role of two types of functional groups, i.e., interactive and non-interactive functional groups, were then investigated, to study their influences on the membrane water/salt transport properties. Our results suggest that non-interactive functional groups, e.g., triptycene groups, could enhance membrane desalination performances via free-volume rearrangement. As for interactive groups, e.g., hydroxyl groups, configuring them in an even-distribution manner could promote membrane desalination performances as water-clustering in the hydrated membrane is minimized. Pioneer works related to the cleaner production of MOFs containing MMMs were conducted to investigate the feasibility of producing/using such MMMs for ion separation. Life-cycle assessment and techno-economic analysis confirmed the largely environmental and economic favorability producing UiO-66-NH_2 from an aqueous-solution based system, while membrane transport studies and material characterizations suggest further research efforts are necessary to fabricate MMMs containing UiO-66-NH_2 from aqueous-solution based systems for selective ion separation.

Contents

List of Figures

List of Tables

Chapter 1. Introduction

1.1 General Motivations

The population growth and societal development in the past several decades have brought several critical challenges (e.g., global warming, water shortage, energy crisis and food deficiency etc.) to the world, and these challenges must be resolved in the near future for the sake of human civilization.[1–4] Figuring out the pathways to solve these challenges is not a simple task, as these challenges, seemingly independent from each other, are actually highly interconnected. Hence, understanding the connections between these challenges, e.g., how water shortage affects energy crisis, is the first step that the science/engineering community must take. [1–4]

The connections between water shortage, energy crisis and food deficiency are interpreted using the ternary water-energy-food nexus, and some key concepts of the water-energy-food nexus are summarized below.[3–8] First, in many conventional energy production systems, e.g., coal fired power plant, water (steam) is used as the energy-carrying working fluid due to its high heat capacity and high latent heat of vaporization/condensation.[9,10] As such, if more energy were to be produced in the conventional manner to mitigate the energy crisis, more water is required, which might cause further water shortage. Next, in many conventional water productions system, e.g., producing reclaimed water at wastewater treatment plant, energy, either thermally or electrically, is required to drive the process.[11,12] Hence, if more water were to be produced to increase the water supply, more energy is required, which could worsen the energy crisis. Finally, both water and energy are necessary for food production, e.g., water is consumed in agricultural irrigation and energy in consumed in the transportation of food.[5–8] Therefore, if more food were to be produced to alleviate the food deficiency, more water and energy are required, which would result in further water shortage and energy crisis. The analysis on the water-energy-food nexus yields general guidelines for pathways to solve water shortage, energy crisis and food deficiency. Briefly, the water and energy consumption/utilization efficiency associated with food production should be minimized/maximized, and the energy demand associated with water production should also be minimized. However, it is still unclear what manners are optimal for energy production, i.e., what systems should be used to produce more energy, and figuring out these manners requires some knowledge on the global warming mitigation.

The ultimate goal of global warming mitigation is to lower the (equivalent) concentration of carbon dioxide (CO_2) in the atmosphere,[2,13,14] and achieving this goal requires efforts from three directions, e.g., reducing the CO_2 generation, limiting the CO_2 discharge and capturing atmospheric CO_2.[15–18] Among these three directions, the first one is highly related to the energy production, while the latter two are often discussed in the context of carbon capture and storage (CCS).[15–18] Currently, a large portion of energy consumed worldwide is produced by the combustion of fossil fuels, and such energy production manner has high global warming potential, i.e., high CO_2 generation rate per MJ energy produced.[19,20] As such, replacing traditional fossil fuels with cleaner energies, e.g., wind, solar, biomass and nuclear, is necessary, and these cleaner energies should also be prioritized in solving the energy crisis, the water shortage and the food deficiency.[7,21,22]

Certain resources are required to enable the production and/or utilization of cleaner energies. For example, large energy storage device, e.g., a battery, are often necessary for wind and solar energy, and certain elements, e.g., uranium (U), are essential for nuclear energy.[7,21,22] Hence, finding cost-effective and energy-efficient methods to supply the resources for clean energies is rather important.

In the past five year, I tried to tackle two of the challenges/problems discussed above. My major research focus is solving the global water shortage with energy-efficient methods, while my minor research focus is promoting the supply of resources required by cleaner energies. For both focuses, the researches started from identifying the optimal reservoirs of the resource, e.g., where additional water should be produced from. Once the optimal resource reservoir was located, the separation method was proposed, and certain factors that affects the separation were investigated. In the rest of the Introduction Section, the selection of resource reservoirs will be briefly justified first, followed by proposing the separation method and identifying the scientific questions to be answered.

1.2 Resource Reservoirs

The most commonly considered reservoirs for both water and minerals are inland reservoirs. For example, water could be taken from rivers and/or lakes, processed at wastewater treatment plants if necessary, and supplied to end users.[23] Similarly, ores containing lithium or uranium could be mined and refined to produce high purity Li or U for battery production or nuclear power plant.[24,25] Harvesting resources from their inland reservoirs is relatively straightforward, yet it might not be the optimal solution for the future production of resources due to two major constraints. The first constraint arises from the geological distribution of the inland resource reservoirs. Some countries have limited to no inland natural waterbody, e.g., lakes or rivers, and many countries do not have access to certain minerals, e.g., Li containing ores.[24,25] Hence, in these regions, harvesting resources from the inland reservoirs is not practical. The second constraint is associated with the total amount of resource that could be harvested from the inland reservoirs, e.g., how much water is available from the lakes or rivers. For example, among all the earth's waterbody, only 3% is inland water, while the rest 97% is seawater.[1] Similarly, the inland Li and U reserves are much lower than the ocean Li and U reserves, e.g., 16 million tonnes Li (inland) vs. 230 billion tonnes Li (seawater) and 40 million tonnes U (inland) vs. 4.6 billion tonnes U (seawater).[24–27] Therefore, the inland reservoirs are unlikely the long-term solution for the supply of critical resources.

The analysis above suggests that seawater/ocean could be the optimal reservoir for multiple critical resources. However, seawater is a highly complicated mixture, e.g., seawater contains water, salts and organic compounds, so some treatments are necessary to extract the desired resources.[1,23] For example, salt must be removed from seawater, i.e., *desalination*, before seawater is used as drinking water or applied as irrigation water.[28] Furthermore, a desired ion, e.g., Li, must be effectively separated from other interfering ions, i.e., *selective ion separation*, before this ion could be sent to refinery for further processing.[29,30] Therefore, applying desalination and selective ion separation on seawater is the direction I took to solve the global water shortage and to promote the supply of resources required by cleaner energies.

1.3 Membrane-based Desalination and Selective Ion Separation

Polymeric membrane-based separation processes, known for their good energy efficiency and low cost, have been widely used in food industry, pharmaceutical industry, and medical industry.[29] In the past two decades, large scale membrane-based desalination processes have been developed to mitigate the stress on global freshwater supply caused by the societal development and the population growth.[1,31,32] Recently, numerous efforts have been put into lab/pilot scale membrane-based separation of high value metal ions, such as Li and U, from seawater to satisfy the long-term needs for the emerging clean-energy production and storage field.[33,34]

So far, two generations of desalination membranes, cellulose acetate (CA) membranes (first generation) and polyamide (PA) membranes (second generation) have been developed and applied in seawater desalination.[1] Both the CA membranes and the PA membranes allow for high water flux, i.e., high productivity, and high salt rejection, i.e., high water/salt selectivity.[1] However, certain drawbacks exist for both the CA membranes and the PA membranes. For example, CA membranes might undergo acid/base-catalyzed hydrolysis and/or bio degradation, and these factors lead to a narrow range of optimal operation conditions for the CA membranes.[35] Nevertheless, the current state-of-art desalination membranes, PA membranes, are vulnerable to oxidation degradation, so any chlorine-based disinfectant, used for controlling the biol-fouling in the desalination process, must be effectively removed prior to the membrane desalination stage, and the chlorine removal stage generally increase the process energy demand and the process cost.[36] Hence, the next generation of desalination membranes are expected to maintain the advantages of the CA and PA membranes, i.e., the new membranes should have similar water flux and salt rejection at the same operation condition, and the new membranes are expected to show improvements in the membrane chemical and mechanical stabilities compared to the CA and PA membranes.[23,37]

The selective ion separation membranes are more diversified, compared to the desalination membranes. For example, dense membranes bearing cationic groups, e.g., $-NR_4^+$, or anionic groups, e.g., $-SO_3^-$, can used in electric-filed driven processes,[29,30,37] e.g., electrodialysis (ED), to selectively separate anions or cations based on their charge. Furthermore, mixed matrix membranes (MMMs) containing porous fillers, e.g., zeolite or metal organic frameworks (MOFs), could be used to separate ions based on their size.[38–40] Similar to the desalination membranes, certain challenges are often encountered in the practical ion separation using selective ion separation membranes. For example, a ligand containing membrane or an ion-imprinted membrane designed for recovering one ion from seawater, e.g., Li^+, may also recover interfering ions with similar physical-chemical properties, e.g., Na^+ and Li^+ has similar charge and hydration size, especially when the concentration of the interfering ion is much higher than the concentration of the target ion, e.g., Na^+ vs. Li^+.[33,34] Moreover, the ion separation membranes that are selective enough are not often productive enough, i.e., ion selectivity is high yet the ion diffusion is slow, so a larger driving force, e.g., current in the ED process, needs to be applied, which leads to higher process energy demand and process cost.[29,30,37] Hence, the future selective ion separations are expected to possess both high ion selectivity and ion productivity.

Considering the high analogous nature of the desalination and sweater ion separation,[1,37] i.e., the process and the small molecule transport mechanism are similar, a better understanding on the fundaments of cross-membranes water/salt transport process could push the membranes field towards solving the challenges discussed above. For dense polymeric membranes (most of the membranes studied in this thesis are dense membranes) used in the desalination and ion separation, the membranes are assumed to be hydrated by water during the entire process, and the cross-membrane water and salt transport processes could be described by the solution-diffusion model.[41–43] The solution diffusion model depicts the transport process as two phases, the water/salt partitioning from the external solution into the membrane, i.e., solution, followed by the water/salt moving across the membranes, i.e., diffusion. The overall membrane water/salt permeability is a product of the solution component and the diffusion component.[41–43] Additionally, the hindered transport theory suggests the cross-membrane transport take place only the water fraction of the hydrated membranes, as the polymer fraction is often considered impermeable to both water and salts.[41,42,44] It has been widely reported that the higher the membrane water fraction, the higher the membrane water/salt permeability and the lower the membrane water-to-salt selectivity or the salt-to-salt selectivity, i.e., a tradeoff between productivity and selectivity exists.[45] Based on the solution-diffusion model, favorable transport of one species over the other, e.g., water over salt or target ion over interfering ions, could be achieved by tuning either (if not both) the solution component or the diffusion component. For example, introducing charged functional groups, e.g., $-SO_3^-$ or $-NR_4^+$, to a desalination membrane leads to lower salt partition *via* Donnan exclusion, so the water transport is more favorable.[23,37,46,47] With the rapid development in polymer chemistry, precise modification of the membranes with task-specific (e.g., salt rejection or ion binding) functional groups is becoming increasingly viable, yet more research efforts are required to fully elucidate the effects of these functional groups on the membrane water/salt transport properties.[23,37,46,47]

Two problems, important but often overlooked, naturally arise from the membrane modifications. First of all, the mismatch of the introduced functional group/filler hydrophilicity and the pristine membrane hydrophilicity, e.g., adding a hydrophilic $-SO_3H$ group to a hydrophobic polysulfone membrane or incorporating hydrophobic MOFs into a hydrophilic poly(vinyl alcohol) (PVA) membrane, would cause changes in the hydrated membrane water fraction and/or water distribution, which eventually affects membrane water/salt transport properties.[42,44,48] In this case, decoupling the effects of water fraction change from the effects of the functional groups/fillers is necessary to investigate the role of the introduced functional groups/fillers, and such decoupling could potentially be hard to achieve.[46,47] Meanwhile, introducing functional groups/fillers into the membrane to alter water/salt partition/diffusion could possibly change the water/salt diffusion/partition as well, e.g., an ion ligand could possibly promote partition but hinders diffusion, thus making the overall effects of functional groups/fillers on the water/salt permeability difficult to predict.[46,47] Solving these two problems, although requiring new model materials with judicious molecular design, is a crucial step towards better understanding the fundaments of cross-membrane water/salt transport processes, and would eventually shed light on the design principles of better membranes, i.e., membranes that are highly selective, highly productive, and chemically and mechanically robust, for desalination and selective ion separation.

1.4 Summary of the works presented in this thesis

In this thesis, chapter 2, 6 and 7 are related to ion separation, while chapter 3 through 5 are related to desalination. In chapter 2, basic theories that are used to model ion separation selectivity were presented and discussed.[37] In chapter 6 and 7, pioneer works related to the cleaner production of MOFs containing MMMs were conducted to investigate the feasibility of producing/using such MMMs for ion separation.[49] In chapter 3, sulfonated polysulfone membranes bearing chemically inert functional groups were studied to elucidate the role of these groups in promoting the membrane water-to-salt selectivity.[23] In chapter 4 and 5, a series of membranes with similar functional groups and equivalent water fraction were examined to clarify the influence of functional group configurations on the membrane water/salt transport properties.[46,47]

1.5 References

[1] G.M. Geise, H.S. Lee, D.J. Miller, B.D. Freeman, J.E. McGrath, D.R. Paul, Water purification by membranes: The role of polymer science, J. Polym. Sci. Part B Polym. Phys. (2010). https://doi.org/10.1002/polb.22037.

[2] IPCC, Global warming of 1.5°C, 2018.

[3] A.M. Hamiche, A.B. Stambouli, S. Flazi, A review of the water-energy nexus, Renew. Sustain. Energy Rev. (2016). https://doi.org/10.1016/j.rser.2016.07.020.

[4] US Department of Energy, The Water Energy Nexus: Challenges and Opportunities, U.S. Dep. Energy. (2014).

[5] P. D'Odorico, K.F. Davis, L. Rosa, J.A. Carr, D. Chiarelli, J. Dell'Angelo, J. Gephart, G.K. MacDonald, D.A. Seekell, S. Suweis, M.C. Rulli, The Global Food-Energy-Water Nexus, Rev. Geophys. (2018). https://doi.org/10.1029/2017RG000591.

[6] D.L. Keairns, R.C. Darton, A. Irabien, The Energy-Water-Food Nexus, Annu. Rev. Chem. Biomol. Eng. (2016). https://doi.org/10.1146/annurev-chembioeng-080615-033539.

[7] IRENA, Renewable energy in the water, energy and food nexus, 2015.

[8] E.M. Biggs, E. Bruce, B. Boruff, J.M.A. Duncan, J. Horsley, N. Pauli, K. McNeill, A. Neef, F. Van Ogtrop, J. Curnow, B. Haworth, S. Duce, Y. Imanari, Sustainable development and the water-energy-food nexus: A perspective on livelihoods, Environ. Sci. Policy. (2015). https://doi.org/10.1016/j.envsci.2015.08.002.

[9] H2O-Online, Water - Heat Capacity (Specific Heat), Eng. Toolbox. (2004).

[10] U. Buskies, The efficiency of coal-fired combined-cycle powerplants, Appl. Therm. Eng. (1996). https://doi.org/10.1016/1359-4311(96)00001-4.

[11] P.L. McCarty, J. Bae, J. Kim, Domestic wastewater treatment as a net energy producer-can this be achieved?, Environ. Sci. Technol. (2011). https://doi.org/10.1021/es2014264.

[12] F.R. Spellman, Handbook of Water and Wastewater Treatment Plant Operations, 2013. https://doi.org/10.1201/b15579.

[13] C.A. Horowitz, Paris Agreement, Int. Leg. Mater. (2016). https://doi.org/10.1017/s0020782900004253.

[14] United Nations, Adoption of the Paris Agreement, Conf. Parties Its Twenty-First Sess. (2015).

[15] M.E. Boot-Handford, J.C. Abanades, E.J. Anthony, M.J. Blunt, S. Brandani, N. Mac Dowell, J.R. Fernández, M.C. Ferrari, R. Gross, J.P. Hallett, R.S. Haszeldine, P. Heptonstall, A. Lyngfelt, Z. Makuch, E. Mangano, R.T.J. Porter, M. Pourkashanian, G.T. Rochelle, N. Shah, J.G. Yao, P.S. Fennell, Carbon capture and storage update, Energy Environ. Sci. (2014). https://doi.org/10.1039/c3ee42350f.

[16] H. Herzog, Carbon Dioxide Capture and Storage, in: Econ. Polit. Clim. Chang., 2015. https://doi.org/10.1093/acprof:osobl/9780199573288.003.0013.

[17] K.W. Bandilla, Carbon capture and storage, in: Futur. Energy Improv. Sustain. Clean Options Our Planet, 2020. https://doi.org/10.1016/B978-0-08-102886-5.00031-1.

[18] J. Gibbins, H. Chalmers, Carbon capture and storage, Energy Policy. (2008). https://doi.org/10.1016/j.enpol.2008.09.058.

[19] A. Whiting, A. Azapagic, Life cycle environmental impacts of generating electricity and heat from biogas produced by anaerobic digestion, Energy. (2014). https://doi.org/10.1016/j.energy.2014.03.103.

[20] R.M. Cuéllar-Franca, A. Azapagic, Carbon capture, storage and utilisation technologies: A critical analysis and comparison of their life cycle environmental impacts, J. CO2 Util. (2015). https://doi.org/10.1016/j.jcou.2014.12.001.

[21] G. Nikitas, S. Bhattacharya, N. Vimalan, Wind energy, in: Futur. Energy Improv. Sustain. Clean Options Our Planet, 2020. https://doi.org/10.1016/B978-0-08-102886-5.00016-5.

[22] L. Phillips, Solar energy, in: Manag. Glob. Warm. An Interface Technol. Hum. Issues, 2018. https://doi.org/10.1016/B978-0-12-814104-5.00009-0.

[23] H. Luo, J. Aboki, Y. Ji, R. Guo, G.M. Geise, Water and Salt Transport Properties of Triptycene-Containing Sulfonated Polysulfone Materials for Desalination Membrane Applications, ACS Appl. Mater. Interfaces. (2018). https://doi.org/10.1021/acsami.7b17225.

[24] H. Vikström, S. Davidsson, M. Höök, Lithium availability and future production outlooks, Appl. Energy. (2013). https://doi.org/10.1016/j.apenergy.2013.04.005.

[25] G. Sedimentary, S. Appendix, Supply of Uranium, Production. (2012).

[26] Lithium, (n.d.). https://en.wikipedia.org/wiki/Lithium.

[27] Uranium, (n.d.). https://en.wikipedia.org/wiki/Uranium.

[28] M. Elimelech, W.A. Phillip, The future of seawater desalination: Energy, technology, and the environment, Science (80-.). (2011). https://doi.org/10.1126/science.1200488.

[29] T. Uragami, Introduction to Membrane Science and Technology, in: Sci. Technol. Sep. Membr., 2017. https://doi.org/10.1002/9781118932551.ch1.

[30] H. Strathmann, Ion-Exchange Membrane Separation Processes, 2004.

[31] U.N.W.W.A.P. WWAP, The United Nations World Water Development Report 2017. Wastewater: The Untapped Resource. Paris, UNESCO, 2017.

[32] C.J. Vörösmarty, A.Y. Hoekstra, S.E. Bunn, D. Conway, J. Gupta, Fresh water goes global, Science (80-.). (2015). https://doi.org/10.1126/science.aac6009.

[33] W. Luo, G. Xiao, F. Tian, J.J. Richardson, Y. Wang, J. Zhou, J. Guo, X. Liao, B. Shi, Engineering robust metal-phenolic network membranes for uranium extraction from seawater, Energy Environ. Sci. (2019). https://doi.org/10.1039/c8ee01438h.

[34] X. Li, Y. Mo, W. Qing, S. Shao, C.Y. Tang, J. Li, Membrane-based technologies for lithium recovery from water lithium resources: A review, J. Memb. Sci. (2019). https://doi.org/10.1016/j.memsci.2019.117317.

[35] J. Puls, S.A. Wilson, D. Hölter, Degradation of Cellulose Acetate-Based Materials: A Review, J. Polym. Environ. (2011). https://doi.org/10.1007/s10924-010-0258-0.

[36] S. Avlonitis, W.T. Hanbury, T. Hodgkiess, Chlorine degradation of aromatic polyamides, Desalination. (1992). https://doi.org/10.1016/0011-9164(92)80014-Z.

[37] H. Luo, W.A.S. Agata, G.M. Geise, Connecting the Ion Separation Factor to the Sorption and Diffusion Selectivity of Ion Exchange Membranes, Ind. Eng. Chem. Res. (2020). https://doi.org/10.1021/acs.iecr.0c02457.

[38] W. Li, Y. Zhang, Q. Li, G. Zhang, Metal−organic framework composite membranes: Synthesis and separation applications, Chem. Eng. Sci. (2015). https://doi.org/10.1016/j.ces.2015.04.011.

[39] S. Horike, D. Umeyama, S. Kitagawa, Ion conductivity and transport by porous coordination polymers and metal-organic frameworks, Acc. Chem. Res. (2013). https://doi.org/10.1021/ar300291s.

[40] V. Tricoli, F. Nannetti, Zeolite-Nafion composites as ion conducting membrane materials, Electrochim. Acta. (2003). https://doi.org/10.1016/S0013-4686(03)00306-2.

[41] D.R. Paul, Reformulation of the solution-diffusion theory of reverse osmosis, J. Memb. Sci. (2004). https://doi.org/10.1016/j.memsci.2004.05.026.

[42] G.M. Geise, D.R. Paul, B.D. Freeman, Fundamental water and salt transport properties of polymeric materials, Prog. Polym. Sci. (2014). https://doi.org/10.1016/j.progpolymsci.2013.07.001.

[43] J.G. Wijmans, R.W. Baker, The solution-diffusion model: a review, J. Memb. Sci. (1995). https://doi.org/10.1016/0376-7388(95)00102-I.

[44] H. Yasuda, C. Lamaze, L.D. Ikenberry, Permeability of solutes through hydrated polymer membranes. Part I. Diffusion of Sodium Chloride, Die Makromol. Chemie. (1968).

[45] G.M. Geise, H.B. Park, A.C. Sagle, B.D. Freeman, J.E. McGrath, Water permeability and water/salt selectivity tradeoff in polymers for desalination, J. Memb. Sci. (2011). https://doi.org/10.1016/j.memsci.2010.11.054.

[46] H. Luo, K. Chang, K. Bahati, G.M. Geise, Engineering Selective Desalination Membranes via Molecular Control of Polymer Functional Groups, Environ. Sci. Technol. Lett. (2019). https://doi.org/10.1021/acs.estlett.9b00351.

[47] H. Luo, K. Chang, K. Bahati, G.M. Geise, Functional group configuration influences salt transport in desalination membrane materials, J. Memb. Sci. (2019). https://doi.org/10.1016/j.memsci.2019.117295.

[48] H. Yasuda, C.E. Lamaze, A. Peterlin, Diffusive and hydraulic permeabilities of water in water-swollen polymer membranes, J. Polym. Sci. Part A-2 Polym. Phys. (1971). https://doi.org/10.1002/pol.1971.160090608.

[49] H. Luo, F. Cheng, L. Huelsenbeck, N. Smith, Comparison between conventional solvothermal and aqueous solution-based production of UiO-66-NH2: Life cycle assessment, techno-economic assessment, and implications for CO2 capture and storage, J. Environ. Chem. Eng. 9 (2021) 105159. https://doi.org/https://doi.org/10.1016/j.jece.2021.105159.

Chapter 2. Connecting the ion separation factor to the sorption and diffusion selectivity of ion exchange membranes

2.1. Introduction

Natural resources and energy, such as freshwater, minerals and electricity, are indispensable to human life and the development of society, yet continuous global population growth continues to lead to increased demand that challenges the supply of each.[1-7] Polymer membrane-based separation processes are known for high efficiency, reliability, and cost-effectiveness, and they have been widely applied to mitigate stresses on the global supply of natural resources (particularly water) and are being considered to address challenges related to emerging production and storage of clean-energy.[8-11] For example, highly selective reverse-osmosis (RO) membranes can effectively desalinate water,[12-24] and ion exchange membranes (IEMs) can be used to selectively extract target ions from a mixture of electrolytes[25-31] or to serve as a selective, conductive barrier in batteries and fuel cells.[25, 32-43] Among these membrane-based separations, electric field-driven membrane-based processes are of particular interest in the field of desalination,[44-50] specific ion separations,[31, 51-66] and energy applications.[67-74] Processes, including electrodialysis (ED) (for desalination and/or specific ion separations) and reverse electrodialysis (for energy production), have been scaled up in response to this interest.

The electric field-driven nature of ED can lead to higher process costs in some cases as electricity can be more expensive compared to other driving forces (e.g. thermal energy and pressure) that are used to accomplish separations.[9, 49, 75] However, when ED is used in ion

---

This chapter is already published and available from: Luo, H., Agata, W. A. S., & Geise, G. M. (2020). Connecting the ion separation factor to the sorption and diffusion selectivity of ion exchange membranes. Industrial & Engineering Chemistry Research, 59(32), 14189-14206.

separation applications, the high cost of electricity could be overcome by the value of the recovered ions. This situation could be particularly true if the ions, lithium[76-79] or rare Earth elements,[80-82] are sufficiently valuable.

In a typical ED application, cation exchange membranes (CEMs, which contain fixed negatively charged functional groups) and anion exchange membranes (AEMs, which contain fixed positively charged functional groups) are stacked in an alternating fashion. As a current is applied, cations will transport preferentially across the CEMs while anions will transport preferentially across the AEMs.[54, 73, 83, 84] If the relative rates of transport of one cation, versus another, through the CEM (or one anion, versus another, through the AEM) are different, then ED can be used to fractionate ions and to enrich a target ion via the process. Different strategies, such as mixing nanomaterials into IEMs[85, 86] or coating oppositely charged layers and/or layer-by-layer deposition of polyelectrolytes,[60, 62-64, 87-89] have been considered to enhance this form of selectivity. These modifications suggest promising strategies for developing novel IEMs that would enable the capture or enrichment of specific ions from a multi-electrolyte solution.

Several critical challenges, such as membrane selectivity, productivity and durability, still need to be addressed before this form of ion separation will likely be viable. First, many of the high value target ions (e.g., Li^+) are present at very low concentrations compared to other ions (e.g., Na^+ and Mg^{2+}) in the solution. Therefore, membranes offering high selectivity for the target ion over other ions are needed.[76-79] Also, the process must be productive enough to be viable. Low productivity in ED leads directly to higher energy consumption and operating costs.[76-79] Finally, membrane durability must also be considered when designing new IEMs. If, for example, ion selective surface coatings[60, 62-64, 87-89] become damaged over time,[90, 91] repair or replacement of the membranes will result in greater cost over time.

Addressing these challenges could be facilitated by improved understanding of structure-property relationships in IEMs. For example, understanding what specific functional groups enhance the separation of specific ions would go a long way toward engineering new ion selective membranes. While efforts have been underway, for some time, to answer these questions, this area represents an opportunity for polymer science and engineering to understand how the interplay of chemistry and membrane structure contribute to transport mechanisms and ultimately transport properties.

Recently, the greater importance of water/salt selectivity compared to productivity has been emphasized.[92, 93] It is likely that the corresponding view (that selectivity is particularly critical) may also be the case for IEMs used in electric field-driven processes because small molecule transport is highly analogous in these membranes. The ion selectivity of an IEM can be deconvoluted into sorption and diffusion selectivities,[94] and both of these selectivity values can be engineered to achieve selective transport of one ion over others. For example, the membrane could be engineered to preferentially sorb the target ion while excluding the others. Additionally or perhaps alternatively, it could be engineered to preferentially restrict the rate of transport of the other ions relative to the target ion. This review discusses the connections between sorption and diffusion selectivity and the overall ion selectivity of an ion exchange membrane.

Here, the ion selectivity and its sorption and diffusion selectivity contributors are discussed for ion exchange membranes using the framework of the solution-diffusion model. First, relevant theory is discussed followed by discussion of some implications of those theories. In addition to introducing and discussing the different ion selectivity measures for ion exchange membranes, we review several methods that are commonly used to quantify sorption and diffusion selectivity. We also review important assumptions and potential artifacts that are associated with the different methods for determining sorption and/or diffusion selectivity properties. Ultimately, the discussion connects measures of ion selectivity to sorption and diffusion contributors in an effort to provide insight for engineering next generation ion exchange membranes.

2.2. Theory

2.2.1 Separation Factor

The separation factor (SF) describes the tendency of a target ion, i, to pass through a membrane relative to some other ion, j. Typically, the separation factor (sometimes also called the selectivity or permselectivity) is defined as a ratio of concentration normalized fluxes:[95, 96]

$$SF \equiv \frac{J_i/C_i^s}{J_j/C_j^s} \tag{2.1}$$

where J_i is the average flux of ion i, and C_i^s is the concentration of ion i in the upstream solution. Normalizing the flux by the ion concentration in the upstream solution accounts for differences in concentration, as J_i/C_i^s is effectively the permeance of ion i in the limit where the ion concentration on the upstream side of the membrane is much greater than that on the downstream side of the membrane.[6, 9, 97] Thus, SF can be viewed as a ratio of the permeance of i to that of j, and it is often used as a measure of the separation effectiveness (i.e., ion i is typically chosen to be the target ion so that $SF > 1$) of a membrane for ion separation applications (e.g., electrodialysis and Donnan dialysis).[76, 98]

The separation of ions can also be evaluated using the separation efficiency parameter, S_{EP}, which is based on the initial concentrations of the ions in the dilute solution and the concentrations of the ions in the dilute solution after a fixed amount of operating time.[99, 100] The two approaches for characterizing the ion separation are related. In an effective separation where i is the target component, the permeance of i is greater than that of component j. Therefore, in an effective separation process, one would expect the retention of component j at any time t to be greater than the retention of component i, and this situation results in a separation efficiency parameter greater than zero and a separation factor greater than unity. For the purpose of this review, we will focus on the separation factor (Eqn (2.1)) as it describes the relative rates of transport of component i to that of component j.

In addition to Eqn (2.1), the separation factor is, in some cases, also expressed as the ratio of the flux of i to that of j.[101] In this approach, the upstream solution concentrations are not used. This approach can be useful from a process engineering point of view because it provides direct insight into how many i ions transfer per each j ion.

Alternatively, when SF is defined as a ratio of ion permeances, it provides insight into how intrinsic membrane properties affect the ion separation. As a ratio of ion permeance values, Eqn (2.1) considers both the relative number of ions transferred (i.e., flux) and the ion availability (i.e., concentration). For example, in typical Li^+/Mg^{2+} separations, the feed solution typically contains much less Li^+ compared to Mg^{2+} (e.g., the molar ratio of Li^+/Mg^{2+} can be on the order of 0.1 depending on the source).[76] In a membrane separation process, the Li^+ flux would be expected to be much less than that of Mg^{2+} as a result of the smaller driving force for Li^+ transport compared to that for Mg^{2+} transport. Consequently, comparing only the Li^+ and Mg^{2+} fluxes could lead to the conclusion that the membrane is ineffective, as a greater flux of Mg^{2+} (i.e., the interfering ion) is observed relative to that of Li^{+} (i.e., the target ion). However, the process may actually enrich Li^{+} (relative to Mg^{2+}) in the product solution if *SF* > 1. This enrichment means that Li^{+} (i.e., the target ion) is concentrated in the product solution compared to the feed solution, which is the hallmark of an effective process.[76, 98] Therefore, *SF*, as defined in Eqn (2.1), is a useful figure of merit to inform membrane performance for ion separations.

The definition of *SF* in Eqn (2.1) can be used to derive alternate expressions for the separation factor.[56, 57] Often, arriving at these expressions requires knowledge of or assumptions about the ion transport mechanism in the membrane. Here we focus on dense, non-porous ion exchange membranes where transport is described using the solution-diffusion model.[102-104] While porous membranes have, in some cases, been used in electrodialysis applications,[51, 105] the scope of this review is limited to dense, non-porous membranes. The solution-diffusion model describes cross-membrane ion transport as a three-step process.[102, 103, 106] First, ions sorb (or partition) into the membrane from the upstream solution. Next, the ion diffuses through the membrane, and finally, the ion desorbs into the downstream solution.

Fick’s law is often used as the constitutive equation to relate flux to an external concentration difference driving force.[3, 107] When the concentration difference across the membrane is approximately equal to the concentration on the upstream side of the membrane (i.e., $C_i^s \gg C_i^{s,downstream}$), Fick’s law can be written as:[107]

$$J_i = \frac{K_i D_i^m}{L} C_i^s \tag{2.2}$$

where D_i^m is the average diffusion coefficient of ion *i* in the membrane phase, L is the membrane thickness, and the ion sorption coefficient is defined as $K_i \equiv C_i^m / C_i^s$ where C_i^m is the concentration of *i* in the membrane phase.[102, 106] The product of the sorption and diffusion coefficient (i.e., $K_i D_i^m$) is typically called the permeability of ion *i*, and this permeability therefore encapsulates the sorption and diffusion components of the solution diffusion model.[97, 103] Correspondingly, the separation factor can be expressed as:

$$SF = \frac{K_i D_i^m}{K_j D_j^m} = \frac{P_i}{P_j} \tag{2.3}$$

where the separation factor is also equal to the ion *i* / *j* permeability selectivity (i.e., the ratio of the permeability of ion *i*, P_i, to that of ion *j*, P_j).

In ion separation processes seeking to separate ions of like charge, electric fields are often used to drive ion transport. Therefore, in the limiting case where ion transport is driven primarily by an electric field, the ion flux and separation factor can be expressed in terms of ion transport numbers as:[89, 108]

$$J_i = \frac{I t_i}{z_i F} \tag{2.4}$$

$$SF = \frac{z_j}{z_i} \frac{t_i / C_i^s}{t_j / C_j^s} \tag{2.5}$$

where I is the current density, z_i is the valence of ion *i*, t_i is the transport number of *i*, and F is Faraday's constant. The appearance of the ion valences in Eqn (2.5) accounts for differences in the influence of the electric field on the transport of ions of different valence. The transport number describes the fraction of current carried by a particular ion and is defined as:[25, 94]

$$t_i = \frac{{z_i}^2 C_i^m D_i^m}{\sum_i {z_i}^2 C_i^m D_i^m} \tag{2.6}$$

Arriving at Eqn (2.5) requires an assumption that electric field-driven migration dominates over diffusive and convective ion transport.[89, 108] This assumption may be valid when the concentration difference between the upstream solution and the downstream solution is relatively low (to suppress the contribution of diffusive transport) and the applied current density is sufficiently high.[94] The full expression for the Nernst-Planck equation,[107] described elsewhere, can be used in place of this assumption to simultaneously describe the contributions of diffusion, migration, and convection to the flux.[109]

By substituting Eqn (2.6) into Eqn (2.5), the separation factor can be expressed as:

$$SF \cong \frac{z_i}{z_j}\frac{K_i}{K_j}\frac{D_i^m}{D_j^m} \tag{2.7}$$

Both Eqns (2.3) and (2.7) suggest that the separation factor can be expressed in terms of the sorption selectivity, K_i/K_j, and the diffusivity selectivity, D_i^m/D_j^m. Both of these selectivity values are intrinsic material properties of the membrane, though as will be discussed subsequently, the sorption selectivity may also depend on characteristics of the solution. A summary of different forms of the separation factor is provided in Table. 2.1.

Table 2. 1 Summary of the SF expressions discussed in Section 2.2.1. The separation efficiency parameter, SEP, stems from an ion retention perspective and is based on the initial concentrations of the ions in the dilute solution and the concentrations of the ions in the dilute solution after a fixed amount of operating time.[99, 100] The criteria for an effective separation, where component i is the target ion, are SF > 1 and SEP > 0.

Index for Separation Efficiency	Definition/Formula	Applicability

Separation Factor (*SF*)	$SF \equiv \frac{J_i/C_i^s}{J_j/C_j^s}$	General by Definition
	$SF = \frac{K_i D_i^m}{K_j D_j^m} = \frac{P_i}{P_j}$	Dense Membranes; Transport Driven by a Concentration Gradient
	$SF \cong \frac{z_i}{z_j} \frac{K_i D_i^m}{K_j D_j^m}$	Dense Membranes; Transport Driven by an Electric Field
Separation Efficiency Parameter (S_{EP})[99, 100]	$S_{EP}(t) = \frac{\left(c_j(t)/c_j(0)\right) - \left(c_i(t)/c_i(0)\right)}{\left(1 - c_j(t)/c_j(0)\right) + \left(1 - c_i(t)/c_i(0)\right)} \times 100\%$	General by Definition

2.2.2 Ion Sorption Selectivity

The equilibrium ion sorption coefficient, K_i, is defined as the ratio of the concentration of *i* in the membrane relative to that in the external solution.[9, 102, 106] The partitioning process, or ultimately the concentration of *i* in the membrane, is affected by the specific properties of the membrane.[3, 6, 97] A particularly profound example of this situation is the one observed when comparing uncharged membranes and ion exchange membranes (IEMs). The fixed charge groups present in ion exchange membranes have a significant influence on ion sorption properties.[3, 6, 97] Furthermore, the choice of ion *i* and/or the way that K_i is used to analyze transport can depend on the application of interest. The following discussion further describes these differences.

To start, we restrict the discussion to single-electrolyte systems. In an uncharged membrane (i.e., a hydrophilic material that does not contain ionizable fixed charges), the equivalent cation and anion concentrations in the membrane must be equal according to the principle of electroneutrality.[106, 110] For monovalent binary salts, this situation simplifies to say that the molar cation and anion concentrations are identical in the membrane.[110] In this case, defining K_i using either the anion or the cation yields the same result.[106, 110]

In IEMs, the concentration of counter-ions (i.e., cations in cation exchange membranes or anions in anion exchange membranes) in the membrane phase is typically greater (and often much greater) than the concentration of co-ions (i.e., ions with the same charge as the fixed charge groups in the membrane).[106, 110-112] When IEMs are used in desalination, co-ion sorption is particularly important because the co-ions are representative of the concentration of mobile salt (i.e., electrically-neutral combinations of ions) in the membrane.[106, 110-112] As such, the co-ion sorption coefficient in an IEM is equivalent to the salt sorption coefficient, K_s, which is useful for studying salt permeability properties of IEMs and ultimately salt rejection for desalination applications.[106, 111, 112]

When IEMs are used in electrodialysis, however, it is desirable to have the counter-ions carry the majority of the current (i.e., account for the majority of the ion transport).[25, 113] As such, it is useful to consider the counter-ion sorption coefficient. For example, when defining the separation factor using Eqn (2.7) one would use the counter-ion sorption coefficient as counter-ion transport is desired in this case.[94, 113]

The previous examples highlight the different contexts and/or uses of the ion sorption coefficient. Accordingly, the mobile salt (S), co-ion (X), or counter-ion (M) ion sorption coefficients (for ion *i*) are defined as:[114]

$$K_{S,i} \equiv \frac{C_S^m}{C_i^s} \tag{2.8}$$

$$K_{X,i} \equiv \frac{C_X^m}{C_i^s} \tag{2.9}$$

$$K_{M,i} \equiv \frac{C_M^m}{C_i^s} \tag{2.10}$$

where in each case the sorption coefficient is the ratio of the membrane phase ion concentration to the solution phase ion concentration. Figure 2.1 further illustrates the nomenclature embodied by Eqns (2.8) through (2.10).

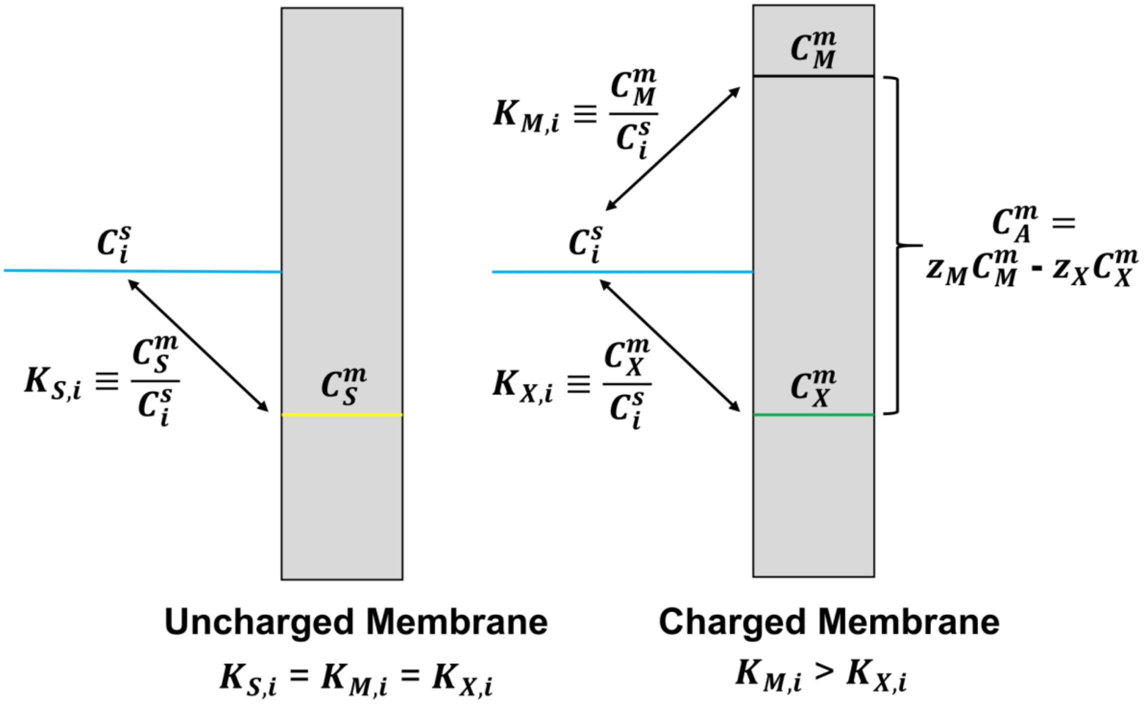

Figure 2. 1. Nomenclature for the ion sorption coefficients and ion concentrations for both uncharged and charged (ion exchange) membranes exposed to a single-electrolyte solution. Often, uncharged membranes exclude salt, and $C_S^m < C_i^s$.[106, 114] In charged (ion exchange) membranes, the counter-ion concentration, C_M^m, is often greater than C_i^s, and co-ions generally are excluded from the membrane (i.e., $C_X^m < C_i^s$).[106, 115] In this example the fixed charge group (the concentration of which is represented by C_A^m) is taken to be monovalent, which is commonly the case in IEMs.[76, 94-96, 113]

The charged (ion exchange) membrane depicted in Figure 2.1 contains fixed charge groups that have charges opposite to that of the counter-ions. To maintain electroneutrality, each fixed charge group (A) must be balanced by a counter-ion, and additionally, each co-ion must be balanced by a counter-ion. If the fixed charge group is monovalent, then the electroneutrality condition requires $C_A^m + z_X C_X^m = z_M C_M^m$.[114, 116]

This charge balance can be divided by the external salt solution concentration to connect the charge balance to the ion sorption coefficient definitions as:

$$K_{M,i} = \frac{z_X}{z_M} K_{X,i} + \frac{1}{z_M} \frac{C_A^m}{C_i^s} \tag{2.11}$$

where z_X is the co-ion valence, z_M is the counter-ion valence, and C_A^m is the membrane fixed charge concentration. For a monovalent (1:1 MX type) electrolyte (e.g., NaCl where M is Na^+ and X is Cl^-), Eqn (2.11) reduces to:

$$K_{M,i} = K_{X,i} + \frac{C_A^m}{C_i^s} \tag{2.12}$$

The relationship for other types of electrolyte (e.g., M_2X) can be obtained in a similar manner from Eqn (2.11) by substituting the corresponding z_X and z_M values into the equation.

Theoretical models can be used, at least in principle, to calculate the value of $K_{X,i}$ (and therefore $K_{M,i}$) for a membrane equilibrated with a single-electrolyte solution. In perhaps the simplest case, the ion sorption process can be described as one where a charge is moved from one dielectric continuum (i.e., the external solution phase) to the membrane phase, which is also taken to be a dielectric continuum, and the Born model describes this relatively simple situation.[106, 117-119] The observation of specific ion effects in ion exchange membranes suggests that dispersion energy may also be important for describing sorption of ions that exhibit Hofmeister series behavior.[114, 119-122] Activity coefficient effects, long neglected in the analysis of ion sorption in polymers, are critical for accurately modeling ion sorption in hydrated polymers, and the Donnan-Manning model can be effective at quantitatively predicting the ion sorption properties of some highly swollen IEMs.[111, 112, 123, 124]

The aforementioned models have been applied to describe single-electrolyte systems. Additional complications arise when considering the multi-electrolyte partitioning problem, which is at the core of ion separation processes.[76, 98, 105] A significant difference between ion partitioning in multi-electrolyte systems and single-electrolyte systems is competition between different counter-ions (e.g., Li^+ and Mg^{2+}) for association with the membrane fixed charge groups (e.g., A^- or SO_3^- in the cation exchange membrane example shown as Figure 2.2).[125, 126] This competition, arising from different affinities between the counter-ions and the membrane fixed charge groups, can be described by an ion-exchange equilibrium constant.[116, 127]

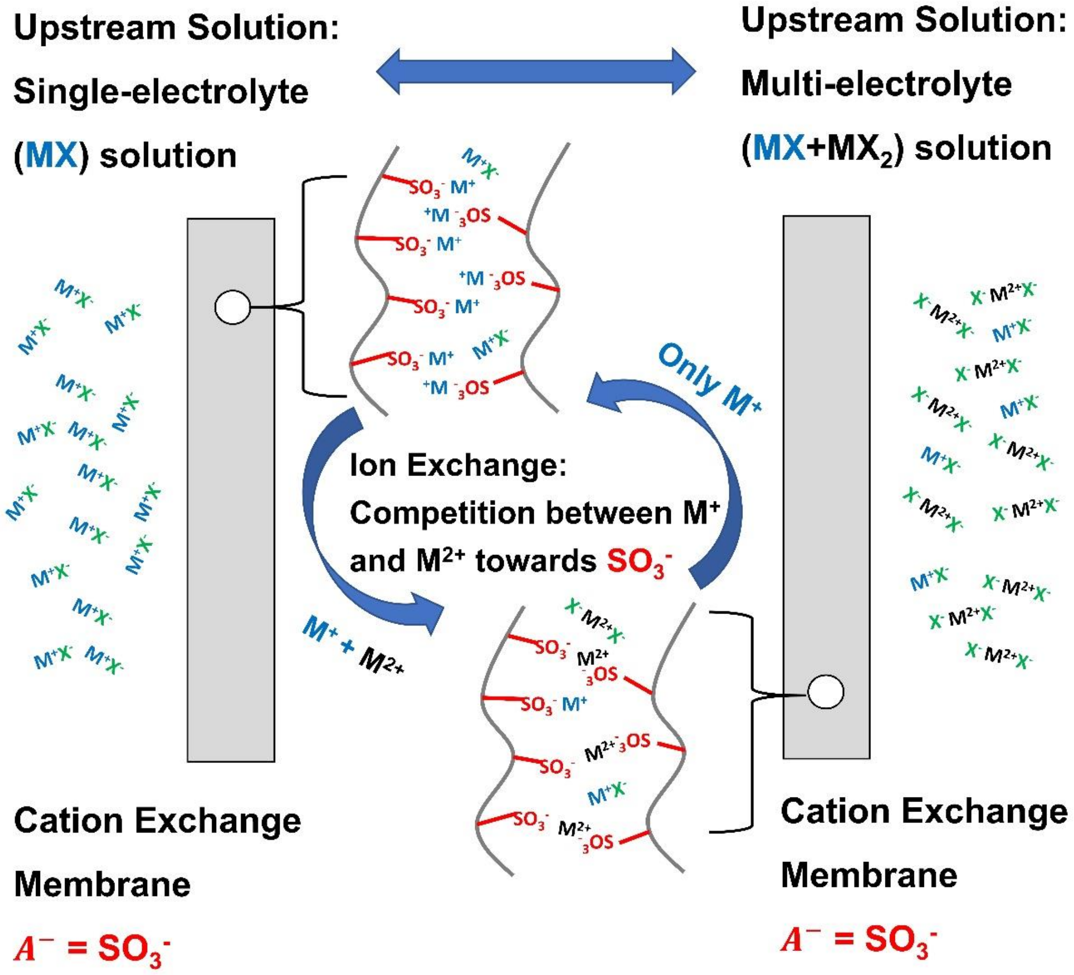

Figure 2. 2. Difference in CEM ion sorption behavior between a single-electrolyte system and a multi-electrolyte system. In the multi-electrolyte system, both cations are present in the membrane phase, and an ion exchange equilibrium constant is generally used to describe the relative composition of the counter-ions associated with the fixed charges.

Ion exchange equilibrium between a cation exchange membrane (CEM) and an electrolyte containing two cations (M_i and M_j) where M_i is a monovalent cation ($z_i = 1$) and M_j is a divalent cation ($z_j = 2$) can be described as:[127, 128]

$$2(A^{-}{M_i}^{+}) + {M_j}^{2+} \rightleftharpoons 2{M_i}^{+} + (A^{-})_2{M_j}^{2+} \tag{2.13}$$

This equilibrium relationship can be used to define the ion exchange equilibrium constant, K_{iex}, which is typically defined using concentrations as opposed to thermodynamic activity values, as:[128]

$$K_{iex} = \frac{C_j^m}{C_j^s}\left(\frac{C_i^s}{C_i^m}\right)^2 = \left(\frac{C_j^m}{C_j^s}\right)^{|z_i|}\left(\frac{C_i^s}{C_i^m}\right)^{|z_j|} \tag{2.14}$$

The expression can be generalized in terms of $|z_i|$ and $|z_j|$ (as shown on the right-hand side of Eqn (2.14)). The value of K_{iex} can be determined experimentally,[127, 128] but values are reported, often for ion exchange resins prepared using chemistry that is similar to that used in many ion exchange membranes.[129]

The ion exchange equilibrium constant can be expressed using dimensionless ion concentrations to facilitate use with ion exchange isotherms. In the solution phase, the dimensionless composition of counter-ion *j* (in a mixture of counter-ions *i* and *j*) can be written as:

$$x_j = \frac{|z_j|C_j^s}{|z_j|C_j^s + |z_i|C_i^s} \tag{2.15}$$

The concentration of cations in the solution phase, in units of equivalents of charge per volume, can be written as:

$$C_0 = |z_j|C_j^s + |z_i|C_i^s \tag{2.16}$$

For example, in the multi-electrolyte (M_iX and M_jX_2) system described in Figure 2.2, $C_0 = 2C_{M_j^{2+}}^s + C_{M_i^+}^s$. The corresponding dimensionless composition of counter-ion *j* in the membrane phase can be written as:

$$y_j = \frac{|z_j| C_j^m}{C_A^m} \tag{2.17}$$

where the fixed charge group has been taken to be monovalent, i.e., $|z_A| = 1$. The value of y_j represents the fraction of fixed charge equivalents that are associated with counter-ion *j*, and if only two counter-ions are present (*i* and *j*), then $y_i = 1 - y_j$ and represents the fraction of fixed charge equivalents that are associated with counter-ion *i*. Using Eqns (2.15) through (2.17) and by taking counter-ion *i* to be a monovalent ion (i.e., $|z_i| = 1$), Eqn (2.14) can be simplified by introducing the dimensionless concentrations:[51]

$$K_{iex} = \frac{(1-x_j)^{|z_j|} y_j}{x_j (1-y_j)^{|z_j|}} \left(\frac{C_0}{C_A^m}\right)^{|z_j|-1} \tag{2.18}$$

If counter-ion *j* is a monovalent ion (i.e., $|z_j| = 1$), then the value of K_{iex} does not depend on either the membrane fixed charge concentration, C_A^m, or the equivalent counter-ion concentration in the solution, C_0.[127] However, if counter-ion *j* is a divalent (i.e., $|z_j| = 2$) or a trivalent (i.e., $|z_j| = 3$) ion, then K_{iex} is affected by the ratio of C_0/C_A^m, either linearly or quadratically.[51] To account for this dependence, K_{iex} can be further normalized by C_0/C_A^m to yield the dimensionless ion exchange affinity, α_i^j:[127]

$$\alpha_i^j = K_{iex} \left(\frac{C_0}{C_A^m}\right)^{1-|z_j|} = \frac{(1-x_j)^{|z_j|} y_j}{x_j (1-y_j)^{|z_j|}} \tag{2.19}$$

Therefore, if the value of α_i^j is known, one can calculate the dimensionless counter-ion composition in the membrane phase, y_j, given a particular solution composition, x_j. If the values of y_j and y_i are known at given values of x_j and x_i, then the dimensionless counter-ion composition values can be used to calculate sorption coefficients for each counter-ion:[127]

$$K_i = \frac{(1-y_j)C_A^m}{(1-x_j)C_0} \tag{2.20}$$

$$K_j = \frac{y_j C_A^m}{x_j C_0} \tag{2.21}$$

The ratio of these sorption coefficients can be taken to define the membrane sorption selectivity of counter-ion *i* relative to counter-ion *j*.

$$K_j^i \equiv \frac{K_i}{K_j} = \frac{x_j(1-y_j)}{y_j(1-x_j)} \tag{2.22}$$

The expression of K_j^i in Eqn (2.22) is related to the expression of α_i^j in Eqn (2.19). The relationship between K_j^i and α_i^j will be discussed in further detail in Section 2.3.1.

2.2.3 **Counter-Ion/Counter-Ion Diffusivity Selectivity**

The counter-ion/counter-ion diffusivity selectivity, D_i^m/D_j^m, represents the relative kinetic rates of diffusion or mobility of counter-ion *i* relative to counter-ion *j* in the membrane.[84, 94] Unlike ion sorption selectivity in multi-electrolyte systems, where the selectivity often is determined experimentally, the ion diffusivity selectivity for multi-electrolyte systems can be either experimentally measured or, in some cases, calculated via theory. This section describes two theoretical models (the theory of Mackie and Meares and free volume theory) that are used to calculate ion diffusion coefficients and experimental approaches to measure ion diffusivity properties.

2.2.3.1 The Theory of Mackie and Meares

The theory of Mackie and Meares is a statistical description of small molecule diffusion in a mixture of polymer and solvent.[130, 131] The theory is based on the assumption that the swollen membrane is a homogeneous mixture of polymer and sorbed water.[130] This mixture is represented on a lattice, and lattice positions occupied by polymer are considered impermeable. Therefore, small molecules can only diffuse by executing diffusional jumps between lattice positions that do not contain polymer.

The physical implication of this treatment is that cross-membrane transport occurs through the volume of the swollen material that is occupied by the sorbed water. As such, the presence of the polymer has two effects on transport. First, the presence of the polymer reduces the effective cross-sectional area available for transport, and second, it increases the tortuosity.[130] Both of these effects lead to reduction in diffusivity.

The Mackie and Meares model connects the membrane phase diffusion coefficient, D_i^m, to that in the external solution via the volume fraction of water as:

$$\frac{D_i^m}{D_i^s} = \left(\frac{\phi_W}{2-\phi_W}\right)^2 \tag{2.23}$$

where D_i^s is the diffusion coefficient in bulk solution, and ϕ_W, the only variable in the model, is the membrane water volume fraction.[130, 131] An important feature of Eqn (2.23) is that it ensures the diffusion coefficient in the membrane converges to the diffusion coefficient in bulk solution as ϕ_W approaches unity (i.e., the pure solution limit).[106] In general, the Mackie and Meares model is most likely to be suitable for describing diffusion in highly swollen membranes (ϕ_W > 0.5)[112, 113] and systems with negligible ion-polymer interactions,[106] and in these cases, the effects described by the Mackie and Meares model can be much greater than electrostatic effects.

Applying the Mackie and Meares model for two different counter-ions, i and j, and assuming the volume fraction of water in the membrane, ϕ_W, is independent of the presence of the ions, the ion diffusivity selectivity reduces to:

$$\frac{D_i^m}{D_j^m} = \frac{D_i^s}{D_j^s} \tag{2.24}$$

This expression suggests that the membrane ion diffusivity selectivity is identical to the diffusivity selectivity observed in solution, i.e., the membrane provides no additional diffusivity selectivity. Such a condition, which might be realized for some highly swollen membranes, is often not valid for many electrodialysis membranes, which typically have lower water content (e.g., ϕ_W ~ 0.3)[104] and potentially non-negligible ion-polymer interactions. Nonetheless, the ion diffusivity selectivity obtained from the Mackie and Meares model can be treated as a limiting value for the membrane ion diffusivity selectivity as it represents the limiting case where the membrane makes no contribution to the diffusivity selectivity.

2.2.3.2 Free Volume Theory

Yasuda *et al.* studied NaCl transport in a series of hydrogels[132] and suggested that cross-membrane transport can be described using a free volume-based model:[133, 134]

$$D_i^m \sim exp\left[-\frac{V^*}{V_f}\right] \tag{2.25}$$

where V^* is the minimum free volume size required by a penetrant, V_f is the total free volume of the membrane. Yasuda *et al.* assumed that the membrane free volume was proportional to the hydration, H, as:[133]

$$H \equiv \frac{Mass\ of\ Water}{Mass\ of\ Hydrated\ Polymer} \tag{2.26}$$

$$V_f = (1-H)V_{f,P} + HV_{f,W} \tag{2.27}$$

where $(1-H)$ is the mass fraction of polymer in the membrane, $V_{f,P}$ is the polymer free volume, and $V_{f,W}$ is the free volume of water. Yasuda *et al.* further assumed that salt alone would not diffusion through the non-hydrated regions (or free volume) of the polymer.[133] Therefore, the free volume available for salt transport, in Eqn (2.27), was taken to be $HV_{f,W}$ or $V_f \sim HV_{f,W}$. Eqns (2.25) and (2.27) lead to a useful correlation, where H is the only variable, for D_i^m/D_i^s:[132]

$$\frac{D_i^m}{D_i^s} = exp\left[b\left(1-\frac{1}{H}\right)\right] \tag{2.28}$$

and b is an adjustable parameter related to the size of the penetrant.

Although Yasuda's free volume-based theory was initially applied to hydrogels, it has also been successfully applied to predict the penetrant diffusivity in IEMs. Xie *et al.* investigated the dependence of membrane salt diffusivity on average free volume element size for a series of sulfonated polysulfone membranes and found that the experimentally measured diffusivity values correlated, in a manner consistent with the free volume-based theory, as:[135]

$$D_i^m = A\exp\left[-\frac{\gamma V^*}{V_F^H}\right] \tag{2.29}$$

where A is a polymer related constant, γ is a correction factor to prevent double counting the free volume elements, and V_F^H is the average free volume element size in the hydrated polymer.

The value of V^* necessarily depends on the penetrant. For example, if NaCl is used as the model penetrant, the V^* value in Eqn (2.29) can be taken as the volume for the hydrated sodium ion.[136] This value is used rather than the combined volume of the hydrated sodium and chloride ions since the former is larger than the latter (i.e., as long as a free volume element is sufficiently large to permit a hydrated sodium ion to execute a diffusional jump, it could also permit a hydrated chloride ion to execute a diffusional jump).[135] Based on Eqn (2.29), the membrane ion diffusivity selectivity, $\alpha_{D(i/j)}$, can be expressed as:

$$\alpha_{D(i/j)} = \frac{D_i^m}{D_j^m} = exp\left[\frac{\gamma(V_j^* - V_i^*)}{V_F^H}\right] \tag{2.30}$$

where V^* is appropriately defined for either counter-ion *i*, V_i^*, or counter-ion *j*, V_j^*.

Use of Eqn (2.30) requires knowledge of the free volume of the hydrated polymer, V_F^H, and this information can, at least in principle, be obtained from Positron Annihilation Lifetime Spectroscopy (PALS) measurements[135, 137-143] or molecular dynamics (MD)[144, 145] simulations. However, both the PALS and MD approaches have some limitations that result in a situation where V_F^H data are not always available or easily obtained for many membranes of interest. This situation limits, at least to some extent, the use of Eqn (2.30).

An alternate approach is to measure the diffusivity selectivity of other molecules. For example, one could measure the water/salt diffusivity selectivity using measurements commonly made on desalination membranes.[115, 146] That information, in principle, can be used to calculate γ/V_F^H using Eqn (2.30). This approach will be discussed in more detail in Section 2.3.2.

2.2.3.3 Conductivity Measurements

In addition to the approaches discussed previously, the membrane ion diffusivity selectivity can also be determined experimentally. For example, ion transport can be measured using Nuclear Magnetic Resonance (NMR),[147-149] neutron spin echo,[150] and/or conductivity measurements.[43, 59, 60, 94-96] Among these experimental techniques, membrane conductivity measurements regularly are used to determine ion diffusivity in ion exchange membranes. When migration dominates over concentration-driven transport, the ion diffusion coefficients in the membrane are linked to the ionic conductivity as:[116]

$$\kappa = \frac{F^2}{RT} \sum_i {z_i}^2 C_i^m D_i^m \tag{2.31}$$

where κ is the ionic conductivity of the membrane, F is Faraday's constant, R is the gas constant, and T is the absolute temperature. For a single electrolyte system, Eqn (2.31) becomes:

$$\kappa = \frac{F^2}{RT} \left({z_M}^2 C_M^m D_M^m + {z_X}^2 C_X^m D_X^m\right) \tag{2.32}$$

Typically, solving for both D_M^m and D_X^m requires two measurements (typically a conductivity measurement and a concentration-driven permeation measurement).[113] In the concentration-driven permeation measurement, the salt permeability is measured, and then, it is used to calculate the salt diffusion coefficient, which can be further deconvoluted into D_M^m and D_X^m.[113] Once the value of D_M^m is known for each counter-ion (e.g., *i* and *j*), the ion diffusivity selectivity, D_i^m / D_j^m, can be calculated.

In the absence of the concentration-driven permeation measurement, an approximation can be used to calculate D_M^m using Eqn (2.32). In ion exchange membranes, due to the presence of fixed charged groups in the polymer matrix, C_M^m is typically much greater than C_X^m (i.e., $z_M C_M^m = z_X C_X^m + C_A^m$ or $C_A^m > C_X^m$).[3, 6, 97] Consequently, the contribution of co-ion migration to the membrane ionic conductivity is often assumed to be negligible.[108] In other words, the co-ion migration term is dropped in Eqn (2.32), and D_M^m can be determined using a single measurement. This approach only works if the counter-ion transport number is sufficiently close to unity.

This assumption can lead to an overestimation of the membrane ion diffusivity and could be propagated forward as error when determining the membrane ion diffusivity selectivity. Therefore, in the Section 2.3.3, we will discuss the importance of accounting for co-ion migration while determining counter-ion diffusion coefficients via conductivity measurements. Specifically, we will discuss the effects of solution composition and membrane physico-chemical properties on co-ion transport.

Furthermore, conductivity measurements also can be used to determine the counter-ion sorption selectivity of the membrane (for counter-ions *i* and *j*).[94, 116, 125] In the limit where the transport number is sufficiently close to unity, a single-electrolyte conductivity measurement can be used to measure the counter-ion diffusion coefficients for both counter-ions (i.e., D_i^m and D_j^m). Also in this limit, Eqn (2.31) can be written in terms of the two counter-ions:

$$\kappa = \frac{F^2}{RT}\left({z_i}^2 C_i^m D_i^m + {z_j}^2 C_j^m D_j^m\right) \tag{2.33}$$

The Nernst-Einstein relation can be used to express the ion diffusion coefficients as ionic mobilities:[113]

$$u_i^m = \frac{z_i F}{RT} D_i^m \tag{2.34}$$

$$\kappa = C_A^m F\big((1 - y_j)u_i^m + y_j u_j^m\big) \tag{2.35}$$

where u_i^m is the membrane phase mobility of ion i, and $(1 - y_j)$ is the dimensionless composition of i in the membrane (per Eqn (2.17)). Arriving at Eqn (2.33) from Eqn (2.31) requires the assumption that co-ion migration is negligible in the binary electrolyte system. This assumption commonly is used for multi-electrolyte systems,[94] since the concentration-driven permeation measurements are less standard for multi-electrolyte systems compared to single electrolyte systems. When D_i^m and D_j^m are available, u_i^m and u_j^m are calculated using Eqn (2.34), and the value of y_j can be obtained using Eqn (2.35). This approach results in a situation where the value of K_j^i can be calculated from Eqn (2.22). Although the mathematical formula for Eqn (2.35) is rather simple, several underlying conditions and assumptions (e.g., solution compositions and ion-polymer interactions) need to be understood to use Eqn (2.35) properly. Those conditions and assumptions will be discussed further in Section 2.3.4.

2.3. Implications

The current density is important when performing electric field-driven experiments to determine the ion separation factor. This consideration is particularly important for characterizing novel membranes and for operating electric field-driven processes. For example, potentiostatic polarization coupled with impedance spectroscopy can result in transport numbers that vary with current density.[151] Many electric field-driven membrane characterization experiments, however, are run below the limiting current density to avoid concentration polarization effects and/or other electrochemical phenomena that occur at elevated current densities. The ion diffusivity and sorption selectivity values are expected to be important at these lower current density values, and the sorption selectivity is expected to remain important at higher current density values.[151] In this section, we discuss the implications of common assumptions and/or analysis/experimental routes on selectivity characterization from the perspective of both the diffusivity and sorption selectivity properties while recognizing that the significance of the diffusivity selectivity may be limited to lower current density situations.

2.3.1 The Relationship between the Dimensionless Ion Exchange Affinity and the Counter-Ion/Counter-Ion Sorption Selectivity

In Section 2.2.2, we suggest that counter-ion sorption in multi-electrolyte systems can be determined from ion exchange isotherms. Specifically, the dimensionless ion exchange affinity, α_i^j, is interconnected to the counter-ion/counter-ion sorption selectivity, K_j^i. Qualitatively, K_j^i is inversely related to α_i^j. This relationship can be realized by considering a given solution composition. An increase in α_i^j suggests that the interactions between counter-ion *j* and the membrane fixed charge groups become more preferential compared to the interactions between counter-ion *i* and the membrane fixed charge groups.[116, 127] Consequently, counter-ion *j* is enriched in the membrane phase relative to counter-ion *i*, which corresponds to a decrease in K_j^i.

A more quantitative interpretation of the relationship between K_j^i and α_i^j, requires knowledge of the valence of counter-ion *j*. When *j* is a monovalent ion (i.e., $|z_j| = 1$), K_j^i is equal to the reciprocal of α_i^j (i.e., $K_j^i = 1/\alpha_i^j$ as can be seen by comparing Eqns (2.19) and (2.22)). Hence, K_j^i is a constant when α_i^j is a constant regardless of the solution composition. When *j* is a multi-valent ion, the only difference between the reciprocal of K_j^i (i.e., K_i^j) and α_i^j, is the valence of counter-ion j. In this case, the value of K_j^i varies with the solution composition when $\alpha_i^j \neq 1$, which can be found by combining Eqns (2.19) and (2.22). For example, if $\alpha_i^j = 5$ for a system containing divalent (*j*) and monovalent (*i*) counter-ions, then K_j^i would increase from 0.26 to 0.43 when x_j increases from 0.1 to 0.9. In general, when the multi-valent ions are considered, the counter-ion/counter-ion sorption selectivity will depend on the solution composition.

The value of α_i^j provides insight into the relationship between y_j and x_j (in addition to its relationship to the counter-ion/counter-ion sorption selectivity). Miyoshi *et al.* reported α_i^j values for a series of commercial ED membranes.[127] Using this range of α_i^j values, ion exchange isotherms were generated using Eqn. (2.19) for systems containing two monovalent counter-ions (Figure 2.3A) or a divalent (*j*) and a monovalent (*i*) counter-ion (Figure 2.3B). These two types of systems are often of interest for practical separation applications.

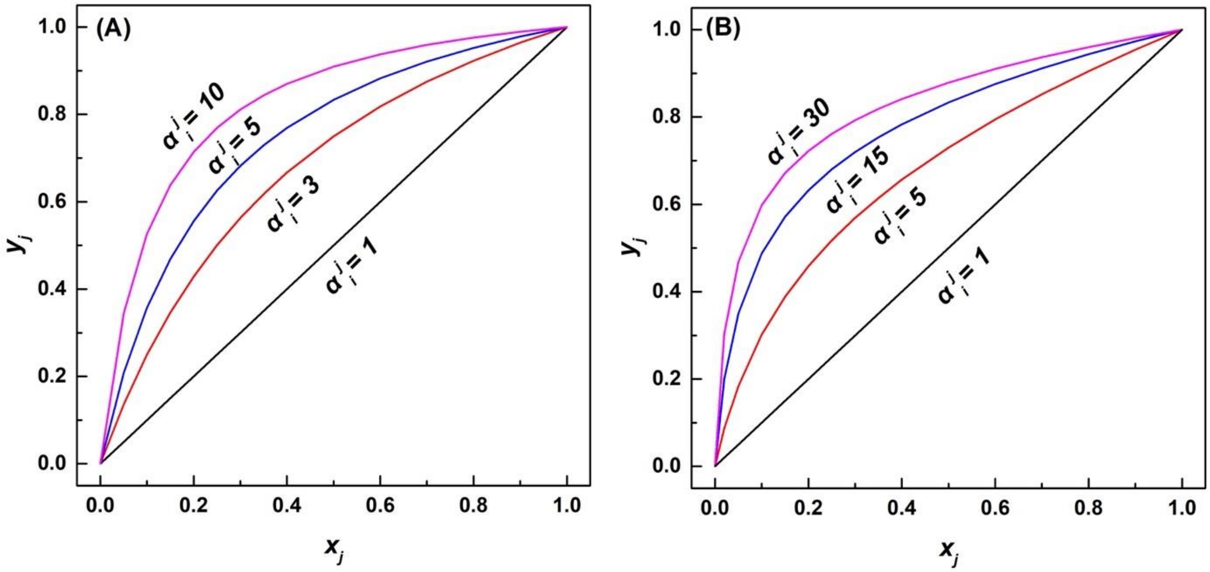

Figure 2. 3. Ion exchange isotherms for systems containing (A) two monovalent counter-ions and (B) a divalent (*j*) and a monovalent (*i*) counter-ion. In both cases, counter-ion *i* was set as a monovalent ion, and values of α_i^j values were chosen to span the range of values reported by Miyoshi *et al.[127]*

When α_i^j is unity (and, accordingly, K_j^i = 1), the dimensionless composition of counter-ion *j* in the membrane phase is identical to its composition in the solution. In other words, counter-ion sorption or ion exchange into the membrane phase does not result in a situation where counter-ion *j* is enriched relative to the composition in the external solution. This situation is the case regardless of whether the solution contains two monovalent counter-ions (Figure 2.3A) or a divalent and a monovalent counter-ion (Figure 2.3B). When α_i^j is greater than 1 (and, accordingly, K_j^i < 1), the dimensionless composition of counter-ion *j* in the membrane phase is always greater than its concentration in the solution (i.e., counter-ion *j* is enriched in the membrane phase and counter-ion *i* is excluded by the membrane phase). When α_i^j values are sufficiently large (e.g., > 5 for a monovalent-monovalent ion pair or > 15 for a divalent-monovalent ion pair), the dimensionless composition of counter-ion *j* in the membrane phase becomes close to unity (i.e., y_j > 0.9, the majority of the counter-ions in the membrane are counter-ion *j*) when the dimensionless composition of counter-ion *j* in the solution is greater than 0.7. This situation is often encountered in practical ion separation processes when the non-target ions, which often have high α_i^j values, are the dominating species in the solution.[76, 98, 152]

For example, in the Li^+/Mg^{2+} separation, the molar ratio of Li^+/Mg^{2+} is around 0.1 in the external solution.[76] In that case, the dimensionless composition of Mg^{2+} in the solution is x_j = 0.947, and the binding affinity of Mg^{2+} towards sulfonate groups is greater than that of Li^+,[129] so the majority of the counter-ions in the membrane will be Mg^{2+} (i.e., $y_j \geq 0.947$). Consequently, the contribution of Mg^{2+} to the membrane ionic conductivity will close to 100% (Eqn (2.35)). Although this behavior does not affect the determination of the ion sorption selectivity using ion exchange experiments, it could result in challenges when determining the ion sorption selectivity from conductivity measurements, as discussed in Section 2.3.4.

2.3.2 Using Free Volume Theory to Relate Measures of Diffusivity Selectivity

In Section 2.2.3, we suggested a free volume theory-based framework that would allow the membrane counter-ion/counter-ion diffusivity selectivity, $\alpha_{D(i/j)}$, to be estimated from a measure of the water/salt diffusivity selectivity, $\alpha_{D(W/S)}$ (or, in principle the selectivity of any two other small molecules). One reason to connect $\alpha_{D(i/j)}$ and $\alpha_{D(W/S)}$ is that some IEMs, and in particular some CEMs,[153-155] are of interest for both desalination and electric field-driven ion separation applications. Using two other probe molecules (e.g., water, *W*, and a single electrolyte, *S*) to measure diffusivity selectivity ($\alpha_{D(W/S)}$ in this case) could provide insight into hydrated polymer free volume as:

$$\frac{\gamma}{V_F^H} = \frac{ln(\alpha_{D(W/S)})}{(V_S^* - V_W^*)} \tag{2.36}$$

The ratio γ/V_F^H is a characteristic of the membrane, and it could then be used in Eqn (2.30) to estimate the counter-ion/counter-ion diffusivity selectivity as:

$$\alpha_{D(i/j)} = \exp\,[ln(\alpha_{D(W/S)})\frac{(V_j^* - V_i^*)}{(V_S^* - V_W^*)}] \tag{2.37}$$

Figure 2.4 shows an example of this relationship where Eqn (2.37) connects transport property data obtained within the context of desalination membranes to that within the context of electric field-driven counter-ion separations.

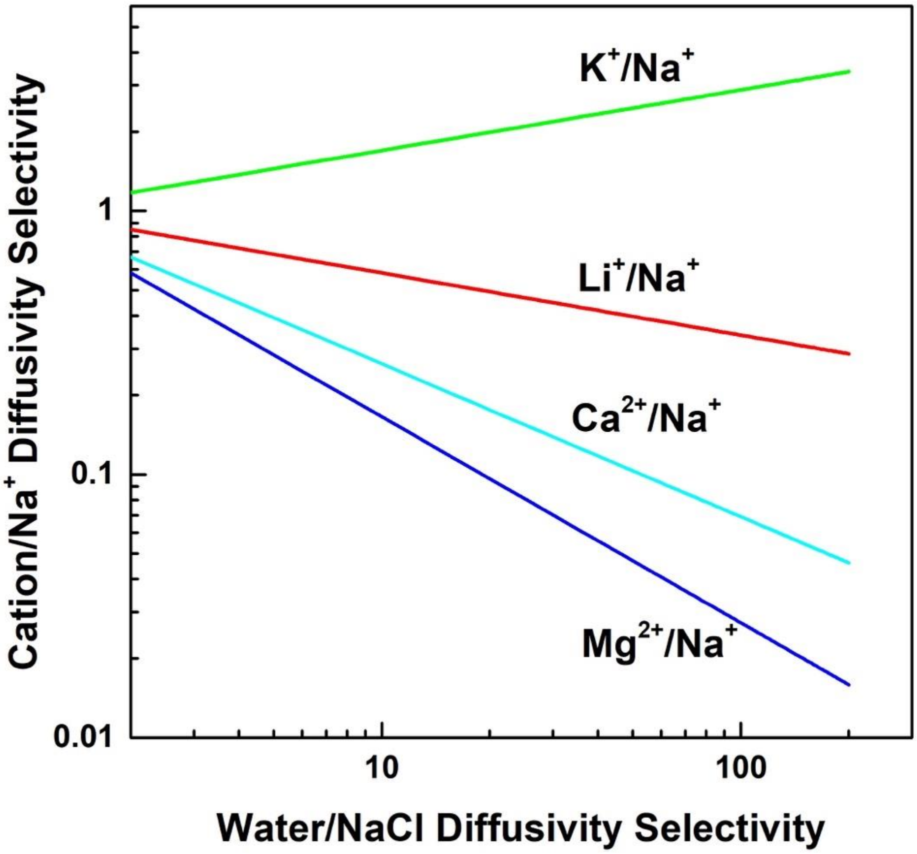

Figure 2. 4. Counter-ion/counter-ion diffusivity selectivity values calculated using the water/salt diffusivity selectivity (Eqn (2.37)). The counter-ion *j* was taken as Na^+, and the salt (water/salt diffusivity selectivity) was taken as NaCl. The range of the water/salt diffusivity selectivity values was chosen based on data reported for a series of sulfonated polysulfones.[135]

When the membrane water/salt diffusivity selectivity is 2, which is the limiting value based on water and NaCl diffusion coefficients in bulk solution, the counter-ion/counter-ion diffusivity selectivity for all of the ion pairs considered reduces to a value close to the corresponding diffusivity selectivity in bulk solution (Figure 2.4).[106] This free volume-based approach also predicts that selectivity for the smaller counter-ion relative to the bigger counter-ion increases as the membrane water/salt diffusivity selectivity increases. It also predicts that the diffusivity selectivity is greater when the size difference between the ions is greater. Both of these observations are generally aligned with Cohen-Turnbull theory, which forms the basis of the free volume-based theory.[134]

As an example of this approach, the water and salt diffusion coefficients for the Neosepta CMX membrane are reported to be 2.5×10^{-6} cm^2/s and 2.1×10^{-7} cm^2/s, respectively, so $\alpha_{D(W/S)} = 12$ for the CMX membrane.[104] According to Eqn (2.37), the values of $\alpha_{D(K^+/Na^+)}$ and $\alpha_{D(Mg^{2+}/Na^+)}$ are 1.77 and 0.147, respectively, when $\alpha_{D(W/S)}$ = 12. These values, predicted using Eqn (2.37), only differ by approximately 10% from the corresponding values measured using a conductivity technique: $\alpha_{D(K^+/Na^+)}$ = 1.62 and $\alpha_{D(Mg^{2+}/Na^+)}$ = 0.165.[94]

While Eqn (2.37) reveals a connection between a measure of diffusion selectivity, commonly considered for desalination membranes, and a measure of counter-ion/counter-ion selectivity that is useful in electric field-driven ion separation applications, the approach does have limitations. Eqn (2.37) suggests that desalination membranes with high $\alpha_{D(W/S)}$ values should also have high $\alpha_{D(i/j)}$ values. While this design criterion results directly from the theory, it may not tell the entire story from a practical perspective. For example, a desalination membrane with a high $\alpha_{D(W/S)}$ value may have very low ionic conductivity due to the lack of fixed charge carriers.[12, 13] This potential situation highlights the need to consider both the selectivity and productivity (in this case, ionic conductivity) properties of membranes for separation applications.

Additionally, the approach to selecting specific values of V_j^* and V_i^* presently is not well defined. When free volume theory is applied to a desalination membrane, the V^* value represents the minimum free volume element size for a molecule to execute a diffusional jump.[135] In electrodialysis, both diffusion and migration occur,[156] and this situation might suggest different interpretation of the V^* values. For the purpose of the example discussed previously, we applied the same interpretation of the V^* values to the counter-ions and the water and single electrolyte used to obtain the desalination-based diffusivity selectivity. While this approach appeared to be sufficient for connecting the two measures of diffusivity selectivity for the Neosepta CMX membrane, additional verification of this V^* value analysis could be necessary for different membranes or ions.

2.3.3 The Influence of Co-ion Transport on Diffusion Coefficients Determined using Conductivity Measurements

As discussed in Section 2.2.3.3, conductivity measurements can be used to measure counter-ion diffusivity (without the use of an additional experiment, e.g., concentration-driven permeation measurements) if the contribution of co-ion migration to conductivity is negligible. This approximation can lead to an overestimation of individual counter-ion diffusivity values, and if these values are used to calculate counter-ion/counter-ion diffusivity selectivity, this overestimation may lead to errors in the membrane ion diffusivity selectivity. This overestimation artifact becomes more significant when the membrane counter-ion transport number decreases and the fraction of the current carried by the co-ions increases. This section discusses an approach to estimate the extent to which neglecting co-ion transport affects the counter-ion diffusivity calculation.

2.3.3.1 Theory to Support Analysis

The co-ion concentration in a charged ion exchange membrane, in the simplest case, is described by Donnan theory.[3, 9, 97, 116, 157] When an IEM is brought into equilibrium with an electrolyte solution, an electric potential (i.e., the Donnan potential) is established at the

IEM/electrolyte interface.[116, 158] This Donnan potential occurs due to the difference in the thermodynamic activity of the ions inside the membrane relative to their corresponding thermodynamic activity values in the external solution caused by the presence of fixed charge groups in the ion exchange membrane.[116, 158] The result of this Donnan potential is that co-ions are excluded from sorbing into the membrane.[116, 158]

The strength or effectiveness of Donnan exclusion increases with the absolute value of the Donnan potential, so co-ion sorption is suppressed to a greater extent in situations where the Donnan potential at the IEM/electrolyte interface is higher.[116] Next, for a given IEM/electrolyte system, the Donnan potential increases (and co-ion sorption decreases) with increases in the difference between the counter-ion activity in the membrane and that in the external solution.[116] The Donnan potential also decreases as the counter-ion valence increases meaning that co-ion sorption tends to be more significant when the multivalent counter-ions are exposed to the membrane.[116] At the same time, Donnan exclusion is more effective at reducing the sorption of multivalent co-ions.[116] Therefore, co-ion sorption (and, thus, co-ion transport) is affected by both solution and membrane factors.

Donnan theory can be used to develop an expression for the co-ion sorption coefficient:[3, 116]

$$K_{X,i} = \frac{C_X^m}{C_i^s} = \sqrt[2]{[\frac{1}{4}\left(\frac{C_A^m}{C_i^s}\right)^2 + \left(\frac{\gamma_\pm^s}{\gamma_\pm^m}\right)^2]} - \frac{1}{2}\frac{C_A^m}{C_i^s} \tag{2.38}$$

where $\gamma_\pm^s$ is the mean ionic activity coefficient in the solution, and $\gamma_\pm^m$ is the mean ionic activity coefficient in the membrane. The value of C_A^m is the fixed charge concentration of the membrane, and the value of $\gamma_{\pm}^{s}$ can be determined using the Pitzer model.[159-161] Determining the value of $\gamma_{\pm}^{m}$, however, is less straightforward.

Manning's counter-ion condensation theory describes the thermodynamic circumstances that lead to a situation where counter-ions condense or un-dissociate in the material.[162] The theory was developed for polyelectrolytes in solution, so it assumes that the fixed charge groups are distributed evenly along the polymer backbone.[162] The so-called Manning parameter, ξ, defines a critical point at which counter-ion condensation occurs in the membrane:

$$\xi = \frac{\lambda_B}{b} = \frac{e^2}{4\pi\varepsilon_0\varepsilon kTb} \tag{2.39}$$

where λ_B is the Bjerrum length (i.e., $\lambda_B = e^2/4\pi\varepsilon_0\varepsilon kT$), b is the spacing between two adjacent charge groups on the polymer backbone, e is the elementary charge, ε_0 is the permittivity of free space, ε is the relative dielectric permittivity (or dielectric constant) of the hydrated membrane, and k is Boltzmann's constant.[111, 162] Above the critical point (i.e., when $\xi > \xi_{crit}$ where $\xi_{crit} = 1$ if the fixed charge group is monovalent), counter-ion condensation occurs such that the value of ξ is to ξ_{crit}.[162] Thus, this condensation process acts to reduce the fixed charge group concentration in the membrane (i.e., C_A^m decreases as a result of counter-ion condensation).[111, 162] Recently, Kamcev *et al.* used Manning's counter-ion condensation theory to calculate the value of $\gamma_{\pm}^{m}$. Their Donnan-Manning model effectively described co-ion sorption in some highly swollen commercial IEMs.[111]

Another result of counter-ion condensation is that the counter-ions in the membrane may exist in one of two different forms.[113] The condensed form is the situation where the counter-ions interact strongly with the fixed charged groups and may reduce the effective membrane fixed charge concentration, and the uncondensed form is the situation where the counter-ions are considered to be dissociated from the fixed charged groups.[113] Condensed counter-ions may have unique transport behavior compared to uncondensed counter-ions. When transport is driven by a concentration gradient, the condensed counter-ions are assumed to be immobile since they are localized near the polymer backbone.[112] When the transport is driven by an electric field, however, these condensed counter-ions are mobile[163-166] and may have greater mobility compared to the uncondensed counter-ions.[113]

2.3.3.2 Analysis for an Idealized Cation Exchange Membrane

With that framework in mind, we return to the analysis about the extent to which neglecting co-ion transport affects the calculation of the counter-ion diffusion coefficient obtained using a single ionic conductivity measurement. To analyze this scenario, we will consider an idealized case where ion-polymer interactions are negligible, and the membrane is a CEM with monovalent fixed charge groups and uncondensed counter-ions. Therefore, we will use the theory of Mackie and Meares[130, 131] to describe the diffusion coefficients in the membrane relative to those in bulk solution. Additionally, we will calculate the membrane phase co-ion concentration, C_X^m, using the Donnan-Manning model (by assuming the membrane fixed charge concentration and dimensionless linear charge density values were 6.21 mol/L and 1.5, respectively, which is representative of the Selemion CMV membrane[104]).[111] The membrane phase counter-ion concentration, C_M^m, will be calculated using the electroneutrality requirement (i.e., $C_A^m + |z_X|C_X^m = |z_M|C_M^m$). Using the information described above, we will define and calculate the minimum counter-ion transport number, $t_{M,min}^m$, as:

$$t_{M,min}^{m} = \frac{z_M{}^2 C_M^m D_M^s}{z_M{}^2 C_M^m D_M^s + z_X{}^2 C_X^m D_X^s} \tag{2.40}$$

Because the minimum counter-ion transport number describes the fraction of ionic current carried by the counter-ions, it can be used to estimate the extent to which the counter-ion diffusion coefficient is overestimated as a result of neglecting co-ion transport. This calculation can be done as:

$$Max. Diffusivity\ Overestimation\ (\%) = \left(\frac{1}{t_{M,min}^{m}} - 1\right) \times 100\% \tag{2.41}$$

where $1/t_{M,min}^{m}$ reflects the over-estimation (i.e., as $t_{M,min}^{m}$ decreases, the counter-ion diffusivity becomes increasingly overestimated). To highlight the effects of solution composition and membrane physico-chemical properties on the co-ion sorption and migration, the minimum counter-ion transport number and the maximum diffusivity overestimation, are plotted against the external salt concentration (Figure 2.5) and the fixed charge group concentration (Figure 2.6) used in the calculations.

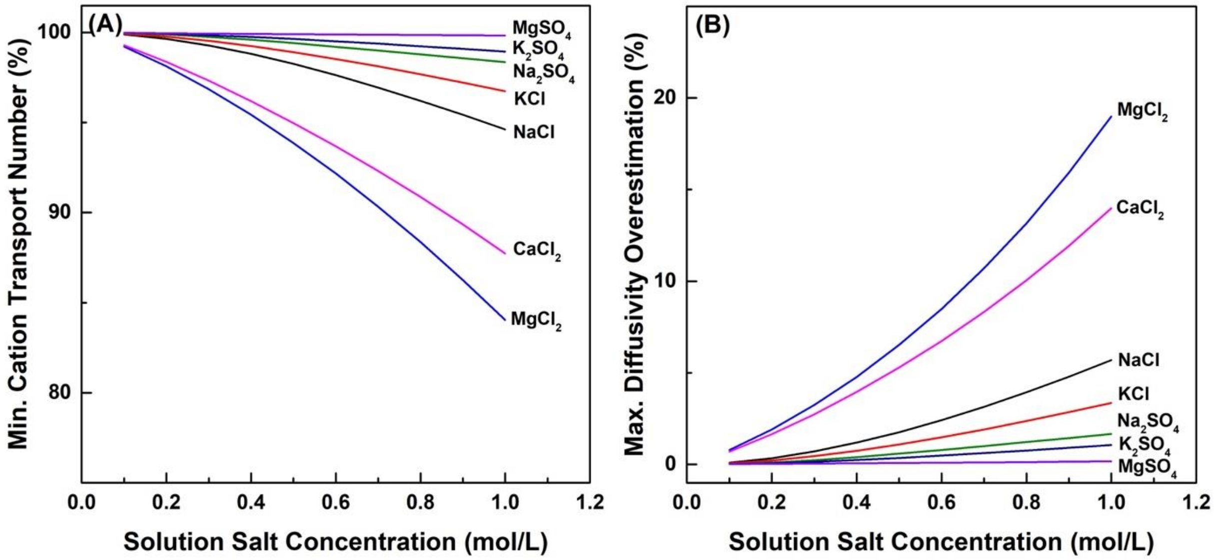

Figure 2. 5. Minimum counter-ion transport number (calculated using Eqn (2.40)) (A) and the maximum diffusivity overestimation (calculated using Eqn (2.41)) (B) in a CEM presented as a function of salt solution concentration for different electrolytes. In those calculations, the co-ion concentration in the membrane was calculated using the Donnan-Manning model,*[111]* the solution activity was calculated using the Pitzer model,[159-161] and the membrane fixed charge concentration and dimensionless linear charge density values were are taken as 6.21 mol/L and 1.5, respectively, to be consistent with the Selemion CMV membrane.[104]

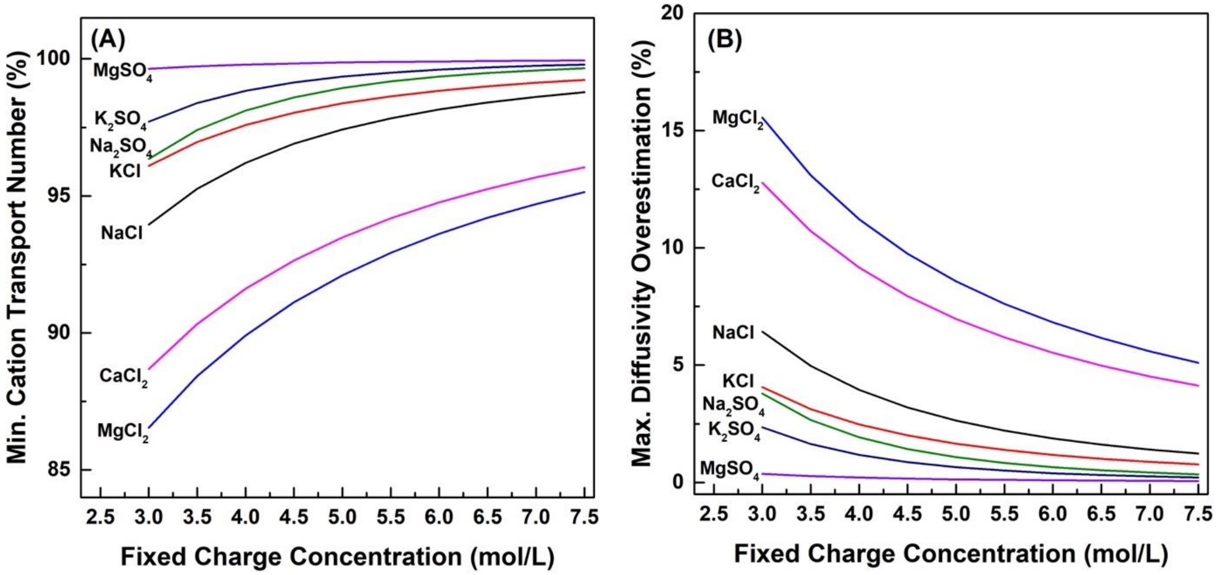

Figure 2. 6. Minimum counter-ion transport number (calculated using Eqn (2.40)) (A) and the maximum diffusivity overestimation (calculated using Eqn (2.41)) (B) in a CEM presented as a function of fixed charge concentration for different electrolytes. The salt solution concentration was fixed at 0.5 M, and the other details of the calculation are provided in the Figure 2.5 caption.

The minimum counter-ion transport number (for this example that is representative of a Selemion CMV cation exchange membrane and all electrolytes considered) decreased by 0.2% to 16% as the solution salt concentration increased (Figure 2.5A), and the maximum diffusivity overestimation increased by 0.2% to 19% as the solution salt concentration increased (Figure 2.5B). These results show that co-ion transport becomes more important as the solution salt concentration increases, and they are consistent with Donnan theory.[116] When the external salt solution concentration increases, the difference between the fixed charge concentration and the ion concentration in solution deceases. This situation leads to a reduction in the Donnan potential (and therefore a reduction in Donnan exclusion effectiveness). Consequently, the values of C_X^m (and, thus, K_X) increase, and co-ion transport becomes more significant.

In addition to the salt solution concentration, the salt type also affects the minimum cation transport number and the maximum diffusivity overestimation. The effects of salt type are secondary, however, compared to the effects of salt solution concentration. In the following discussion, we will hold the salt solution concentration constant.

When the salt type is the same (e.g., NaCl vs. KCl), the value of $\gamma_{\pm}^{s}$ is the only difference in the Donnan-Manning model,[112] and the salt with the lower value of $\gamma_{\pm}^{s}$ (i.e., KCl) will have lower co-ion sorption and transport compared to the salt with the greater value of $\gamma_{\pm}^{s}$. When the co-ion is the same in both electrolytes (e.g., NaCl and $CaCl_2$), several factors affect co-ion sorption. First, the Donnan potential that results from the divalent Ca^{2+} ion is lower compared to the monovalent Na^+ ion, and the lower Donnan potential directly translates into higher co-ion sorption.[116] Next, counter-ion condensation is more likely to occur with the divalent Ca^{2+} ion than with the monovalent Na^+ ion.[112] Counter-ion condensation reduces the Donnan potential and leads to an increase in co-ion sorption.[116] These two effects overpower the effect of the lower value of $\gamma_{\pm}^{s}$ for $CaCl_2$ compared to that of NaCl. As such, having a counter-ion with a greater valence will lead to greater co-ion sorption and transport. When the counter-ion is the same (e.g., KCl vs. K_2SO_4), Donnan exclusion is more effective at excluding the co-ion with the higher valence.[116] Additionally, the value of $\gamma_{\pm}^{s}$ commonly is lower for higher valent co-ions (e.g., SO_4^{2-}) compared to monovalent co-ions. As such, both activity coefficient and Donnan exclusion effects lead to lower co-ion sorption and transport.

The minimum cation transport number increased by 0.2% to 16% as the fixed charge concentration increased (Figure 2.6A), and the maximum diffusivity overestimation decreased by 0.2% to 19% as the fixed charge concentration increased (Figure 2.6B). Similar to the results in Figure 2.5, the results in Figure 2.6 are consistent with Donnan theory.[116] If the solution composition is held constant and counter-ion condensation behavior does not change, increasing the value of the fixed charge concentration leads to an increase in the Donnan potential (and, therefore, an enhancement in Donnan exclusion effectiveness). Consequently, the values of C_X^m (and, thus, K_X) decrease, and the co-ion transport becomes less important.

This analysis could inform the design of conductivity measurements for diffusivity selectivity calculations. The assumption of negligible co-ion transport will be most applicable when the solution salt concentration is moderate (e.g., ~0.5 M), the membrane fixed charge concentration is high (i.e., $C_A^m > 6$ mol/L), and the co-ion is chosen to be the sulfate ion. In situations where greater salt concentration is required, the membrane fixed charge concentration is low (e.g., a CR61 membrane with $C_A^m < 3.5$ mol/L), or the sulfate co-ion cannot be used, the

Donnan-Manning analysis should be performed to estimate influence of co-ion transport on the counter-ion diffusion coefficient. Preferably, the ionic conductivity measurement should be coupled with the concentration-driven permeation measurement to determine the diffusivity selectivity without the need for an assumption about the contribution of the co-ion to the ionic conductivity.

2.3.4 Determining the Counter-Ion/Counter-Ion Sorption Selectivity using Conductivity Measurements

An attractive feature of conductivity measurements is that they can be used to determine the dimensionless composition of counter-ion j in the membrane (i.e., y_j) using Eqn (2.35). Coupled with Eqn (2.22), the value of K_j^i can be calculated. However, the applicability of Eqn (2.22) depends on the ion/polymer interactions and the solution compositions.

The linearity of Eqn (2.35) suggests that the ionic conductivity of the membrane exposed to a multi-electrolyte system containing two different counter-ions is bounded by the separate ionic conductivity values of the membrane in contact with each of the two corresponding single-electrolyte systems. Furthermore, it suggests that the membrane ionic conductivity is expected to vary linearly with y_j (i.e., as the counter-ion composition in the membrane changes, the conductivity of the membrane will change accordingly between the two limiting cases (i.e., $y_j = 0$ and $y_j = 1$). Arriving at this linear relationship requires an assumption that the mobility of each ionic species is independent of the other ionic species in a solution of interest and that the conductivity of this solution is the weighted average of the conductivity of each ionic species (i.e., an assumption that Kohlrausch's law is valid).[167]

In a hydrated CEM, the value of C_M^m is often high (e.g., C_M^m > 3 mol/L), so the membrane cannot be treated as a dilute or ideal system. Furthermore, the presence of fixed charge groups prevents the ions from moving freely inside the membrane. Logette *et al.*[125] studied membrane ionic conductivity for a series of ion pairs, and found that the membrane conductivity for monovalent/divalent and monovalent/trivalent ion pairs deviated more from the Kohlrausch's law predicted values than the conductivity for monovalent/monovalent ion pairs.

Nevertheless, if counter-ion condensation occurs in the membrane, as discussed earlier, the condensed counter-ions may have a greater mobility than the uncondensed counter-ions.[113] Hence, if two counter-ions, i and j, have different condensation behavior, the membrane ion conductivity might not vary linearly with y_j. Therefore caution is warranted when using Eqn (2.35) with different multi-electrolyte systems of interest. The validity of Kohlrausch's law for a particular electrolyte solution should be verified. If Eqn (2.35) does not describe the particular system, ion exchange experiments would be needed to obtain y_j and K_j^i.

If Eqn (2.35) does describe the system of interest, y_j can be determined by interpolation. The interpolation, however, requires that the difference in membrane ionic conductivity between the multi-electrolyte system and each single-electrolyte system is measurable. This requirement might not always be met in practical ion separation processes. For example, in the Li^+/Mg^{2+} separation case discussed earlier,[76] the membrane counter-ions are mostly Mg^{2+}, so the contribution of Mg^{2+}, in the Li^+/Mg^{2+} mixture, to the membrane ion conductivity is nearly 100%. Consequently, it could be difficult to differentiate between the membrane ionic conductivity measured using the Li^+/Mg^{2+} solution and that measured using the pure Mg^{2+} salt solution, which would compromise this approach for characterizing K_j^i based on ionic conductivity measurements.

Eqn (2.35) may be most suitable for systems where the difference between the dimensionless concentrations of counter-ions i and j in the solution is not dramatic (e.g., $0.2 < x_j < 0.6$), as this situation is likely to translate into a situation where the dimensionless compositions of counter-ions i and j in the membrane are not pushed toward the limiting values. For systems similar to the Li^+/Mg^{2+} case encountered in practical separations, an alternative method could be used. A model solution, where $0.2 < x_j < 0.6$, could be prepared for the conductivity measurements, and Eqn (2.35) could be applied to calculate y_j, which could be further translated into α_i^j using Eqn (2.19). The α_i^j value could then be used to calculate a new set of corresponding y_j values at x_j values of interest, and K_j^i could be calculated from this set of data using Eqn (2.22).

2.4. Summary

In this review, definitions of the separation factor were discussed along with connections to the sorption and diffusivity selectivity properties of ion exchange membranes to provide insight into the use of IEMs in electric field-driven specific ion separation applications. The ion sorption selectivity can be determined from ion exchange isotherm or ionic conductivity measurements. When ion exchange isotherm measurements are used to determine the sorption selectivity, a dimensionless ion exchange affinity is used to connect the ion concentration in the membrane for a given solution composition and membrane fixed charge concentration. Alternatively, conductivity measurements can be used to determine the sorption selectivity when the counter-ion form of the membrane is not dominated by a single counter-ion and when ion specific interactions with the polymer are negligible. The diffusivity selectivity can be estimated using theory or be determined using ionic conductivity measurements. Free volume theory may be useful for connecting membrane water/salt selectivity, which is often measured for materials that are of interest for desalination, and the counter-ion/counter-ion diffusivity selectivity that is critical for specific ion separations. The influence of co-ion transport on diffusivity measurements made via conductivity measurements was estimated via sample calculations to highlight situations where neglecting co-ion transport is inappropriate. The discussion here is most applicable to homogeneous ion exchange membranes, but the connections between the ion separation factor and the sorption and diffusivity selectivity values could form the basis for understanding a wide range of membranes that are of interest for electric field-driven ion separation processes.

2.5. References

1. M. Elimelech and W.A. Phillip, The future of seawater desalination: energy, technology, and the environment. science, 2011. **333**(6043): p. 712-717.
2. *The water-energy nexus: Challenges and opportunities*. 2014, U.S. Department of Energy.
3. G.M. Geise, H.S. Lee, D.J. Miller, B.D. Freeman, J.E. McGrath, and D.R. Paul, Water purification by membranes: the role of polymer science. Journal of Polymer Science Part B: Polymer Physics, 2010. **48**(15): p. 1685-1718.
4. R. Connor, A. Renata, C. Ortigara, E. Koncagül, S. Uhlenbrook, B.M. Lamizana-Diallo, S.M. Zadeh, M. Qadir, M. Kjellén, and J. Sjödin, The united nations world water development report 2017. wastewater: The untapped resource. The United Nations World Water Development Report, 2017.
5. C.J. Vörösmarty, A.Y. Hoekstra, S. Bunn, D. Conway, and J. Gupta, Fresh water goes global. Science, 2015. **349**(6247): p. 478-479.
6. G.M. Geise, H.B. Park, A.C. Sagle, B.D. Freeman, and J.E. McGrath, Water permeability and water/salt selectivity tradeoff in polymers for desalination. Journal of Membrane Science, 2011. **369**(1-2): p. 130-138.
7. R. Connor, *The United Nations world water development report 2015: water for a sustainable world*. Vol. 1. 2015: UNESCO publishing.
8. K. Nath, *Membrane separation processes*. 2nd ed. 2017: PHI Learning Pvt. Ltd.
9. R.W. Baker, *Membrane technology and applications*. 3rd ed. 2012, New York: Wiley.
10. J. Kamcev and B.D. Freeman, Charged Polymer Membranes for Environmental/Energy Applications. Annual Review of Chemical and Biomolecular Engineering, 2016. **7**(1): p. 111-133.
11. M.A. Hickner, Ion-containing polymers: New energy & clean water. Materials Today, 2010. **13**(5): p. 34-41.

12. A.P. Rao, N. Desai, and R. Rangarajan, Interfacially synthesized thin film composite RO membranes for seawater desalination. Journal of membrane science, 1997. **124**(2): p. 263-272.

13. N. Misdan, W. Lau, and A. Ismail, Seawater Reverse Osmosis (SWRO) desalination by thin-film composite membrane—Current development, challenges and future prospects. Desalination, 2012. **287**: p. 228-237.

14. W. Lau, A. Ismail, N. Misdan, and M. Kassim, A recent progress in thin film composite membrane: a review. Desalination, 2012. **287**: p. 190-199.

15. R. Verbeke, V. Gomez, and I.F. Vankelecom, Chlorine-resistance of reverse osmosis (RO) polyamide membranes. Progress in Polymer Science, 2017. **72**: p. 1-15.

16. M.R. Chowdhury, J. Steffes, B.D. Huey, and J.R. McCutcheon, 3D printed polyamide membranes for desalination. Science, 2018. **361**(6403): p. 682-686.

17. Z. Tan, S. Chen, X. Peng, L. Zhang, and C. Gao, Polyamide membranes with nanoscale Turing structures for water purification. Science, 2018. **360**(6388): p. 518-521.

18. Z. Jiang, S. Karan, and A.G. Livingston, Water transport through ultrathin polyamide nanofilms used for reverse osmosis. Advanced Materials, 2018. **30**(15): p. 1705973.

19. W. Xie, G.M. Geise, B.D. Freeman, H.-S. Lee, G. Byun, and J.E. McGrath, Polyamide interfacial composite membranes prepared from m-phenylene diamine, trimesoyl chloride and a new disulfonated diamine. Journal of Membrane Science, 2012. **403**: p. 152-161.

20. Z. Yang, H. Guo, and C.Y. Tang, The upper bound of thin-film composite (TFC) polyamide membranes for desalination. Journal of Membrane Science, 2019: p. 117297.

21. Y. Cohen, R. Semiat, and A. Rahardianto, A perspective on reverse osmosis water desalination: Quest for sustainability. AIChE Journal, 2017. **63**(6): p. 1771-1784.

22. K.P. Lee, T.C. Arnot, and D. Mattia, A review of reverse osmosis membrane materials for desalination - Development to date and future potential. Journal of Membrane Science, 2011. **370**: p. 1-22.

23. H. Luo, K. Chang, K. Bahati, and G.M. Geise, Functional group configuration influences salt transport in desalination membrane materials. Journal of Membrane Science, 2019. **590**: p. 117295.

24. H. Luo, K. Chang, K. Bahati, and G.M. Geise, Engineering Selective Desalination Membranes via Molecular Control of Polymer Functional Groups. Environmental Science & Technology Letters, 2019. **6**(8): p. 462-466.

25. Y. Tanaka, ed. *Ion Exchange Membranes: Fundamentals and Applications*. Membrane Science Technology: Elsevier, Netherlands. Vol. 12. 2007, Elsevier: Amsterdam.

26. J. Ran, L. Wu, Y. He, Z. Yang, Y. Wang, C. Jiang, L. Ge, E. Bakangura, and T. Xu, Ion exchange membranes: New developments and applications. Journal of Membrane Science, 2017. **522**: p. 267-291.

27. Y. Guo, Y. Ying, Y. Mao, X. Peng, and B. Chen, Polystyrene sulfonate threaded through a metal–organic framework membrane for fast and selective lithium-ion separation. Angewandte Chemie International Edition, 2016. **55**(48): p. 15120-15124.

28. J. Song, X. Niu, X.-M. Li, and T. He, Selective separation of copper and nickel by membrane extraction using hydrophilic nanoporous ion-exchange barrier membranes. Process Safety and Environmental Protection, 2018. **113**: p. 1-9.

29. D. Rall, D. Menne, A.M. Schweidtmann, J. Kamp, L. von Kolzenberg, A. Mitsos, and M. Wessling, Rational design of ion separation membranes. Journal of membrane science, 2019. **569**: p. 209-219.

30. Y. Zhao, Y. Li, J. Zhu, A. Lejarazu-Larrañaga, S. Yuan, E. Ortega, J. Shen, C. Gao, and B. Van der Bruggen, Thin and robust organic solvent cation exchange membranes for ion separation. Journal of Materials Chemistry A: Materials for Energy and Sustainability, 2019. **7**(23): p. 13903-13909.

31. W. Zhang, M. Miao, J. Pan, A. Sotto, J. Shen, C. Gao, and B. Van der Bruggen, Separation of divalent ions from seawater concentrate to enhance the purity of coarse salt by electrodialysis with monovalent-selective membranes. Desalination, 2017. **411**: p. 28-37.

32. Z. Yuan, Q. Dai, L. Qiao, Y. Zhao, H. Zhang, and X. Li, Highly stable aromatic poly (ether sulfone) composite ion exchange membrane for vanadium flow battery. Journal of Membrane Science, 2017. **541**: p. 465-473.

33. G.-J. Hwang, S.-W. Kim, D.-M. In, D.-Y. Lee, and C.-H. Ryu, Application of the commercial ion exchange membranes in the all-vanadium redox flow battery. Journal of Industrial and Engineering Chemistry, 2018. **60**: p. 360-365.

34. D. Chen, X. Chen, L. Ding, and X. Li, Advanced acid-base blend ion exchange membranes with high performance for vanadium flow battery application. Journal of Membrane Science, 2018. **553**: p. 25-31.

35. Y. Li, J. Sniekers, J.C. Malaquias, C. Van Goethem, K. Binnemans, J. Fransaer, and I.F. Vankelecom, Crosslinked anion exchange membranes prepared from poly (phenylene oxide)(PPO) for non-aqueous redox flow batteries. Journal of Power Sources, 2018. **378**: p. 338-344.

36. R. Xue, F. Jiang, F. Wang, and X. Zhou, Towards cost-effective proton-exchange membranes for redox flow batteries: A facile and innovative method. Journal of Power Sources, 2020. **449**: p. 227475.

37. Z. Fu, J. Liu, and Q. Liu, SPEEK/PVDF/PES composite as alternative proton exchange membrane for vanadium redox flow batteries. Journal of Electronic Materials, 2016. **45**(1): p. 666-671.

38. L. Zhu, X. Yu, and M.A. Hickner, Exploring backbone-cation alkyl spacers for multi-cation side chain anion exchange membranes. Journal of Power Sources, 2018. **375**: p. 433-441.

39. J. Pan, J. Han, L. Zhu, and M.A. Hickner, Cationic side-chain attachment to poly (phenylene oxide) backbones for chemically stable and conductive anion exchange membranes. Chemistry of Materials, 2017. **29**(12): p. 5321-5330.

40. L. Liu, X. Chu, J. Liao, Y. Huang, Y. Li, Z. Ge, M.A. Hickner, and N. Li, Tuning the properties of poly (2, 6-dimethyl-1, 4-phenylene oxide) anion exchange membranes and their performance in H 2/O 2 fuel cells. Energy & Environmental Science, 2018. **11**(2): p. 435-446.

41. L. Zhu, J. Pan, Y. Wang, J. Han, L. Zhuang, and M.A. Hickner, Multication side chain anion exchange membranes. Macromolecules, 2016. **49**(3): p. 815-824.

42. R.S. Kingsbury, K. Chu, and O. Coronell, Energy storage by reversible electrodialysis: The concentration battery. Journal of Membrane Science, 2015. **495**: p. 502-516.

43. P.M. McCormack, H. Luo, G.M. Geise, and G.M. Koenig Jr, Conductivity, permeability, and stability properties of chemically tailored poly (phenylene oxide) membranes for Li+ conductive non-aqueous redox flow battery separators. Journal of Power Sources, 2020. **460**: p. 228107.

44. H.-J. Lee, F. Sarfert, H. Strathmann, and S.-H. Moon, Designing of an electrodialysis desalination plant. Desalination, 2002. **142**(3): p. 267-286.

45. H.-J. Lee, H. Strathmann, and S.-H. Moon, Determination of the limiting current density in electrodialysis desalination as an empirical function of linear velocity. Desalination, 2006. **190**(1-3): p. 43-50.

46. M. Sadrzadeh and T. Mohammadi, Sea water desalination using electrodialysis. Desalination, 2008. **221**(1-3): p. 440-447.

47. S. Adhikary, U. Tipnis, W. Harkare, and K. Govindan, Defluoridation during desalination of brackish water by electrodialysis. Desalination, 1989. **71**(3): p. 301-312.

48. H. AlMadani, Water desalination by solar powered electrodialysis process. Renewable Energy, 2003. **28**(12): p. 1915-1924.

49. R.K. McGovern, A.M. Weiner, L. Sun, C.G. Chambers, and S.M. Zubair, On the cost of electrodialysis for the desalination of high salinity feeds. Applied Energy, 2014. **136**: p. 649-661.

50. M. Turek, Cost effective electrodialytic seawater desalination. Desalination, 2003. **153**(1-3): p. 371-376.

51. B. Van der Bruggen, A. Koninckx, and C. Vandecasteele, Separation of monovalent and divalent ions from aqueous solution by electrodialysis and nanofiltration. Water research, 2004. **38**(5): p. 1347-1353.

52. T. Mohammadi, A. Moheb, M. Sadrzadeh, and A. Razmi, Modeling of metal ion removal from wastewater by electrodialysis. Separation and Purification Technology, 2005. **41**(1): p. 73-82.

53. T. Mohammadi, A. Moheb, M. Sadrzadeh, and A. Razmi, Separation of copper ions by electrodialysis using Taguchi experimental design. Desalination, 2004. **169**(1): p. 21-31.

54. T. Xu and C. Huang, Electrodialysis-based separation technologies: a critical review. AIChE journal, 2008. **54**(12): p. 3147-3159.

55. Y. Zhang, S. Paepen, L. Pinoy, B. Meesschaert, and B. Van der Bruggen, Selectrodialysis: Fractionation of divalent ions from monovalent ions in a novel electrodialysis stack. Separation and Purification Technology, 2012. **88**: p. 191-201.

56. T. Sata, Studies on anion exchange membranes having permselectivity for specific anions in electrodialysis—effect of hydrophilicity of anion exchange membranes on permselectivity of anions. Journal of Membrane Science, 2000. **167**(1): p. 1-31.

57. T. Sata, T. Sata, and W. Yang, Studies on cation-exchange membranes having permselectivity between cations in electrodialysis. Journal of Membrane Science, 2002. **206**(1-2): p. 31-60.

58. S.U. Hong, R. Malaisamy, and M.L. Bruening, Optimization of flux and selectivity in $Cl^{-}/SO_4{}^{2-}$ separations with multilayer polyelectrolyte membranes. Journal of Membrane Science, 2006. **283**(1–2): p. 366-372.

59. C. Cheng, A. Yaroshchuk, and M.L. Bruening, Fundamentals of selective ion transport through multilayer polyelectrolyte membranes. Langmuir, 2013. **29**(6): p. 1885-1892.

60. C. Cheng, N. White, H. Shi, M. Robson, and M.L. Bruening, Cation separations in electrodialysis through membranes coated with polyelectrolyte multilayers. Polymer, 2014. **55**(6): p. 1397-1403.

61. C. Sheng, S. Wijeratne, C. Cheng, G.L. Baker, and M.L. Bruening, Facilitated ion transport through polyelectrolyte multilayer films containing metal-binding ligands. Journal of Membrane Science, 2014. **459**: p. 169-176.

62. N. White, M. Misovich, A. Yaroshchuk, and M.L. Bruening, Coating of Nafion membranes with polyelectrolyte multilayers to achieve high monovalent/divalent cation electrodialysis selectivities. ACS Applied Materials & Interfaces, 2015. **7**(12): p. 6620-6628.

63. Y. Zhu, M. Ahmad, L. Yang, M. Misovich, A. Yaroshchuk, and M.L. Bruening, Adsorption of polyelectrolyte multilayers imparts high monovalent/divalent cation selectivity to aliphatic polyamide cation-exchange membranes. Journal of Membrane Science, 2017. **537**: p. 177-185.

64. L. Yang, C. Tang, M. Ahmad, A. Yaroshchuk, and M.L. Bruening, High selectivities among monovalent cations in dialysis through cation-exchange membranes coated with polyelectrolyte multilayers. ACS Applied Materials & Interfaces, 2018. **10**(50): p. 44134-44143.

65. M. Ahmad, C. Tang, L. Yang, A. Yaroshchuk, and M.L. Bruening, Layer-by-layer modification of aliphatic polyamide anion-exchange membranes to increase Cl^-/SO_4^{2-} selectivity. Journal of Membrane Science, 2019. **578**: p. 209-219.

66. Y. Ji, H. Luo, and G.M. Geise, Effects of fixed charge group physicochemistry on anion exchange membrane permselectivity and ion transport. Physical Chemistry Chemical Physics, 2020. **22**(14): p. 7283-7293.

67. R.D. Cusick, Y. Kim, and B.E. Logan, Energy capture from thermolytic solutions in microbial reverse-electrodialysis cells. Science, 2012. **335**(6075): p. 1474-1477.

68. Y. Kim and B.E. Logan, Hydrogen production from inexhaustible supplies of fresh and salt water using microbial reverse-electrodialysis electrolysis cells. Proceedings of the National Academy of Sciences, 2011. **108**(39): p. 16176-16181.

69. X. Luo, J.-Y. Nam, F. Zhang, X. Zhang, P. Liang, X. Huang, and B.E. Logan, Optimization of membrane stack configuration for efficient hydrogen production in microbial reverse-electrodialysis electrolysis cells coupled with thermolytic solutions. Bioresource technology, 2013. **140**: p. 399-405.

70. G.M. Geise, A.J. Curtis, M.C. Hatzell, M.A. Hickner, and B.E. Logan, Salt concentration differences alter membrane resistance in reverse electrodialysis stacks. Environmental Science & Technology Letters, 2014. **1**(1): p. 36-39.

71. J.W. Post, J. Veerman, H.V. Hamelers, G.J. Euverink, S.J. Metz, K. Nymeijer, and C.J. Buisman, Salinity-gradient power: Evaluation of pressure-retarded osmosis and reverse electrodialysis. Journal of membrane science, 2007. **288**(1-2): p. 218-230.

72. R. Lacey, Energy by reverse electrodialysis. Ocean engineering, 1980. **7**: p. 1-47.

73. Y. Mei and C.Y. Tang, Recent developments and future perspectives of reverse electrodialysis technology: A review. Desalination, 2018. **425**: p. 156-174.

74. R.A. Tufa, S. Pawlowski, J. Veerman, K. Bouzek, E. Fontananova, G. di Profio, S. Velizarov, J.G. Crespo, K. Nijmeijer, and E. Curcio, Progress and prospects in reverse electrodialysis for salinity gradient energy conversion and storage. Applied energy, 2018. **225**: p. 290-331.

75. M. Demircioglu, N. Kabay, I. Kurucaovali, and E. Ersoz, Demineralization by electrodialysis (ED)—separation performance and cost comparison for monovalent salts. Desalination, 2003. **153**(1-3): p. 329-333.

76. X.-Y. Nie, S.-Y. Sun, Z. Sun, X. Song, and J.-G. Yu, Ion-fractionation of lithium ions from magnesium ions by electrodialysis using monovalent selective ion-exchange membranes. Desalination, 2017. **403**: p. 128-135.

77. Z. Zhao, G. Liu, H. Jia, and L. He, Sandwiched liquid-membrane electrodialysis: Lithium selective recovery from salt lake brines with high Mg/Li ratio. Journal of Membrane Science, 2020. **596**: p. 117685.

78. Z.-y. Ji, Q.-b. Chen, J.-s. Yuan, J. Liu, Y.-y. Zhao, and W.-x. Feng, Preliminary study on recovering lithium from high Mg2+/Li+ ratio brines by electrodialysis. Separation and Purification Technology, 2017. **172**: p. 168-177.

79. X.-Y. Nie, S.-Y. Sun, X. Song, and J.-G. Yu, Further investigation into lithium recovery from salt lake brines with different feed characteristics by electrodialysis. Journal of Membrane Science, 2017. **530**: p. 185-191.

80. S. Massari and M. Ruberti, Rare earth elements as critical raw materials: Focus on international markets and future strategies. Resources Policy, 2013. **38**(1): p. 36-43.

81. L. Chen, Y. Wu, H. Dong, M. Meng, C. Li, Y. Yan, and J. Chen, An overview on membrane strategies for rare earths extraction and separation. Separation and Purification Technology, 2018. **197**: p. 70-85.

82. K. Binnemans, P.T. Jones, B. Blanpain, T. Van Gerven, Y. Yang, A. Walton, and M. Buchert, Recycling of rare earths: a critical review. Journal of Cleaner Production, 2013. **51**: p. 1-22.

83. T. Luo, S. Abdu, and M. Wessling, Selectivity of ion exchange membranes: A review. Journal of membrane science, 2018. **555**: p. 429-454.

84. G.M. Geise, Experimental characterization of polymeric membranes for selective ion transport. Current Opinion in Chemical Engineering, 2020. **28**: p. 36-42.

85. L. Cseri, J. Baugh, A. Alabi, A. AlHajaj, L. Zou, R.A. Dryfe, P.M. Budd, and G. Szekely, Graphene oxide–polybenzimidazolium nanocomposite anion exchange membranes for electrodialysis. Journal of Materials Chemistry A, 2018. **6**(48): p. 24728-24739.

86. S. Hosseini, E. Jashni, M. Habibi, and B. Van der Bruggen, Fabrication of novel electrodialysis heterogeneous ion exchange membranes by incorporating PANI/GO functionalized composite nanoplates. Ionics, 2018. **24**(6): p. 1789-1801.

87. N. White, M. Misovich, E. Alemayehu, A. Yaroshchuk, and M.L. Bruening, Highly selective separations of multivalent and monovalent cations in electrodialysis through Nafion membranes coated with polyelectrolyte multilayers. Polymer, 2016. **103**: p. 478-485.

88. S. Mulyati, R. Takagi, A. Fujii, Y. Ohmukai, and H. Matsuyama, Simultaneous improvement of the monovalent anion selectivity and antifouling properties of an anion exchange membrane in an electrodialysis process, using polyelectrolyte multilayer deposition. Journal of membrane science, 2013. **431**: p. 113-120.

89. R. Femmer, A. Mani, and M. Wessling, Ion transport through electrolyte/polyelectrolyte multi-layers. Scientific reports, 2015. **5**: p. 11583.

90. V. Izumrudov and S.A. Sukhishvili, Ionization-controlled stability of polyelectrolyte multilayers in salt solutions. Langmuir, 2003. **19**(13): p. 5188-5191.

91. N.J. Fredin, J. Zhang, and D.M. Lynn, Nanometer-scale decomposition of ultrathin multilayered polyelectrolyte films. Langmuir, 2007. **23**(5): p. 2273-2276.

92. H.B. Park, J. Kamcev, L.M. Robeson, M. Elimelech, and B.D. Freeman, Maximizing the right stuff: The trade-off between membrane permeability and selectivity. Science, 2017. **356**(6343): p. eaab0530.

93. J.R. Werber, A. Deshmukh, and M. Elimelech, The critical need for increased selectivity, not increased water permeability, for desalination membranes. Environmental Science & Technology Letters, 2016. **3**(4): p. 112-120.

94. T. Luo, F. Roghmans, and M. Wessling, Ion mobility and partition determine the counter-ion selectivity of ion exchange membranes. Journal of Membrane Science, 2020. **597**: p. 117645.

95. G. Saracco and M.C. Zanetti, Ion transport through monovalent-anion-permselective membranes. Industrial & Engineering Chemistry Research, 1994. **33**(1): p. 96-101.

96. G. Saracco, Transport properties of monovalent-ion-permselective membranes. Chemical Engineering Science, 1997. **52**(17): p. 3019-3031.

97. G.M. Geise, D.R. Paul, and B.D. Freeman, Fundamental water and salt transport properties of polymeric materials. Progress in Polymer Science, 2014. **39**(1): p. 1-42.

98. X. Wen, P. Ma, C. Zhu, Q. He, and X. Deng, Preliminary study on recovering lithium chloride from lithium-containing waters by nanofiltration. Separation and Purification Technology, 2006. **49**(3): p. 230-236.

99. Y. Zhao, Y. Li, S. Yuan, J. Zhu, S. Houtmeyers, J. Li, R. Dewil, C. Gao, and B. Van der Bruggen, A chemically assembled anion exchange membrane surface for monovalent anion selectivity and fouling reduction. Journal of materials chemistry A, 2019. **7**(11): p. 6348-6356.

100. Y. Zhao, Y. Liu, C. Wang, E. Ortega, X. Wang, Y.F. Xie, J. Shen, C. Gao, and B. Van der Bruggen, Electric field-based ionic control of selective separation layers. Journal of Materials Chemistry A, 2020. **8**(8): p. 4244-4251.

101. R.W. Baker, J. Wijmans, and Y. Huang, Permeability, permeance and selectivity: A preferred way of reporting pervaporation performance data. Journal of Membrane Science, 2010. **348**(1-2): p. 346-352.

102. D.R. Paul, Reformulation of the solution-diffusion theory of reverse osmosis. Journal of membrane science, 2004. **241**(2): p. 371-386.

103. J.G. Wijmans and R.W. Baker, The solution-diffusion model: a review. Journal of Membrane Science, 1995. **107**(1): p. 1-21.

104. R.S. Kingsbury, K. Bruning, S. Zhu, S. Flotron, C. Miller, O.J.I. Coronell, and E.C. Research, Influence of water uptake, charge, Manning parameter, and contact angle on water and salt transport in commercial ion exchange membranes. Industrial & Engineering Chemistry Research, 2019. **58**(40): p. 18663-18674.

105. J. Liu, J. Yuan, Z. Ji, B. Wang, Y. Hao, and X. Guo, Concentrating brine from seawater desalination process by nanofiltration–electrodialysis integrated membrane technology. Desalination, 2016. **390**: p. 53-61.

106. H. Zhang and G.M. Geise, Modeling the water permeability and water/salt selectivity tradeoff in polymer membranes. Journal of Membrane Science, 2016. **520**: p. 790-800.

107. R.B. Bird, Transport phenomena. Appl. Mech. Rev., 2002. **55**(1): p. R1-R4.

108. V.V. Nikonenko, N.D. Pismenskaya, E.I. Belova, P. Sistat, P. Huguet, G. Pourcelly, and C. Larchet, Intensive current transfer in membrane systems: Modelling, mechanisms and application in electrodialysis. Advances in Colloid and Interface Science, 2010. **160**(1-2): p. 101-123.

109. Y. Kim, W.S. Walker, and D.F. Lawler, Competitive separation of di-vs. mono-valent cations in electrodialysis: Effects of the boundary layer properties. Water Research, 2012. **46**(7): p. 2042-2056.

110. G.M. Geise, L.P. Falcon, B.D. Freeman, and D.R. Paul, Sodium chloride sorption in sulfonated polymers for membrane applications. Journal of Membrane Science, 2012. **423-424**: p. 195-208.

111. J. Kamcev, M. Galizia, F.M. Benedetti, E.-S. Jang, D.R. Paul, B.D. Freeman, and G.S. Manning, Partitioning of mobile ions between ion exchange polymers and aqueous salt solutions: importance of counter-ion condensation. Physical Chemistry Chemical Physics, 2016. **18**(8): p. 6021-6031.

112. J. Kamcev, D.R. Paul, G.S. Manning, and B.D. Freeman, Predicting salt permeability coefficients in highly swollen, highly charged ion exchange membranes. ACS Applied Materials & Interfaces, 2017. **9**(4): p. 4044-4056.

113. J. Kamcev, D.R. Paul, G.S. Manning, and B.D. Freeman, Ion diffusion coefficients in ion exchange membranes: significance of counterion condensation. Macromolecules, 2018. **51**(15): p. 5519-5529.

114. Y. Ji, H. Luo, and G.M. Geise, Specific co-ion sorption and diffusion properties influence membrane permselectivity. Journal of Membrane Science, 2018. **563**: p. 492-504.

115. H. Luo, J. Aboki, Y. Ji, R. Guo, and G.M. Geise, Water and salt transport properties of triptycene-containing sulfonated polysulfone materials for desalination membrane applications. ACS Applied Materials & Interfaces, 2018. **10**(4): p. 4102-4112.

116. F.G. Helfferich, *Ion exchange*. 1995, New York: Dover Publications.

117. A.E. Yaroshchuk, Non-steric mechanisms of nanofiltration: Superposition of Donnan and dielectric exclusion. Separation and Purification Technology, 2001. **22-23**(0): p. 143-158.

118. A. Yaroshchuk, Dielectric exclusion of ions from membranes. Advances in Colloid and Interface Science, 2000. **85**: p. 193-230.

119. M. Boström and B.W. Ninham, Energy of an ion crossing a low dielectric membrane: the role of dispersion self-free energy. Biophysical Chemistry, 2005. **114**(2–3): p. 95-101.

120. G.M. Geise, H.J. Cassady, D.R. Paul, B.E. Logan, and M.A. Hickner, Specific ion effects on membrane potential and the permselectivity of ion exchange membranes. Physical Chemistry Chemical Physics, 2014. **16**(39): p. 21673-21681.

121. A. Salis and B.W. Ninham, Models and mechanisms of Hofmeister effects in electrolyte solutions, and colloid and protein systems revisited. Chemical Society Reviews, 2014. **43**(21): p. 7358-7377.

122. T.T. Duignan, D.F. Parsons, and B.W. Ninham, A Continuum Solvent Model of the Multipolar Dispersion Solvation Energy. Journal of Physical Chemistry B, 2013. **117**(32): p. 9412-9420.

123. R.S. Kingsbury, J. Wang, and O. Coronell, Comparison of water and salt transport properties of ion exchange, reverse osmosis, and nanofiltration membranes for desalination and energy applications. Journal of Membrane Science, 2020. **604**: p. 117998.

124. R.S. Kingsbury, K. Bruning, S. Zhu, S. Flotron, C.T. Miller, and O. Coronell, Influence of Water Uptake, Charge, Manning Parameter, and Contact Angle on Water and Salt Transport in

Commercial Ion Exchange Membranes. Industrial & Engineering Chemistry Research, 2019. **58**(40): p. 18663-18674.

125. S. Logette, C. Eysseric, G. Pourcelly, A. Lindheimer, and C. Gavach, Selective permeability of a perfluorosulphonic membrane to different valency cations. Ion-exchange isotherms and kinetic aspects. Journal of membrane science, 1998. **144**(1-2): p. 259-274.

126. A. Chapotot, G. Pourcelly, and C. Gavach, Transport competition between monovalent and divalent cations through cation-exchange membranes. Exchange isotherms and kinetic concepts. Journal of membrane science, 1994. **96**(3): p. 167-181.

127. H. Miyoshi, M. Chubachi, M. Yamagami, and T. Kataoka, Characteristic coefficients for equilibrium between solution and Neosepta or Selemion cation exchange membranes. Journal of Chemical & Engineering Data, 1992. **37**(1): p. 120-124.

128. J.D. Seader, E.J. Henley, and D.K. Roper, *Separation process principles: Chemical and biochemical operations*. 3rd ed. 2011, Hoboken: John Wiley & Sons, Inc.

129. R.E. Anderson, *Ion-Exchange Separations*, in *Handbook of Separation Techniques for Chemical Engineers*, P.A. Schweitzer, Editor. 1997, McGraw-Hill: New York.

130. J. Mackie and P. Meares, The diffusion of electrolytes in a cation-exchange resin membrane I. Theoretical. Proceedings of the Royal Society of London. Series A. Mathematical Physical Sciences, 1955. **232**(1191): p. 498-509.

131. J. Mackie and P. Meares, The diffusion of electrolytes in a cation-exchange resin membrane. II. Experimental. Proceedings of the Royal Society of London. Series A. Mathematical Physical Sciences, 1955. **232**(1191): p. 510-518.

132. H. Yasuda, C. Lamaze, and L. Ikenberry, Permeability of solutes through hydrated polymer membranes. Part I. Diffusion of sodium chloride. Die Makromolekulare Chemie, 1968. **118**(1): p. 19-35.

133. H. Yasuda, C. Lamaze, and A. Peterlin, Diffusive and hydraulic permeabilities of water in water-swollen polymer membranes. Journal of Polymer Science: Part A-2, 1971. **9**(6): p. 1117-1131.

134. D. Turnbull and M.H. Cohen, Free-volume model of the amorphous phase: glass transition. Journal of Chemical Physics, 1961. **34**(1): p. 120-125.

135. W. Xie, H. Ju, G.M. Geise, B.D. Freeman, J.I. Mardel, A.J. Hill, and J.E. McGrath, Effect of free volume on water and salt transport properties in directly copolymerized disulfonated poly (arylene ether sulfone) random copolymers. Macromolecules, 2011. **44**(11): p. 4428-4438.

136. H. Ohtaki and T. Radnai, Structure and dynamics of hydrated ions. Chemical Reviews, 1993. **93**(3): p. 1157-1204.

137. G. Dlubek, V. Bondarenko, J. Pionteck, M. Supej, A. Wutzler, and R. Krause-Rehberg, Free volume in two differently plasticized poly(vinyl chloride)s: A positron lifetime and PVT study. Polymer, 2003. **44**(6): p. 1921-1926.

138. A.J. Hill, B.D. Freeman, M. Jaffe, T.C. Merkel, and I. Pinnau, Tailoring nanospace. Journal of Molecular Structure, 2005. **739**: p. 173-178.

139. R.A. Pethrick, Positron annihilation - A probe for nanoscale voids and free volume? Progress in Polymer Science, 1997. **22**: p. 1-47.

140. Y.C. Jean, P.E. Mallon, and D.M. Schrader, eds. *Principles and applications of positron & positronium chemistry*. 2003, World Scientific Publishing Co.: London.

141. A.W. Dong, C. Pascual-Izarra, S.J. Pas, A.J. Hill, B.J. Boyd, and C.J. Drummond, Positron annihilation lifetime spectroscopy (PALS) as a characterization technique for nanostructured self-assembled amphiphile systems. Journal of Physical Chemistry B, 2008. **113**(1): p. 84-91.

142. Y. Kobayashi, H.F.M. Mohamed, and A. Ohira, Positronium formation in aromatic polymer electrolytes for fuel cells. Journal of Physical Chemistry B Letters, 2009. **113**: p. 5698–5701.

143. Y.C. Jean, J.D. Van Horn, W.-S. Hung, and K.-R. Lee, Perspective of positron annihilation spectroscopy in polymers. Macromolecules, 2013. **46**(18): p. 7133-7145.

144. D. Rigby and R. Roe, Molecular dynamics simulation of polymer liquid and glass. 4. Free-volume distribution. Macromolecules, 1990. **23**(26): p. 5312-5319.

145. M. Shen, S. Keten, and R.M. Lueptow, Dynamics of water and solute transport in polymeric reverse osmosis membranes via molecular dynamics simulations. Journal of Membrane Science, 2016. **506**: p. 95-108.

146. W. Xie, J. Cook, H.B. Park, B.D. Freeman, C.H. Lee, and J.E. McGrath, Fundamental salt and water transport properties in directly copolymerized disulfonated poly (arylene ether sulfone) random copolymers. Polymer, 2011. **52**(9): p. 2032-2043.

147. T. Ogino, J. Den Hollander, and R. Shulman, 39K, 23Na, and 31P NMR studies of ion transport in Saccharomyces cerevisiae. Proceedings of the National Academy of Sciences, 1983. **80**(17): p. 5185-5189.

148. H. Degani and G.A. Elgavish, Ionic permeabilities of membranes: 23Na and 7Li NMR studies of ion transport across the membrane of phosphatidylcholine vesicles. FEBS letters, 1978. **90**(2): p. 357-360.

149. T. Ogino, G. Shulman, M. Avison, S. Gullans, J. Den Hollander, and R. Shulman, 23Na and 39K NMR studies of ion transport in human erythrocytes. Proceedings of the National Academy of Sciences, 1985. **82**(4): p. 1099-1103.

150. C. Do, P. Lunkenheimer, D. Diddens, M. Götz, M. Weiß, A. Loidl, X.-G. Sun, J. Allgaier, and M. Ohl, Li+ transport in poly (ethylene oxide) based electrolytes: neutron scattering, dielectric spectroscopy, and molecular dynamics simulations. Physical review letters, 2013. **111**(1): p. 018301.

151. J.T. Vardner, T. Ling, S.T. Russell, A.M. Perakis, Y. He, N.W. Brady, S.K. Kumar, and A.C. West, Method of measuring salt transference numbers in ion-selective membranes. Journal of The Electrochemical Society, 2017. **164**(13): p. A2940.

152. A. Somrani, A. Hamzaoui, and M. Pontie, Study on lithium separation from salt lake brines by nanofiltration (NF) and low pressure reverse osmosis (LPRO). Desalination, 2013. **317**: p. 184-192.

153. W. Xie, H.-B. Park, J. Cook, C.H. Lee, G. Byun, B.D. Freeman, and J.E. McGrath, Advances in membrane materials: desalination membranes based on directly copolymerized disulfonated poly (arylene ether sulfone) random copolymers. Water Science and Technology, 2010. **61**(3): p. 619-624.

154. H.B. Park, B.D. Freeman, Z.B. Zhang, M. Sankir, and J.E. McGrath, Highly chlorine-tolerant polymers for desalination. Angewandte Chemie International Edition, 2008. **47**(32): p. 6019-6024.

155. J. Balster, O. Krupenko, I. Pünt, D. Stamatialis, and M. Wessling, Preparation and characterisation of monovalent ion selective cation exchange membranes based on sulphonated poly (ether ether ketone). Journal of membrane science, 2005. **263**(1-2): p. 137-145.

156. Y. Tanaka, Concentration polarization in ion-exchange membrane electrodialysis—the events arising in a flowing solution in a desalting cell. Journal of Membrane Science, 2003. **216**(1-2): p. 149-164.

157. F.G. Donnan, The theory of membrane equilibria. Chemical reviews, 1924. **1**(1): p. 73-90.

158. T. Sata, ed. *Ion exchange membranes: Preparation, characterization, modification and application*. 2004, The Royal Society of Chemistry: Cambridge. 308.

159. K.S. Pitzer, Thermodynamics of electrolytes. I. Theoretical basis and general equations. Journal of Physical Chemistry, 1973. **77**(2): p. 268-277.

160. K.S. Pitzer and G. Mayorga, Thermodynamics of electrolytes. II. Activity and osmotic coefficients for strong electrolytes with one or both ions univalent. Journal of Physical Chemistry, 1973. **77**(19): p. 2300-2308.

161. K.S. Pitzer and G. Mayorga, Thermodynamics of electrolytes. III. Activity and osmotic coefficients for 2–2 electrolytes. Journal of Solution Chemistry, 1974. **3**(7): p. 539-546.

162. G.S. Manning, Limiting laws and counterion condensation in polyelectrolyte solutions II. Self-diffusion of the small ions. Journal of Chemical Physics, 1969. **51**(3): p. 934-938.

163. G.S. Manning, Polyelectrolytes. Annual review of physical chemistry, 1972. **23**(1): p. 117-140.

164. G.S. Manning, Counterion binding in polyelectrolyte theory. Accounts of Chemical Research, 1979. **12**(12): p. 443-449.

165. R. Netz, Polyelectrolytes in electric fields. Journal of Physical Chemistry B, 2003. **107**(32): p. 8208-8217.

166. F. Bordi, C. Cametti, and R.H. Colby, Dielectric spectroscopy and conductivity of polyelectrolyte solutions. Journal of Physics: Condensed Matter, 2004. **16**(49): p. R1423.

167. P.W. Atkins, J. de Paula, and J. Keeler, *Atkins' Physical Chemistry*. 11th ed. 2018, Oxford: Oxford University Press.

Chapter 3: Water and salt transport properties of triptycene-containing sulfonated polysulfone materials for desalination membrane applications

3.1. Introduction

Freshwater is a critical resource for human life, and it plays a key role in economic and societal development.[1-6] However, global population growth continues to amplify stress on existing freshwater supplies, and water scarcity increasingly is becoming a worldwide problem.[4, 7-10] According to the United Nations, more than one-third of the world's population is suffering from either physical water scarcity or economic water shortage.[1, 2, 4] Numerous efforts are focused on increasing global freshwater supply, and wastewater treatment[11-13] and desalination of saline water[2, 4, 12, 14] are among the most common approaches. Wastewater treatment focuses on the removal of contaminants using physical and/or chemical treatment (e.g., filtration, adsorption, flocculation, and photocatalytic degradation),[11-13, 15] and desalination aims to produce freshwater by separating salt and water (e.g., using distillation,[16, 17] electrodialysis,[18, 19] reverse osmosis,[20-24] or solar evaporation[25]). Membrane-based processes are used in both wastewater treatment and desalination processes. Due to generally high energy efficiency and low cost, membrane-based desalination processes are widely used to desalinate water, and membrane-based desalination processes are expected to continue to play a key role in the desalination industry in the future.[2, 4, 12, 14]

Current state-of-the-art desalination membranes are based on polyamide chemistry that was introduced in the early 1980s.[21, 26] These membranes possess favorable combinations of water and salt transport properties and are very efficient.[14, 27] The polyamide linkages in these

---

This chapter is already published and available from: Luo, H., Aboki, J., Ji, Y., Guo, R., & Geise, G. M. (2018). Water and salt transport properties of triptycene-containing sulfonated polysulfone materials for desalination membrane applications. ACS applied materials & interfaces, 10(4), 4102-4112.

polymers, however, are susceptible to oxidative degradation that can be accelerated by the use of chlorine-based disinfectants, which are used to prevent biofouling in water purification systems.[28-33] Consequently, pretreatment steps (e.g., chlorine removal and pH adjustment) are needed to prolong the useful life of desalination membranes, and pretreatment increases the overall cost of desalination.[28-30, 34]

Chemically stable desalination membrane polymers would address this issue. Hydrocarbon polymers can be chemically stable but are often too hydrophobic to function effectively as water treatment membranes, so strategies, including sulfonation, have been used to increase the hydrophilicity of otherwise hydrophobic hydrocarbon polymers.[4, 23, 28, 35-45] While promising for desalination applications, sulfonated polymer membranes have not yet achieved the desalination selectivity and water permeance characteristics of commercially available polyamide membranes.[42, 45, 46] Recent recognition of the importance of water/salt selectivity properties of desalination membrane polymers[47] underscores the need for studies that focus on understanding how membrane chemistry and structure can be used to enhance the water/salt selectivity properties of materials, such as sulfonated polysulfone, that are of interest for desalination membrane applications.

Incorporating bulky co-monomers into membrane polymers is one strategy used to tune membrane selectivity.[48-51] For example, triptycene and pentiptycene based polymer membranes have exhibited promise for gas separation applications,[52-58] and their transport properties can exceed the gas permeability-selectivity tradeoff barrier (i.e., the so-called upper bound).[59, 60] In these materials, the incorporation of bulky, space occupying moieties (i.e. triptycene and pentiptycene) can generate additional free volume and simultaneously narrow the free volume distribution in the polymer.[52-54, 61, 62] Increased membrane free volume enables higher permeability, and a narrow free volume element size distribution enhances selectivity.[52-54, 61, 62] The success of incorporating triptycene in gas separation membranes motivated us to study the influence of incorporating triptycene moieties in sulfonated polysulfone materials, as the mechanism of small molecule transport in gas separation and desalination membranes is similar.[4, 34, 45, 47, 63, 64]

In this study, a series of triptycene-containing sulfonated polysulfone membranes (TRP-BP) was prepared, and the fundamental water and salt transport properties of the materials were characterized. The TRP-BP materials sorbed more water compared to sulfonated polysulfones without triptycene. The incorporation of triptycene in sulfonated polysulfone did not appear to influence salt sorption, suggesting that triptycene does not dramatically influence the bulk thermodynamic interactions between salt and the polymer. Both the water and salt diffusion coefficients were lower in the TRP-BP materials compared to other sulfonated polysulfone materials at comparable water content. Many of the TRP-BP materials exhibited improved water/salt permeability selectivity compared to other sulfonated polysulfone materials. In particular, acid counter-ion form TRP-BP materials exhibited greater water/salt permeability selectivity compared to acid counter-ion form sulfonated polymers that did not contain triptycene. Experimental results suggest that incorporation of triptycene into sulfonated polysulfone polymers may be a viable strategy for increasing desalination membrane selectivity.

3.2. Experimental Methods

3.2.1 Materials

Triptycene-1,4-hydroquinone (TRP) was prepared, as described previously, and dried overnight at 90°C under vacuum prior to use.[52] 4,4'-biphenol (BP) and 3,3'-disulfonated-4,4'-dichlorodiphenylsulfone (SDCDPS) were purchased from Akron Polymer Systems and dried under vacuum for 24 h at 120°C prior to use. Monomer grade 4,4'-dichlorodiphenylsulfone (DCDPS) and anhydrous potassium carbonate (K_2CO_3) were purchased from Alfa Aesar and dried under vacuum for 24 h at 110°C prior to use. Anhydrous *N*,*N*-dimethylacetamide (DMAc), anhydrous *N*-Methyl-2-pyrrolidinone (NMP), toluene, and 2-propanol were purchased from Sigma-Aldrich and used as received.

3.2.2 Polymer Synthesis and Membrane Preparation

A series of triptycene-containing di-sulfonated poly(arylene ether sulfone) random copolymers (TRP-BP) with different degrees of sulfonation and varied molar ratios of triptycene-1,4-hydroquinone (TRP) to 4,4'-biphenol (BP) were synthesized via nucleophilic step growth polymerization. It should be noted that random copolymers with TRP as the only bisphenol moiety did not have sufficiently high molecular weight for film formation due to the low reactivity of TRP and SDCDPS. The nomenclature used for the copolymers is TRP-BP a:b-X, where a:b is the molar ratio of TRP to BP and X is the molar percentage of sulfonated SDCDPS in the copolymers as shown in Scheme 1. For example, TRP-BP 1:1-35 refers to the copolymer containing 1:1 molar ratio of TRP to BP, 35 mol% sulfonated monomer (SDCDPS), and 65 mol% non-sulfonated monomer (DCDPS). An example polymerization of TRP-BP 1:1-35 is: 1.8621 g (10.0 mmol) of BP, 2.8633 g (10.0 mmol) of TRP, 3.5450 g (7.0 mmol) of SDCDPS, 3.7707 g (13.0 mmol) of DCDPS, and 3.3169 g (24.0 mmol) of anhydrous K_2CO_3 were charged into a three-necked round bottom flask equipped with a condenser, mechanical stirrer, Dean-Stark trap, and nitrogen inlet. Anhydrous NMP (60 mL) and toluene (30 mL) were then added to the flask, and the reaction was heated, under a N_2 purge, to 150°C while stirring. The reaction was refluxed at 150°C for 4 h to azeotropically dehydrate the system. Afterwards, toluene was removed from the reaction by slowly increasing the temperature to 185°C. The reaction was allowed to proceed at 185°C for another 48 h until a viscous solution formed. The polymer solution was then cooled to room temperature, filtered to remove salts, and coagulated in a stirred isopropanol bath. The precipitated fibrous TRP-BP copolymer was collected and dried under vacuum at 120°C for 24 h.

Scheme 3. 1. Synthesis of triptycene-containing sulfonated poly(arylene ether sulfone)s

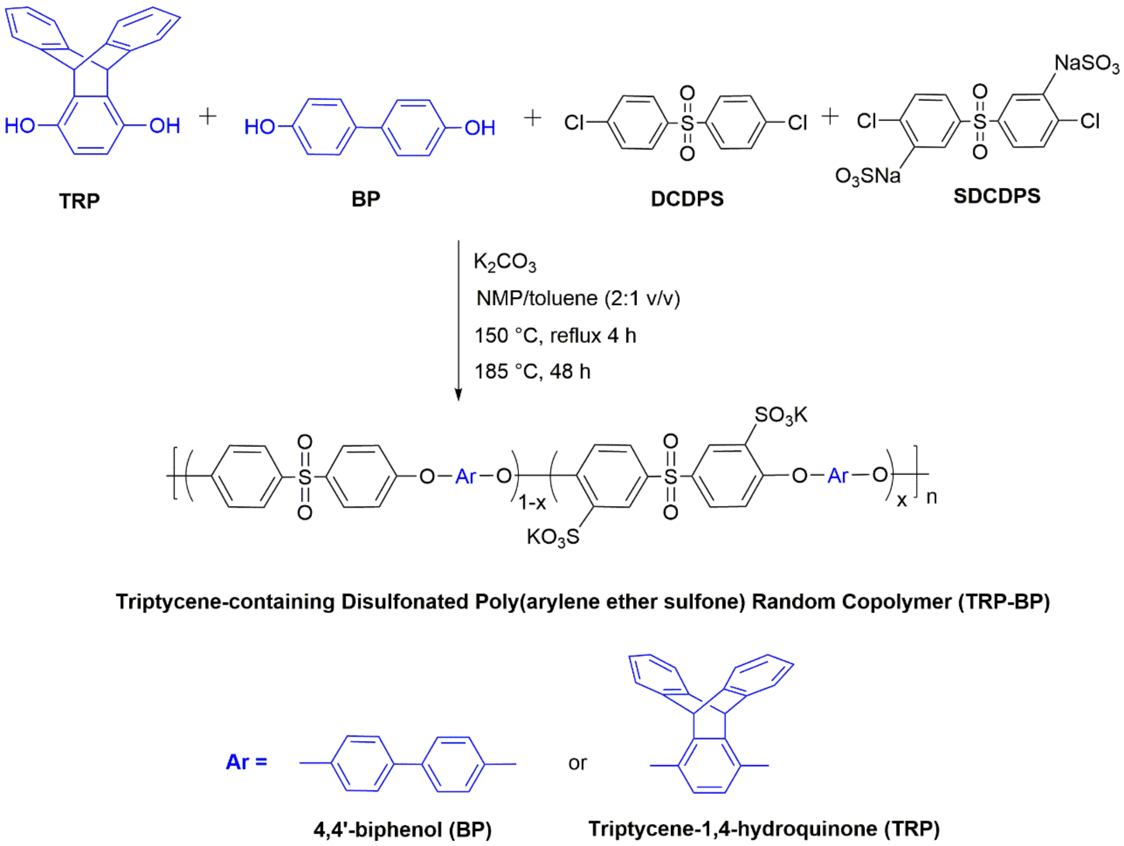

All salt-form (as synthesized) copolymer films were prepared via a solution casting method. The TRP-BP copolymers were dissolved in DMAc (~7% w/v), and the solution was filtered through a 0.45 μm PTFE syringe filter. To form polymer films, the filtered solution was cast onto a clean leveled glass substrate and dried for 24 h under an infrared lamp at ~55°C. The films were subsequently dried under vacuum at 110°C for 24 h to further remove residual solvent.

The salt counter ion form (salt-form) membranes were converted to the sulfonic acid form (acid-form), i.e., replacing K with H in the TRP-BP structure shown in Scheme 1, by boiling the films in a 0.5 M sulfuric acid solution for 2 h followed by boiling the films in de-ionized (DI) water (18.2 MΩ cm) for 2 h. The acid-form TRP-BP membranes were subsequently stored in DI water until use. The suffix "salt" or "acid" was added to the copolymer names to indicate whether the films were in the salt-form (as polymerized) or acid-form (converted as described above) before characterization.

3.2.3 Water Sorption and Polymer Density Measurements

Cast TRP-BP membranes were soaked in DI water, and the hydrated membrane mass, $m_{hydrated}$, was measured periodically until a constant value was obtained. A laboratory wipe was used to remove residual water from the membrane surface before measuring $m_{hydrated}$. After reaching equilibrium, hydrated membranes were placed in vented plastic petri dishes and dried under vacuum at 25℃ for 7 days.[65] After drying, the dry membrane mass, m_{dry}, was measured, and water uptake, *W.U.*, was calculated as:

$$W.U. = \frac{m_{hydrated} - m_{dry}}{m_{dry}} \tag{3.1}$$

Immediately following the m_{dry} measurement, the dry polymer density, ρ_{dry}, was measured. An analytic balance (XSE204, Mettler Toledo) equipped with a density measurement kit was used, and cyclohexane was chosen as the auxiliary liquid to be consistent with previous studies on sulfonated polysulfone materials.[65, 66] The temperature of the auxiliary liquid was measured during the density measurement, and Archimedes' principle was used to determine ρ_{dry}:

$$\rho_{dry} = \frac{A}{A-B}(\rho_{aux} - \rho_{air}) \tag{3.2}$$

where *A* and *B* are the membrane masses in the auxiliary liquid and in air, respectively, ρ_{aux} is the density of the auxiliary liquid,[67, 68] which was evaluated at the measurement temperature, and the density of air, ρ_{air}, was taken as 0.0012 g/cm^3.[67] The volume fraction of water in the polymer, ϕ_W, was calculated, assuming additive mixing of water and the polymer, as:[65]

$$\phi_W = \frac{W.U./\rho_W}{W.U./\rho_W + 1/\rho_{dry}} \tag{3.3}$$

where the density of water, ρ_W, was taken as 1 g/cm^3.[65]

The membrane water sorption coefficient, K_W, was defined as the ratio of the membrane water concentration, g(water)/cm^3(hydrated polymer), to the water concentration in the external solution, g(water)/cm^3(external solution), in equilibrium with the membrane:[69, 70]

$$K_W = \frac{C_W^m}{C_W^S} \tag{3.4}$$

where C_W^S was taken as 1 g/cm^3 at room temperature.[64] The value of C_W^m was calculated as:

$$C_W^m = \frac{\phi_W M_W}{\bar{V}_W} [=] \frac{g(water)}{cm^3(hydrated\ polymer)} \tag{3.5}$$

where M_W is the molecular weight of water (18 g/mol), $\bar{V}_W$ is the partial molar volume of water (taken as the molar volume of water, 18 cm^3/mol),[65] and ϕ_W is the volume fraction of water in the polymer determined using Eq. (3.3). By substituting Eq. (3.5) into Eq. (3.4) and simplifying the expression, the water sorption coefficient was determined to be equivalent to the volume fraction of water in the polymer:

$$K_W = \phi_W \tag{3.6}$$

3.2.4 Water Transport Measurements

Hydraulic water permeability was measured using a dead-end stainless-steel permeation cell (HP4750 Stirred Cell, Sterlitech, Corp., Kent, WA). Pure water hydrated TRP-BP membranes were cut into 5 cm diameter discs using a die and were stored in DI water until use. Qualitative filter paper (Whatman^{TM}, 1001-125) sheets also were cut into 5 cm diameter discs and were washed gently with DI water several times. Each polymer sample was placed onto a filter paper disc and subsequently was placed onto a porous stainless-steel support such that the filter paper separated the polymer from the support. The permeation cell was assembled, filled with approximately 250 mL DI water, sealed, and pressurized to 400 psi (27.2 atm) using nitrogen. Permeate volume was recorded, using a 25 mL graduated cylinder, as a function of time to determine the volumetric permeation rate. To minimize the effects of evaporation, the top of the cylinder was sealed using Parafilm®.

The permeate water flux, J_W, was calculated from the volumetric permeation rate as:

$$J_W = \frac{1}{A_{PW}} \frac{dV}{dt} \tag{3.7}$$

where *dV/dt* is the slope of the linear steady-state permeate volume versus time data and represents the volumetric permeation rate. The effective area of the sample available for water permeation, A_{PW}, was 14.6 cm^2. Hydraulic water permeability, P_W^H, was calculated as:[64]

$$P_W^H = \frac{J_W l}{\Delta p} \tag{3.8}$$

where Δp is the pressure difference across the membrane and *l* is the hydrated membrane thickness, which was taken as the hydrated sample thickness measured immediately following the water permeability measurement.[65] Diffusive water permeability, P_W^D, was calculated from the measured P_W^H data as:[45, 70, 71]

$$P_W^D = P_W^H \frac{RT}{\bar{V}_W} [\frac{1-K_W}{\delta}] \tag{3.9}$$

where R is the gas constant, T is absolute temperature, and the term in square brackets is a correction factor that accounts for both convective frame of reference (i.e., the 1 – K_W term) and thermodynamic non-ideality (i.e., δ).[45]

In other sulfonated polysulfone studies, Flory-Huggins theory[72, 73] was used to estimate the value of δ.[45, 65, 74] These analyses, however, used a single-point fit to determine the Flory-Huggins interaction parameter that is needed to evaluate δ (c.f., Appendix B).[45] Given the uncertainty about whether Flory-Huggins theory describes the TRP-BP materials, the value of δ in Eq. (3.9) was set equal to unity during calculation of the diffusive water permeability for the TRP-BP materials and the BPS(H) and BisAS materials considered:

$$P_W^D = P_W^H \frac{RT}{\bar{V}_W} [1 - K_W] \tag{3.10}$$

In the Appendix B, the single point Flory-Huggins theory fit method was used during calculation of the diffusive water permeability for all of the materials considered, and this alternate approach to the analysis is provided in the Appendix B with the caveat discussed above about whether Flory Huggins theory is applicable to these materials. After converting the hydraulic water permeability to diffusive water permeability, using Eq. (3.10), the average water diffusion coefficient, D_W, was calculated from P_W^D and K_W as:[70]

$$D_W = \frac{P_W^D}{K_W} \tag{3.11}$$

3.2.5 Salt Transport Measurements

Salt permeability, P_S, was measured at 25°C using a direct salt permeation technique and a custom dual chamber permeation cell. Prior to the measurement, the sample was soaked in 1 M NaCl solution, and a laboratory wipe was used to remove residual salt solution from the membrane surface. Two rubber gaskets, with 1.59 cm diameter openings, were used to seal the membrane in the cell and define the area available for salt transport, A_{PS}. The donor chamber was initially filled with 100 mL of 1 M NaCl solution, and the receiver chamber was initially filled with 100 mL of DI water. The system temperature was maintained at 25℃ using a water bath to circulate water through jackets surrounding the donor and receiver chambers. The solutions in both chambers were mixed by mechanical stirring (Caframo$^{\text{TM}}$ BDC250, 350 rpm). A conductivity meter (Inolab$^{®}$ Cond 7310) was used to track the change in the receiver chamber solution conductivity over time, and the solution conductivity was converted to salt concentration via a calibration curve. Salt permeability, P_S, was calculated as:[75]

$$\ln\left[1 - 2\frac{C_R(t)}{C_D(0)}\right]\left[-\frac{Vl}{2A_{PS}}\right] = P_S t \tag{3.12}$$

where $C_R(t)$ is the receiver chamber salt concentration at time t, $C_D(0)$ is the initial donor chamber salt concentration (1 M), V is the solution volume in each chamber (100 mL), l is the hydrated sample thickness (measured following the experiment), and the effective transport area A_{PS} was 1.98 cm^2. The pseudo steady-state condition was verified by observing a linear variation of $\ln\left[1 - 2\frac{C_R(t)}{C_D(0)}\right]\left[-\frac{Vl}{2A}\right]$ *vs.* t, and the slope of this line was taken as P_S according to Eq. (3.12).

The membrane salt sorption coefficient, K_s, was defined as the ratio of membrane salt concentration (mol(salt)/cm^3(hydrated polymer)) to salt concentration in the external solution (mol(salt)/cm^3(external solution)) in equilibrium with the membrane.[69, 70] Salt sorption was measured using a desorption method[76] where the TRP-BP samples were cut into 1.59 cm diameter discs and soaked in 50 mL of 1 M NaCl solution for two days to reach sorption equilibrium. The time needed for a sample to reach sorption equilibrium was estimated using the salt permeability of the sample as $l^2/4P_S$. This time was found to be on the order of 1000 sec and was recognized to be an overestimation of the characteristic time for diffusion, $l^2/4D_S$, since P_S =

D_S K_S and $K_S < 1$.[45] Soaking the samples in salt solution for a factor of 10 greater than this characteristic time for diffusion was taken to be sufficient for reaching sorption/desorption equilibrium.[76]

After equilibration, the membranes were removed from the salt solution, wiped with a laboratory wipe to remove salt solution from the sample surface, and soaked in 20 mL of DI water for two days to allow the sorbed salt to desorb from the polymer. The desorption solution concentration, which was targeted to be near 1 mg(NaCl)/L by controlling the sample volume and desorption solution volume, was measured using ion-chromatography (Dionex ICS-2100), and K_s was calculated as:

$$K_S = \frac{C_f V_f}{C_0 V_m} \tag{3.13}$$

where C_f is the desorption solution concentration, V_f is the desorption solution volume (20 mL), C_0 is the initial soaking solution concentration (1 M), and V_m is the hydrated membrane volume, which was calculated using measured sample thickness and area. Following the measurements of P_S and K_S, the average salt diffusion coefficient, D_S, was calculated as:[70]

$$D_S = \frac{P_S}{K_S} \tag{3.14}$$

3.3. Results and Discussions

3.3.1 Polymer Properties and Water Content

Experimental results for the TRP-BP materials were compared to results reported for sulfonated polysulfone materials that did not contain the triptycene group (BPS(H))[65] and sulfonated polysulfone materials prepared using a bisphenol-A group (BisAS)[77] as opposed to the biphenol group used in the TRP-BP and BPS(H) materials. The chemical structures of the BPS(H) and BisAS materials are shown in Fig. 3.1. The BPS(H) materials contain linear BP moieties on the polymer backbone, and the BisAS materials contain bisphenol-A (BPA) moieties that have a bent configuration due to the bond angle of the carbon that separates the phenyl rings in the BPA moiety. Thus, both the TRP-BP and BisAS materials contain moieties that can disrupt chain packing in the material compared to the BPS(H) materials.

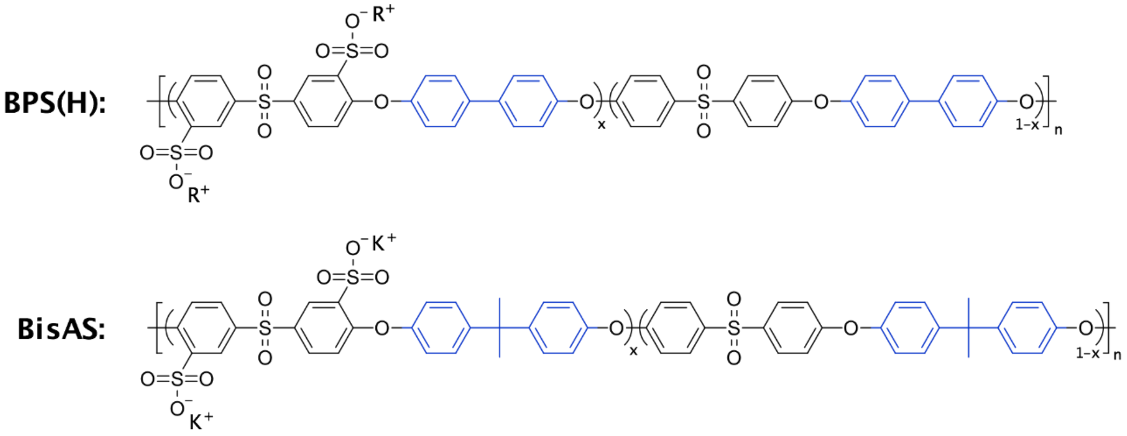

Figure 3. 1 Chemical structures for the BPS(H)[65] and BisAS[77] random copolymers. The value of x represents the degree of sulfonation, and the copolymer compositions are given as BPS(H)-100•x and BisAS-100•x. The R^+ group in the BPS(H) structure represents the initial counter-ion form of the polymer: H^+ for the BPSH materials or K^+ for the BPS materials.[65]

The dry polymer densities of the TRP-BP 1:1-35 and TRP-BP 2:1-35 materials were similar to the dry polymer densities of the BPS(H)-35 materials with the exception of the TRP-BP 1:1-35-salt material that had an approximately 6% greater density than the BPS-35 material (Table

1). The greater density of the TRP-BP 1:1-35-salt material compared to the BPS-35 material may be due to the higher repeat unit molecular weight of the TRP moiety compared to the BP moiety. In the absence of significant chain packing disruption, an increase in repeat unit molecular weight could result in an increased density upon incorporation of the TRP moiety in the polymer. Alternatively, incorporation of the BPA moiety in the BisAS materials resulted in an approximately 5-10% lower density compared to the BPS and TRP-BP materials (Table 1), and this result is consistent with a disruption in chain packing due to the bent structure of the BPA moiety. In the dry state, however, incorporating triptycene into sulfonated polysulfone does not dramatically affect the dry density of the polymer, suggesting that chain packing disruptions are less significant compared to that of the BisAS materials

Table 3. 1. Density and transport properties of the TRP-BP polymers. Previously reported data for the BPS(H)[65, 78] polymers and the BisAS[77] polymers are included for comparison.

Material	K_W	**Dry density (g/cm^3)**	K_S [a]	D_W [b] (×10^{-6} cm^2/s)	D_S [c] (×10^{-7} cm^2/s)	P_W^H [d] (L·µm/m^2·h·bar)	P_W^D [e] (× 10^{-6} cm^2/s)	P_S [f] (×10^{-9} cm^2/s)
TRP-BP 1:1-35-acid	**0.46±0.01**	**1.41±0.04**	**0.105±0.005**	**12.6±0.9**	**6.9±0.9**	**2.8±0.2**	**5.8±0.4**	**74±1**
TRP-BP 1:1-35-salt	**0.38±0.01**	**1.43±0.03**	**0.050±0.008**	**3.4±0.4**	**1.2±0.2**	**0.55±0.07**	**1.3±0.2**	**5.8±0.1**
TRP-BP 2:1-35-acid	**0.48±0.01**	**1.37±0.06**	**0.094±0.003**	**12.0±0.4**	**8.2±0.3**	**2.9±0.1**	**5.8±0.2**	**76±2**
TRP-BP 2:1-35-salt	**0.36±0.01**	**1.39±0.06**	**0.066±0.004**	**5.1±0.5**	**1.5±0.2**	**0.75±0.07**	**1.8±0.2**	**9.2±0.9**
TRP-BP 1:1-50-salt	**0.48±0.01**	**1.42±0.01**	**0.159±0.020**	**15.7±1.0**	**12±2**	**3.8±0.23**	**7.6±0.5**	**199±6**
BPS-35[65]	**0.26**	**1.353[78]**	**0.034**	**4.2**	**1.2**	**0.39**	**1.1**	**3.9**
BPS-40[65]	**0.29**	**1.358[78]**	**0.043**	**6.1**	**3**	**0.65**	**1.8**	**8.7**
BPSH-35[65]	**0.4**	**1.386[78]**	**0.057**	**12**	**9.8**	**2.1**	**4.8**	**103**
BPSH-40[65]	**0.48**	**1.420[78]**	**0.081**	**18**	**20**	**4.4**	**8.7**	**226**
BisAS-30[77]	**0.24±0.01**	**1.26±0.02**	**0.056±0.007**	**5.6±0.2**	**1.6±0.2**	**0.46±0.02**	**1.3±0.1**	**9.0±0.3**
BisAS-40[77]	**0.34±0.01**	**1.32±0.02**	**0.080±0.005**	**11±2**	**6.6±0.5**	**1.53±0.23**	**3.9±0.6**	**53±4**

Measured via desorption at room temperature (concentration of NaCl in the initial soaking solution = 1 M; membranes were soaked for 3 days before desorption in atmospherically equilibrated DI water)

[b] Calculated from P_W^D and K_W values using Eq. (3.11)

[c] Calculated from P_S and K_S values using Eq. (3.14)

[d] Measured at room temperature using a dead-end permeation cell pressurized (using N_2) to 400 psig

[e] Calculated from K_w and P_W^H values using Eq. (3.10)

[f] Measured at 25°C via direct permeation (concentration of NaCl in the donor cell = 1 M)

The acid-form TRP-BP materials sorb more water compared to the corresponding salt-form materials at equivalent degree of sulfonation. This observation is consistent with data reported for the BPS(H) materials.[65] This result also is consistent with observations made on a variety of sulfonated polymers.[66, 79]

The water sorption coefficient of the acid- and salt-form TRP-BP 1:1-35 and TRP-BP 2:1-35 materials increased by 15% to 46% compared to the BPSH-35 and BPS-35 materials, respectively (Table 3.1). Often the water content of hydrated polymers is taken to be proportional to free volume.[45, 75, 76, 80] Therefore, the observed increase in water content upon incorporation of triptycene into sulfonated polysulfone (at comparable degree of sulfonation) suggests that the hydrated TRP-BP materials may have greater free volume compared to the BPS(H) and BisAS materials.

The dry polymer density results suggest that incorporation of the TRP moiety does not appreciably affect chain packing (or free volume) with the exception of one case, discussed above, where the density of TRP-BP 1:1-35-salt is greater (suggesting a lower free volume) than BPS-35. Alternatively, the water content data suggest that incorporation of triptycene in sulfonated polysulfone results in an increase in free volume (using the relationship, proposed by Yasuda et al., that suggests free volume is proportional to water content in hydrated polymers[75]). These results (that may appear to conflict) may be rationalized by considering the differences between dry and hydrated sulfonated polymers.

In the dry state, sulfonate groups can hydrogen bond strongly, and these interactions can result in a reduction in the free volume of the polymer, compared to an uncharged material, because the polymer chains are drawn together by the favorable interactions between the sulfonate groups.[76, 78] When water sorption occurs, these hydrogen bonds can be disrupted as the sulfonate groups solvate with water.[76, 78] In the dry TRP-BP materials, strong interactions between sulfonate groups may dominate over possible chain packing disruption due to the TRP moieties, and this situation would be consistent with dry polymer density values that are not appreciably affected by the incorporation triptycene in sulfonated polysulfone in contrast to other reports where triptycene incorporation in uncharged polyimides[52] disrupts chain packing. In the hydrated TRP-BP materials, the strong interactions between sulfonate groups may be disrupted as the sulfonate groups hydrate, and the increased water content of the TRP-BP compared to the BPS(H) and BisAS materials may be due to the incorporation of triptycene in sulfonated polysulfone.

3.3.2 Water Transport

Incorporating triptycene into sulfonated polysulfone generally resulted in an increase in hydraulic water permeability, P_W^H, for the TRP-BP materials compared to the BPS(H) materials at comparable degrees of sulfonation (Table 3.1). This result is qualitatively consistent with the observation that water permeability generally is greater in materials that sorb more water.[45] Additional analysis, however, reveals that the greater hydraulic water permeability of the TRP-BP materials, compared to the BPS(H) and BisAS materials at comparable degree of sulfonation, is driven by a combination of increased water content and suppressed water diffusivity compared to the sulfonated polysulfones that do not contain triptycene.

To analyze water transport further, the water diffusivity properties of the polymers were considered (Fig. 3.2). The water diffusion coefficient for the TRP-BP materials is more sensitive to changes in water content, K_W, compared to the BPS(H) and BisAS materials. The decision to plot the water diffusion coefficient data in Fig. 3.2 versus $1/K_W$ was motivated by a free volume-based scaling argument proposed by Yasuda et al. where the free volume in hydrated polymers was taken to be proportional to the free volume available for transport in the material.[75]

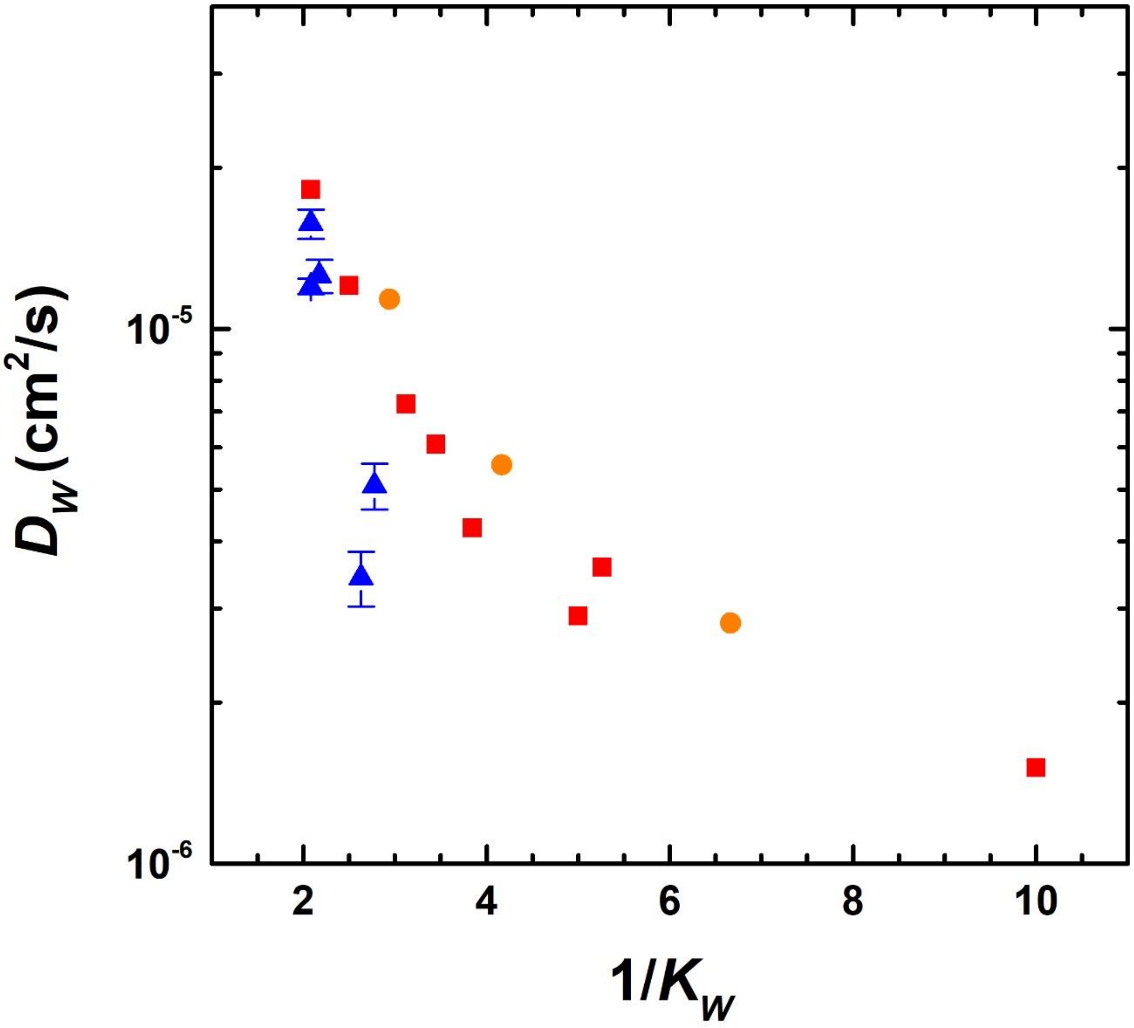

Figure 3. 2. Water diffusivity, D_W, as a function of $1/K_W$ for the TRP-BP (▲), BPS(H) (■)[65], and BisAS (●)[77] materials. The D_W values for the TRP-BP materials were calculated from measured P_W^D and K_W using Eq. (3.11).

The TRP-BP water diffusion coefficients are lower than that of the BPS(H) and BisAS materials at comparable water content (Fig. 3.2). The BisAS material exhibited greater D_W values compared to the BPS(H) materials at comparable water content, and this result has been attributed to additional free volume introduced into the BisAS structure by the BPA group (Fig. 3.1), which is not linear like the BP group.[77]

These results suggest that incorporating triptycene in sulfonated polysulfone has an influence on water transport that is fundamentally different from the situation when the BP group (in the BPS(H) polymers) is replaced with the BPA group (in the BisAS polymers) as observed by comparing the D_W values for the BPS(H) and BisAS materials at comparable water content.

The observed reduction in D_W for the TRP-BP materials compared to the BPS(H) materials and the BisAS materials (at comparable water content) may be due to the influence of the triptycene groups on polymer chain packing or configuration. Improvements in membrane gas transport properties have been ascribed to changes in the polymer free volume distribution as a result of incorporating triptycene units into the backbone of a polyimide.[52] In the TRP-BP materials, the bulky triptycene groups may serve as “molecular baffles” that could disrupt larger free volume elements to form smaller and more tortuous transport pathways (see Section B2 in the Appendix B for more discussion). The observed decrease in the water diffusivity of the TRP-BP materials relative to the other sulfonated polysulfone materials suggests that incorporating triptycene in sulfonated polysulfone may either fill free volume within the polymer, which contrasts the water sorption data discussed previously, or make the transport pathways more tortuous.

The TRP-BP diffusive water permeability values are greater than those values for the corresponding BPS(H) materials[65] but are lower than those values for the corresponding BisAS materials[77] (Table 3.1). This result is likely due to competing water sorption and diffusion effects, as the diffusive water permeability, P_W^D, can be expressed as the product of the water sorption, K_W, and diffusion, D_W, coefficients, i.e., Eq. (3.11).[64, 70] Incorporating triptycene into sulfonated polysulfone causes an increase in K_W and a reduction in D_W compared to comparable water content materials. Alternatively, the BisAS materials, compared to the TRP-BP materials, have slightly lower K_W values but higher D_W values, so diffusive water permeability in the BisAS materials is greater than that in the salt-form TRP-BP and BPS materials.

3.3.3 Salt Transport

Incorporating triptycene into sulfonated polysulfone did not have a dramatic effect on salt sorption properties. It did, however, influence the salt diffusivity and, because permeability can be taken as the product of the sorption and diffusion coefficients, i.e., Eq. (3.14),[70] permeability properties. Much like the water transport analysis, salt sorption and permeability properties were measured and used to calculate effective diffusion coefficients using Eq. (3.14).

Salt sorption in the TRP-BP materials increased as the water content of the polymer increased (Fig. 3.3), which is similar to results for many polymers.[45] The salt sorption coefficients for the TRP-BP materials were also relatively similar to the salt sorption coefficients of the BPS(H) and BisAS materials. This result is not surprising given that the chemistry of the polymer backbones for all three families of materials is very similar. The structural changes made in the TRP-BP and BisAS polymers, relative to the BPS(H) materials, do not appear to have a profound influence on the thermodynamics of salt transport. Furthermore, salt sorption in charged polymers is highly linked to characteristics related to the charged groups on the polymer,[23, 46, 74, 81] and all three classes of materials contain the same sulfonate groups.

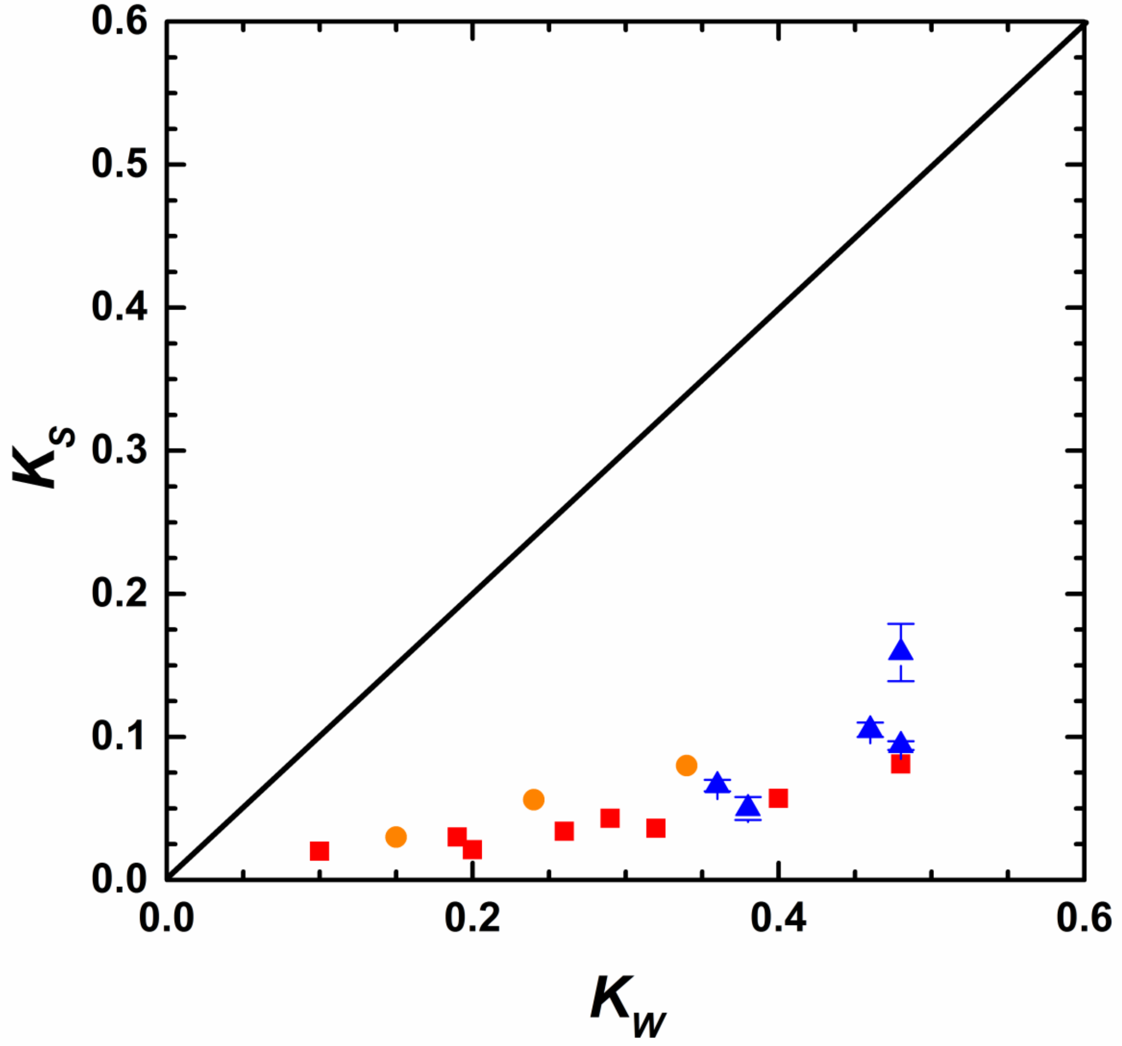

Figure 3. 3. Salt sorption coefficient, K_S, values as a function of the water sorption coefficient, K_W, for the TRP-BP (▲), BPS(H) (■)[65], and BisAS (●)[77] materials. The K_S values for the TRP-BP materials were measured via a desorption process at room temperature (concentration of NaCl in soaking solution = 1 M; samples were equilibrated for 3 days prior to desorption in atmospherically equilibrated DI water).

The TRP-BP 1:1-50 salt-form material, however, may be an exception. The salt sorption coefficient for that material was measured to be roughly 60% greater than other samples with comparable water content (Fig. 3.3). This result may be due to the fact that the degree of sulfonation of TRP-BP 1:1-50-salt is greater than the BPS(H) or BisAS materials. With more sulfonate groups on the polymer backbone and a similar water content to TRP-BP 2:1-35-acid, it is likely that additional counter-ion condensation could occur in TRP-BP 1:1-50-salt compared to TRP-BP 2:1-35-acid, and this situation would result in a higher salt sorption coefficient at equivalent water content.[81]

The TRP-BP diffusive salt permeability is suppressed relative to that of the BPS(H) and BisAS materials at comparable K_W (Table 3.1 and Fig. 3.4). This reduction in salt permeability suggests that incorporating triptycene into sulfonated polysulfone may be a favorable strategy for desalination applications where low salt permeability is desired.[2, 4, 47, 74] Additionally, the observation that the water permeability values for the TRP-BP materials were generally greater than that of the BPS(H) materials further suggests that the TRP-BP materials may be of interest for desalination applications. The salt permeability properties of the TRP-BP materials are similar to the other sulfonated polysulfone materials and uncharged hydrogels, studied by Yasuda et al.[75], in that all of the materials exhibit the free volume-based scaling relationship proposed by Yasuda et al. Therefore, the general transport mechanism appears to be similar for the three sulfonated polysulfone materials, but the use of triptycene in sulfonated polysulfone appears to suppress salt permeability.

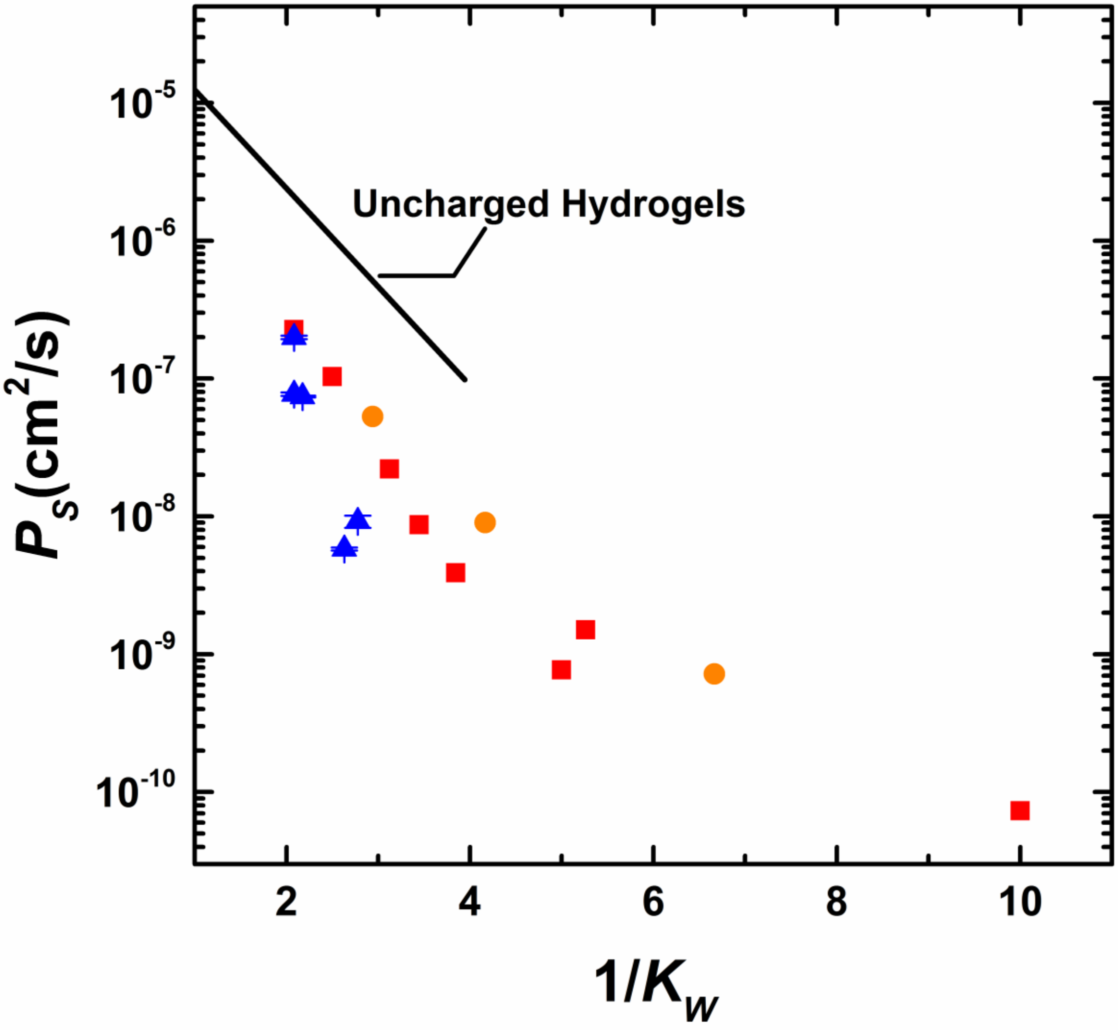

Figure 3. 4. Salt permeability, P_S, as a function of $1/K_W$ for the TRP-BP (▲), BPS(H) (■)[65], and BisAS (●)[77] materials. The P_S values for the TRP-BP materials were measured at 25˚C via a direct permeation method with an upstream NaCl concentration of 1 M. The data are compared to a general representation (solid line) of uncharged hydrogel data reported by Yasuda et al.[75]

Using the measured salt sorption coefficients and permeability values, effective salt diffusion coefficients can be calculated using Eq. (3.14). At equivalent water content, salt diffusion in the TRP-BP materials was slower than that in the BPS(H) and BisAS materials, which both had comparable D_S values at equivalent water content (Fig. 3.5). This result was expected given that the salt sorption coefficients, as a function of water content, were similar for the three materials and that the TRP-BP materials had lower salt permeability than the other sulfonated polysulfone materials (Fig. 3.4).

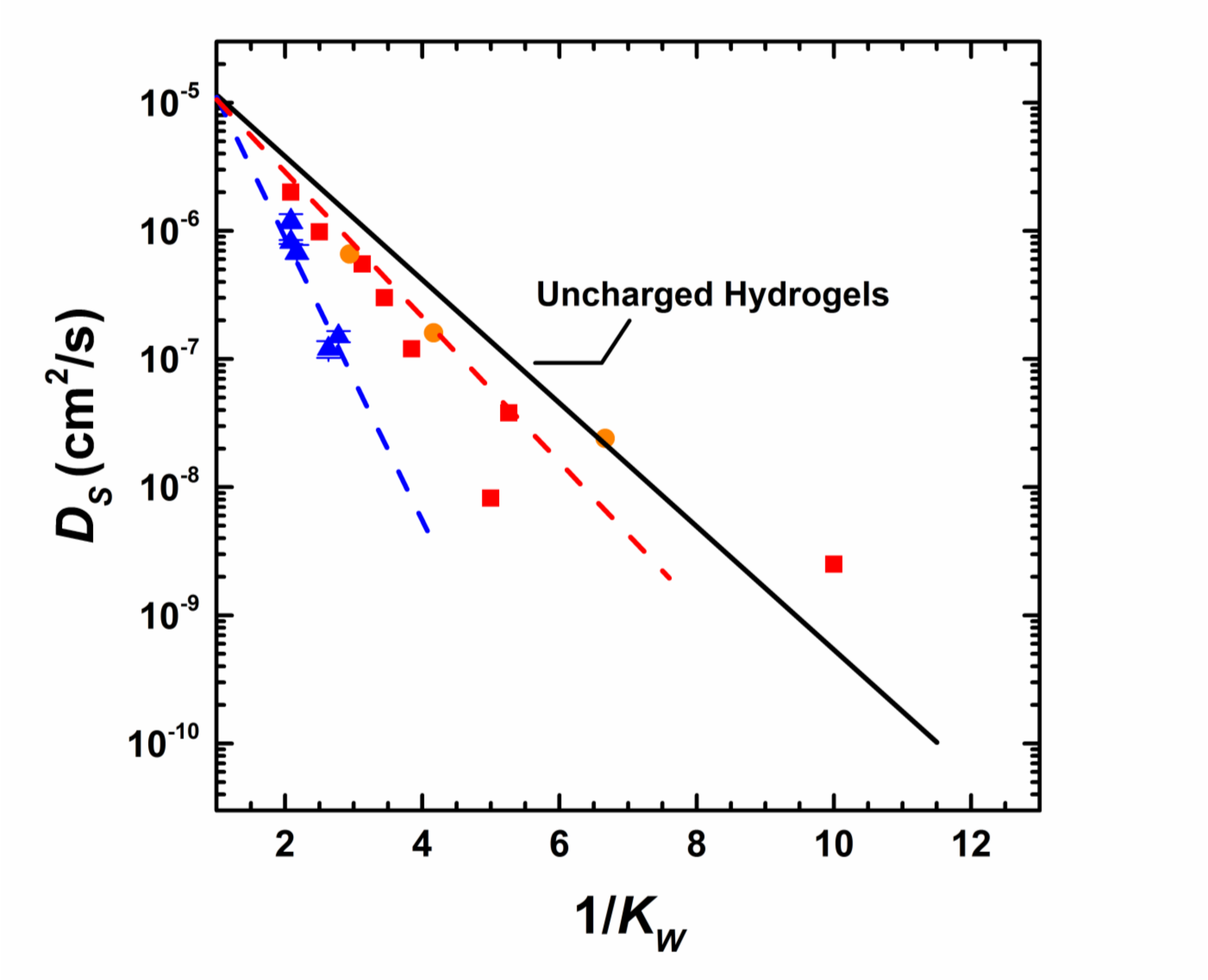

Figure 3. 5. Salt diffusivity, D_S, plotted versus $1/K_W$ for the TRP-BP (▲), BPS(H) (■)[65], and BisAS (●)[77] materials. The D_s values for the TRP-BP materials were calculated from measured P_S and K_S values using Eq. (3.14). The data are compared to a general representation (solid line) of uncharged hydrogel data reported by Yasuda et al.[75]

Similar to the situation discussed for water diffusion and salt permeability, a free volume-based scaling relationship[75] describes the salt diffusion properties of the TRP-BP materials as a function of water content (Fig. 3.5). The correlation also passes through the NaCl diffusion coefficient in aqueous solution (1.47×10^{-5} cm^2/s)[75] at $K_W = 1$. This observation further supports the view, in accord with the work of Yasuda et al.,[75] that water content may be proportional to free volume in these materials.[75]

The reduction in the salt diffusivity in the TRP-BP polymers, relative to the other sulfonated polysulfone materials, is likely related to the observed reduction in TRP-BP water diffusivity compared to the other sulfonated polysulfone materials. If the presence of triptycene in the polymer causes the polymer chains to pack differently (causing a change in the distribution of free volume and/or increasing the tortuosity of transport pathways in the material, c.f., Appendix B for more discussion) compared to the other polysulfone materials, then these effects would be expected to influence larger hydrated salts to a greater extent than water. Salt diffusion in the TRP-BP materials was observed to be more sensitive to changes in water content compared to the dependence of water diffusion on water content as the slope of the salt diffusion coefficient regression in Fig. 3.6 was nearly twice the slope of the of the water diffusion coefficient regression in Fig. 3.6.

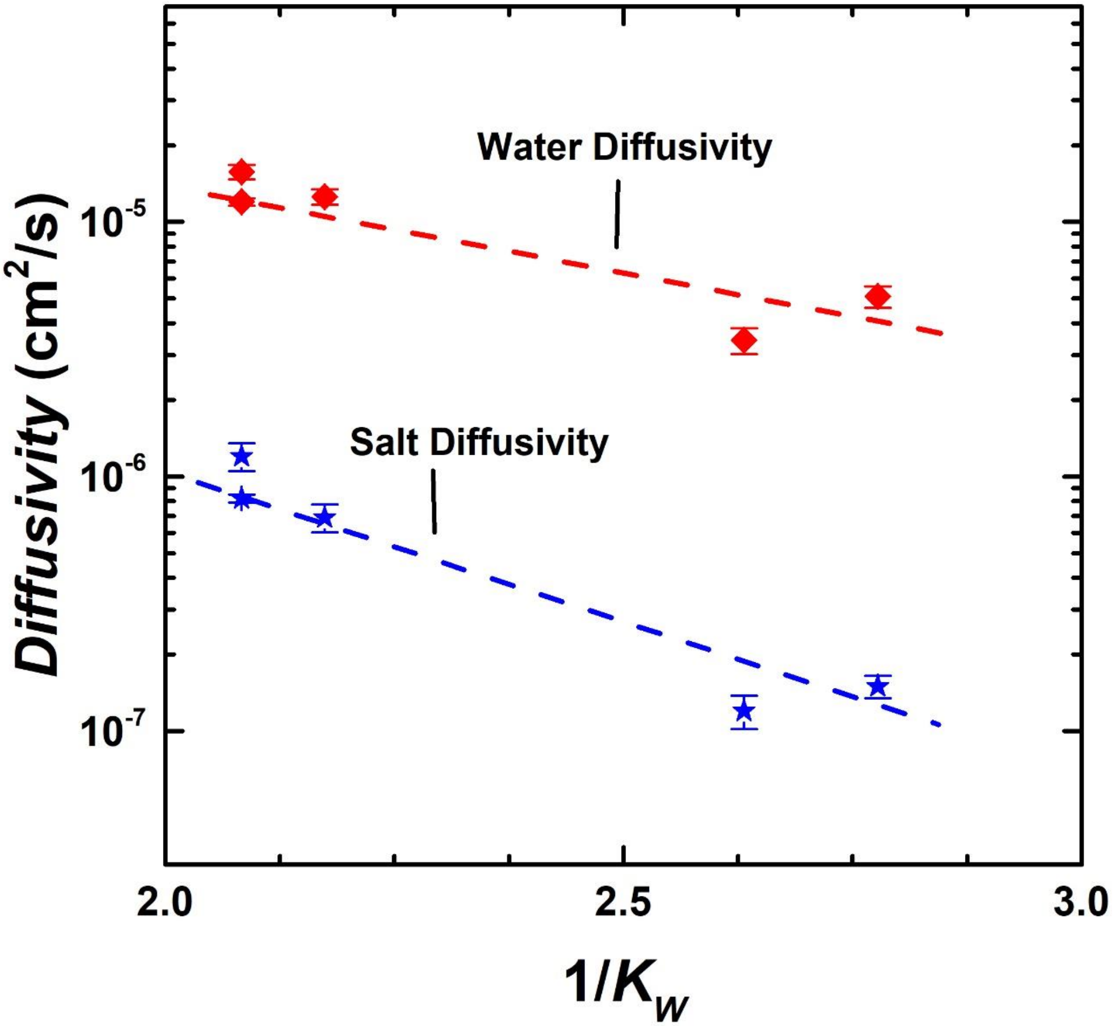

Figure 3. 6. TRP-BP water diffusivity (D_W, ◆, calculated from P_W^D and K_W values using Eq. (3.11)) and salt diffusivity (D_S, ★, calculated from P_S and K_S values using Eq. (3.14)) as a function of 1/K_W.

The data in Fig. 3.6 are consistent with free volume theory, as the diffusion of larger penetrants, i.e., hydrated ions, are expected to be more sensitive to changes in free volume compared to smaller penetrants, i.e., water.[72, 75, 82, 83] The water/salt diffusivity selectivity, D_W/D_S, or the difference between the values of D_W and D_S at a given water content increases as the water content of the polymers decreases (left to right on the horizontal axis of Fig. 3.6), which is consistent with Cohen/Turnbull free volume theory.[63] TRP-BP materials with lower water content (TRP-BP 1:1-35-salt and TRP-BP 2:1-35-salt) have greater water/salt diffusivity selectivity, which is favorable for desalination applications, compared to those materials with higher water content.

3.3.4 Water/Salt Selectivity

In desalination processes, membrane performance typically is evaluated in terms of water flux (related to P_W^D via Eqs. (8) and (9)) and salt rejection, which is related to the water/salt permeability selectivity of the material and reflects the ability of the membrane to separate water and salt.[47, 74] In general, high water flux (high water permeability) and high salt rejection (high water/salt permeability selectivity) is desirable for desalination membrane applications.[2, 4, 5, 45, 47] Selectivity is particularly important for membrane applications,[47, 84] and the water/salt permeability selectivity can be expressed in terms of a water/salt diffusivity selectivity and water/salt sorption selectivity given that permeability can be expressed in terms of the sorption and diffusivity components.[45, 74]

Using the water and salt transport properties discussed previously, the water/salt selectivity properties of the TRP-BP materials can be compared to those properties of the BPS(H) and BisAS materials. In making this comparison, we calculated the diffusive water permeability for all of the materials under comparison using Eq. (3.10), i.e., we included the convective frame of reference term in the calculation. This approach contrasts previous studies on the BPS(H) and BisAS materials that neglected the convective frame of reference term.[2, 79] Also in contrast to previous studies on the BPS(H) and BisAS materials, we set the thermodynamic term, δ in Eq. (3.9), equal to unity in order to compare material properties without the influence of potential artifacts that could be introduced by the single point Flory-Huggins interaction parameter calculation. This alternate analysis, however, was performed and is included separately as part of the Appendix B. The water diffusion coefficient was calculated from the diffusive water permeability using Eq. (3.11).

A tradeoff exists, between water/salt diffusion selectivity, D_W/D_S, and water diffusion coefficient, D_W, for the TRP-BP materials (Fig. 3.7), and it is consistent with free volume theory.[2, 63, 74] Fig. 3.7 shows that some of the TRP-BP materials exhibit greater diffusion selectivity at equivalent D_W values compared to the BPS(H) and the BisAS materials. The TRP-BP 1:1-35-salt material is an exception to these observations. The TRP-BP materials that exhibit improved diffusivity selectivity compared to the BPS(H) and BisAS materials at comparable values of D_W realize the improved selectivity from the stronger suppression of D_s compared to D_W properties observed for the TRP-BP polymers at comparable water content (Figs. 3.2 and 3.5). The selectivity results suggest that it may be possible to use triptycene to modify the distribution of free volume in the polymer in a manner that enhances diffusivity selectivity without the typical corresponding reduction in the water diffusion coefficient that is seen for many materials (including the BPS(H) and BisAS materials shown in Fig. 3.7).

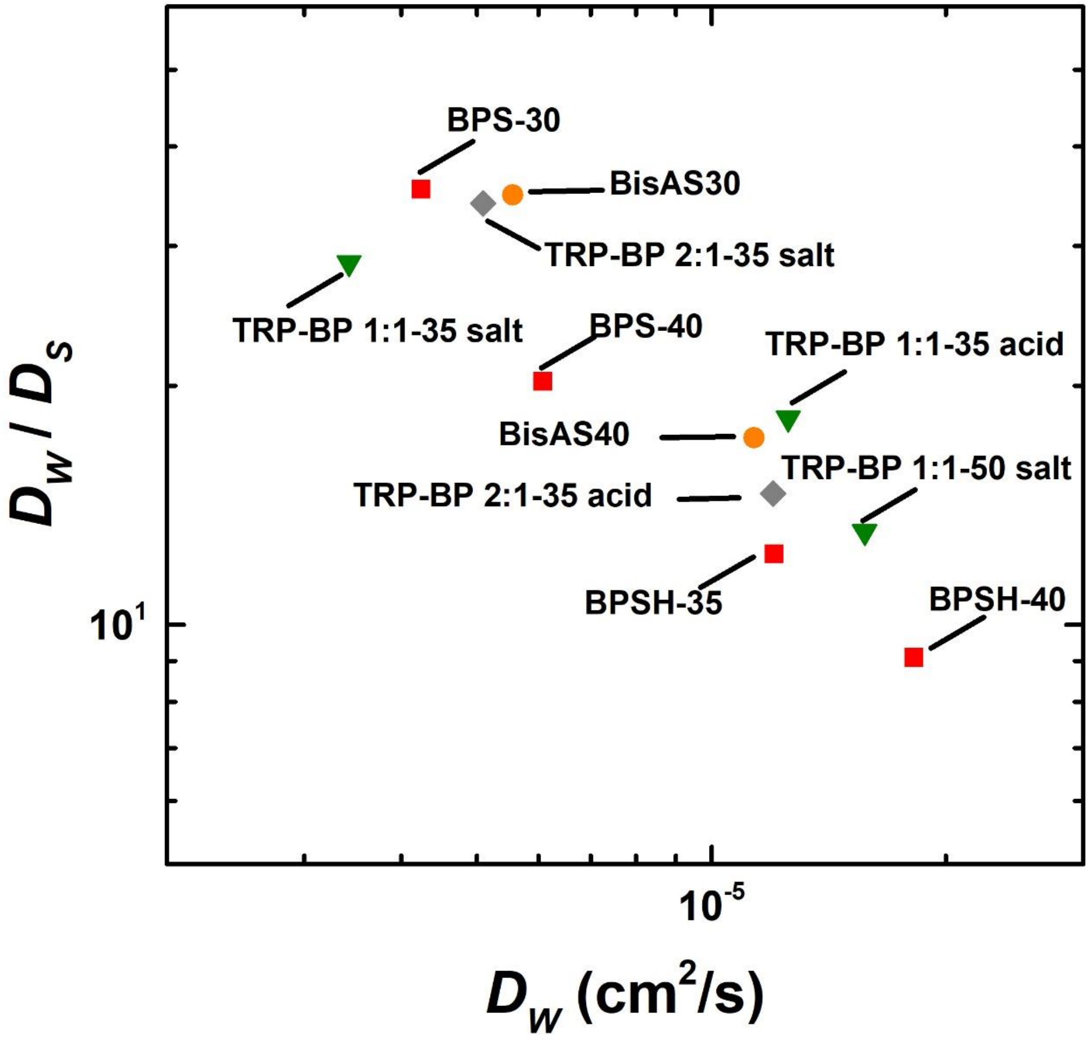

Figure 3. 7. Diffusion selectivity, D_W/D_S, as a function of D_W for the TRP-BP 1:1 (▼), TRP-BP 2:1 (◆), BPS(H) (■)[65], and BisAS (●)[77] materials.

Increasing the triptycene content from 1:1 (50% TRP) to 2:1 (66% TRP) caused an increase in both water/salt diffusivity selectivity and water diffusion coefficient for the salt form polymers that contained 35% (by mole) sulfonated monomer. The corresponding increase in triptycene content for the acid from polymers that contained 35% (by mole) sulfonated monomer resulted in a decrease in diffusivity selectivity and a statistically insignificant change in the water diffusion coefficient (Table 3.1). Therefore, the incorporation of triptycene into sulfonated polysulfone appears to influence diffusivity selectivity in a way that might be leveraged to engineer selective desalination membranes, but the compositional space needs to be more thoroughly explored to understand the fundamental influence of triptycene content on transport properties.

The water/salt sorption selectivity values, K_W/K_S, for the TRP-BP materials generally are comparable to those selectivity values for the BPS(H)[65] and BisAS[77] materials. The TRP-BP 1:1-50 salt-form material is an exception (Fig. 3.8). The low sorption selectivity of TRP-BP 1:1-50-salt may originate from its high salt sorption coefficient as discussed previously (Fig. 3.3), which may be due to counter-ion condensation effects.[81] The water/salt sorption selectivity in the TRP-BP materials is approximately an order of magnitude less than the water/salt diffusivity selectivity, which suggests that diffusivity contributes more to permeability selectivity than sorption effects in these materials.

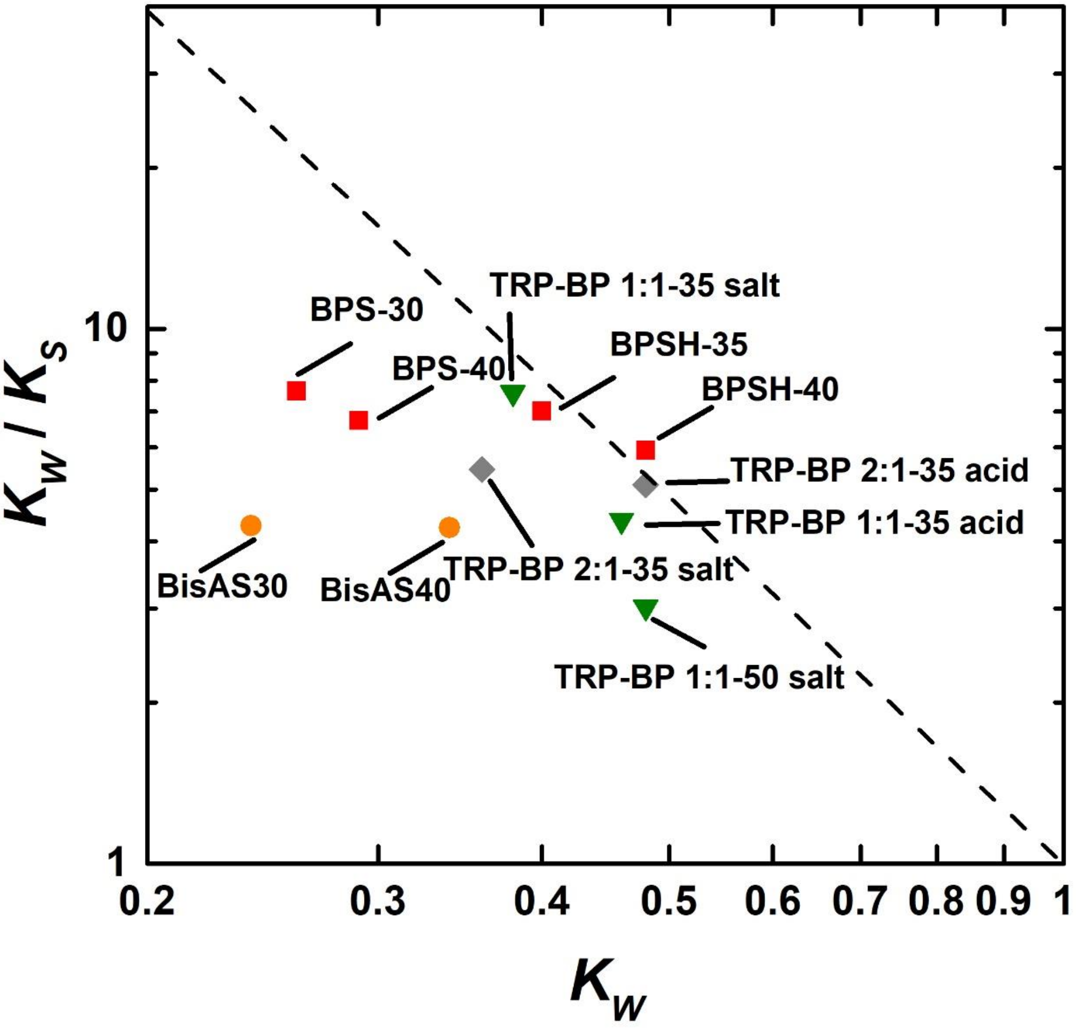

Figure 3. 8. Sorption selectivity, K_W/K_S, as a function of K_W for the TRP-BP 1:1 (▼), TRP-BP 2:1 (◆), BPS(H) (■)[65], and BisAS (●)[77] materials. The dashed line represents an empirical sorption tradeoff frontier reported for desalination membranes.[2, 74]

Incorporation of the triptycene group in sulfonated polysulfone generally resulted in a modest increase in the water/salt permeability selectivity, P_W^D/P_S, at comparable diffusive water permeability, P_W^D, compared to the BisAS[77] sulfonated polysulfones that do not contain triptycene (Fig. 3.9). Furthermore, the acid counter-ion form TRP-BP polymers (i.e., TRP-BP 1:1-35-acid and TRP-BP 2:1-35-acid) exhibit higher water/salt permeability selectivity compared to the BPSH[65] sulfonated polysulfones that do not contain triptycene and higher water permeability than the BisAS-40 material. One exception is the TRP-BP 1:1-50 salt-form material that has comparable selectivity to the BPSH-40 material. The low water/salt permeability selectivity of TRP-BP 1:1-50-salt is likely due to low sorption selectivity, which may be due to counter-ion condensation as discussed previously, that is not completely compensated for by the higher water/salt diffusivity selectivity compared to the BPSH-40 material (Fig. 3.7).

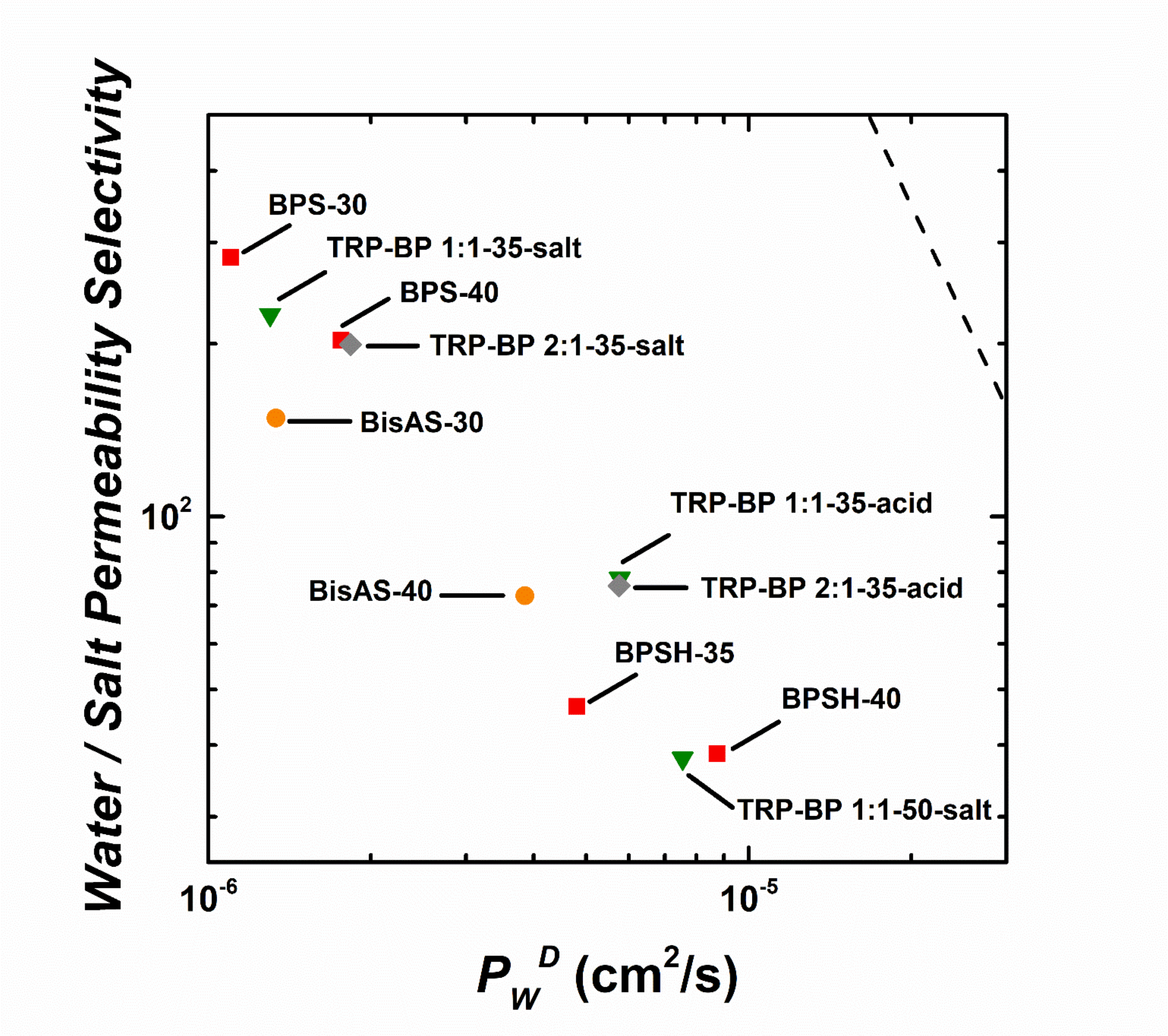

Figure 3. 9. Trade-off between water/salt permeability selectivity and water permeability for the TRP-BP 1:1 (▼), TRP-BP 2:1 (◆), BPS(H) (■)[65], and BisAS (●)[77] materials. The dashed line represents an empirical permeability tradeoff frontier reported for desalination membranes.[2, 74]

3.4. Conclusions

Water and salt transport properties of triptycene-containing sulfonated polysulfones have been studied, and the water/salt selectivity properties of the materials suggest that incorporating triptycene groups into sulfonated polysulfone materials may increase modestly water/salt permeability selectivity, particularly for acid counter-ion form materials. The triptycene-containing sulfonated polysulfones sorb more water than sulfonated polysulfones without triptycene (at comparable degrees of sulfonation), but the dry polymer density is not greatly affected by incorporation of triptycene in the polymer possibly due to strong hydrogen bond interactions between sulfonate groups in the dry polymers. No significant difference in salt sorption was observed between the TRP-BP materials and other sulfonated polysulfone materials as a function of water content. Both water and salt diffusion coefficients in the TRP-BP materials were suppressed compared to those values measured for BPS(H) and BisAS materials (at comparable water content). These observations may result from the influence of triptycene on polymer chain packing and/or on the distribution of free volume in the polymer, which could result in more tortuous transport pathways in the triptycene-containing polymers. Water/salt permeability selectivity was analyzed by considering both diffusion selectivity and sorption selectivity. The observed increase in water/salt permeability selectivity for some of the TRP-BP sulfonated polysulfone materials compared to the other materials that do not contain triptycene, suggests that incorporating bulky functional groups, such as triptycene, in polymers may be a strategy to increase the selectivity of desalination membrane materials.

3.5. References

1. R. Connor, *The United Nations world water development report 2015: Water for a sustainable world*. 2015: United Nations Educational, Scientific and Cultural Organization.
2. G.M. Geise, H.B. Park, A.C. Sagle, B.D. Freeman, and J.E. McGrath, Water permeability and water/salt selectivity tradeoff in polymers for desalination. Journal of Membrane Science, 2011. **369**(1): p. 130-138.
3. K. Bourzac, Water: The flow of technology. Nature, 2013. **501**(7468): p. S4-S6.
4. G.M. Geise, H.S. Lee, D.J. Miller, B.D. Freeman, J.E. McGrath, and D.R. Paul, Water purification by membranes: The role of polymer science. Journal of Polymer Science Part B: Polymer Physics, 2010. **48**(15): p. 1685-1718.
5. M. Elimelech and W.A. Phillip, The future of seawater desalination: Energy, technology, and the environment. Science, 2011. **333**: p. 712-717.
6. R.F. Service, Desalination freshens up. Science, 2006. **313**(5790): p. 1088-1090.
7. WWAP (United Nations World Water Assessment Programme). *The United Nations World Water Development Report 2017: Wastewater, The Untapped Resource*. 2017, UNESCO: Paris.
8. G. Korte and I. James, *White House launches 'moonshot for water'*, in *USA Today*. 2015.
9. NAE. *Grand challenges for engineering: Provide access to clean water*. 2015 October 2015]; Available from: http://www.engineeringchallenges.org/challenges/water.aspx.
10. C.J. Vörösmarty, A.Y. Hoekstra, S.E. Bunn, D. Conway, and J. Gupta, Fresh water goes global. Science, 2015. **349**(6247): p. 478-479.
11. F. Cheng, H. Luo, L. Hu, B. Yu, Z. Luo, and M.F. de Cortalezzi, Sludge carbonization and activation: From hazardous waste to functional materials for water treatment. Journal of Environmental Chemical Engineering, 2016. **4**(4): p. 4574-4586.
12. R. Valladares Linares, Z. Li, S. Sarp, S.S. Bucs, G. Amy, and J.S. Vrouwenvelder, Forward osmosis niches in seawater desalination and wastewater reuse. Water Research, 2014. **66**(Supplement C): p. 122-139.
13. M. Meneses, J.C. Pasqualino, and F. Castells, Environmental assessment of urban wastewater reuse: Treatment alternatives and applications. Chemosphere, 2010. **81**(2): p. 266-272.
14. Y. Cohen, R. Semiat, and A. Rahardianto, A perspective on reverse osmosis water desalination: Quest for sustainability. AIChE Journal, 2017. **63**(6): p. 1771-1784.
15. D. Chen, J. Zhou, and Q. Zhang, Effects of heating rate on slow pyrolysis behavior, kinetic parameters and products properties of moso bamboo. Bioresource Technology, 2014. **169**: p. 313-319.
16. H. Sayyaadi and A. Saffari, Thermoeconomic optimization of multi effect distillation desalination systems. Applied Energy, 2010. **87**(4): p. 1122-1133.
17. D. Zhao, J. Xue, S. Li, H. Sun, and Q.-d. Zhang, Theoretical analyses of thermal and economical aspects of multi-effect distillation desalination dealing with high-salinity wastewater. Desalination, 2011. **273**(2): p. 292-298.
18. H. Strathmann, Electrodialysis, a mature technology with a multitude of new applications. Desalination, 2010. **264**(3): p. 268-288.

19. Y. Kim and B.E. Logan, Series assembly of microbial desalination cells containing stacked electrodialysis cells for partial or complete seawater desalination. Environmental Science & Technology, 2011. **45**(13): p. 5840-5845.

20. G.M. Geise, H.B. Park, A.C. Sagle, B.D. Freeman, and J.E. McGrath, Water permeability and water/salt selectivity tradeoff in polymers for desalination. Journal of Membrane Science, 2011. **369**(1-2): p. 130-138.

21. K.P. Lee, T.C. Arnot, and D. Mattia, A review of reverse osmosis membrane materials for desalination—Development to date and future potential. Journal of Membrane Science, 2011. **370**(1): p. 1-22.

22. D. Li and H. Wang, Recent developments in reverse osmosis desalination membranes. Journal of Materials Chemistry, 2010. **20**(22): p. 4551-4566.

23. G.M. Geise, B.D. Freeman, and D.R. Paul, Characterization of a sulfonated pentablock copolymer for desalination applications. Polymer, 2010. **51**(24): p. 5815-5822.

24. W. Xie, G.M. Geise, B.D. Freeman, H.-S. Lee, G. Byun, and J.E. McGrath, Polyamide interfacial composite membranes prepared from m-phenylene diamine, trimesoyl chloride and a new disulfonated diamine. Journal of Membrane Science, 2012. **403**(Supplement C): p. 152-161.

25. E. Guillén-Burrieza, J. Blanco, G. Zaragoza, D.-C. Alarcón, P. Palenzuela, M. Ibarra, and W. Gernjak, Experimental analysis of an air gap membrane distillation solar desalination pilot system. Journal of Membrane Science, 2011. **379**(1): p. 386-396.

26. R.J. Petersen, Composite reverse osmosis and nanofiltration membranes. Journal of Membrane Science, 1993. **83**: p. 81-150.

27. S. Miller, H. Shemer, and R. Semiat, Energy and environmental issues in desalination. Desalination, 2015. **366**: p. 2-8.

28. P.L. Parise, A.E. Allegrezza Jr., and B.S. Parekh, Reverse osmosis: Chlorine-resistant polysulfone reverse osmosis membrane and module. Ultrapure Water, 1987. **4**(7): p. 54-65.

29. S. Avlonitis, W.T. Hanbury, and T. Hodgkiess, Chlorine degradation of aromatic polyamides. Desalination, 1992. **85**(3): p. 321.

30. T. Knoell, Municipal wastewater: Chlorine's impact on the performance and properties of polyamide membranes. Ultrapure Water, 2006. **23**(April): p. 24-31.

31. A. Dey and R. Kulkarni, Chlorine: The use of UV technology to dechlorinate water. Ultrapure Water, 2009. **26**(2): p. 14-18.

32. N. Dam and P.R. Ogilby, On the mechanism of polyamide degradation in chlorinated water. Helvetica Chimica Acta, 2001. **84**(9): p. 2540-2549.

33. S. Robinson, S.Z. Abdullah, P. Bérubé, and P. Le-Clech, Ageing of membranes for water treatment: Linking changes to performance. Journal of Membrane Science, 2016. **503**(Supplement C): p. 177-187.

34. R.W. Baker, *Membrane technology and applications*. 3rd ed. 2012, New York: Wiley.

35. S.G. Kimura, Reverse osmosis performance of sulfonated poly(2,6-dimethylphenylene ether) ion exchange membranes. Industrial & Engineering Chemistry Research, 1971. **10**(3): p. 335-339.

36. M.A. Dinno, Y. Kang, D.R. Lloyd, J.E. McGrath, and J.P. Wightman. *Characterization of dense sulfonated polysulfone membranes*. in *Physicochem. Aspects Polym. Surf., [Proc. Int. Symp.]*. 1981. Plenum, New York, N. Y.

37. Y.-J. Kim, K.-S. Lee, M.-H. Jeong, and J.-S. Lee, Highly chlorine-resistant end-group crosslinked sulfonated-fluorinated poly(arylene ether) for reverse osmosis membrane. Journal of Membrane Science, 2011. **378**: p. 512-519.

38. J.E. McGrath, H.B. Park, and B.D. Freeman, *Chlorine resistant desalination membranes based on directly sulfonated poly(arylene ether sulfone) copolymers*. 2011.

39. Y. Zhang, C. Zhao, H. Yan, G. Pan, M. Guo, H. Na, and Y. Liu, Highly chlorine-resistant multilayer reverse osmosis membranes based on sulfonated poly(arylene ether sulfone) and poly(vinyl alcohol). Desalination, 2014. **336**: p. 58-63.

40. A.E. Allegrezza Jr., B.S. Parekh, P.L. Parise, E.J. Swiniarski, and J.L. White, Chlorine resistant polysulfone reverse osmosis modules. Desalination, 1987. **64**: p. 285-304.

41. J. Glater, S.-k. Hong, and M. Elimelech, The search for a chlorine-resistant reverse osmosis membrane. Desalination, 1994. **95**(3): p. 325-345.

42. H.B. Park, B.D. Freeman, Z.-B. Zhang, M. Sankir, and J.E. McGrath, Highly chlorine-tolerant polymers for desalination. Angewandte Chemie, 2008. **120**: p. 6108-6113.

43. M. Paul, H.B. Park, B.D. Freeman, A. Roy, J.E. McGrath, and J.S. Riffle, Synthesis and crosslinking of partially disulfonated poly(arylene ether sulfone) random copolymers as candidates for chlorine resistant reverse osmosis membranes. Polymer, 2008. **49**: p. 2243-2252.

44. W. Xie, G.M. Geise, B.D. Freeman, H.-S. Lee, G. Byun, and J.E. McGrath, Polyamide interfacial composite membranes prepared from *m*-phenylene diamine, trimesoyl chloride and a new disulfonated diamine. Journal of Membrane Science, 2012. **403-404**: p. 152-161.

45. G.M. Geise, D.R. Paul, and B.D. Freeman, Fundamental water and salt transport properties of polymeric materials. Progress in Polymer Science, 2014. **39**: p. 1-42.

46. J. Kamcev and B.D. Freeman, Charged polymer membranes for environmental/energy applications. Annual Review of Chemical and Biomolecular Engineering, 2016. **7**(1): p. 111-133.

47. H.B. Park, J. Kamcev, L.M. Robeson, M. Elimelech, and B.D. Freeman, Maximizing the right stuff: The trade-off between membrane permeability and selectivity. Science, 2017. **356**(6343): p. 1-10.

48. S. Tas, B. Zoetebier, M.A. Hempenius, G.J. Vancso, and K. Nijmeijer, Monovalent cation selective crown ether containing poly(arylene ether ketone)/SPEEK blend membranes. RSC Advances, 2016. **6**(60): p. 55635-55642.

49. S. Tas, B. Zoetebier, O.S. Sukas, M. Bayraktar, M. Hempenius, G.J. Vancso, and K. Nijmeijer, Ion-selective ionic polymer metal composite (IPMC) actuator based on crown ether containing sulfonated poly(arylene ether ketone). Macromolecular Materials and Engineering, 2017. **302**(4): p. 1600381-n/a.

50. B. Zoetebier, S. Tas, G.J. Vancso, K. Nijmeijer, and M.A. Hempenius, Synthesis of poly(arylene ether ketone)s bearing skeletal crown ether units for cation exchange membranes. Journal of Polymer Science Part A: Polymer Chemistry, 2015. **53**(23): p. 2786-2793.

51. M.A.C. Stuart, W.T.S. Huck, J. Genzer, M. Muller, C. Ober, M. Stamm, G.B. Sukhorukov, I. Szleifer, V.V. Tsukruk, M. Urban, F. Winnik, S. Zauscher, I. Luzinov, and S. Minko, Emerging applications of stimuli-responsive polymer materials. Nat Mater, 2010. **9**(2): p. 101-113.

52. J.R. Wiegand, Z.P. Smith, Q. Liu, C.T. Patterson, B.D. Freeman, and R. Guo, Synthesis and characterization of triptycene-based polyimides with tunable high fractional free volume for gas separation membranes. Journal of Materials Chemistry A, 2014. **2**(33): p. 13309-13320.

53. S. Luo, Q. Liu, B. Zhang, J.R. Wiegand, B.D. Freeman, and R. Guo, Pentiptycene-based polyimides with hierarchically controlled molecular cavity architecture for efficient membrane gas separation. Journal of Membrane Science, 2015. **480**: p. 20-30.

54. S. Luo, J.R. Wiegand, B. Kazanowska, C.M. Doherty, K. Konstas, A.J. Hill, and R. Guo, Finely tuning the free volume architecture in iptycene-containing polyimides for highly selective and fast hydrogen transport. Macromolecules, 2016. **49**(9): p. 3395-3405.

55. S. Luo, J. Liu, H. Lin, B.A. Kazanowska, M.D. Hunckler, R.K. Roeder, and R. Guo, Preparation and gas transport properties of triptycene-containing polybenzoxazole (PBO)-based polymers derived from thermal rearrangement (TR) and thermal cyclodehydration (TC) processes. Journal of Materials Chemistry A, 2016. **4**(43): p. 17050-17062.

56. N. Alaslai, X. Ma, B. Ghanem, Y. Wang, F. Alghunaimi, and I. Pinnau, Synthesis and characterization of a novel microporous dihydroxyl-functionalized triptycene-diamine-based polyimide for natural gas membrane separation. Macromolecular Rapid Communications, 2017. **38**(18): p. 1700303.

57. F. Alghunaimi, B. Ghanem, N. Alaslai, M. Mukaddam, and I. Pinnau, Triptycene dimethyl-bridgehead dianhydride-based intrinsically microporous hydroxyl-functionalized polyimide for natural gas upgrading. Journal of Membrane Science, 2016. **520**: p. 240-246.

58. B. Ghanem, F. Alghunaimi, X. Ma, N. Alaslai, and I. Pinnau, Synthesis and characterization of novel triptycene dianhydrides and polyimides of intrinsic microporosity based on 3, 3′-dimethylnaphthidine. Polymer, 2016. **101**: p. 225-232.

59. L.M. Robeson, The upper bound revisited. Journal of Membrane Science, 2008. **320**(1): p. 390-400.

60. L.M. Robeson, Correlation of separation factor versus permeability for polymeric membranes. Journal of membrane science, 1991. **62**(2): p. 165-185.

61. S. Luo, J.R. Wiegand, P. Gao, C.M. Doherty, A.J. Hill, and R. Guo, Molecular origins of fast and selective gas transport in pentiptycene-containing polyimide membranes and their physical aging behavior. Journal of Membrane Science, 2016. **518**: p. 100-109.

62. J.R. Weidman, S. Luo, C.M. Doherty, A.J. Hill, P. Gao, and R. Guo, Analysis of governing factors controlling gas transport through fresh and aged triptycene-based polyimide films. Journal of Membrane Science, 2017. **522**: p. 12-22.

63. D. Turnbull and M.H. Cohen, Free-volume model of the amorphous phase: Glass transition. The Journal of Chemical Physics, 1961. **34**(1): p. 120-125.

64. D.R. Paul, Reformulation of the solution-diffusion theory of reverse osmosis. Journal of Membrane Science, 2004. **241**(2): p. 371-386.

65. W. Xie, J. Cook, H.B. Park, B.D. Freeman, C.H. Lee, and J.E. McGrath, Fundamental salt and water transport properties in directly copolymerized disulfonated poly(arylene ether sulfone) random copolymers. Polymer, 2011. **52**(9): p. 2032-2043.

66. C.H. Lee, D. VanHouten, O. Lane, J.E. McGrath, J. Hou, L.A. Madsen, J. Spano, S. Wi, J. Cook, and W. Xie, Disulfonated poly (arylene ether sulfone) random copolymer blends tuned for rapid water permeation via cation complexation with poly (ethylene glycol) oligomers. Chemistry of Materials, 2011. **23**(4): p. 1039-1049.

67. H. Ju, B.D. McCloskey, A.C. Sagle, Y.-H. Wu, E. Van Wagner, H.B. Park, B.D. Freeman, L. Shimko, D.F. Lawler, and M.M. Sharma. *Synthesis and characterization of surface coated ultrafiltration membranes to enhance oil/water fouling resistance*. in *ACS*. 2006.

68. C.L. Yaws and R.W. Pike, *Chapter 3 - Density of liquid—Organic compounds*, in *Thermophysical Properties of Chemicals and Hydrocarbons*. 2009, William Andrew Publishing: Norwich, NY. p. 106-197.

69. U. Merten, *Desalination by reverse osmosis*. 1966, Cambridge: M.I.T. Press.

70. J.G. Wijmans and R.W. Baker, The solution-diffusion model: a review. Journal of Membrane Science, 1995. **107**(1): p. 1-21.

71. D.R. Paul, Relation between hydraulic permeability and diffusion in homogeneous swollen membranes. Journal of Polymer Science: Polymer Physics Edition, 1973. **11**(2): p. 289-296.

72. P.J. Flory, Thermodynamics of high polymer solutions. The Journal of Chemical Physics, 1941. **9**(8): p. 660-660.

73. M.L. Huggins, Solutions of long chain compounds. The Journal of Chemical Physics, 1941. **9**(5): p. 440-440.

74. H. Zhang and G.M. Geise, Modeling the water permeability and water/salt selectivity tradeoff in polymer membranes. Journal of Membrane Science, 2016. **520**: p. 790-800.

75. H. Yasuda, C.E. Lamaze, and L.D. Ikenberry, Permeability of solutes through hydrated polymer membranes. Part I. Diffusion of sodium chloride. Die Makromolekulare Chemie, 1968. **118**(1): p. 19-35.

76. G.M. Geise, C.L. Willis, C.M. Doherty, A.J. Hill, T.J. Bastow, J. Ford, K.I. Winey, B.D. Freeman, and D.R. Paul, Characterization of aluminum-neutralized sulfonated styrenic pentablock copolymer films. Industrial & Engineering Chemistry Research, 2013. **52**(3): p. 1056-1068.

77. J. Cook, *Fundamental water and ion transport characterization of sulfonated polysulfone desalination materials*. 2014, Ph.D. Thesis, The University of Texas at Austin.

78. W. Xie, H. Ju, G.M. Geise, B.D. Freeman, J.I. Mardel, A.J. Hill, and J.E. McGrath, Effect of free volume on water and salt transport properties in directly copolymerized disulfonated poly(arylene ether sulfone) random copolymers. Macromolecules, 2011. **44**(11): p. 4428-4438.

79. W. Xie, H.-B. Park, J. Cook, C.H. Lee, G. Byun, B.D. Freeman, and J.E. McGrath, Advances in membrane materials: desalination membranes based on directly copolymerized disulfonated poly(arylene ether sulfone) random copolymers. Water Science and Technology, 2010. **61**(3): p. 619-624.

80. H. Ju, A.C. Sagle, B.D. Freeman, J.I. Mardel, and A.J. Hill, Characterization of sodium chloride and water transport in poly(ethylene oxide) hydrogels. Journal of Membrane Science, 2010. **358**: p. 131-141.

81. J. Kamcev, D.R. Paul, G.S. Manning, and B.D. Freeman, Predicting salt permeability coefficients in highly swollen, highly charged ion exchange membranes. ACS Applied Materials & Interfaces, 2017. **9**(4): p. 4044-4056.

82. B.D. Freeman, Basis of permeability/selectivity tradeoff relations in polymeric gas separation membranes. Macromolecules, 1999. **32**(2): p. 375-380.

83. E.L. Cussler, *Diffusion: Mass transfer in fluid systems*. 2009: Cambridge University Press.

84. J.R. Werber, A. Deshmukh, and M. Elimelech, The Critical Need for Increased Selectivity, Not Increased Water Permeability, for Desalination Membranes. Environmental Science & Technology Letters, 2016. **3**(4): p. 112-120.

Chapter 4 Functional group configuration influences salt transport in desalination membrane materials

4. 1 Introduction

Desalination is one strategy to improve access to clean water and address global water shortage [1-7]. Membrane-based desalination techniques, such as reverse osmosis, are widely used due to high energy efficiency and low cost compared to thermal desalination technologies [4, 5, 8-10]. The effectiveness of desalination membranes is intimately coupled to the water and salt transport properties of the polymer used to prepare the membrane, and materials that afford high water/salt selectivity, whether by enhancing water transport or by suppressing salt transport, are desirable for desalination applications [11, 12].

Polyamide-based reverse osmosis membranes, with high water permeance and low salt passage, are the current state-of-the-art for membrane-based desalination [1, 2, 5, 7]. Polyamides, however, are susceptible to oxidative degradation via chlorine-based chemicals used to disinfect water and to limit biofouling, so advanced chlorine-tolerant, or chemically stable, desalination membranes are needed [13-16]. Several candidate materials have been considered [4, 5, 16-18], but a combination of excellent chlorine tolerance and favorable water/salt selectivity properties remains elusive [11, 12, 19]. Engineering the next generation of desalination membranes with desirable combinations of transport properties, chemical and mechanical stability, and surface properties requires knowledge of how specific chemical functional groups influence material properties.

This chapter is already published and available from: Luo, H., Chang, K., Bahati, K., & Geise, G. M. (2019). Functional group configuration influences salt transport in desalination membrane materials. Journal of Membrane Science, 590, 117295.

One approach to designing effective desalination membranes is to engineer polymers that suppress salt permeability. So long as water transport properties are not simultaneously suppressed to the same or greater extent, this approach would increase salt rejection [4, 19, 20]. The solution-diffusion model (for non-porous polymers such as those often used in desalination membranes) suggests that salt permeability can be suppressed by reducing salt partitioning (i.e., sorption) into the membrane and/or salt diffusion through the membrane as salt permeability is the product of salt sorption and diffusion [21, 22].

In relatively simple uncharged hydrated polymers, salt sorption properties are linked to the relative permittivity (or dielectric constant) of the material [19, 23-25], and polymer chemistry can be used to engineer relative permittivity to influence the thermodynamics of salt sorption [23]. Additionally, preparing membranes (with low water content – similar to desalination membranes) with rigid polymer backbones and/or bulky side groups can result in favorable water/salt transport selectivity [26-28]. These findings inform opportunities to engineer polymers to achieve the necessary combination of properties to purify water effectively.

One challenge in many fundamental studies of membrane transport properties is that modification of the polymer often changes the hydrophilicity of the material [4-6, 29]. In other words, a change in water content often accompanies systematic variations in polymer chemistry. Water content can have a profound impact on the water and salt transport properties of polymers [4, 19, 30-32], and it can be difficult to decouple the influences of changing water content and polymer chemistry on transport properties. Doing so, however, is critical to understanding how molecular engineering can be used to design advanced membrane materials.

Here we prepared five methacrylate-based co-polymers that have statistically equivalent water content but different ratios of two co-monomers that have different numbers of hydroxyl groups: 2-hydroxyethyl methacrylate (HEMA) and glycerol methacrylate (GMAOH). Selecting these co-monomers enabled a systematic variation of the position and number density of hydroxyl groups in the co-polymers without changing the water content of the material. The chemical composition of the co-polymer was systematically varied from a vicinal diol-rich configuration (GMAOH-rich co-polymer) to a HEMA-rich material with single hydroxyl groups on the side chains. Shifting the co-polymer composition from a GMAOH-rich configuration to a HEMA-rich configuration suppressed both salt sorption and salt diffusion properties, and these results were supported by dielectric permittivity property measurements and state of water analysis. The results suggest, without complication from changing water content, that a more distributed hydrophilic functional group configuration may suppress salt transport to a greater extent than a more vicinal functional group-rich configuration within the co-polymer. As such, this study provides information about how specific chemical functional groups influence salt transport properties in a unique manner that is decoupled from polymer water content.

4.2 Experimental methods

4.2.1 Materials

Co-polymers (Figure 4.1) were prepared by photo-initiated cross-linking of 2-hydroxyethyl methacrylate (HEMA, 99%, Sigma-Aldrich, St. Louis, MO), glycidyl methacrylate (GMA, 97%, Sigma-Aldrich, St, Louis, MO), and glycerol methacrylate (GMAOH, synthesized as reported by Tan et al. [33]). The cross-linker was poly(ethylene glycol) dimethacrylate (PEGDMA, average Mn = 550 g/mol, Sigma-Aldrich, St. Louis, MO). The cross-linker content (10% of the total mass of the co-monomers) was chosen to mitigate two competing objectives: minimizing the cross-linker content to study the influence of co-monomer functionality on transport properties while incorporating enough cross-linker to yield mechanically robust materials. The initiator was 1-

hydroxycyclohexyl phenyl ketone (HCPK, 99%, Sigma-Aldrich, St. Louis, MO), and the amount of initiator used was 1% of the total co-monomer mass [26, 27].

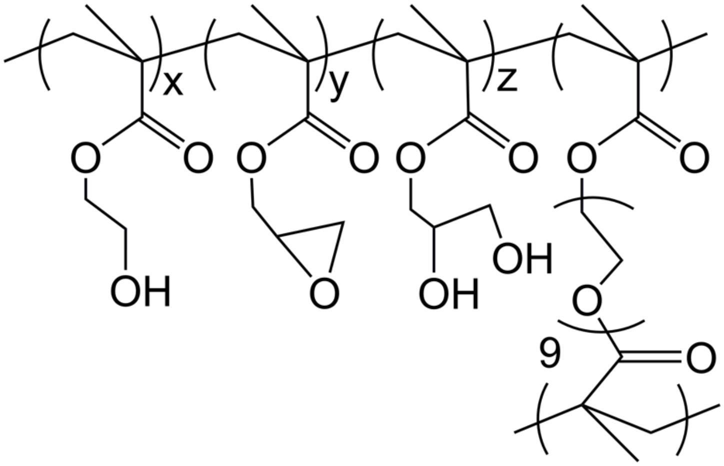

Figure 4. 1. Chemical structure of the cross-linked HEMA:GMA:GMAOH co-polymer. The co-polymers were prepared from pre-polymerization solutions that contained a x:y:z, by mass, ratio of HEMA:GMA:GMAOH co-monomers (such that x + y + z = 100). The cross-linker was added such that the mass of cross-linker was 10% of the total mass of the co-monomers.

In a typical preparation of the 15:55:30 HEMA:GMA:GMAOH material, 0.15 g of HEMA, 0.55 g of GMA, 0.3 g of GMAOH, 0.1 g of PEGDMA, and 10 mg of HCPK were mixed, via magnetic stirring, in a 20 mL glass vial. The mixture was stirred at room temperature for 30 min and then was degassed for 10 min in an ultrasonic bath (VWR, 97043). The result of this process was a homogeneous and bubble-free pre-polymerization solution.

This solution subsequently was deposited slowly onto a clean glass plate. Two 100 µm thick metal spacers were placed on either side of the solution, and a quartz plate was placed on top of the spacers to create a uniformly thick film of the pre-polymerization solution. This assembly was placed on a leveled platform in a UV-crosslinking chamber (Spectroline, Select^{TM} Series). The pre-polymerization solution was irradiated with 120 µJ/cm^2 312 nm light for 5 min, which was sufficiently long to form mechanically robust membranes, to obtain a colorless and transparent membrane film.

The transparent nature of the films was an indicator that the materials are relatively homogeneous. Glass transition temperatures can also provide additional information about the morphology of these dense thick films [34]. Homogeneous co-polymers, i.e., materials where the co-monomers are well-mixed at the molecular level, are expected to exhibit a single glass transition temperature [26, 34]. Unfortunately, the glass transition temperatures of all of the HEMA:GMA:GMAOH co-polymers appear to be obscured by vaporization of some of the water initially sorbed by the co-polymer. The Fox equation [35, 36], which can be used to calculate a first approximation estimate of the co-polymer glass transition temperature based on homopolymer glass transition temperatures and co-polymer composition, provides evidence for this situation. Furthermore, the Fox equation has been used to calculate values in good agreement with experimentally measured glass transition temperatures for HEMA-containing materials [27]. The Fox equation estimated hydrated co-polymer glass transition temperatures increased in the order of 108ºC, 113ºC, 116ºC, 121ºC, and 126ºC as the HEMA composition of the pre-polymerization solution increased from 0 to 60% (by mass). Importantly, we did not observe glass transition temperatures at the temperatures where a glass transition would be expected if the co-monomers were prepared as homopolymers, and this result further suggests that the co-polymers were relatively homogeneous. As such, the transparent nature of the films and the glass transition temperature data/analysis suggest that the co-polymers considered here are relatively homogeneous.

Following the cross-linking process, the membrane was removed carefully from the surface and immersed in de-ionized (DI) water (18.2 MΩ cm). Five materials, with different ratios of the co-monomers (Figure 4.2), were prepared using this process. The mass composition of the pre-polymerization solution used to prepare the co-polymers was used to distinguish the materials, and Fourier-transform infrared (FT-IR) spectroscopy (see Supplementary Information and Figure 4.S1) suggests that the pre-polymerization solution composition is representative of the composition of these cross-linked networks. All materials were stored in DI water until use.

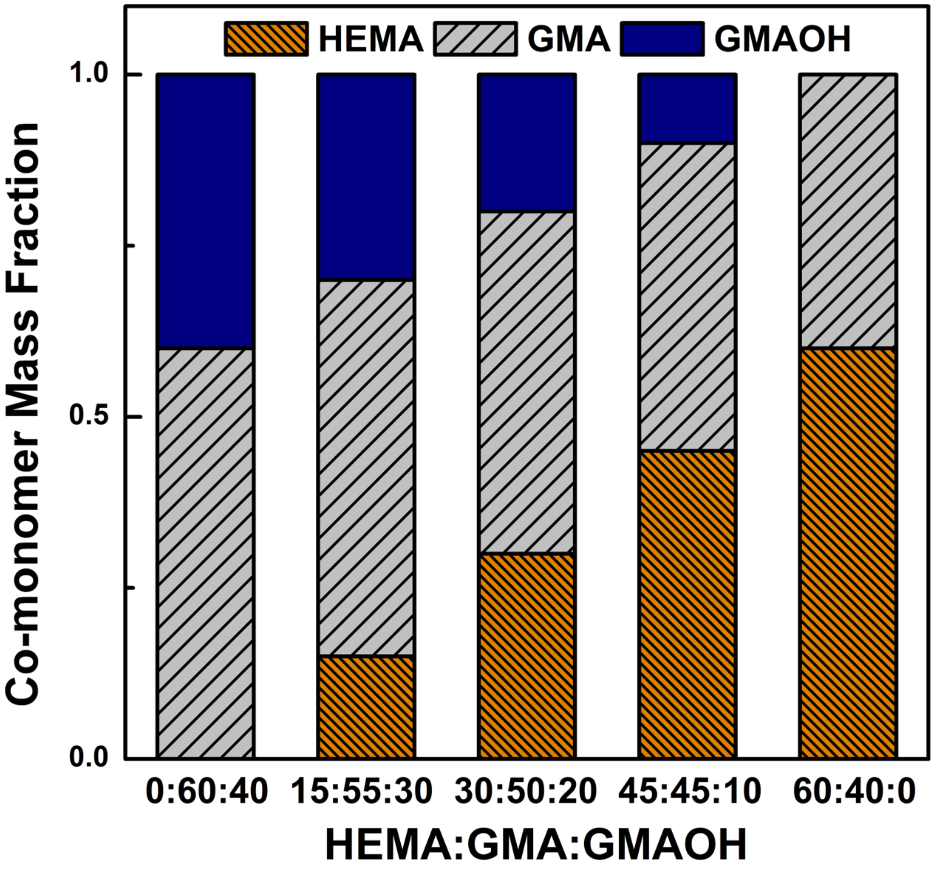

Figure 4. 2. The co-monomer content of the co-polymer was systematically varied (by adjusting the composition of the pre-polymerization solution used to prepare the co-polymers) to probe the influence of hydroxyl group configuration on the salt transport properties of the five HEMA:GMA:GMAOH materials considered. The nomenclature on the horizontal axis corresponds to the pre-polymerization solution mass composition.

4.2.2 Methods

4.2.2.1 Water uptake

After an initial equilibration period of at least 48 hours, samples were removed from the DI water. Residual surface water was wiped from the film, and the wet sample mass, m_w, was measured immediately thereafter. Samples were subsequently dried under vacuum at 22 ± 1 ºC (ambient temperature) for at least 48 hours to remove sorbed water. After drying, samples were removed quickly from the oven, and the dry mass, m_d, of the sample was measured. Pure water uptake, w_u, was calculated as:

$$w_u = \frac{m_w - m_d}{m_d} \tag{4.1}$$

Dry polymer density, ρ_p, was measured immediately after the dry mass measurement using an Archimedes' principle method [26-28, 37, 38]. The dry polymer density, ρ_p, was calculated as:

$$\rho_p = \frac{m_{air}}{m_{air} - m_{aux}}(\rho_{aux} - \rho_{air}) + \rho_{air} \tag{4.2}$$

where m_{air} was the sample mass measured in air, m_{aux} was the sample mass measured in an auxiliary liquid, ρ_{aux} was the auxiliary liquid density, and ρ_{air} was the air density. Cyclohexane was chosen as the auxiliary liquid [26-28], and the cyclohexane density was evaluated at the measurement temperature [39, 40]. The cyclohexane uptake by all of the materials considered was measured to be less than 2% (by mass) over a 12 hour period of time, which is considerably longer than the approximately 30 sec density measurement.

Assuming volume additivity between sorbed water and polymer [4, 41], the volume fraction of water sorbed in the polymer, ϕ_w, was determined as [4]:

$$\phi_w = \frac{w_u}{w_u + \frac{\rho_w}{\rho_p}} \tag{4.3}$$

where ρ_w was taken as the density of water (1.0 g/cm^3 [39]). The value of ϕ_w is effectively equivalent to the water sorption coefficient, K_w, which is defined as the ratio of the concentration of water in the polymer to that in the bulk external solution [4, 5, 21, 22].

4.2.2.2 Salt sorption

The partitioning of salt from an external solution into the polymer was characterized using a desorption method [20]. First, samples were equilibrated with 0.5 mol/L sodium chloride (NaCl) solution for at least 3 days. This equilibration time was well in excess of the characteristic time for salt diffusion, which was conservatively estimated as film thickness squared divided by measured salt permeability [20, 42], in these materials. After equilibration, samples were removed from the salt solution, the residual surface solution was wiped quickly using laboratory wipes, sample thickness was measured using digital calipers (Mitutoyo, Item # 293-344), sample diameter was measured, and the sample was placed in 20 mL of DI water to allow sorbed salt in the sample to desorb from the polymer. The salt sorption coefficient, K_s, which is defined as the ratio of the salt concentration in the polymer relative to the salt concentration of the external solution in equilibrium with the polymer [20], was calculated as:

$$K_s = \frac{C_s^m}{C_s^s} = \frac{C_d V_d}{C_s^s V_p} \tag{4.4}$$

where C_s^m is the salt concentration in the polymer, C_s^s is the salt concentration in the initial external solution (i.e., 0.5 mol/L NaCl), C_d is the final salt concentration in the desorption solution, V_d is the desorption solution volume, and V_p is the volume of the hydrated polymer sample, which was determined geometrically using the average thickness and diameter of the circular sample coupon.

4.2.2.3 Salt transport

Salt permeability was characterized using a custom-built diffusion cell apparatus consisting of two jacketed chambers (i.e., donor and receiver chambers) that were separated by the sample. Silicone rubber gaskets were used to tightly seal the sample into the cell (i.e., to prevent leaks from the donor and/or receiver chambers). The donor chamber was filled with 100 mL of 0.5 mol/L NaCl solution, and the receiver chamber was filled with 100 mL of DI water. These solutions were stirred at a rate of 360 rpm using overhead mechanical stirrers to keep the solutions well mixed and minimize boundary layer effects.

The conductivity of the receiver chamber solution was recorded as a function of time using a conductivity meter (Cond 7310, WTW), and the solution temperature was maintained at 25°C by circulating water through the chamber jackets using a water circulator with a temperature controller [43]. Conductivity was subsequently converted to salt concentration via a calibration curve. Salt permeability, P_s, was modeled as one-dimensional transient Fickian diffusion and was determined via a linear regression of the time-dependent salt concentration data in the form [26, 31, 43]:

$$-\frac{VL}{2A}\ln\left(1-2\frac{C_R(t)}{C_D(0)}\right)=P_s t \tag{4.5}$$

where V is the volume of liquid (i.e., salt solution or DI water) in the donor and receiver chambers, A is the sample area available for transport, t is time, $C_R(t)$ is the salt concentration in receiver chamber at time t, and $C_D(0)$ is the initial salt concentration in donor chamber (at t = 0). The measured salt permeability and salt sorption coefficients were used to calculate the apparent salt diffusion coefficient, D_s, as [4, 5, 21, 22]:

$$D_s=\frac{P_s}{K_s} \tag{4.6}$$

4.2.2.4 Microwave dielectric spectroscopy

Hydrated polymer dielectric permittivity properties were characterized as the frequency-dependent relative complex permittivity, ε^* [44, 45], using a Keysight N9928A vector network analyzer (VNA) [23]. S-parameters, related to the relative complex permittivity, were measured over a frequency range of 450 MHz to 20 GHz using the VNA [23]. Analysis software interpreted the measured S-parameters as the relative complex permittivity properties of the samples [21, 23, 46]. The VNA calibration and S-parameter analysis were performed as described previously [23]. The real part of the relative complex permittivity was the relative permittivity, ε', (often referred to as the dielectric constant) of the sample, and the imaginary part of the relative complex permittivity was the dielectric loss, ε'', of the sample [44].

A 5 cm long and 3.5 mm diameter coaxial transmission line or waveguide (Maury Microwave, catalog number 8043S5) was used as the sample holder. Shielded coaxial cables (Keysight Technologies, catalog number N9910X0-708) were used to connect the VNA and the transmission line. Co-polymer samples were carefully cut, using a razor blade, into small rectangular-shaped strips that were approximately 0.5 cm wide, and these strips were carefully and tightly wrapped around the inner conductor of the transmission line until sufficient polymer was wrapped to fill the annular space of the transmission line with the absence of air gaps.

4.2.2.5 State of water analysis

Differential scanning calorimetry (DSC, TA Instruments Q1000) was used to characterize the state of water sorbed in the materials. First, DI water equilibrated samples were loaded in well-sealed hermetic aluminum pans, which prevented water loss during the experiment. The samples were quenched to –70 °C in the DSC instrument and then scanned once from –70 °C to 90 °C at a heating rate of 10 °C/min. The DSC sample chamber was continuously purged with dry nitrogen during the experiment [26, 27, 47].

The results were analyzed to quantify the relative amounts of freezable (i.e., bulk-like, or weakly bound water) and non-freezable water (i.e., strongly bound water) in the co-polymer [23, 48-56]. Freezable, w_f, and non-freezable, w_{nf}, water content were calculated as:

$$w_f(\%) = \frac{m_f}{m_d} \times 100\% = \frac{\Delta H_{polymer}}{\Delta H^{\circ}_{m,H_2O}} \times (w_u + 100) \tag{4.7}$$

$$w_{nf}(\%) = W_c - W_f \tag{4.8}$$

where m_f was the freezable water mass in the co-polymer, $\Delta H_{polymer}$ was the enthalpy of melting in the co-polymer determined by integrating the water melting peak (at 0 °C) measured using DSC, and $\Delta H^{\circ}_{m,H_2O}$ was the enthalpy of melting for water (333.5 J/g) [56].

4.3 Results and discussion

4.3.1 Water uptake

The primary goal of this study was to determine the influence of hydroxyl group configuration on salt transport properties. To accomplish this goal, five HEMA:GMA:GMAOH materials were prepared with different ratios of HEMA and GMAOH (Figure 4.2), which have different numbers of hydroxyl groups (Figure 4.1). As polymer water content critically affects the salt transport properties of hydrated polymers [4, 31], it was important to prepare the materials used in this study such that the water content of all of the materials was statistically equivalent. By doing so, transport property differences between the materials can be ascribed to changes in the functional group configuration of the polymer without needing to consider the effect of changing water content.

Over the range of co-monomer compositions considered, a series of materials were prepared such that the water uptake and water sorption coefficient properties were statistically indistinguishable (Table 4.1). As the HEMA content of the co-polymer increased (and the GMAOH content of the co-polymer decreased), the overall hydroxyl group content in the co-polymer decreased by approximately 8%. We also observed similar dry density values for all co-polymers (Table 4.1), suggesting that the changing of functional group orientation does not significantly affect chain packing in the materials. As the HEMA content of the co-polymer increases, the cross-link density likely decreases to a small extent (estimated to be approximately 7% using the molar composition of the polymer [57]) to offset the small decrease in hydroxyl group content and yield a series of materials that have statistically indistinguishable water content (Table 4.1). It is also possible, however, that differences in the intrinsic hydrophilicity of the HEMA and GMAOH co-monomers may contribute to this balance. The water uptake of HEMA is reported to be 0.60 g(water)/g(dry polymer), and GMAOH is reported to be water soluble [26, 33]. Additionally, molar enthalpy of mixing data for mixtures of water and either ethanol [58] or 1,2-propanediol [59], which are representative of the HEMA and GMAOH side chains, respectively, suggest that mixing of water and 1,2-propanediol is more thermodynamically favored compared to the situation for water and ethanol. If ethanol and 1,2-propanediol are taken to be representative of the side chains of HEMA and GMAOH, respectively, these results suggest that mixing of water and GMAOH may be more thermodynamically favored compared to that of water and HEMA [57]. Both analyses suggest that the GMAOH side chain is more hydrophilic compared to the HEMA side chain. Subsequent transport property data will be discussed within the framework of the co-monomer composition and hydroxyl group content of the co-polymer.

Table 4. 1. Water content and dry polymer density data measured at 22 ± 1 °C. Water content measurements were made on samples initially equilibrated with DI water. The water sorption coefficient, K_w, was taken as equivalent to the volume fraction of water in the material, which was calculated using Equation 3. Co-polymer composition is reported as in Figure 4.2. The uncertainty was taken as one standard deviation from the mean of three measurements.

HEMA:GMA:GMAOH Composition (by mass)	Water Uptake [g(water)/g(dry polymer)]	Dry Density (g/cm^3)	K_w	Hydroxyl Group Content [meq(-OH)/g(dry polymer)]
0:60:40	0.24 ± 0.02	1.29 ± 0.02	0.23 ± 0.01	5.0
15:55:30	0.24 ± 0.01	1.30 ± 0.03	0.24 ± 0.01	4.9
30:50:20	0.24 ± 0.01	1.27 ± 0.01	0.23 ± 0.01	4.8
45:45:10	0.23 ± 0.01	1.27 ± 0.01	0.23 ± 0.01	4.7
60:40:0	0.23 ± 0.01	1.26 ± 0.02	0.23 ± 0.01	4.6

4.3.2 Salt transport properties

As the HEMA content of the polymer increases and the GMAOH content of the polymer decreases, the configuration of hydroxyl groups on the polymer side chains shifts from a vicinal diol-rich material (when the GMAOH content is high compared to HEMA) to a material where most side chains contain a single hydroxyl group (when the HEMA content is high compared to GMAOH). Therefore, we were able to use the HEMA:GMA:GMAOH materials to study the influence of hydroxyl group distribution on salt transport properties without concern for changing water content (as the water content of the HEMA:GMA:GMAOH series of materials was equivalent, Table 4.1). Salt transport properties can be engineered by controlling the molecular distribution of hydroxyl groups within the polymer, and this observation may have implications for molecular design of desalination membrane materials.

The co-monomer content of the materials was varied by adjusting the mass composition of the co-monomers in the pre-polymerization solution used to prepare the co-polymers. While Fourier transform infrared (FT-IR) spectroscopy (see Supplementary Information) indicates that the co-polymer composition reflects the pre-polymerization solution composition, the similar chemistry and cross-linked network architecture of the co-polymers impedes quantitative measurement of the co-polymer composition. The hydroxyl group content, reported in Table 4.1, was calculated from the pre-polymerization solution composition under the assumption that the pre-polymerization solution composition translates directly into the co-polymer composition.

While the hydroxyl group content of the co-polymers may vary slightly over the compositional range considered (as suggested in Table 4.1), we expect this change to be small in light of the expected changes in co-monomer composition. The pre-polymerization solution composition is given by mass, but the molar composition is more representative of the distribution of hydroxyl groups. For example, in the HEMA:GMA:GMAOH 60:40:0 sample, 62% (by mole) of the side chains have a single hydroxyl group. By comparison, the HEMA:GMA:GMAOH 0:40:60 sample has 37% (by mole) side chains that contain two hydroxyl groups. As such, the hydroxyl groups are highly localized in the HEMA:GMA:GMAOH 0:40:60 sample compared to the HEMA:GMA:GMAOH 60:40:0 sample. While we recognize the possibility for small variations in cross-link density and/or hydroxyl group content of the co-polymers, we believe that the configuration of the hydroxyl groups in the co-polymers primarily influences the resulting material properties, and the subsequent discussion is focused accordingly.

4.3.2.1 Salt sorption

Increasing the HEMA content, while simultaneously reducing the GMAOH content of HEMA:GMA:GMAOH, drives a reduction in the salt sorption coefficient or an increase in the ability of the polymer to exclude salt (Table 4.2). In many hydrated polymers, salt sorption coefficients tend to vary proportionally with the water content of the polymer (i.e., K_s typically increases as K_w increases) [4, 19, 31]. The cross-linked hydrogel data in Figure 4.3 illustrate this type of relationship. Engineering the molecular position of the functional groups in the HEMA:GMA:GMAOH materials, however, allows access to different salt sorption properties without changing the water content of the polymer (Figure 4.3).

Table 4. 2. Salt transport property data for the series of HEMA:GMA:GMAOH materials. The salt sorption coefficient measurements were made at 22 ± 1 °C using sample that initially had been equilibrated with 0.5 mol/L NaCl. Salt permeability was measured at 25 ± 0.2 °C using an upstream salt concentration of 0.5 mol/L NaCl. For each experimentally determined value, the uncertainty was taken as one standard deviation from the mean of three measurements. The apparent salt diffusion coefficient was calculated from the measured salt sorption and salt permeability coefficients using Equation 6, and standard propagation of error [60] was used to estimate the uncertainty in the salt diffusion coefficient. Co-polymer composition is reported as in Figure 4.2.

HEMA:GMA:GMAOH Composition (by mass)	K_s	P_s (x 10^{-9} cm^2/s)	D_s (x 10^{-8} cm^2/s)
0:60:40	0.118 ± 0.004	16.2 ± 0.6	13.7 ± 0.1
15:55:30	0.104 ± 0.004	11.6 ± 0.4	11.2 ± 0.1
30:50:20	0.097 ± 0.001	8.7 ± 0.1	9.0 ± 0.1
45:45:10	0.090 ± 0.002	7.0 ± 0.1	7.8 ± 0.1
60:40:0	0.080 ± 0.002	6.0 ± 0.1	7.5 ± 0.1

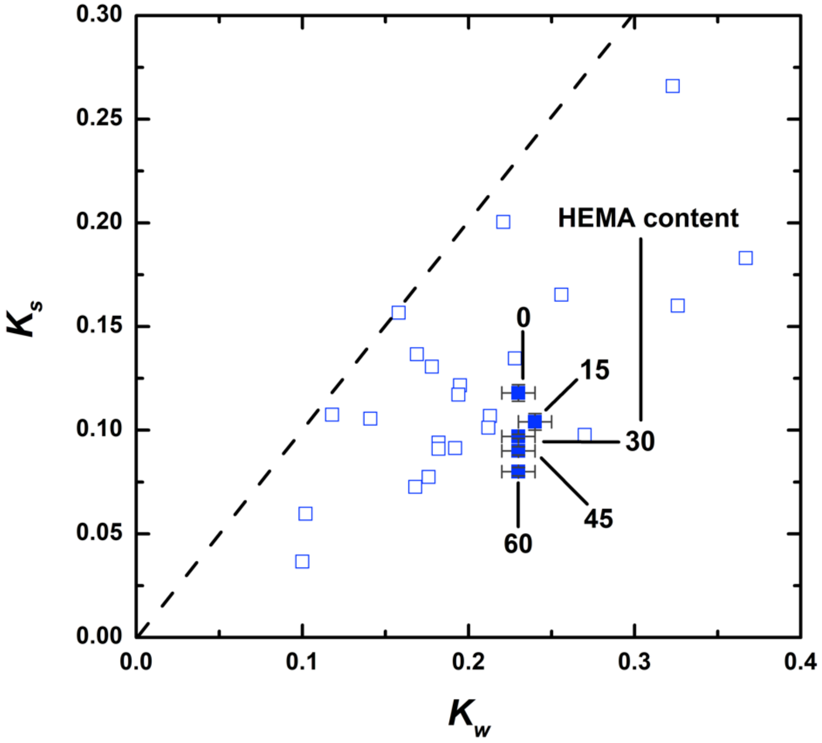

Figure 4. 3. Salt sorption coefficient data as a function of the water sorption coefficient for HEMA:GMA:GMAOH (this study, ■) and hydrogels (□) [31]. The dashed line on this parity plot indicates the border between salt exclusion from the polymer (points below the line) and salt enrichment in the polymer (points above the line). For HEMA:GMA:GMAOH, the HEMA co-monomer composition of the pre-polymerization solution used to prepare each co-polymer is reported for each data point.

This result may suggest that adjusting the distribution of a given functional group within a polymer can have a pronounced influence on salt sorption properties. The observed change in the salt sorption coefficient without a corresponding change in water content suggests that the change in functional group configuration affects the thermodynamic environment of the hydrated polymer. As discussed subsequently, we believe that the observed salt sorption properties are highly related to changes in the hydrogen bonding environment within the co-polymer, which can be probed via DSC and microwave dielectric spectroscopy measurements.

4.3.2.2 Salt permeability and diffusivity

To further explore the influence of hydroxyl functional group configuration on salt transport, we characterized the salt permeability of the HEMA:GMA:GMAOH materials. Similar to the salt sorption coefficient observations (Figure 4.3), the salt permeability decreased as the HEMA content of the co-polymer increased (Figure 4.4A). This decrease in salt permeability, P_s, is related to the observed decrease in the salt sorption coefficient, K_s, by the solution-diffusion model where $P_s = K_s \times D_s$ (i.e., Equation 6) [21].

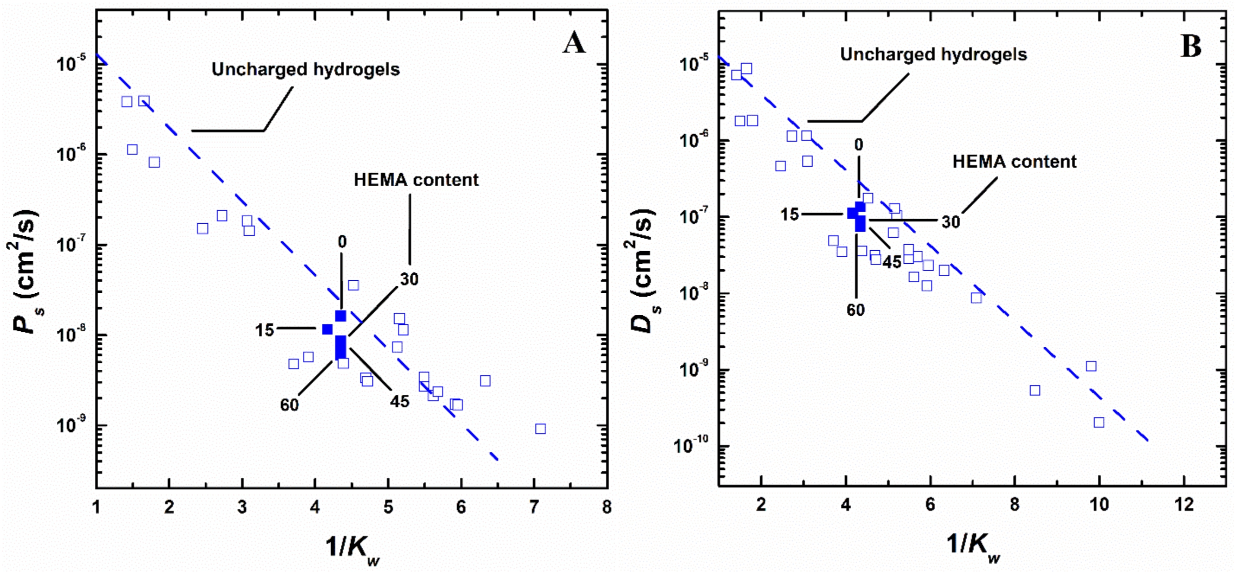

Figure 4. 4. Salt permeability (A) and apparent salt diffusion (B) coefficients as a function of inverse water sorption coefficient for HEMA:GMA:GMAOH (this study, ■) and hydrogels (□) [31]. For HEMA:GMA:GMAOH, the HEMA co-monomer composition of the pre-polymerization solution used to prepare each co-polymer is reported for each data point. The dashed lines are drawn to guide the eye for the hydrogel data. The uncertainty in the data for the HEMA:GMA:GMAOH materials is within the size of the data points.

Unique to this study is the fact that the observed changes in salt sorption and permeability occur at a fixed water content. Several studies have established that water content has a significant impact on salt sorption and permeability properties (e.g., the open symbols in Figures 4.3 and 4.4)

[4, 5, 31]. Our results, however, suggest that the functional group configuration of a polymer (not simply water content alone) can be used to control salt sorption and permeability properties, and this observation suggests new opportunities for membrane science.

Free volume theory provides a framework to explain the dashed line relationships shown in Figure 4.4 [4, 31, 61]. Yasuda proposed a free volume-based model where the water content of the polymer was taken to be proportional to the polymer free volume [31]. This model suggests that the natural logarithms of both the permeability and diffusion coefficients should scale with inverse water content provided that water content is a proxy for free volume and that transport can be described by the free volume model [31]. As such, the natural logarithm of salt permeability and diffusion coefficients tend to decrease linearly with the inverse water sorption coefficient (i.e., $1/K_w$). An example of this relationship is illustrated in Figure 4.4A where the salt permeability of several uncharged hydrogels decrease with $1/K_w$. One implication of this model is that movement along the dashed line in Figure 4.4A indicates that salt permeability is changing in response to changes in free volume brought about by water content changes in the polymer, i.e., other polymer compositional effects are secondary.

In the HEMA:GMA:GMAOH materials considered in this study, the water content of all 5 samples is statistically indistinguishable, so the observed decrease in salt permeability as HEMA content increases is due to factors other than water content. As such, the HEMA:GMA:GMAOH data points in Figure 4.4A move vertically downward as HEMA content increases and not along the dashed line, as would be expected if water content was driving the changes in permeability. This unique behavior is a result of changing the functional group configuration within the polymer.

A similar trend is observed when the salt sorption and permeability coefficients are used to calculate apparent salt diffusion coefficients that can also be plotted versus $1/K_w$ (Figure 4.4B).

We observed a decrease in the apparent salt diffusion coefficient as HEMA content increased at equivalent water content (Table 4.1, Figure 4.4B), and the decrease was 1.5 times less than the decrease in salt permeability for these HEMA:GMA:GMAOH materials. This result is expected because the decrease in both salt sorption and diffusion coefficients contribute to the overall decrease in salt permeability, according to the solution-diffusion model ($P_s = K_s \times D_s$).

Additionally, we compared the apparent salt diffusion coefficients of HEMA:GMA:GMAOH to those values for other cross-linked hydrogels [31]. At similar water content values (i.e., similar values of $1/K_w$), the magnitudes of the salt diffusivity are similar among these chemically similar materials (Figure 4.4B). This observation suggests that molecular motions are similarly facilitated by comparable amounts of sorbed water in these materials.

The hydroxyl group configuration in the HEMA:GMA:GMAOH materials influences salt sorption, diffusivity, and permeability. Investigating this effect using materials of comparable water content reveals unique structure property relationships. Distributing the hydroxyl groups more evenly throughout the polymer (i.e., on the HEMA side chain versus the vicinal diol of the GMAOH side chain) appears to suppress salt sorption and diffusion coefficients. This result may suggest more broadly that distributed hydrophilic functionality may be advantageous for desalination membrane materials.

4.3.3 Microwave dielectric spectroscopy

To further explore the underpinnings of the salt transport property results discussed in the previous section, we characterized the dielectric properties of the hydrated HEMA:GMA:GMAOH co-polymers. We performed the analysis in the microwave frequency range where dipolar relaxation motions of water molecules can be probed [45, 62-66]. The relative permittivity properties of these materials provide insight into the thermodynamic environment of the polymer and, thus, salt sorption properties [19, 24, 25, 67-71].

We fit the HEMA:GMA:GMAOH relative permittivity data (Figure 4.5) to a single Debye relaxation process to determine the static permittivity (i.e., static dielectric constant) of the material [23, 72]. Though the single Debye relaxation model is likely an oversimplified description of dipolar relaxations in these hydrated polymers (i.e., agreement between the data and the single Debye relaxation is not perfect), this approach provides a uniform method to approximate the static permittivity properties (i.e., the value of the ε' plateau at low frequency) of the materials [23]. The static permittivity is useful for quantifying the extent of water dipole relaxation and for modeling ion sorption thermodynamics in hydrated polymers [19, 23, 24].

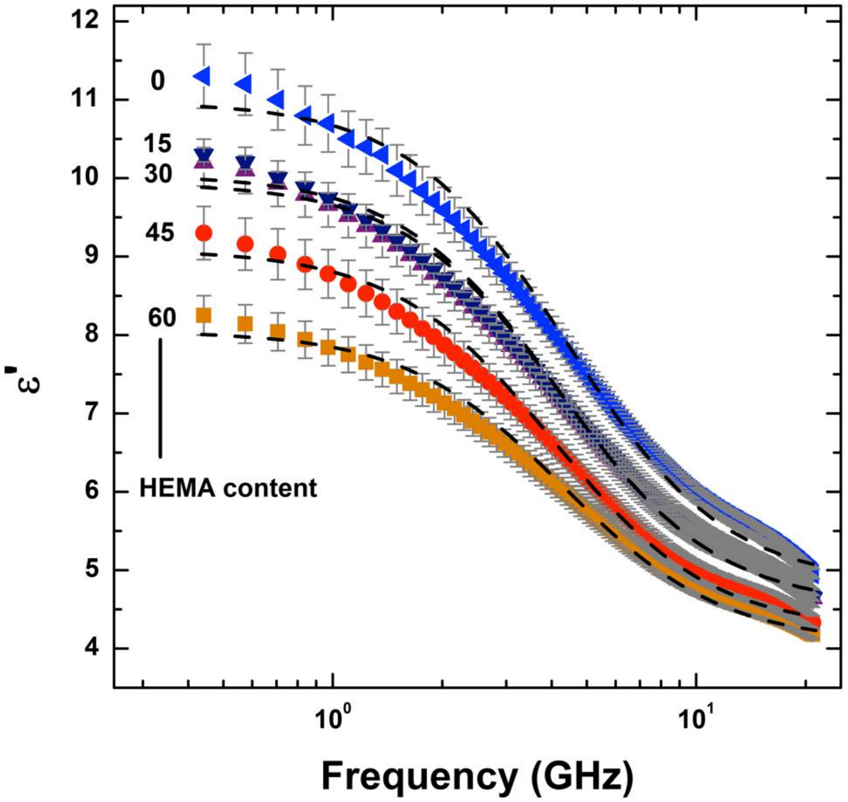

Figure 4. 5. Frequency-dependent relative permittivity, ε', data for the HEMA:GMA:GMAOH co-polymers. The data sets are labeled with the HEMA co-monomer composition of the pre-polymerization solution used to prepare each co-polymer. Dashed curves are a single Debye relaxation fit to the measured data. All measurements were made at 22 ± 1 °C, and the uncertainty was taken as one standard deviation from the mean of three measurements.

The single Debye relaxation fitting process revealed that the static permittivity values of the HEMA:GMA:GMAOH materials decreased from 11.0, 10.0, 9.9, 9.1, to 8.1 as HEMA content increased from 0, 15, 30, 45, to 60 %. It is important to note, again, that the water content of all of the co-polymers was statistically indistinguishable. This result is consistent with previous work suggesting that polymer chemistry (and not water content alone) plays an important role in determining the dielectric properties of hydrated polymers [23].

The observed decrease in the magnitude of the relative permittivity and the regressed static permittivity properties as the HEMA content of the co-polymer increased could be interpreted as a reduction in the dielectric constant of the co-polymer as HEMA content increases. Consistent with electrostatic theory, lower dielectric constant materials often exclude salt to a greater extent than higher dielectric constant materials [19, 23]. As such, the relative permittivity data shown in Figure 4.5 are qualitatively consistent with the salt sorption data reported in Table 4.2 as the relative permittivity and salt sorption coefficient decreased as the HEMA content of HEMA:GMA:GMAOH increased.

Another molecular interpretation of the data in Figure 4.5 is that dipolar relaxation processes are weaker, or less energy is dissipated during the dipolar relaxations, in materials that contain more HEMA co-monomer. We believe this result may suggest that transitioning from a vicinal diol-based co-polymer to a system where hydroxyl groups are more distributed throughout the polymer matrix may have the effect of slowing water molecule motions within the hydrated co-polymer. This result is also consistent with the observed reduction in salt diffusion coefficient values as the HEMA content of the co-polymer increases (Figure 4.4B).

4.3.4 State of water analysis

The dielectric permittivity data discussed in the previous section suggest that different states of water may exist within the co-polymers and mobility of sorbed water in each sample may be affected by the configuration of hydroxyl groups in the polymer. Several studies have investigated the state of water in hydrated polymers [23, 48-55, 64, 73]. Many of these studies use differential scanning calorimetry to quantify the state of water in hydrated polymers, and we applied that approach to the HEMA:GMA:GMAOH materials.

All of the thermograms for the HEMA:GMA:GMAOH co-polymers (Figure 4.6) indicated the presence of freezable sorbed water (i.e., we observed a melting transition at 0 °C for each material). We calculated the amount of freezable and non-freezable water sorbed in the co-polymers, and freezable water content decreased from 2.3 to 0.9 % as HEMA content increased (Table 4.3). Non-freezable water content remained similar among all of the co-polymers (Table 4.3) presumably because the concentration of hydroxyl groups only decreased slightly as HEMA content increased (Table 4.1).

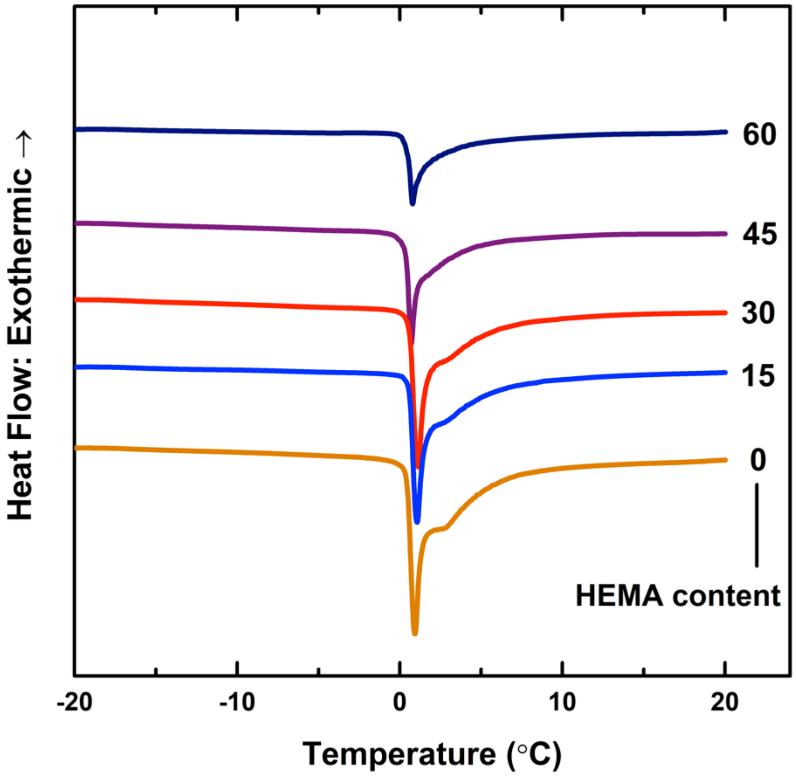

Figure 4. 6. Differential scanning calorimetry (DSC) thermograms for the hydrated GMA:HEMA:GMAOH materials. The HEMA co-monomer composition of the pre-polymerization solution used to prepare each co-polymer is reported for each data set.

Table 4. 3. The distribution of freezable and non-freezable water in the HEMA:GMA:GMAOH materials was calculated using water uptake (Table 4.1) and DSC data. The sum of w_f and w_{nf} is equivalent to the total water uptake of the material. The co-polymer composition is reported as in Figure 4.2.

HEMA:GMA:GMAOH Composition (by mass)	W_f (%)	W_{nf} (%)
0:60:40	2.3	21.2
15:55:30	1.9	22.3
30:50:20	1.8	21.7
45:45:10	1.2	22.3
60:40:0	0.9	22.4

State of water analysis suggests that materials with more HEMA had less freezable water than the materials containing more GMAOH. As such, the more distributed hydroxyl group configuration in the HEMA-rich materials may promote stronger water-polymer interactions. These interactions could reduce the likelihood of forming water clusters that contain freezable (or bulk-like) water; such clusters may be more favorable in the vicinal diol-rich materials that contain more GMAOH compared to HEMA. Formation of such bulk-like water clusters may reduce transport selectivity, so engineering materials to have more distributed functional groups throughout the polymer matrix may favor transport selectivity, which is critical for desalination applications [11, 57].

The decrease in the HEMA:GMA:GMAOH apparent salt diffusion coefficient with increasing HEMA content (Figure 4.4B) may be the result of less freezable water (i.e., bulk-like water) clustering around the hydroxyl groups in the HEMA-rich materials. To illustrate this point, we calculated the freezable (i.e., bulk-like) water content per equivalent of hydroxyl group in the co-polymers, and increasing the HEMA content of the pre-polymerization solution from 0% to 60% by mass caused the amount of freezable water, in the co-polymer film, per equivalent of hydroxyl group to decrease by more than a factor of 2 (See the Supplementary Information for additional details). This result suggests that freezable water content may be suppressed by preparing polymers with more distributed hydrophilic functional groups. Such a situation could also result in more tortuous transport pathways [23, 74], which could impact salt diffusivity properties.

Additionally, the state of water results are consistent with the dielectric permittivity analysis (Figure 4.5) as they provide quantitative insight into the lower static permittivity of higher HEMA content materials. A more evenly distributed hydroxyl group configuration may allow water to interact with the polymer backbone to a greater extent, and this situation could reduce freezable water content compared to the situation where hydroxyl groups are situated closer together (i.e., the GMAOH-rich materials). In other polymers, freezable water content and relative permittivity properties appear to be related [23], so the simultaneous reduction in freezable water content and relative permittivity observed in these materials, as HEMA content increases, is consistent with previously observed phenomena.

This study focused on salt transport properties, but water transport properties are also important for desalination applications. The water permeability, like salt permeability, can be described using the solution diffusion model (i.e., water permeability is taken as the product of the water sorption coefficient and an apparent water diffusion coefficient) [21, 22]. The slowing of water molecule motions, suggested by the dielectric permittivity data and state of water analysis presented here, cause a decrease in the apparent water diffusion coefficient reported in a separate study [57]. Importantly, however, the water sorption coefficient (unlike the salt sorption coefficient) remains constant as the HEMA content of the co-polymer increases. Therefore, the salt permeability decreases to a greater extent than the water permeability. As such, the water/salt selectivity, which is coupled to salt rejection and important for desalination applications, increases as the co-polymer composition shifts from the vicinal diol-rich material to the HEMA-rich co-polymer with more evenly distributed hydroxyl groups [57].

4.4 Conclusions

The molecular configuration of hydroxyl groups in a series of equivalent water content methacrylate-based HEMA:GMA:GMAOH co-polymers influences salt transport properties. Shifting from a vicinal diol-rich hydroxyl group configuration (GMAOH-rich co-polymer) to a configuration where only a single hydroxyl group is present on the co-polymer side chain (HEMA-rich co-polymer) leads to a reduction in salt sorption and permeability coefficients, which is favorable for desalination membrane applications. The observed reduction in salt sorption as the HEMA content of the co-polymer increases is consistent with a simultaneous reduction in the relative permittivity (or dielectric constant) and the freezable water content of the hydrated co-polymer. A reduction in the apparent salt diffusion coefficient as the HEMA content of the co-polymer increases is also consistent with a hydrogen bonding environment where water molecules interact to a greater extent with the polymer backbone, and both of these conditions are consistent with the observed reduction in relative permittivity and freezable water content as the HEMA content of the co-polymer increased. These results suggest that salt transport properties can be engineered by exercising molecular control over functional group position in hydrated polymers. The results suggest that a more distributed functional group configuration may facilitate low rates of salt transport, which could be a viable strategy for preparing water/salt selective polymers for desalination membrane applications.

4.5 References

[1] Y. Cohen, R. Semiat, A. Rahardianto, A perspective on reverse osmosis water desalination: Quest for sustainability, AIChE Journal, 63 (2017) 1771-1784.

[2] M. Elimelech, W.A. Phillip, The future of seawater desalination: Energy, technology, and the environment, Science, 333 (2011) 712-717.

[3] M.A. Shannon, P.W. Bohn, M. Elimelech, J.G. Georgiadis, B.J. Marinas, A.M. Mayes, Science and technology for water purification in the coming decades, Nature, 452 (2008) 301-310.

[4] G.M. Geise, D.R. Paul, B.D. Freeman, Fundamental water and salt transport properties of polymeric materials, Progress in Polymer Science, 39 (2014) 1-42.

[5] G.M. Geise, H.-S. Lee, D.J. Miller, B.D. Freeman, J.E. McGrath, D.R. Paul, Water purification by membranes: The role of polymer science, Journal of Polymer Science Part B: Polymer Physics, 48 (2010) 1685-1718.

[6] J. Kamcev, B.D. Freeman, Charged polymer membranes for environmental/energy applications, Annual Review of Chemical and Biomolecular Engineering, 7 (2016) 111-133.

[7] C. Fritzmann, J. Löwenberg, T. Wintgens, T. Melin, State-of-the-art of reverse osmosis desalination, Desalination, 216 (2007) 1-76.

[8] R.F. Service, Desalination Freshens Up, Science, 313 (2006) 1088-1090.

[9] R. Semiat, Energy Issues in Desalination Processes, Environmental Science & Technology, 42 (2008) 8193-8201.

[10] S. Miller, H. Shemer, R. Semiat, Energy and environmental issues in desalination, Desalination, 366 (2015) 2-8.

[11] J.R. Werber, A. Deshmukh, M. Elimelech, The critical need for increased selectivity, not increased water permeability, for desalination membranes, Environmental Science & Technology Letters, 3 (2016) 112-120.

[12] H.B. Park, J. Kamcev, L.M. Robeson, M. Elimelech, B.D. Freeman, Maximizing the right stuff: The trade-off between membrane permeability and selectivity, Science, 356 (2017) eaab0530.

[13] D.M. Stevens, J.Y. Shu, M. Reichert, A. Roy, Next-generation nanoporous materials: Progress and prospects for reverse osmosis and nanofiltration, Industrial & Engineering Chemistry Research, 56 (2017) 10526-10551.

[14] S. Surawanvijit, A. Rahardianto, Y. Cohen, An integrated approach for characterization of polyamide reverse osmosis membrane degradation due to exposure to free chlorine, Journal of Membrane Science, 510 (2016) 164-173.

[15] T. Knoell, Municipal wastewater: Chlorine's impact on the performance and properties of polyamide membranes, Ultrapure Water, (2006) 24-31.

[16] H.B. Park, B.D. Freeman, Z.-B. Zhang, M. Sankir, J.E. McGrath, Highly chlorine-tolerant polymers for desalination, Angewandte Chemie International Edition, 47 (2008) 6019-6024.

[17] A.E. Allegrezza, B.S. Parekh, P.L. Parise, E.J. Swiniarski, J.L. White, Chlorine resistant polysulfone reverse osmosis modules, Desalination, 64 (1987) 285-304.

[18] S.G. Kimura, Reverse osmosis performance of sulfonated poly(2,6-dimethylphenylene ether) ion exchange membranes, Industrial & Engineering Chemistry Research, 10 (1971) 335-339.

[19] H. Zhang, G.M. Geise, Modeling the water permeability and water/salt selectivity tradeoff in polymer membranes, Journal of Membrane Science, 520 (2016) 790-800.

[20] G.M. Geise, L.P. Falcon, B.D. Freeman, D.R. Paul, Sodium chloride sorption in sulfonated polymers for membrane applications, Journal of Membrane Science, 423 (2012) 195-208.

[21] J.G. Wijmans, R.W. Baker, The solution-diffusion model: A review, Journal of Membrane Science, 107 (1995) 1-21.

[22] D.R. Paul, Reformulation of the solution-diffusion theory of reverse osmosis, Journal of Membrane Science, 241 (2004) 371-386.

[23] K. Chang, H. Luo, G.M. Geise, Water content, relative permittivity, and ion sorption properties of polymers for membrane desalination, Journal of Membrane Science, 574 (2019) 24-32.

[24] A.E. Yaroshchuk, Dielectric exclusion of ions from membranes, Advances in Colloid and Interface Science, 85 (2000) 193-230.

[25] A.E. Yaroshchuk, Non-steric mechanisms of nanofiltration: Superposition of Donnan and dielectric exclusion, Separation and Purification Technology, 22-23 (2001) 143-158.

[26] K. Chang, T. Xue, G.M. Geise, Increasing salt size selectivity in low water content polymers via polymer backbone dynamics, Journal of Membrane Science, 552 (2018) 43-50.

[27] K. Chang, A. Korovich, T. Xue, W.A. Morris, L.A. Madsen, G.M. Geise, Influence of rubbery versus glassy backbone dynamics on multiscale transport in polymer membranes, Macromolecules, 51 (2018) 9222-9233.

[28] H. Luo, J. Aboki, Y. Ji, R. Guo, G.M. Geise, Water and salt transport properties of triptycene-containing sulfonated polysulfone materials for desalination membrane applications, ACS Applied Materials & Interfaces, 10 (2018) 4102-4112.

[29] M.A. Hickner, Ion-containing polymers: New energy & clean water, Materials Today, 13 (2010) 34-41.

[30] J.S. Mackie, P. Meares, The diffusion of electrolytes in a cation-exchange resin membrane I. Theoretical, Proceedings of the Royal Society of London. Series A. Mathematical and Physical Sciences, 232 (1955) 498-509.

[31] H. Yasuda, C.E. Lamaze, L.D. Ikenberry, Permeability of solutes through hydrated polymer membranes. Part I. Diffusion of sodium chloride, Die Makromolekulare Chemie, 118 (1968) 19-35.

[32] H. Yasuda, C.E. Lamaze, A. Peterlin, Diffusive and hydraulic permeabilities of water in water-swollen polymer membranes, Journal of Polymer Science Part A-2: Polymer Physics, 9 (1971) 1117-1131.

[33] J. Tan, D. Liu, Y. Bai, C. Huang, X. Li, J. He, Q. Xu, X. Zhang, L. Zhang, An insight into aqueous photoinitiated polymerization-induced self-assembly (photo-PISA) for the preparation of diblock copolymer nano-objects, Polymer Chemistry, 8 (2017) 1315-1327.

[34] W. Brostow, R. Chiu, I.M. Kalogeras, A. Vassilikou-Dova, Prediction of glass transition temperatures: Binary blends and copolymers, Materials Letters, 62 (2008) 3152-3155.

[35] T.G.J. Fox, P.J. Flory, Second-order transition temperatures and related properties of polystyrene. I. Influence of molecular weight, Journal of Applied Physics, 21 (1950) 581-591.

[36] P.C. Hiemenz, T.P. Lodge, Polymer Chemistry, 2nd ed., CRC Press LLC, Boca Raton, Florida, 2007.

[37] D. Halliday, R. Resnick, J. Walker, Fundamentals of Physics, 7th ed., Wiley, Hoboken, New Jersey, 2005.

[38] H. Ju, A.C. Sagle, B.D. Freeman, J.I. Mardel, A.J. Hill, Characterization of sodium chloride and water transport in crosslinked poly(ethylene oxide) hydrogels, Journal of Membrane Science, 358 (2010) 131-141.

[39] J. Rumble, CRC Handbook of Chemistry and Physics, 98th ed., CRC Press LLC, Boca Raton, Florida, 2017.

[40] C.L. Yaws, R.W. Pike, Thermophysical Properties of Chemicals and Hydrocarbons, William Andrew, Norwich, New York, 2009.

[41] G.M. Geise, C.L. Willis, C.M. Doherty, A.J. Hill, T.J. Bastow, J. Ford, K.I. Winey, B.D. Freeman, D.R. Paul, Characterization of aluminum-neutralized sulfonated styrenic pentablock copolymer films, Industrial & Engineering Chemistry Research, 52 (2013) 1056-1068.

[42] E.L. Cussler, Diffusion: Mass Transfer in Fluid Systems, 3rd ed., Cambridge University Press, Cambridge, New York, 2009.

[43] G.M. Geise, B.D. Freeman, D.R. Paul, Characterization of a sulfonated pentablock copolymer for desalination applications, Polymer, 51 (2010) 5815-5822.

[44] L.F. Chen, Microwave Electronics: Measurement and Materials Characterization, Wiley, Hoboken, New Jersey, 2004.

[45] Z. Lu, M. Lanagan, E. Manias, D.D. Macdonald, Two-port transmission line technique for dielectric property characterization of polymer electrolyte membranes, The Journal of Physical Chemistry B, 113 (2009) 13551-13559.

[46] P.G. Bartley, S.B. Begley, A new technique for the determination of the complex permittivity and permeability of materials, IEEE Instrumentation & Measurement Technology Conference Proceedings, (2010) 54-57.

[47] TA Instruments, Purge Gas Recommendations for use in Modulated DSC®, http://www.tainstruments.com/pdf/literature/TN44.pdf (Accessed: June 13th, 2018).

[48] S.J. Paddison, Proton conduction mechanisms at low degrees of hydration in sulfonic acid–based polymer electrolyte membranes, Annual Review of Materials Research, 33 (2003) 289-319.

[49] K.A. Mauritz, R.B. Moore, State of understanding of Nafion®, Chemical Reviews, 104 (2004) 4535-4586.

[50] K.-D. Kreuer, S.J. Paddison, E. Spohr, M. Schuster, Transport in proton conductors for fuel-cell applications: Simulations, elementary reactions, and phenomenology, Chemical Reviews, 104 (2004) 4637-4678.

[51] J.A. Elliott, S.J. Paddison, Modelling of morphology and proton transport in PFSA membranes, Physical Chemistry Chemical Physics, 9 (2007) 2602-2618.

[52] F.X. Quinn, E. Kampff, G. Smyth, V.J. McBrierty, Water in hydrogels. 1. A study of water in poly(N-vinyl-2-pyrrolidone/methyl methacrylate) copolymer, Macromolecules, 21 (1988) 3191-3198.

[53] R.M. Hodge, T.J. Bastow, G.H. Edward, G.P. Simon, A.J. Hill, Free volume and the mechanism of plasticization in water-swollen poly(vinyl alcohol), Macromolecules, 29 (1996) 8137-8143.

[54] H. Yoshida, Y. Miura, Behavior of water in perfluorinated ionomer membranes containing various monovalent cations, Journal of Membrane Science, 68 (1992) 1-10.

[55] N. Shinyashiki, M. Shimomura, T. Ushiyama, T. Miyagawa, S. Yagihara, Dynamics of water in partially crystallized polymer/water mixtures studied by dielectric spectroscopy, The Journal of Physical Chemistry B, 111 (2007) 10079-10087.

[56] TA Instruments, Thermal Analysis to Determine Various Forms of Water Present in Hydrogels, http://www.tainstruments.com/pdf/literature/TA384.pdf (Accessed: June 12th, 2018).

[57] H. Luo, K. Chang, K. Bahati, G.M. Geise, Engineering selective desalination membranes via molecular control of polymer functional groups, Environmental Science & Technology Letters, DOI: 10.1021/acs.estlett.9b00351 (2019).

[58] R.F. Lama, B.C.Y. Lu, Excess thermodynamic properties of aqueous alcohol solutions, Journal of Chemical & Engineering Data, 10 (1965) 216-219.

[59] D.V. Batov, A.M. Zaichikov, V.P. Slyusar, V.P. Korolev, Enthalpies of mixing and state of components in aqueous-organic mixtures with nets of hydrogen bonds, Russian Journal of General Chemistry, 71 (2001) 1208-1214.

[60] P.R. Bevington, D.K. Robinson, Chapter 4: Propagation of Errors, in: Data reduction and error analysis for the physical sciences, McGraw Hill, New York, 2003, pp. 56-65.

[61] W. Xie, H. Ju, G.M. Geise, B.D. Freeman, J.I. Mardel, A.J. Hill, J.E. McGrath, Effect of free volume on water and salt transport properties in directly copolymerized disulfonated poly(arylene ether sulfone) random copolymers, Macromolecules, 44 (2011) 4428-4438.

[62] S.J. Paddison, D.W. Reagor, T.A. Zawodzinski Jr, High frequency dielectric studies of hydrated Nafion®, Journal of Electroanalytical Chemistry, 459 (1998) 91-97.

[63] S. Paddison, G. Bender, T.A. Zawodzinski Jr, The microwave region of the dielectric spectrum of hydrated Nafion® and other sulfonated membranes, Journal of New Materials for Electrochemical Systems, 3 (2000) 293-302.

[64] Z. Lu, G. Polizos, D.D. Macdonald, E. Manias, State of water in perfluorosulfonic ionomer (Nafion® 117) proton exchange membranes, Journal of The Electrochemical Society, 155 (2008) B163-B171.

[65] Z. Lu, E. Manias, D.D. Macdonald, M. Lanagan, Dielectric relaxation in dimethyl sulfoxide/water mixtures studied by microwave dielectric relaxation spectroscopy, The Journal of Physical Chemistry A, 113 (2009) 12207-12214.

[66] G. Smith, A.P. Duffy, J. Shen, C.J. Olliff, Dielectric relaxation spectroscopy and some applications in the pharmaceutical sciences, Journal of Pharmaceutical Sciences, 84 (1995) 1029-1044.

[67] E. Glueckauf, On the mechanism of osmotic desalting with porous membranes, Proceedings of the First International Symposium on Water Desalination, (1967) 143-150.

[68] J.E. Anderson, W. Pusch, The membrane/water partition coefficients of ions: Electrostatic calculations of dielectric heterogeneity, Berichte der Bunsengesellschaft für physikalische Chemie, 80 (1976) 846-849.

[69] V. Freger, S. Bason, Characterization of ion transport in thin films using electrochemical impedance spectroscopy: I. Principles and theory, Journal of Membrane Science, 302 (2007) 1-9.

[70] J. Kamcev, M. Galizia, F.M. Benedetti, E.-S. Jang, D.R. Paul, B.D. Freeman, G.S. Manning, Partitioning of mobile ions between ion exchange polymers and aqueous salt solutions: Importance of counter-ion condensation, Physical Chemistry Chemical Physics, 18 (2016) 6021-6031.

[71] J. Kamcev, D.R. Paul, G.S. Manning, B.D. Freeman, Predicting salt permeability coefficients in highly swollen, highly charged ion exchange membranes, ACS Applied Materials & Interfaces, 9 (2017) 4044-4056.

[72] Z. Lu, State of water in perfluorosulfonic acid membranes studied by microwave dielectric relaxation spectroscopy, Ph.D. Thesis, Department of Materials Science and Engineering, The Pennsylvania State University, University Park, Pennsylvania (2006).

[73] T. Tran, C. Lin, S. Chaurasia, H. Lin, Elucidating the relationship between states of water and ion transport properties in hydrated polymers, Journal of Membrane Science, 574 (2019) 299-308.

[74] K.D. Kreuer, On the development of proton conducting polymer membranes for hydrogen and methanol fuel cells, Journal of Membrane Science, 185 (2001) 29-39.

Chapter 5 Engineering Selective Desalination Membranes via Molecular Control of Polymer Functional Groups

5.1 Introduction

Meeting global demand for clean water is a pressing engineering challenge.[1] Membrane-based technologies are used widely to desalinate water, and more efficient membranes are needed to meet growing demand for purified water from increasingly contaminated and/or saline water.[2-6] Water purification membranes are generally polymeric, and highly selective membranes are needed to meet the growing separation challenges in desalination technologies including reverse osmosis and nanofiltration.[6-10] The selective properties of these desalination membranes result from the preferential transport of water relative to hydrated ions.[11] Engineering highly selective materials has been frustrated by a lack of fundamental structure-property relationships to guide the design of advanced polymer membranes to address global water needs.

The ability to precisely place functional groups along a polymer backbone, with a high degree of molecular control over functional group position, is becoming increasingly viable.[12, 13] This structural control, facilitated by advances in synthesis capabilities, could be important for engineering advanced desalination membranes. Little is known, however, about how functional group placement within a polymer influences water/salt selectivity.

We report the desalination (i.e., water/salt) selectivity properties of a series of model materials where the distribution of hydroxyl functional groups along the polymer backbone was varied from a clustered to a more uniform configuration. Importantly, this series of materials was

---

This chapter is already published and available from: Luo, H., Chang, K., Bahati, K., & Geise, G. M. (2019). Engineering selective desalination membranes via molecular control of polymer functional groups. Environmental Science & Technology Letters, 6(8), 462-466.

prepared such that the membrane water content did not change as the distribution of the hydroxyl groups changed. Membrane water content has a significant influence on water/salt selectivity properties,[9, 14] so the ability to vary the distribution of functional groups within the material without perturbing the water content enabled us to ascribe the observed results to changes in the functional group configuration.

Shifting the functional group configuration to space the hydroxyl groups out more evenly (compared to the more clustered configuration) resulted in increased water/salt permeability selectivity, which is directly related to desalination-critical salt rejection.[11] This increase in selectivity was largely driven by sorption, or thermodynamic, effects. The results suggest that an even distribution of hydrophilic chemical functionality in polymers may lead to more selective membranes to address global demand for desalinated water.

5.2 Materials and Methods

5.2.1 HEMA:GMA:GMAOH Co-Polymers

Five co-polymers containing 2-hydroxyethyl methacrylate (HEMA), glycidyl methacrylate (GMA), and glycerol methacrylate (GMAOH) co-monomers and cross-linked using poly(ethylene glycol) dimethacylate (PEGDMA) were prepared via UV-initiated free radical polymerization. These model materials are chemically different from the aromatic polyamide-based membranes commonly used in reverse osmosis and nanofiltration membranes.[15] The structure of these materials (i.e., the choice of co-monomers) was chosen to enable preparation of a series of materials where the distribution of hydrophilic functional groups (in this case, hydroxyl groups) could be varied by changing the composition of the co-polymer without changing the water content of the polymer.

The hydroxyl group distribution in the co-polymer was varied by changing co-monomer composition of the pre-polymerization solution used to prepare the materials (Table 5.1). The sample nomenclature, HEMA:GMA:GMAOH x:y:z, reflects the composition (by mass) of the pre-polymerization solution used to prepare that material (e.g., 15:55:30 was prepared from a pre-polymerization solution containing 15%, 55%, and 30%, by mass, of HEMA, GMA, and GMAOH, respectively). The PEGDMA cross-linker and initiator (1-hydroxycyclohexyl phenyl ketone) were added to the co-monomer solution at compositions of 0.1 and 0.01 g/g(total co-monomer), respectively, to form the pre-polymerization solution, which was stirred for 30 min at room temperature to ensure the solution was well-mixed. The pre-polymerization solution was degassed (via sonication for 10 min), confined between quartz plates (separated by spacers to control film thickness), and irradiated, for 5 min, with 120 μJ/cm^2 of 312 nm light to form transparent and homogeneous polymer films that were approximately 100 μm thick. The chemical structure and additional information about the co-polymers are reported in Section S1 of the Supporting Information.

Table 5. 1 Co-monomer mass fraction in the pre-polymerization solution used to prepare the HEMA:GMA:GMAOH co-polymers defines the sample nomenclature. The water uptake and dry density data were measured at ambient temperature, and the water sorption coefficient, K_w, was calculated using the water uptake and dry polymer density. Uncertainty in the measured data is one standard deviation from the mean of at least three measurements, and the uncertainty in the water sorption coefficient was calculated using standard propagation of error.[16]

Co-Polymer Sample	**Co-Monomer Mass Fraction in the Pre-Polymerization Solution**			**Water Uptake**^{a}	**Dry Polymer Density (g/cm^3)**	K_w
	HEMA	**GMA**	**GMAOH**			
0:60:40	0.0	0.60	0.40	0.24 ± 0.02	1.29 ± 0.02	0.23 ± 0.01
15:55:30	0.15	0.55	0.30	0.24 ± 0.01	1.30 ± 0.03	0.24 ± 0.01

30:50:20	0.30	0.50	0.20	0.24 ± 0.01	1.27 ± 0.01	0.23 ± 0.01
45:45:10	0.45	0.45	0.10	0.23 ± 0.01	1.27 ± 0.01	0.23 ± 0.01
60:40:0	0.60	0.40	0.0	0.23 ± 0.01	1.26 ± 0.02	0.23 ± 0.01

[a] Units: g(water) / g(dry polymer)

5.2.2 Water and Salt Transport Property Characterization

To characterize the potential desalination performance of the HEMA:GMA:GMAOH co-polymers, we measured water uptake, salt sorption coefficient, and water and salt permeability properties at ambient temperature. Water uptake was combined with dry polymer density to calculate the water sorption coefficient, K_w (Table 1).[17] Water ($i \rightarrow w$) and salt ($i \rightarrow s$) sorption coefficients, K_i, were combined with permeability properties, P_i, to calculate, via the solution-diffusion model,[18] apparent diffusion coefficients, D_i, as:[19]

$$D_i = P_i / K_i \tag{5.1}$$

At least three measurements, per sample, were made for each property, and the uncertainty in the measurement was one standard deviation from the mean. Standard propagation of error was used to quantify the uncertainty in calculated quantities.[16] Details about the specific methods used to measure water uptake, salt sorption, pure water permeability, salt permeability, and hydrated polymer dielectric properties are reported in Section S2 of the Supporting Information.

5.3 Results and Discussion

Each composition of HEMA:GMA:GMAOH had equivalent water content (Table 1). Water content affects the transport (and, thus, desalination) selectivity of hydrated polymers, and increases in water content often correlate with decreases in selectivity.[9, 14] Therefore, preparing materials with equivalent water content is critical for decoupling the influence of functional group configuration on water/salt transport selectivity from the influence of changing water content on water/salt transport selectivity.

The equivalent water content of this series of HEMA:GMA:GMAOH co-polymers likely results from subtle changes in the extent of cross-linking and hydroxyl group content across the series of co-polymers. These changes were estimated to be reasonably small, as discussed in Section S1.1 of the Supporting Information. Ultimately, maintaining equivalent water content in the series of materials was prioritized due to the strong influence of water content on the water and salt transport properties of hydrated polymers.[9, 14]

We compared the HEMA:GMA:GMAOH transport properties to those of cross-linked poly(ethylene glycol) diacrylate (PEG) hydrogels, as these materials also preferentially transport water over salt via a solution-diffusion mechanism.[20] The water content of these hydrogels can be manipulated by changing the ethylene glycol chain length or by adding a diluent to the pre-polymerization mixture.[20] Thus, the PEG materials illustrate how transport properties change with water content to contrast the situation in equivalent water content HEMA:GMA:GMAOH.

The water/salt transport selectivity is defined as the ratio of water to salt permeability, P_w/P_s, sorption K_w/K_s, or diffusion, D_w/D_s, coefficients, and the three selectivity values are related via the solution-diffusion model:[9]

$$P_w/P_s = (K_w/K_s) \times (D_w/D_s) \tag{5.2}$$

This water/salt permeability selectivity can be directly related to salt rejection, which is a critical characteristic of effective desalination membranes.[11] The salt rejection, **R**, is defined as the salt concentration reduction from the bulk solution on the feed side of the membrane, $c_{s,feed}$, to the bulk solution on the permeate (or product) side of the membrane normalized by $c_{s,feed}$ and depends on the water/salt permeability selectivity:

$$\mathbf{R} = \frac{c_{s,feed} - c_{s,permeate}}{c_{s,feed}} = \frac{\frac{P_w V_w}{P_s\, RT}(\Delta p - \Delta\pi)}{1 + \frac{P_w V_w}{P_s\, RT}(\Delta p - \Delta\pi)} \qquad (5.3)$$

where V_w is the molar volume of water, Δp is the hydraulic pressure difference across the membrane, $\Delta\pi$ is the osmotic pressure difference across the membrane, R is the gas constant, and T is the absolute temperature.[9]

Water/salt permeability selectivity depends on a combination of both water/salt sorption and diffusivity selectivity properties (Equation 2). Functional group configuration significantly influenced the water/salt sorption selectivity of HEMA:GMA:GMAOH (Figure 5.1A). A distributed hydroxyl group configuration (HEMA-rich co-polymer) led to higher sorption selectivity compared to a vicinal-diol rich configuration (GMAOH-rich co-polymer), and this result can be attributed to more effective exclusion of salt from the HEMA-rich co-polymer compared to the GMAOH-rich co-polymer.

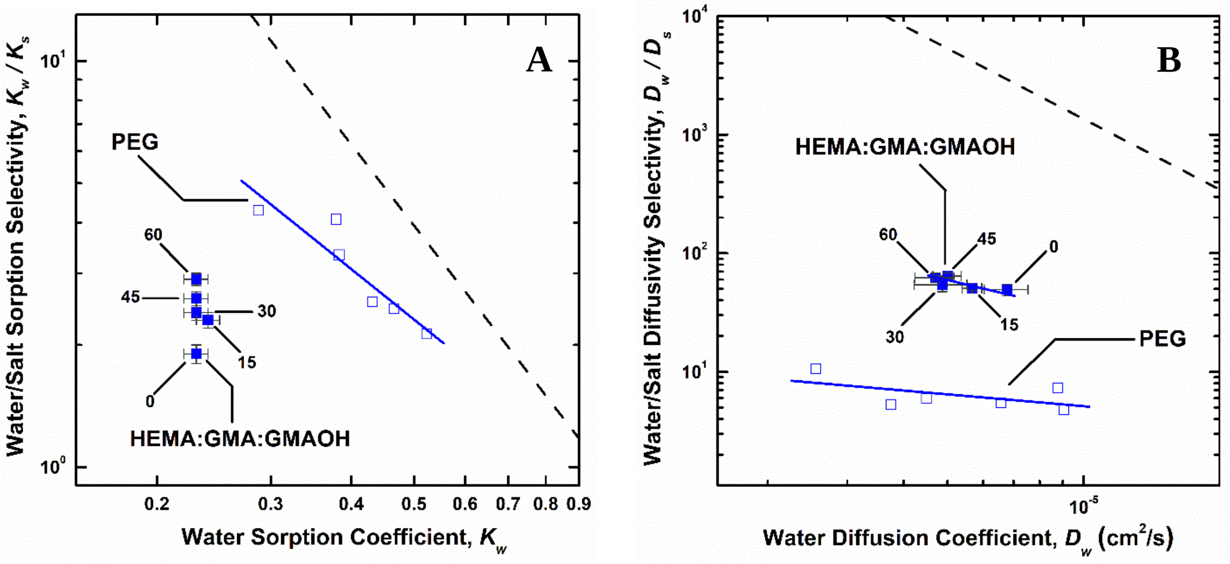

Figure 5. 1. Water/salt sorption selectivity (A) and water/salt diffusivity selectivity (B) as a function of water sorption coefficient and apparent water diffusion coefficient, respectively, for HEMA:GMA:GMAOH (■) and PEG (□)[20] materials. For HEMA:GMA:GMAOH, the HEMA co-monomer composition of the pre-polymerization solution used to prepare the co-polymer is reported for each data point. The dashed lines represent reported empirical sorption (left) and diffusivity (right) trade-off frontiers for desalination membrane materials,[21, 22] and the solid lines are least-squares fits to the data.

Comparing HEMA:GMA:GMAOH water/salt sorption selectivity with that of poly(ethylene glycol) diacrylate (PEG) hydrogels, we observed that the HEMA:GMA:GMAOH data points move vertically upwards as HEMA content increases in a manner different from the PEG materials (Figure 5.1A). The PEG result is expected if water content primarily drives sorption selectivity properties.[20] The HEMA:GMA:GMAOH result suggests that polymer chemistry, not changing water content, is responsible for the change in sorption selectivity of HEMA:GMA:GMAOH. Thus, preparing polymers with a distributed functional group configuration may be a viable strategy to increase the water/salt sorption selectivity.

The HEMA:GMA:GMAOH materials are approximately an order of magnitude more water/salt diffusion selective compared to the PEG materials (Figure 5.1B). This result may be due to the glassy nature of hydrated HEMA:GMA:GMAOH compared to the rubbery nature of PEG (see Section S1.3 of the Supporting Information).[23] More rigid (glassy) polymer backbones are often more diffusion selective compared to more flexible (rubbery) polymer backbones.[24-26]

The apparent water diffusion coefficient decreases and the water/salt diffusivity selectivity increases as the co-polymer composition shifts toward a more HEMA rich (or distributed hydroxyl group configuration). This observed trend is similar to that observed for PEG. The water content of the PEG materials was varied systematically, and the explanation for the observed relationship between water/salt diffusivity selectivity and water diffusion coefficient is that reduction in the free volume of the polymer (as water content decreases) causes a general reduction in diffusion that influences the larger hydrated ions to a greater extent than water.[20] In HEMA:GMA:GMAOH, the change in co-monomer composition (and thus, distribution of hydroxyl groups) results in a situation where water diffusion slows as HEMA content increases. This reduction in water diffusivity is accompanied by an increase in water/salt diffusion selectivity that is similar in proportion to that of PEG. Therefore, changes in water diffusivity, due to compositional changes in the HEMA:GMA:GMAOH materials, may influence water/salt diffusivity selectivity in a manner similar to that in the free volume-based explanation where water diffusion depends strongly on free volume.[9, 14]

Water/salt diffusivity selectivity is affected to a lesser extent, compared to water/salt sorption selectivity, by changing the HEMA content of the pre-polymerization solution. The water/salt diffusivity selectivity increases by 26% over the range of HEMA compositions considered. The water/salt sorption selectivity, by comparison, increases by 53% over the range of HEMA compositions considered. Importantly, the 53% increase in sorption selectivity comes without a change in the water sorption coefficient, which as discussed subsequently, means that, as co-polymer composition changes, the water permeability will not change because of sorption effects.

The decrease in the apparent water diffusivity as the co-polymer composition changes at constant water content could be considered unexpected, as diffusivity in hydrated polymers is often a strong function of water content.[9, 14, 27-29] Dielectric permittivity properties, however, provide insight into the observed water diffusivity. As further discussed in Section S3 of the Supporting Information, the dielectric loss spectra can be interpreted in terms of time constants, which describe the dipole relaxation dynamics of different modes of water motion, and the dielectric strengths of those relaxations, which describe the relative amount of water in the material that is participating in each relaxation mode.[30]

Dielectric spectroscopy suggests three populations of dipolar water motion: highly restricted motion that relaxes on an order 0.1 ns timescale, less restricted motion that relaxes with a time constant of approximately 45 ps, and non-restricted (i.e., bulk water) motion that relaxes with a time constant of 8.8 ps (see Supporting Information for additional discussion). In general, the dielectric strength associated with each mode of motion decreases as HEMA content increases (Table D1), though the reduction is more pronounced for the non-restricted relaxation mode compared to the other two modes. This decrease in the dielectric strength associated with all three relaxation modes, coupled with the statistically equivalent water content of the materials, suggests that increasing HEMA content promotes water-polymer interactions that relax at frequencies lower than that probed in our experiments.

An example of such interactions would be water that is very tightly associated with the hydroxyl groups. Such (effectively immobile) water will not be detected by dielectric spectroscopy in the frequency range considered here.[31] As such, the dielectric strength data suggests that distributing the hydroxyl groups in the polymer causes more water to tightly associate with hydroxyl groups compared to the situation in the vicinal diol-rich materials.

This molecular picture is consistent with a steric explanation suggesting that water molecules may be able to hydrate the hydroxyl group on a HEMA side chain to a greater extent compared to the more sterically hindered GMAOH side chain. This explanation is also consistent with estimates of the enthalpy of hydration for the hydroxyl groups on the side chains (see Section S4 of the Supporting Information). Ultimately, this reduction in water motion within the polymer appears to have a similar effect on both water and salt diffusion as reducing the water content of the polymer (as supported by the similar slopes of the data in Figure 5.1B).

Primarily due to the strong increase in water/salt sorption selectivity at constant water content, the HEMA:GMA:GMAOH water/salt permeability selectivity increases as the HEMA content of the pre-polymerization solution used to prepare the materials increases (Figure 5.2). A distributed hydroxyl group configuration (HEMA-rich) is more selective for water over salt transport compared to the vicinal-diol rich configuration (GMAOH-rich). The overall selectivity of the HEMA:GMA:GMAOH series of materials is greater than that of the PEG materials due to the previously discussed differences in the diffusivity selectivity properties.

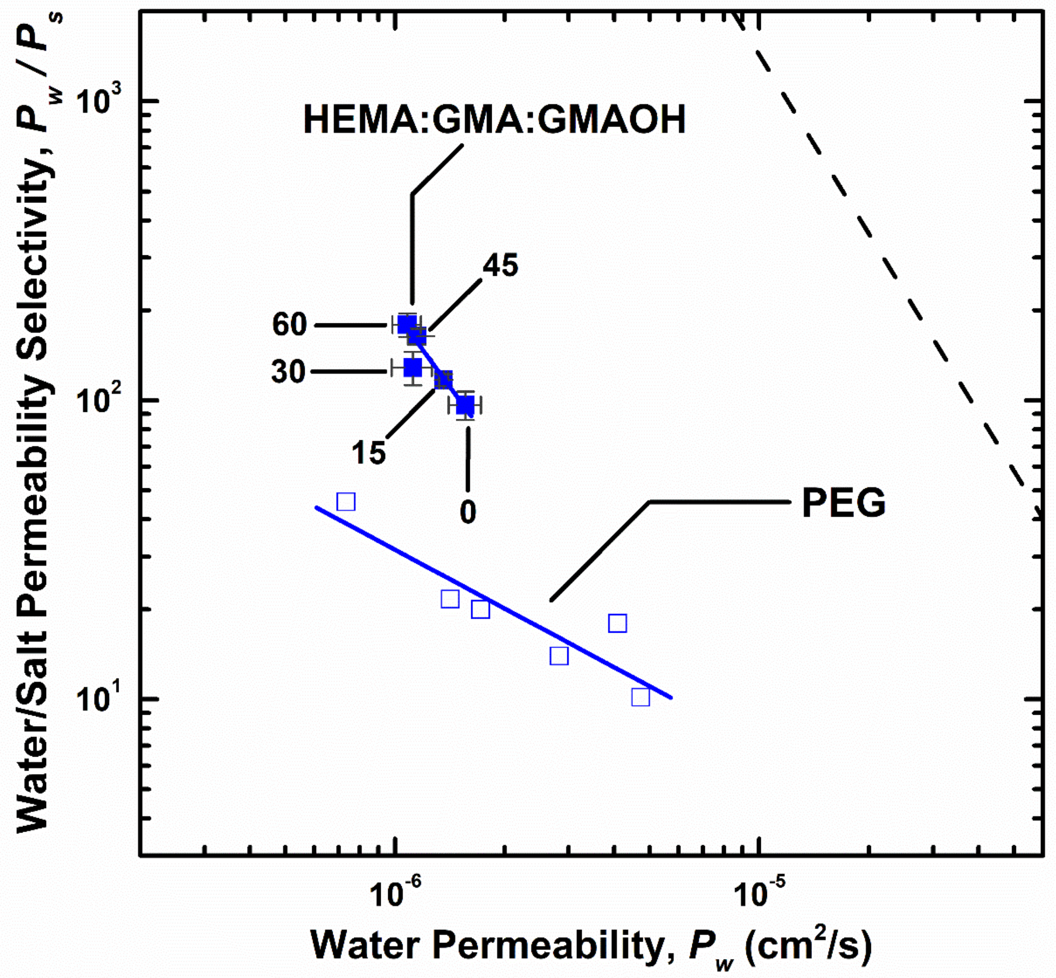

Figure 5. 2. Water/salt permeability selectivity as a function of diffusive water permeability for HEMA:GMA:GMAOH (■) and PEG (□)[20] materials. For HEMA:GMA:GMAOH, the HEMA co-monomer composition of the pre-polymerization solution used to prepare the co-polymer is reported for each data point. The dashed line represents a reported empirical permeability trade-off frontier for desalination membrane materials,[21, 22] and the solid lines are least-squares fits to the data.

The PEG materials exhibit a typical tradeoff relationship whereby water/salt selectivity tends to decrease as materials become more permeable to water. This tradeoff is often observed in cases where the water content of a series of materials is varied systematically.[22] In these cases, the higher water content polymers tend to have higher water permeability and lower water/salt selectivity compared to the lower water content polymers.

The HEMA:GMA:GMAOH materials suffer less of a reduction in the diffusive water permeability as water/salt selectivity increases compared to the PEG materials (i.e., the slope of the HEMA:GMA:GMAOH dashed line is steeper than that of the PEG dashed line in Figure 5.2). This result stems from the equivalent water content nature of the HEMA:GMA:GMAOH series of materials and the fact that both water/salt sorption and diffusivity selectivity increase with increasing content of HEMA in the pre-polymerization solution.

Chemical modification of a series of water content equivalent co-polymers, from a vicinal diol-rich to a distributed hydroxyl group-rich configuration, increased water/salt permeability selectivity with a smaller water permeability penalty compared to that often observed in hydrated polymers. These results, obtained using a model series of co-polymers, suggest that controlling the spatial arrangement of functional groups in hydrated membrane materials may be important for engineering highly selective polymers for desalination applications. The results on these model materials represent a step toward establishing general water and salt transport structure-property relationships for membrane materials including polymers that are more chemically similar to commercial desalination membranes than those materials considered here. The results suggest that distributed hydrophilic functional groups may lead to increased selectivity and may represent a strategy for improving water/salt selectivity of advanced membrane materials to address global water shortages.

5.4 References

1. M.M. Mekonnen and A.Y. Hoekstra, Four billion people facing severe water scarcity. Science Advances, 2016. **2**(2): p. e1500323.
2. C.Y. Tang, Z. Yang, H. Guo, J.J. Wen, L.D. Nghiem, and E. Cornelissen, Potable Water Reuse through Advanced Membrane Technology. Environmental Science & Technology, 2018. **52**(18): p. 10215-10223.
3. S. Miller, H. Shemer, and R. Semiat, Energy and environmental issues in desalination. Desalination, 2015. **366**: p. 2-8.

4. A. Subramani and J.G. Jacangelo, Emerging desalination technologies for water treatment: A critical review. Water Research, 2015. **75**: p. 164-187.

5. G. Amy, N. Ghaffour, Z. Li, L. Francis, R.V. Linares, T. Missimer, and S. Lattemann, Membrane-based seawater desalination: Present and future prospects. Desalination, 2017. **401**: p. 16-21.

6. Y. Cohen, R. Semiat, and A. Rahardianto, A perspective on reverse osmosis water desalination: Quest for sustainability. AIChE Journal, 2017. **63**(6): p. 1771-1784.

7. J.R. Werber, A. Deshmukh, and M. Elimelech, The Critical Need for Increased Selectivity, Not Increased Water Permeability, for Desalination Membranes. Environmental Science & Technology Letters, 2016. **3**(4): p. 112-120.

8. H.B. Park, J. Kamcev, L.M. Robeson, M. Elimelech, and B.D. Freeman, Maximizing the right stuff: The trade-off between membrane permeability and selectivity. Science, 2017. **356**(6343): p. 1-10.

9. G.M. Geise, D.R. Paul, and B.D. Freeman, Fundamental water and salt transport properties of polymeric materials. Progress in Polymer Science, 2014. **39**(1): p. 1-42.

10. G.M. Geise, H.-S. Lee, D.J. Miller, B.D. Freeman, J.E. McGrath, and D.R. Paul, Water purification by membranes: The role of polymer science. Journal of Polymer Science Part B: Polymer Physics, 2010. **48**(15): p. 1685-1718.

11. R.W. Baker, *Membrane technology and applications*. 3rd ed. 2012, New York: Wiley.

12. S.C. Solleder, D. Zengel, K.S. Wetzel, and M.A.R. Meier, A Scalable and High-Yield Strategy for the Synthesis of Sequence-Defined Macromolecules. Angewandte Chemie International Edition, 2016. **55**(3): p. 1204-1207.

13. J.-F. Lutz, Defining the Field of Sequence-Controlled Polymers. Macromolecular Rapid Communications, 2017. **38**(24): p. 1700582.

14. H. Yasuda, C.E. Lamaze, and L.D. Ikenberry, Permeability of solutes through hydrated polymer membranes Part I. Diffusion of sodium chloride. Die Makromolekulare Chemie, 1968. **118**: p. 19-35.

15. R.J. Petersen, Composite reverse osmosis and nanofiltration membranes. Journal of Membrane Science, 1993. **83**: p. 81-150.

16. P.R. Bevington and D.K. Robinson, *Chapter 4: Propagation of Errors*, in *Data reduction and error analysis for the physical sciences*. 2003, McGraw Hill: New York. p. 56-65.

17. K. Chang, H. Luo, and G.M. Geise, Water content, relative permittivity, and ion sorption properties of polymers for membrane desalination. Journal of Membrane Science, 2019. **574**: p. 24-32.

18. J.G. Wijmans and R.W. Baker, *The solution-diffusion model: A unified approach to membrane permeation,* in *Materials science of membranes for gas and vapor separation*, Y.P. Yampolskii, I. Pinnau, and B.D. Freeman, Editors. 2006, John Wiley & Sons, Ltd: West Sussex. p. 159-189.

19. G.M. Geise, B.D. Freeman, and D.R. Paul, Sodium chloride diffusion in sulfonated polymers for membrane applications. Journal of Membrane Science, 2013. **427**: p. 186-196.

20. H. Ju, A.C. Sagle, B.D. Freeman, J.I. Mardel, and A.J. Hill, Characterization of sodium chloride and water transport in crosslinked poly(ethylene oxide) hydrogels. Journal of Membrane Science, 2010. **358**(1): p. 131-141.

21. H. Zhang and G.M. Geise, Modeling the water permeability and water/salt selectivity tradeoff in polymer membranes. Journal of Membrane Science, 2016. **520**: p. 790-800.

22. G.M. Geise, H.B. Park, A.C. Sagle, B.D. Freeman, and J.E. McGrath, Water permeability and water/salt selectivity tradeoff in polymers for desalination. Journal of Membrane Science, 2011. **369**(1-2): p. 130-138.

23. H. Ju, B.D. McCloskey, A.C. Sagle, V.A. Kusuma, and B.D. Freeman, Preparation and characterization of crosslinked poly(ethylene glycol) diacrylate hydrogels as fouling-resistant membrane coating materials. Journal of Membrane Science, 2009. **330**(1): p. 180-188.

24. K. Chang, A. Korovich, T. Xue, W.A. Morris, L.A. Madsen, and G.M. Geise, Influence of Rubbery versus Glassy Backbone Dynamics on Multiscale Transport in Polymer Membranes. Macromolecules, 2018. **51**(22): p. 9222-9233.

25. K. Chang, T. Xue, and G.M. Geise, Increasing salt size selectivity in low water content polymers via polymer backbone dynamics. Journal of Membrane Science, 2018. **552**: p. 43-50.

26. D.R. Paul and Y.P. Yampol'skii, eds. *Polymeric gas separation membranes*. 1994, CRC Press: Boca Raton.

27. H. Yasuda, L.D. Ikenberry, and C.E. Lamaze, Permeability of solutes through hydrated polymer membranes Part II. Permeability of water soluble organic solutes. Die Makromolekulare Chemie, 1969. **125**: p. 108-118.

28. J.S. Mackie and P. Meares, The diffusion of electrolytes in a cation-exchange resin membrane. I. Theoretical. Proceedings of the Royal Society of London. Series A, Mathematical and Physical Sciences, 1955. **232**(1191): p. 498-509.

29. P. Meares, The mechanism of water transport in membranes. Philosophical Transactions of the Royal Society of London B, 1977. **278**: p. 113-150.

30. Z. Lu, G. Polizos, D.D. Macdonald, and E. Manias, State of water in perfluorosulfonic ionomer (Nafion® 117) proton exchange membranes. Journal of The Electrochemical Society, 2008. **155**(2): p. B163-B171.

31. G. Smith, A.P. Duffy, J. Shen, and C.J. Olliff, Dielectric relaxation spectroscopy and some applications in the pharmaceutical sciences. Journal of Pharmaceutical Sciences, 1995. **84**(9): p. 1029-1044.

Chapter 6. Comparison Between Conventional Solvothermal and Aqueous Solution-based Production of UiO-66-NH_2: Life Cycle Assessment, Techno-economic Assessment, and Implications for CO_2 Capture and Storage

6.1. Introduction:

Metal-organic frameworks (MOFs) are a new class of materials, consisting of metal ions or clusters coordinated with organic linkers, and they are known for their high porosity, uniform and tunable pore size, good crystallinity, and a high degree of chemical tunability [1-3]. As such, MOFs have been applied either independently in catalysis [4-6], sensing [7-10], and gas storage [11-16] or in hybrid materials in gas separation [17-20], ion sieving [21-23], and desalination [24-27], and MOFs are expected to play a more important role in high-impact applications in the near future [8, 28, 29].

Despite their huge potential in various applications, MOFs are currently synthesized at lab-scale, and several challenges must be resolved before MOFs are produced at/above pilot-scale (e.g., the annual production rate is at least on the order of 10s of kilograms) [30-32]. These challenges mainly arise from two aspects, the process economic feasibility and the process environmental impacts [30-33]. The process economic feasibility has two significant measures, the production cost (e.g., capital cost and operating cost) and the process space-time yield (STY) [33-35]. The first measure, production cost, is an indicator for the product market price that makes the process breakeven. The lower the production cost, the higher the product economic favorability is at the same market price. The second measure, process STY, is an indicator for the effectiveness of the

---

This chapter is already published and available from: Luo, H., Cheng, F., Huelsenbeck, L., & Smith, N. (2021). Comparison Between Conventional Solvothermal and Aqueous Solution-based Production of UiO-66-NH2: Life Cycle Assessment, Techno-economic Assessment, and Implications for CO2 Capture and Storage. Journal of Environmental Chemical Engineering, 105159.

space and time usage of the production process [33-35]. The process STY contributes to the product economic favorability in two manners. As the process STY increases, the same production line produces more products in its lifetime. As a result, the effective capital cost decreases while the total product sales increases. Hence, a process with lower cost and higher STY is desired for the MOFs production [33-35]. The process environmental impacts, on the other hand, measures the environmental burdens (e.g., greenhouse gas emissions and water pollution) the synthesis generates and is an indicator for the process sustainability [36-38]. The process environmental impacts, although often overlooked, are as important as the process economic feasibility. They could be even more significant if the produced MOFs are used for sustainability-related applications [13, 39-44] (e.g., greenhouse gas capture/storage and energy storage). In other words, if MOFs were to be used for those applications, the environmental benefits they create (e.g., the amount of greenhouse gas captured/transferred) in their lifetime must surpass the environmental burdens their production process creates, otherwise the rationality of those applications might be jeopardized. To date, the lab-scale synthesis of many MOFs (e.g., ZIF-8, HKUST-1 and UiO-66 derivatives) is not attractive enough from either the process economic feasibility aspect or the process environmental impacts aspect. These limitations are likely caused by the synthesis method of those MOFs [30-33].

Conventionally, the lab-scale synthesis of many MOFs is done via the slow nucleation-growth in organic solvents (e.g., solvothermal synthesis of UiO-66 derivatives would take 12 to 24 hrs) [30-33, 45]. Such synthesis methods have two major drawbacks. First, the slow nucleation-growth process leads to long batch-to-batch time which lowers STY [30-33]. Second, the use of a large amount of organic solvents greatly increases the production costs and creates significant environmental burdens [30-33]. As such, finding better alternatives (i.e., environmentally friendly and/or cost-effective alternatives) for the conventional slow organic solution-based synthesis of MOFs becomes an urgent need, and more recent efforts have been made to develop rapid aqueous-solution based synthesis methods of MOFs [33, 46-50]. In our recent work, Huelsenbeck *et al.* reported a generalized aqueous solution-based approach for the rapid synthesis of several MOFs (e.g., synthesis of UiO-66(-NH_2), ZIF-L and HKUST-1 within 10 min). This work systematically studied the effects of solution chemistry on both the process STY and the product quality (e.g., surface area and defects) [33]. For all MOFs studied, the aqueous solution-based process has higher STY than the conventional organic solution-based process. The quality of some MOFs (e.g., UiO-66-NH_2 and HKUST-1) obtained from the aqueous solution-based is comparable to their counterpart obtained from the organic solution-based process, as demonstrated by material characterization (e.g., X-ray Diffraction, Thermalgravimetric Analysis, and Surface Analysis) [33]. These findings encourage us to further investigate the environmental and economic benefits of using the aqueous solution-based process as an alternative for the organic solution-based process in the MOFs production, and we will quantify those benefits via life-cycle analysis (LCA) and techno-economic assessment (TEA). Both LCA and TEA are useful tools in the analysis of novel-material productions, and their applications have also been extended to the MOFs production in the recent years by few pioneer studies [44, 51-53]. For example, Grande *et al.* carried out LCA on CPO-27-Ni production via different synthesis approaches [51], and DeSantis *et al.* conducted TEA on MOF adsorbents, including Ni_2(dobdc), Mg_2(dobdc), $Zn_4O(bdc)_3$, and HKUST-1[44]. However, these studies only considered one aspect of the MOF productions, and none of them further applied the LCA/TEA results to justify the applications of the studied MOFs. Hence, comprehensive LCA-TEA studies on the MOF productions are necessary to fill the knowledge gap, and ideally, such studies should relate the productions to the applications of the target MOFs.

In this work, UiO-66-NH_2 was selected as the target MOF due to its successful synthesis from the aqueous solution-based system and its great potential in applications like gas separation, ion sieving, and carbon dioxide capture (CCS) etc. [21-23, 39-43, 54-59]. Here we mainly focused on the applications of UiO-66-NH_2 in CCS application, which is a promising route to achieve significant CO_2 reduction in the near term [60]. Recently, UiO-66-NH_2 and other UiO-66 derivatives have attracted a lot of research interests in terms of CO_2 capture and storage [39-43, 54-58]. Most of the studies on UiO-66-NH_2 and other UiO-66 derivatives focused on the evaluation of CO_2 uptake, adsorption/desorption performance, selectivity, and stability. However, the life cycle emissions associated with UiO-66-NH_2 has not been determined yet, as well as the production costs. The overall goal of this work is to evaluate and compare the environmental and economic performances of the conventional solvothermal production and the aqueous solution-based production of UiO-66-NH_2 and apply the analysis results to provide insights on the use of UiO-66-NH_2 in CCS. This goal is further divided into four specific objectives. First, the lab-scale synthesis of UiO-66-NH_2 using the conventional solvothermal system and the aqueous solution-based system was analyzed, and both systems were scaled up to their corresponding hypothetical pilot-scale productions using chemical engineering design criteria [61, 62]. Next, LCA was applied to both hypothetical pilot-scale productions to evaluate their overall environmental impacts and analyze the contribution of each component to the overall impacts. Further, TEA was applied to both production methods to assess their economic feasibility and investigate the distribution of the costs. Finally, the LCA results were used to justify the use of UiO-66-NH_2 in CCS application, and suggestions were made on the potential directions that would make UiO-66-NH_2 a better candidate in CCS. To the best of our knowledge, this work is the first comprehensive LCA-TEA study on UiO-66-NH_2 productions via solvothermal and aqueous-based systems, and we believe the results of this work will motivate further studies on the sustainable and economical productions and feasible applications of UiO-66-NH_2 as well as a vast majority of other MOFs.

6.2. Method

The accuracy and comprehensiveness for any LCA-TEA study depend on the description of the process, the choice of the system boundary, the data availability and the calculation methods [36-38]. Therefore, the process associated with UiO-66-NH_2 was described first in section 2.1, followed by the system boundary selection in section 2.2. The calculation methods for LCA and TEA were presented in section 2.2 and 2.3, respectively.

6.2.1 Process description

The ultimate goal of this study is to examine the environmental and economic performances for the pilot-scale production of UiO-66-NH_2 using the conventional solvothermal system and the aqueous solution-based system. However, the life cycle impact data for three key components, zirconium tetrachloride ($ZrCl_4$), zirconyl chloride octahydrate ($ZrOCl_2 \cdot 8H_2O$) and the 2-aminoterephthalic acid (2-ATA), were not available in the Econivent v3.6 database [63]. Therefore, we decided to include the production of these three components in the process description to calculate their life cycle impact data and estimate the price of 2-ATA. A brief block flow diagram for all associated processes is presented in Figure 6.1. These processes are either well-established in industry or representative at lab-scale [33, 59, 64-69]. In brief, $ZrCl_4$ is fabricated from zircon via chlorination, $ZrOCl_2 \cdot 8H_2O$ is obtained from $ZrCl_4$ via hydrolysis, 2-ATA is synthesized from TPA via nitration and hydrogenation, and UiO-66-NH_2 is produced using either the combination of $ZrCl_4$ and ATA in DMF (solvothermal system) or the combination of $ZrOCl_2 \cdot 8H_2O$ and 2-NTA-Na_2 in water (aqueous solution-based system) [33, 59, 64-69]. In the hypothetical pilot-scale production of UiO-66-NH_2, only 2-ATA and UiO-66-NH_2 are produced on site (i.e., Zr sources are purchased). Hence, the information from all three boxes was used in LCA, while the information from the middle and the bottom box was used in TEA.

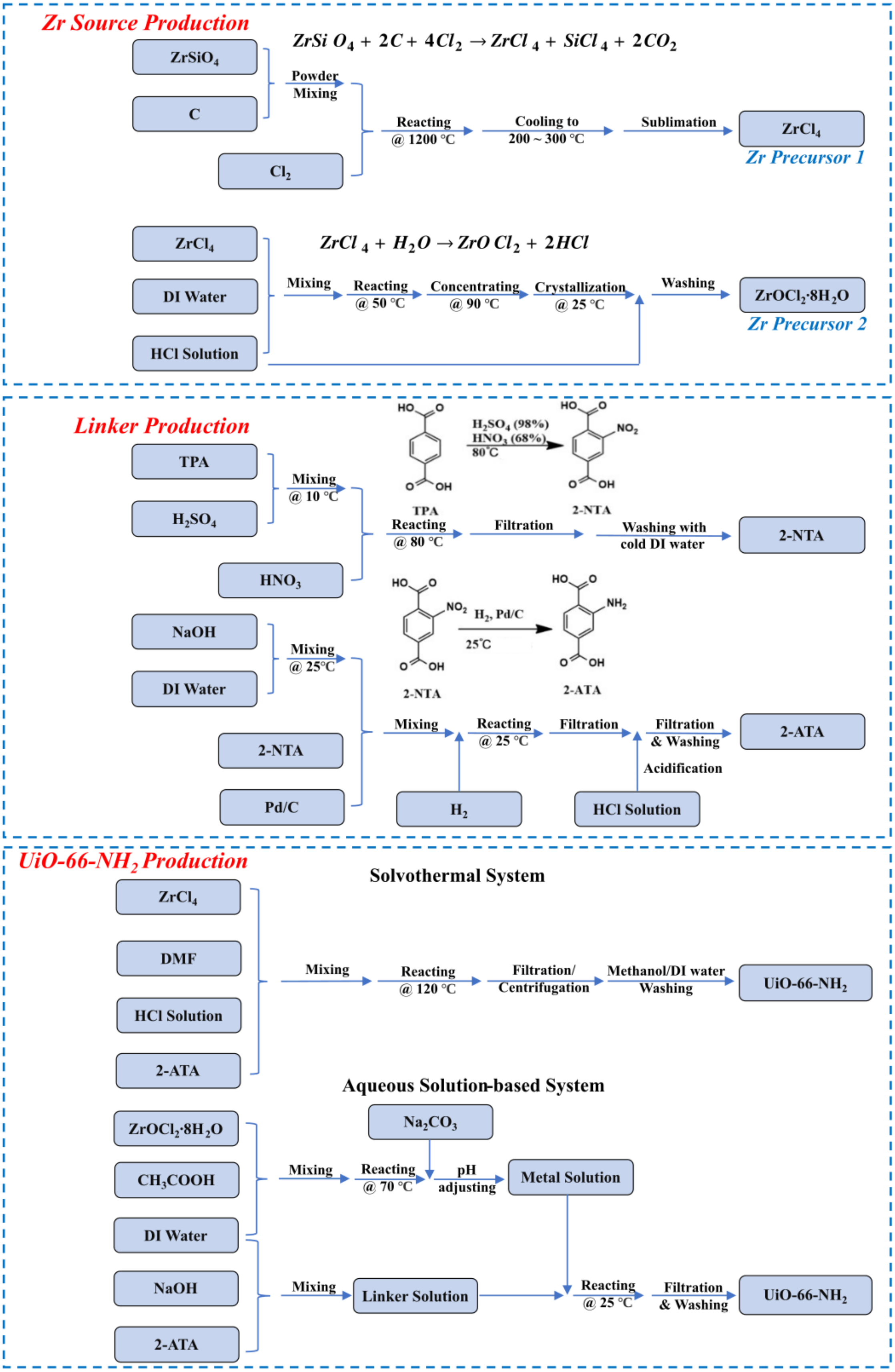
Zr Source Production
$ZrSiO_4 + 2C + 4Cl_2 \rightarrow ZrCl_4 + SiCl_4 + 2CO_2$
$ZrSiO_4$
C
Cl_2
Powder Mixing
Reacting @ 1200 °C
Cooling to 200 ~ 300 °C
Sublimation
$ZrCl_4$
Zr Precursor 1
$ZrCl_4 + H_2O \rightarrow ZrOCl_2 + 2HCl$
$ZrCl_4$
DI Water
HCl Solution
Mixing
Reacting @ 50 °C
Concentrating @ 90 °C
Crystallization @ 25 °C
Washing
$ZrOCl_2 \cdot 8H_2O$
Zr Precursor 2
Linker Production
TPA
H_2SO_4
HNO_3
Mixing @ 10 °C
HO
O
OH
TPA
H_2SO_4 (98%)
HNO_3 (68%)
80 °C
NO_2
2-NTA
Reacting @ 80 °C
Filtration
Washing with cold DI water
2-NTA
NaOH
DI Water
2-NTA
Pd/C
Mixing @ 25°C
NO_2
H_2, Pd/C
25 °C
NH_2
2-NTA
2-ATA
Mixing
Reacting @ 25 °C
Filtration
Filtration & Washing
Acidification
2-ATA
H_2
HCl Solution
UiO-66-NH_2 Production
Solvothermal System
$ZrCl_4$
DMF
HCl Solution
2-ATA
Mixing
Reacting @ 120 °C
Filtration/ Centrifugation
Methanol/DI water Washing
UiO-66-NH_2
Aqueous Solution-based System
$ZrOCl_2 \cdot 8H_2O$
CH_3COOH
DI Water
NaOH
2-ATA
Na_2CO_3
Mixing
Reacting @ 70 °C
pH adjusting
Metal Solution
Mixing
Linker Solution
Reacting @ 25 °C
Filtration & Washing
UiO-66-NH_2

Figure 6. 1. Brief block flow diagram of the Zr source production (top box), the 2-ATA linker production (middle box), and the UiO-66-NH_2 production (bottom box).

6.2.1.1 Production of $ZrCl_4$, $ZrOCl_2·8H_2O$ and 2-ATA

As shown in Figure 6.1, two types of Zr source, $ZrCl_4$, and $ZrOCl_2·8H_2O$, were used in UiO-66-NH_2 productions. The $ZrCl_4$ is synthesized from the high-temperature chlorination reaction of zircon ($ZrSiO_4$), using charcoal as the reducing agent and chlorine gas as the chlorine source [65]. The post-reaction gaseous mixture is cooled down to allow for the sublimation of $ZrCl_4$, and the obtained $ZrCl_4$ can be directly used in other productions without further purifications. The $ZrOCl_2·8H_2O$ is obtained from the direct hydrolysis of $ZrCl_4$ in a dilute hydrochloric acid (HCl) solution. The post-reaction mixture is first concentrated at elevated temperature and then cooled down to room temperature for crystallization [59, 66, 67]. The crude $ZrOCl_2·8H_2O$ is washed with an HCl solution, and the purified $ZrOCl_2·8H_2O$ is used in other productions. A more detailed process description that includes the mass of the chemicals and the reaction conditions could be found in the Supporting Information (Page 2-3).

The linker, 2-ATA, is synthesized from a two-step nitration-hydrogenation reaction of terephthalic acid (TPA) [68, 69]. In the first step, a nitro group is introduced to the TPA by the nitration reaction at elevated temperature, using concentrated nitric acid (HNO_3) as the nitration reagent and concentrated sulfuric acid (H_2SO_4) as the dehydrator [67]. The post-reaction mixture from this step is first cooled down to room temperature and then filtered to obtain the crude product, 2-nitroterephthalic acid (2-NTA). The crude 2-NTA is further washed with DI water prior to the hydrogenation reaction [69]. In the second step, the nitro group is reduced to the amino group by the aqueous solution hydrogenation reaction of disodium 2-NTA (2-NTA-Na_2) at room temperature, using palladium-on-carbon (Pd/C) as the catalyst and hydrogen gas as the hydrogen source. The post-reaction mixture from this step is first filtered to recover Pd/C and then acidified to precipitate 2-ATA. The 2-ATA is obtained by filtration, and is further washed with DI water prior to the UiO-66-NH_2 production. A more detailed process description that includes the mass of the chemicals and the reaction conditions is available in the Supporting Information (Page 3-4).

6.2.1.2 Production of UiO-66-NH_2

The production of UiO-66-NH_2 is achieved from both the conventional solvothermal system and the aqueous solution-based system [33, 64]. In the conventional solvothermal system, $ZrCl_4$ and 2-ATA are co-dissolved in DMF, and this DMF mixture is acidified with an HCl solution [64]. The acidified DMF mixture is heated at elevated temperature to allow for the formation of UiO-66-NH_2 *via* slow nucleation and growth. The post-reaction mixture is first cooled down to room temperature, and the UiO-66-NH_2 is then separated from the mixture by filtration or centrifugation. The obtained crude UiO-66-NH_2 is washed with methanol or water to remove any residual DMF and unreacted linker/metal components. In the aqueous solution-based system, the zirconium-oxo-cluster solution (referred to as the metal solution for brevity) and the linker solution are prepared separately [33]. The metal solution is prepared by heating the $ZrOCl_2 \cdot 8H_2O$ in an acetic acid-water mixture at elevated temperature for a designated time. When the heating process is completed, the metal solution is partially neutralized to a designated pH value using Na_2CO_3. The linker solution is prepared by co-dissolving 2-ATA and NaOH in DI water. The metal solution and the linker solution are mixed under vigorous stirring, and the formed UiO-66-NH_2 is separated from the mixture by filtration or centrifugation. The obtained crude UiO-66-NH_2 is washed with a dilute sodium hydroxide solution and DI water to remove any residual 2-ATA linker, sodium acetate and acetic acid. The production of UiO-66-NH_2 is described in further detail (e.g., reactant mass, reaction conditions and product yield) in the Supporting Information (Page 4-5).

The processes described above are mostly on the lab scale, yet they will serve as the basis for the scaling up production of UiO-66-NH_2 to the pilot scale. In scaling up the process, the differences between the pilot-scale productions and the lab-scale productions (e.g., solvent recovery, reaction medium reuse, and heating methods) need to be properly accounted for. Hence, several assumptions were made, according to the chemical engineering design criteria, for the scale up process [61, 62], and these assumptions were introduced and discussed in detail in the Supporting Information. The final material and energy inputs for the hypothetical pilot-scale production of UiO-66-NH_2 were summarized in Table E.3 through Table E.8, and those values were used in conjunction with other data (e.g., life cycle impact data and market prices) in LCA and TEA calculations.

6.2.2 Life cycle Assessment

Life cycle assessment (LCA) is an environmental accounting tool that evaluates the environmental impacts of products, processes, and systems. LCA was performed following the steps defined by ISO 14040 [70], including goal and scope, inventory analysis, impact assessment, and interpretation. In this section, a detailed environmental assessment of UiO-66-NH_2 production via the conventional solvothermal system and the aqueous solution-based system was conducted based on the framework displayed in Figure 6.2. In this study, a cradle-to-gate type LCA was carried out, and seven metrics were chosen to estimate the environmental impacts associated with the UiO-66-NH_2 production via both the solvothermal system and the aqueous solution-based system. The production cost of UiO-66-NH_2 from both systems was estimated by TEA. However, the labor costs and engineering construction cost (shaded in grey) were not accounted for in TEA due to their large regional variability and uncertainty.

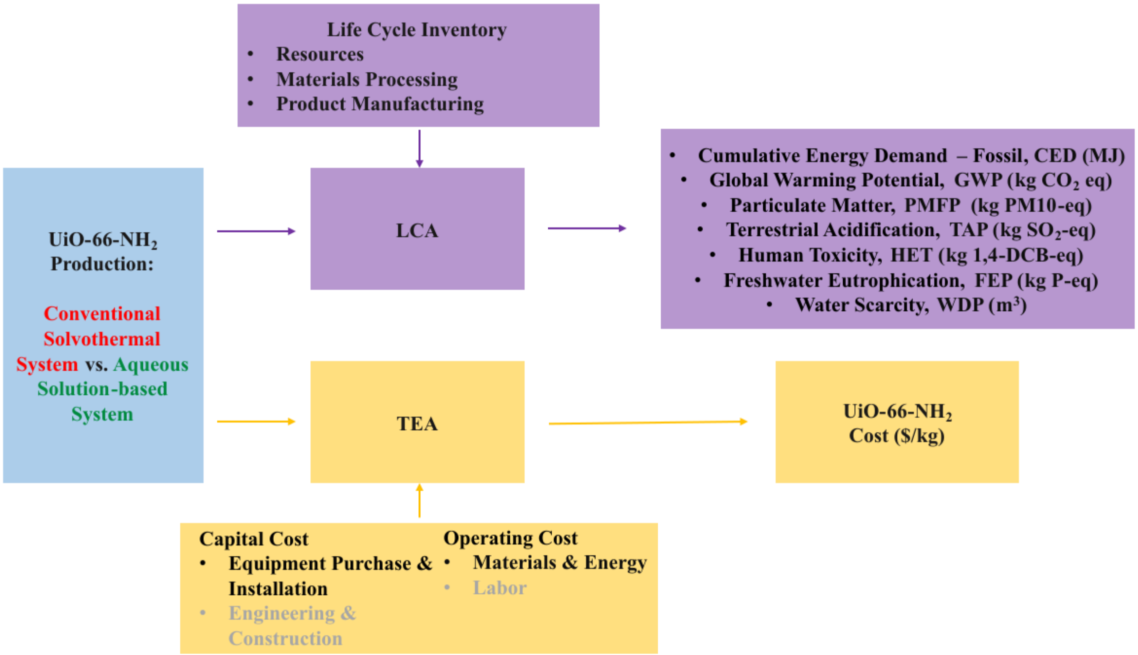

Figure 6. 2. Representation of the overall LCA and TEA framework.

6.2.2.1 Goal and scope

The goal of LCA in this study is first to analyze and understand the environmental burdens associated with UiO-66-NH2 production via the conventional solvothermal system and the aqueous solution-based system and find the most environmentally friendly production route. We focused on the evaluation of environmental impacts of UiO-66-NH2 production, while its utilization and end of life were not considered. Therefore, a cradle-to-gate scope of LCA was chosen. The system boundary comprised the chemical and energy consumptions associated with the raw material extraction and processing for UiO-66-NH2 production. To compare the environmental impacts of the two production systems, a function unit (FU) needed to be designated first. A mass-based FU was suitable in this study as it revealed the relationships between the production environmental impacts (e.g., GWP) and the production outcome (e.g., the mass of UiO-66-NH_2) [51, 71]. As such, the FU was selected to be 1 kg of UiO-66-NH_2 on a dry basis.

6.2.2.2 Life Cycle Inventory

The life cycle inventory (LCI) is a critical step in LCA as it creates the full inventory of the input/output of the target process. In this work, the LCI was created based on the chemical consumptions, the energy calculations, and the important assumptions for process scaling up. All these pieces of information were documented in the Supporting Information (Page 6-12), and some of the key information was provided below.

Chemical and pharmaceutical industries minimize solvent consumption for conventional solvothermal systems by recycling organic solvents at a rate of 90% by vacuum/ambient pressure distillation [44]; therefore, we adapted this technique in our analysis to ensure the economic feasibility and environmental favorability of the system [44]. We also assumed the washing step in the conventional solvothermal systems could be done with either methanol (route 1) or water (route 2). As such, three production routes were defined and evaluated in this work, including route 1, solvothermal system with methanol for cleaning; route 2, solvothermal system with DI water for cleaning; and route 3, aqueous solution-based system. Analyzing these three routes can reveal the change in the environmental favorability and economic feasibility of the UiO-66-NH_2 production when organic solvents are partially or fully replaced by water.

Since no information on the UiO-66-NH_2 production beyond lab-scale is available, the chemical consumptions were estimated from the corresponding lab-scale data, presented in Table E.1 and E.2, using the stoichiometric relationship and the limiting reactant-to-product yield. However, the definition of “yield” is somewhat ambiguous in literature [33]. Traditionally, researchers assume the percentage yield is identical to the percentage conversion of the limiting reactant, regardless of the percentage crystallinity of the obtained MOFs. Alternatively, the percentage yield could be taken as the product of the percentage conversion of the limiting reactant and the percentage crystallinity of the MOFs. This alternative definition is more conservative, as it assumes the crystalline MOFs are the desired product. In this work, we assessed the environmental impacts of UiO-66-NH_2 production based on three scenarios: 1) the yield is the conversion rate regardless of crystallinity (mass-based FU); 2) yield is the product of conversion rate and crystallinity (crystallinity-based FU), which will eventually translate into the maximum process environmental impacts; and 3) yield is 100% (ideal case), which will eventually translate into the ideal minimum process environmental impacts.

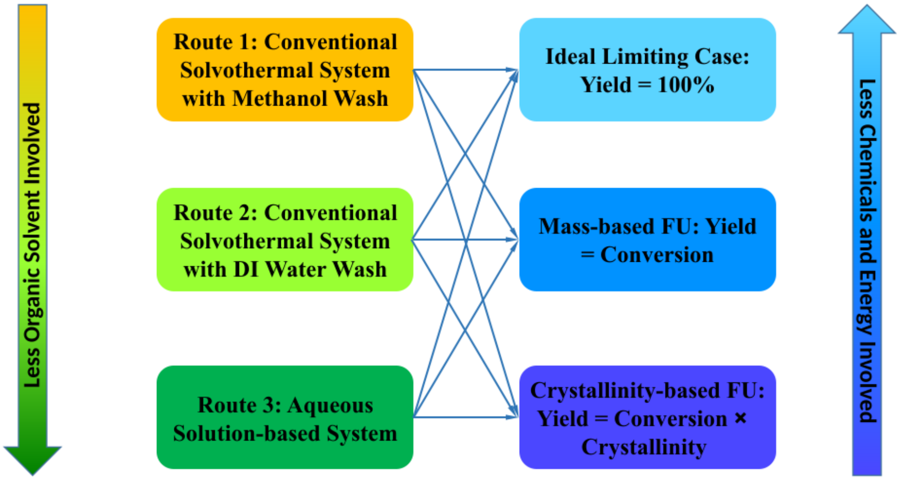

Figure 6. 3. Illustration of the nine scenarios considered in this work.

In summary, three production routes were defined, and three yield definitions were used for each yield (Figure 6.3). These nine scenarios could represent a possible and reasonable range of the environmental burdens associated with the UiO-66-NH_2 production. In the main text, we focused our discussions on the mass-based FU, and the corresponding LCI data were summarized in Table 6.1 (combined from Table E.5, E.6 and E.13). Linear calculations were performed to convert these inventory data to crystallinity-based FU and ideal case (yield = 100%), and the full life cycle inventories for other FU cases could be found in Table E.3, E.4, E.7, E.8 (chemical consumptions and heat), and E.13 (electricity).

Table 6. 1. Summary of the materials and energy input for the conventional solvothermal and aqueous production of 1 kg UiO-66-NH_2 (mass-based FU) after scaling up. The products yield corresponding to this FU are 38% and 96% for the conventional solvothermal system and the aqueous solution-based system, respectively.

	Material/Energy	**Solvothermal**	**Aqueous**
Zr Precursor Production	**Input**		
	$ZrSiO_4$ (kg)	1.878	0.825
	C (kg)	0.250	0.110
	Cl_2 (kg)	4.694	2.063
	HCl (kg)	-	0.149
	Water (kg)	-	2.984
	Energy consumption		
	Heat (MJ)	6.668	5.24
	Output		
	$ZrCl_4$ (kg)	2.150	-
	$ZrOCl_2 \cdot 8H_2O$ (kg)	-	1.176
Linker Production	**Input**		
(Nitration of TPA)	TPA (kg)	4.895	1.404
	H_2SO_4 (kg)	7.995	2.293
	HNO_3 (kg)	2.092	0.832
	Water (kg)	2.060	0.591
	Energy consumption		
	Heat (MJ)	18.702	5.363
	Electricity (kWh)	6.414	6.405
	Output		
	2-NTA (kg)	4.479	1.285
Linker Production	**Input**		
(Hydrogenation of 2-NTA)	2-NTA (kg)	4.479	1.285
	NaOH (kg)	1.697	0.487
	H_2 (kg)	0.116	0.033
	Pd/C (kg)	0.053	0.015
	HCl (kg)	1.549	0.444
	Water (kg)	108.758	31.190

	Energy consumption		
	Heat (MJ)	7.503	2.152
	Electricity (kWh)	6.733	6.496
	Output		
	2-ATA (kg)	2.305	0.661
UiO-66-NH_2 Synthesis	**Input**		
	2-ATA (kg)	2.305	0.661
	$ZrCl_4$ (kg)	2.150	-
	HCl (kg)	7.368	-
	Water (route 1) (kg)	13.099	-
	Water (route 2) (kg)	787.093	-
	Water (route 3) (kg)	-	138.767
	DMF (kg)	24.355	-
	MeOH (route 1) (kg)	61.300	-
	$ZrOCl_2 \cdot 8H_2O$ (kg)		1.176
	AcOH (kg)	-	4.793
	NaOH (kg)	-	0.347
	Na_2CO_3 (kg)	-	1.210
	Energy consumption		
	Heat (route 1) (MJ)	1182.227	
	Heat (route 2) (MJ)	296.044	
	Heat (route 3) (MJ)	-	6.946
	Electricity (kWh)	8.939	6.411
	Output		
	UiO-66-NH_2 (kg)	1	1

6.2.2.3 Life cycle impact modeling

LCA was conducted using Excel spreadsheet and Econivent v3.6 database [63]. Cumulative energy demand - fossil (MJ), global warming potential (kg CO_2-Eq), particulate matter (kg PM10-Eq), terrestrial acidification (kg SO_2-Eq), freshwater eutrophication (kg P-Eq), human toxicity (kg 1,4-DCB-Eq), and water scarcity (m^3) were chosen as the metrics to evaluate the environmental impacts of the two UiO-66-NH_2 production systems (three routes) [72]. Cumulative energy demand and ReCiPe Midpoint method were used to calculate the life cycle environmental impacts mentioned above [73].

6.2.3 Techno-economic assessment

Techno-economic assessment was conducted to assess the total cost of producing 1 kg UiO-66-NH_2 via the conventional solvothermal system and the aqueous solution-based system. The total cost can be broadly categorized into the operating cost and the capital cost (Figure 6.2). Operating cost is comprised of the chemicals and energy consumption required for UiO-66-NH_2 productions. We collected the minimum, average, and maximum market price of chemicals from commercial selling websites, and these data were summarized in Table E.9. The market price of electricity and natural gas was 0.0682 \$/kWh [45] and \$0.004/MJ [74], which stands for the average market price in the United States. The operating cost were then calculated by multiplying the chemical/energy consumption (Table 6.1) and their corresponding market price (Table E.9). The capital costs were also assessed, and detailed information can be found in the Appendix E (Table E.11). It should be noted that the labor costs and engineering construction (shaded in grey in Figure 6.2) were not accounted for in this analysis due to their large regional variability and uncertainty. Finally, the total cost for UiO-66-NH_2 productions via different routes were calculated by summing operating costs and capital costs per FU.

Due to the variability associated with market price and process parameters (e.g., solvent recycle rate, MOF yield, etc.), we used a Monte Carlo simulation to quantify the effects of uncertainty. Monte Carlo simulation was conducted in the “R environment” for 10,000 trials. In each trial, values for variables were randomly drawn from the defined distribution (triangular distribution, Table E.14), and the aggregated results were used to produce probability distributions of the production costs for producing 1 kg UiO-66-NH_2 from three routes. In addition, a sensitivity analysis of UiO-66-NH_2 production costs from three routes was performed by varying one input parameter to its minimum value or maximum value while keeping other parameters at the baseline values (Table E.14). The most sensitive parameters are the ones with the largest relative differences in production costs.

6.2.4 UiO-66-NH_2 for CCS application

The cradle-to-grave life cycle analysis of utilizing UiO-66-NH_2 as sorbents for pulverized coal (PC) coupled with post-combustion CCS was carried out, and the results were compared with conventional PC fired power plant without CCS (reference case) and with post-combustion monoethanolamine (MEA)-based CCS system. Three configurations, including the base PC power plant without CCS, PC with amine-based CCS, and PC with UiO-66-NH_2 based CCS, were analyzed. The power plant was assumed to have 30-year plant life and 7000 operating hour per year. The base power plant (configuration 1) was assumed to have a gross power output of 650 MW and steam cycle efficiency to be 38.5% [75]. In terms of PC with MEA-based and UiO-66-NH_2-based CCS (configuration 2 and 3), it was assumed CCS equipment was installed to capture the CO_2 from the flue gas by using MEA/UiO-66-NH_2, the captured CO_2 was then regenerated, compressed, and ready for the pipeline. The heat for solvent/sorbent regeneration was supplied by the steam from the steam cycle. For better comparison, the functional unit was chosen to be the life cycle GWP associated with exporting 1 MWh electricity (tonne CO_2 eq/MWh) to the grid. The system boundary for coal-based power plants without and with post-combustion CCS was represented in Figure 6.4.

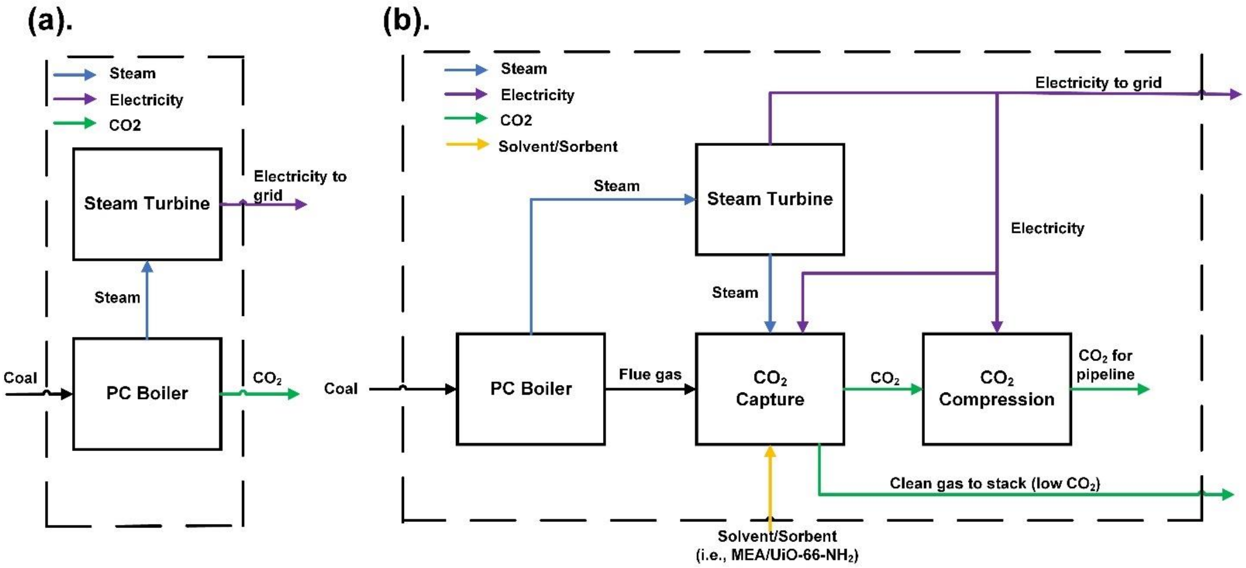

Figure 6. 4. System boundary of (a) reference coal-fired plant without CCS and (b) coal-fired plant coupled with post-combustion CCS.

The GWP for three configurations were calculated by taking the life cycle GWP associated with coal and solvent/sorbents consumptions per exporting 1 MWh electricity. For configuration 1, the GWP was simply associated with coal consumptions. The emissions from coal comprised the direct emissions via combustion and indirect emissions that included coal production, fugitive methane emissions, and transportation [76]. The upstream GWP associated with coal was assumed to be 5.7 g CO_2 eq/MJ [76]. For configuration 2 and 3, the direct emissions released from coal combustion was significantly reduced due to CCS. We also accounted for indirect emissions associated with coal, as well as the upstream greenhouse gas emissions associated with solvent/sorbent loss and loading. The initial solvent/sorbent loading was assumed to satisfy the CO_2 capture for the first hour, and extra solvent/sorbent was replenished to the capture unit to meet the material demand. Table 6.2 summarizes the technical parameters for three evaluated configurations.

Table 6. 2. The technical performance of three configurations, data adapted from [75, 77-79]

Parameters	**Base**	**Amine-based CCS**	**MOF based CCS**
Gross output (MW)	650	650	650
Fuel Input (MW_{th})	1581	1581	1581
Steam cycle efficiency (%)	0.385	0.385	0.385
Coal energy content (MJ/tonne)	27140	27140	27140
Coal carbon content (%)	63.75%	63.75%	63.75%
Regenerator heat requirement (MJ/tonne CO_2)	0	3519	680
CO_2 capture/compression electricity requirement (MWh/tonne CO_2)	0	0.111	0.111
Co_2 capture efficiency (%)	0	90	90

6.3. Result and discussion

6.3.1 Life cycle assessment

Cumulative energy demand (CED, MJ), climate change (GWP, kg CO_2 eq), particulate matter formation (PMFP, kg PM10-eq), terrestrial acidification (TAP, kg SO_2-eq), human toxicity (HTP, kg 1,4-DCB-eq), freshwater eutrophication (FEP, kg P-eq), and water depletion (WDP, m^3) were evaluated for the UiO-66-NH_2 production via three routes. Before looking at the full life cycle of UiO-66-NH_2 production, we first examined the environmental impacts associated with the Zr precursor manufacturing. The relative impacts of producing 1 kg of Zr precursor (e.g., $ZrCl_4$ and $ZrOCl_2 \cdot 8H_2O$) as well as the percentage contribution of each input are presented in Figure 6.5.

As shown in Figure 6.5(a), $ZrCl_4$ has relatively higher environmental burdens than $ZrOCl_2 \cdot 8H_2O$ under all metrics other than HTP. This observation might be counterintuitive since $ZrOCl_2 \cdot 8H_2O$ is produced from $ZrCl_4$, and additional chemicals and energy are used in the $ZrOCl_2 \cdot 8H_2O$ manufacturing. However, the molar conversion of $ZrCl_4$ to $ZrOCl_2 \cdot 8H_2O$ is high (90%), and the molar mass of $ZrOCl_2 \cdot 8H_2O$ (322 g/mol) is also much higher than that of $ZrCl_4$

(233 g/mol). Accordingly, 1 kg of $ZrCl_4$ could yield 1.244 kg of $ZrOCl_2 \cdot 8H_2O$, and such 24% mass gain eventually led to lower environmental burdens (except for HTP) associated with $ZrOCl_2 \cdot 8H_2O$ since all the metrics are per mass-based.

The overall impacts of producing 1 kg of Zr precursor was further itemized to investigate the contribution of each input, and the results are shown in Figure 6.5(b) ($ZrCl_4$) and Figure 6.5(c) ($ZrOCl_2 \cdot 8H_2O$). In general, the environmental impacts associated with the $ZrCl_4$ manufacturing and the $ZrOCl_2 \cdot 8H_2O$ manufacturing have a highly similar structure, and the Zr resource, zircon, is the dominating factor that accounts for 66% to 100% of the total environmental impacts in all metrics other than HTP. This observation, that an inorganic precursor (e.g., $ZrCl_4$) has similar environmental impacts as its first-generation source (e.g., zircon), will be further discussed quantitatively later. As for the HTP metric, its environmental burdens are mainly attributed to the reagent consumption (e.g., HCl and Cl_2). Despite the highly similar environmental impacts structure, certain differences exist in the GWP metric, the CED metric and the HTP metric between the $ZrCl_4$ manufacturing and the $ZrOCl_2 \cdot 8H_2O$ manufacturing. Compared to $ZrCl_4$, reagents and energy associated $ZrOCl_2 \cdot 8H_2O$ manufacturing has slightly higher shares in GWP, CED and HTP. This observation could be explained from the use of extra material (i.e., HCl) and heat in the conversion of $ZrCl_4$ into $ZrOCl_2 \cdot 8H_2O$, which have slight impacts on GWP, CED and HTP. Meanwhile, the use of extra material and heat has negligible impacts on other metrics; therefore, the percentage contribution of each input is identical for those metrics.

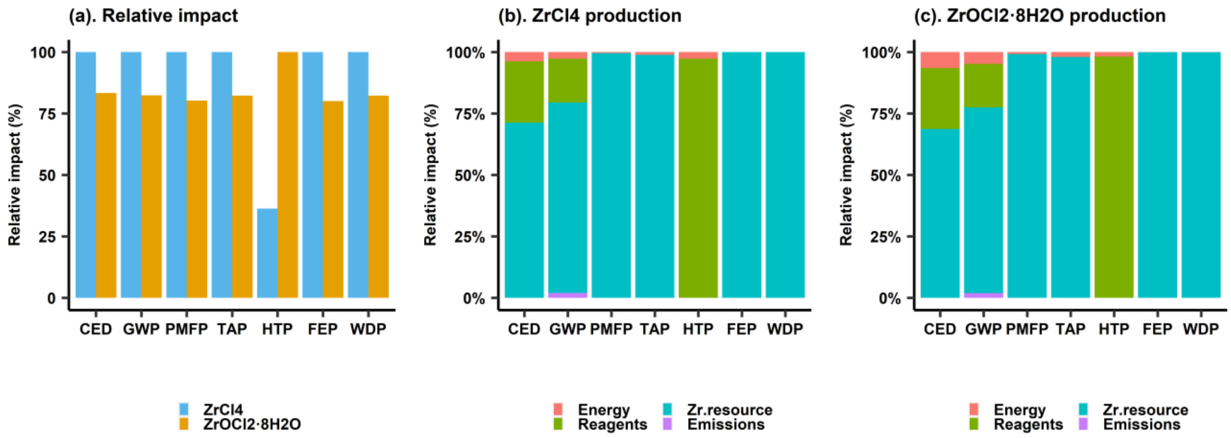

Figure 6. 5. Relative environmental impacts of Zr precursor productions (a) and their breakdown for $ZrCl_4$ (b) and $ZrOCl_2{\cdot}8H_2O$ (c). Chemicals other than the Zr source are merged as “Reagents” in the plot.

The environmental burdens associated with three routes were evaluated, including (1) conventional solvothermal system with methanol wash; (2) conventional solvothermal system with water wash; and (3) aqueous solution-based system. To better understand the effects of yield definition on the environmental impacts of UiO-66-NH_2 production, we computed the results of each route based on the mass-based FU, the crystallinity-based FU, and the ideal case. The product yield associated with mass-based FU, crystallinity-based FU and ideal case are [36%,96%], [18%,38%], and [100%,100%] for the solvothermal system (route 1 and 2) and the aqueous solution-based system (route 3), respectively. For all metrics, the higher the percentage value or absolute value, the greater environmental burdens associated with UiO-66-NH_2 production are. A comparison between the relative environmental impacts of producing 1 kg UiO-66-NH_2 via the three routes is presented in Figure 6.6, and the absolute value of the environmental impacts is shown in Figure E.1. The results in Figure E.1 suggest the absolute environmental burdens associated with UiO-66-NH_2 production increase monotonically with the decreasing product yield, regardless of the choice of production route. This observation is not surprising, as more chemicals and energy are supposed to be consumed at lower product yield, leading to higher environmental burdens. The results in Figure 6.6 reveal that route 1 has the highest environmental burdens for metric, route 3 has the lowest environmental burdens, and the environmental burdens of route 2 lies in between. This observation holds true for the mass-based FU, the crystallinity-based FU and the ideal case. Our discussion in the following section will be mainly based on mass-based FU, i.e., the results in Figure 6.6 (a), unless otherwise specified, and we believe the conclusions drawn below hold true for the other two FUs.

As shown in Figure 6.6(a), the environmental burdens of route 1 are higher than those of route 2 in all metrics, and the differences in environmental burdens are very prominent (greater than 25%) in CED, GWP, and TAP. The major process difference between route 1 and route 2 is the choice of washing agent (methanol for route 1 and water for route 2). Methanol is reported to have considerably higher carbon intensity, energy intensity, and terrestrial acidification intensity (1.46 kg CO_2 eq/kg , 43.7 MJ/kg, and 0.0012 kg SO_2-eq/kg) [63] when compared to water. Consequently, we observe considerable reductions (up to 50%) in CED, GWP, and TAP but marginal changes in the remaining categories by switching the washing agent from methanol to water.

The environmental burdens of UiO-66-NH_2 production are readily alleviated by simply replacing the organic washing agent with water, and a much better environmental performance is achieved by completely eliminating the organic solvents in the production. We did a further comparison between route 1 and route 3 and found significant reductions (up to 91%) on all the environmental metrics when using the aqueous solution-based system (route 3). Such observation can be explained from two aspects. First, the use of the aqueous solution-based system completely eliminates the consumption of organic solvents. Organic solvents, especially DMF, have high environmental burdens in most metrics evaluated in this work. Replacing these organic solvents with water in the UiO-66-NH_2 production completely eliminates their environmental burdens. Next, higher product yield was achieved when using the aqueous solution-based system. Compared with the conventional solvothermal system, the aqueous solution-based system has a product yield of 96% (on mass-based FU) and 36% (on crystallinity-based FU), which is 2-3 times higher than the product yield from the conventional solvothermal system. Higher production yield eventually translates into lower chemical consumptions, which leads to lower environmental burdens. To say the least, even if the product yield is 100% for both systems, which represents the ideal case for both systems, the aqueous solution-based system still has the lowest environmental impacts in all metrics.

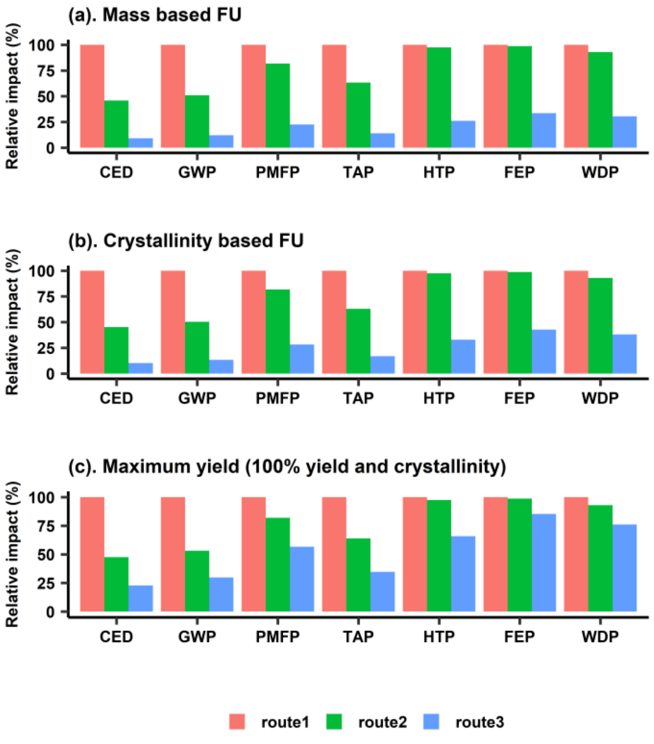

Figure 6. 6. Relative environmental impacts of route 1, conventional solvothermal with methanol for cleaning; route 2, conventional solvothermal system with water for cleaning; and route 3, rapid aqueous system with water for cleaning. Mass based FU, crystallinity-based FU, and maximum yield correspond to product yield of [38%, 18%, 100%] and [96%, 36%, 100%] for the solvothermal system (route 1 and 2) and the aqueous solution-based system

(route 3), respectively. Relative values as regard to the largest value among the three routes, and the absolute values are available in Figure E.1.

Similar to the analysis in Figure 6.5(b) and (c), the overall relative environmental impacts in Figure 6.6 were itemized to identify the contributions of each input to every environmental metric, and the results are shown in Figure 6.7. In general, the environmental impacts associated with route 1 and route 2 have a similar structure, so route 1 and route 2 will be discussed together first. In both route 1 and route 2, the organic solvents, DMF and methanol, are the major or dominating contributor to all the environmental metrics, despite the high recycling rate (90%) assumed for the solvothermal system. In other words, if the DMF and methanol recycle is not considered, as was done in some other works [51], these two organic solvents would possibly contribute to almost 100% of the total environmental impacts of UiO-66-NH_2 production. Beside DMF and methanol, heat has considerable impacts on CED, GWP, PMFM, and TAP, and those impacts are more prominent in route 1 compared to route 2. This observation could be explained from two aspects. On the one hand, heat was assumed to be generated by the natural gas combustion, which has major impacts on CED, GWP, PMFM, and TAP. On the other hand, a large amount of extra heat, as will be discussed later, was required for the methanol recycle in route 1. Compared to the organic solvents and heat, reagents, linker, and Zr precursors have less significant impacts on GWP and CED (less than 20%) but considerable impacts on the remaining metrics. Finally, electricity has negligible impacts on all the categories for the solvothermal system. The environmental impact structure of route 3 is significantly different from that of route 1 or route 2. In route 3, reagents, linker, and Zr precursors have the major shares across all the environmental categories, and together they account for 90-100% of the impacts. Electricity and heat have minor to negligible impacts on all the categories. The results from Figure 6.7 suggest that, as the UiO-

66-NH_2 production is shifted from the conventional solvothermal system to the aqueous solution-based system, the environmental burdens associated with the production are approaching their minimum values, i.e., the limit set by the chemicals.

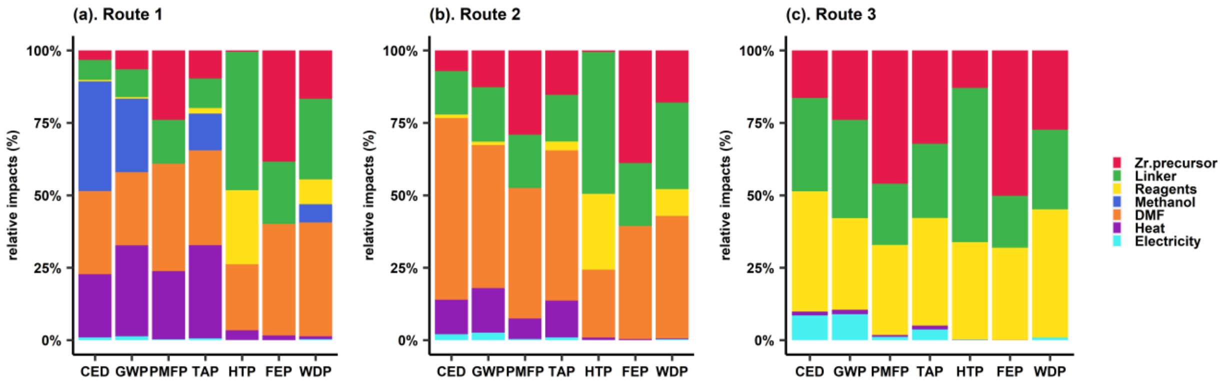

Figure 6. 7. Breakdown of the relative environmental impacts of producing 1 kg UiO-66-NH_2 via route 1, 2, and 3. Chemicals other than the Zr precursors and the linker are merged as “Reagents” in the plot.

Among all the environmental metrics studied in Figure 6.5 through Figure 6.7, CED and GWP are often regarded as the most important metrics since the energy and climate change performances usually gain the most attention in practical chemical productions [80]. As such, the GWP and CED data were plotted with their absolute values in Figure 6.8 to help understand the energy and climate change performances of the Zr precursor production and the UiO-66-NH_2 production. As shown in Figure 6.8(a) and (c), the GWP and CED associated with the two Zr precursors, $ZrOCl_2{\cdot}8H_2O$ and $ZrCl_4$, are comparable, and both precursors have 9-10 kg CO_2 eq/kg GWP and 90-100 MJ/kg CED. The GWP and CED values of the two Zr precursors are not significantly different from those for the Zr source (zircon), which has a 9.4 kg CO_2 eq/kg GWP and an 87.7 MJ/kg CED. The inorganic precursors ($ZrOCl_2{\cdot}8H_2O$ and $ZrCl_4$) have comparable GWP and CED as their first-generation source (zircon), which is likely due to the fact that only inorganic reagents (e.g., Cl_2 and HCl) were used in the precursor manufacturing and these reagents have minor impacts on the GWP and CED. Similar results were reported in other literature that estimated the GWP and CED of different metal precursor (e.g., Ti salt) for nanoparticle synthesis [71, 80]. To the best of our knowledge, few studies on the life cycle impact assessment of different Zr precursors have been conducted, yet we expect a growing need for this analysis as more studies might be done in the future to evaluate the life cycle environmental performances of other Zr-based MOFs/materials. The values calculated in this work could be used when $ZrCl_4$ or $ZrOCl_2 \cdot 8H_2O$ is used to produce UiO-66 derivatives or ZrO_2. When other Zr precursors were to be used, perhaps the data for zircon could be used as a first pass approximation, if no organic reagent is used in the precursor manufacturing. However, if organic reagents are consumed, the manufacturing process needs to be analyzed to get those data, and examples were provided in the Supporting Information of this work.

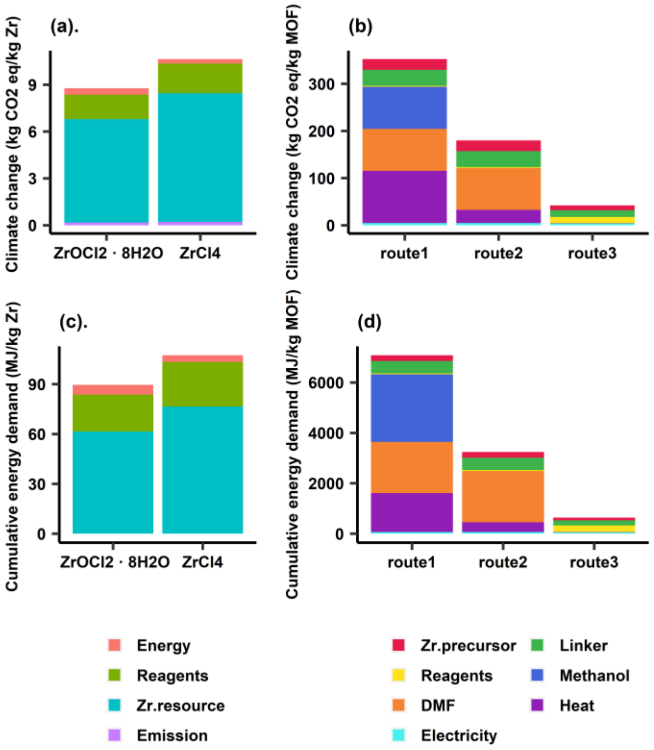

Figure 6. 8. Global warming potential (kg CO_2 eq) for producing (a) 1 kg of Zr precursors and (b) 1 kg of UiO-66-NH_2 and Cumulative energy demand (MJ) for producing (c) 1 kg of Zr precursors and (d) 1 kg of UiO-66-NH_2 (on mass basis). The definition of "Reagents" can be found in Figure 6.5 and 6.7.

In the UiO-66-NH_2 production (Figure 6.8(b) and (d)), the GWP and CED associated with route 1, 2, and 3 are 353, 180, and 43 kg CO_2 eq/kg, and 7080, 3244, and 649 MJ/kg, respectively. For both route 1 and route 2, the same amount of DMF was used and the heat required for DMF recycle is the same. The difference in GWP and CED between route 1 and route 2 came from the methanol consumption and the heat for methanol regeneration. In route 1, 61.3 kg of methanol was assumed to be consumed in the cleaning process, and such consumption eventually translated into a CED of 2677 MJ (energy intensity of 43.7 MJ/kg) and a GWP of 89 kg CO_2 eq (carbon intensity of 1.46 kg CO_2 eq/kg) per 1kg UiO-66-NH_2. Besides methanol, route 1 requires a significant amount of heat to power the organic solvent recovery process. It is estimated that 1182 MJ of heat was consumed, and this amount of heat corresponds to a CED of 1577 MJ (energy intensity of

1.3MJ/MJ) and a GWP of 113 kg CO_2 eq (carbon intensity of 0.094 kg CO_2 eq/kg). By replacing the solvothermal system with the aqueous solution-based system, a substantial reduction of both GWP and CED, up to 88% and 91 %, was observed. The quantitative analysis results here further emphasized the superior environmental performance of the aqueous solution-based system in UiO-66-NH_2 production. If the organic solvents are essential for the synthesis of other MOFs (i.e., if certain chemistry does not work in water), then the following ideas could be considered to alleviate the environmental burdens of the production: (1) replacing the organic solvent with water in the washing step; and (2) recycle/reuse as much organic solvent as possible from the washing step if water cannot be used for cleaning purposes (e.g., HKUST-1 degrades in water over time[81]).

The LCA results in this work are in good agreement with results reported by Grande *et al.* Their study suggested the climate change impacts of producing CPO-27-Ni decreased by two orders of magnitude (from 1136.2 to 12.3 kg CO_2 eq) when an all water-based synthesis and cleaning process was used [51]. However, the results from their study were based on the laboratory-scale batches, where the reutilization of organic solvents and other chemicals were not optimized. Our analysis accounted for the solvent recovery (recycle rate of 90%) and the corresponding energy requirement, so our results are possibly more representative for the pilot/large scale UiO-66-NH_2 production (and perhaps other MOFs production). In summary, our results highlight the high environmental favorability of the aqueous solution-based system in the production of UiO-66-NH_2, and we expect similar outcomes in the production of other MOFs where an aqueous-solution based system could be used.

6.3.2 Techno-economic assessment

The economic profitability of different UiO-66-NH_2 production routes is evaluated by TEA. In TEA, the major metric is the production cost (Figure 6.9), i.e., the minimum selling price of

UiO-66-NH_2 that makes the production breakeven. A breakdown of the production cost (Figure 6.10) and sensitivity analysis (Figure 6.11) is also provided.

As mentioned earlier, Monte Carlo simulation was used to account for the variability associated with market price and process parameters, and the simulated production cost distributions for route 1, 2, and 3 on the mass-based FU are displayed in Figure 6.9(a), (b) and (c), respectively. Across the uncertainty range (e.g., market price, solvent recovery rate, yield, etc.) defined in Table E.14, route 1 has the highest mean production cost (98 \$/kg), with 90% of results from 78 \$/kg to 117 \$/kg. The average production cost of route 2 (66 \$/kg) is slightly lower than that of route 1, with 90% of outcomes from 56 \$/kg to 78 \$/kg. Finally, route 3 has the lowest average production cost (15.8 \$/kg), with 90% of outcomes from 14.2 \$/kg to 17.5 \$/kg. The simulated production cost distributions for route 1, 2, and 3 on crystallinity-based FU and for the ideal case are presented in Figure E.2 and Figure E.3. The mean values of production costs for route 1, 2, and 3 are found to be 196 \$/kg, 131 \$/kg, and 33.8 \$/kg for the crystallinity-based FU, and 44 \$/kg, 32 \$/kg, and 15.5 \$/kg for the ideal case. The economic analysis suggests that, in addition to the superior environmental favorability, the aqueous solution-based system is also much more economically feasible in UiO-66-NH_2 production compared to the conventional solvothermal system, regardless of the yield definition. This result is in good agreement with some of the previous TEA studies on other MOFs. For example, DeSantis *et al.* conducted TEA on several MOF adsorbents, including Mg_2(dobdc), Ni_2(dobdc), HKUST-1 (H_3btc), and MOF-5 (H_2bdc). In their study, significant cost reduction (34-83% reduction) was achieved by replacing the solvothermal synthesis with liquid assisted grinding synthesis or aqueous synthesis [44]. The production cost of UiO-66-NH_2 from the aqueous solution-based system (15.8 \$/kg) is comparable to that of Ni and Mg-based MOFs estimated by DeSantis *et al* (10-20 \$/kg for aqueous synthesis, [yield = 92%]), yet the production cost of UiO-66-NH_2 from the solvothermal system (56 \$/kg to 117 \$/kg) evaluated in our study is higher than the results from DeSantis *et al.* (35 \$/kg to 71 \$/kg). We attributed the higher production cost for the solvothermal system to the low UiO-66-NH_2 yield (38% ± 4%) used in this study, as opposed to the higher product yield (44% - 69%) used by DeSantis *et al.* If the UiO-66-NH_2 yield from the solvothermal system is comparable to the yield of those Ni/Mg-based MOFs, then the production cost should be similar.

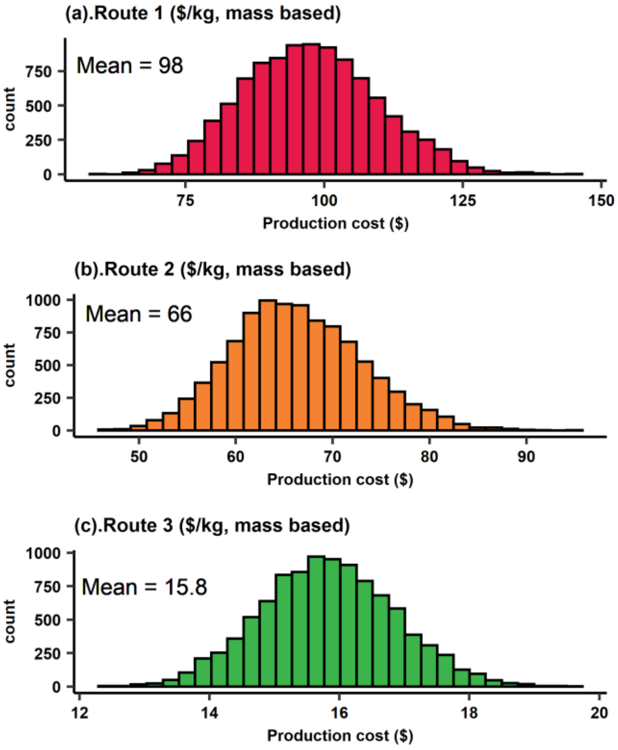

Figure 6. 9. Production cost distributions of UiO-66-NH_2 on mass basis for (a) route 1, (b) route 2 and (c) route 3.

The detailed breakdown of the production cost for UiO-66-NH_2 via route 1, 2, and 3 is displayed in Figure 6.10. The total cost can be broadly categorized into the operating cost and the capital cost (Figure 6.2). The operating cost includes the raw chemicals for linker production, the Zr precursors, other reagents (e.g., HCl), organic solvents (i.e., methanol and DMF), water, and energy consumption (i.e., heat and electricity). The capital cost is taken as the purchasing and installation cost of all pieces of equipment in the project lifetime. Similar to the breakdown of environmental impacts in Figure 6.7, route 1 and route 2 have a similar structure for their total cost, and operating cost is the major contributor, accounting for 82% of the total cost for route 1 and 75% for route 2, respectively. In particular, organic solvents have significant impacts on the operating cost, contributing to 47 $/kg (59%) and $26/kg (43%) of the operating cost for route 1 and 2, respectively. Again, the main difference between the production cost of route 1 and route 2 (i.e., 31 $/kg difference) came from the consumption of methanol and the use of extra heat in methanol recovery, while other parameters are almost identical between the two routes. Such observation reveals the economic favorability of using water as the cleaning agent, even in the solvothermal system. In the aqueous solution-based system, the equipment and linker cost became the major contributor to the total costs, accounting for 5.4 $/kg and 5.7 $/kg of the total cost, respectively. The remaining total cost is shared by other chemicals and energy. Compared to route 1 or route 2, a significant cost reduction (up to 84%) is achieved for route 3. Such observation can be explained from both the operating cost aspect and the capital cost aspect. On the operating cost aspect, the aqueous solution-based system completely eliminates the use of expensive organic solvents, leading to a substantial reduction in terms of the production financial burdens. Additionally, the high UiO-66-NH_2 yield in the aqueous solution-based system allows for lower linker consumptions compared to the solvothermal system (Table 6.1), so therefore the cost for linkers is also minimized (5.7 $/kg in route 3 vs. 19 $/kg in route 1 and route 2). On the capital cost aspect, the cost for the aqueous-solution based system is only one third of that for the solvothermal system, i.e., 5.4 $/kg vs. 17.4 $/kg. This significant saving on the capital cost is a direct outcome of the high STY nature of the aqueous solution-based system in UiO-66-NH_2 production. On the one hand, the precursor concentration in the aqueous solution-based system is much higher than that in the solvothermal system, so the required reactor volume per kg UiO-66-NH_2 is greatly reduced such that the total equipment purchasing cost is reduced. On the other hand, the shortened production time, i.e., 2 hrs in the aqueous solution-based system vs. 24 hrs in the solvothermal system, allows the same production line to produce more batches of UiO-66-NH_2 in its life time, which also reduces the capital cost per FU. It should be noted that we made a rather conservative assumption on the production rate of the aqueous solution-based system (3 batches per day), but this assumption could be relaxed if further evidence supports a higher production rate. In that case, the capital cost associated with the aqueous solution-based system could be further reduced, and route 3 will become more economically favorable. The results from Figure 6.10 suggest that, as the UiO-66-NH_2 production is shifted from the conventional solvothermal system to the aqueous solution-based system, the production economic favorability greatly increased from both the operating cost aspect and the capital cost aspect.

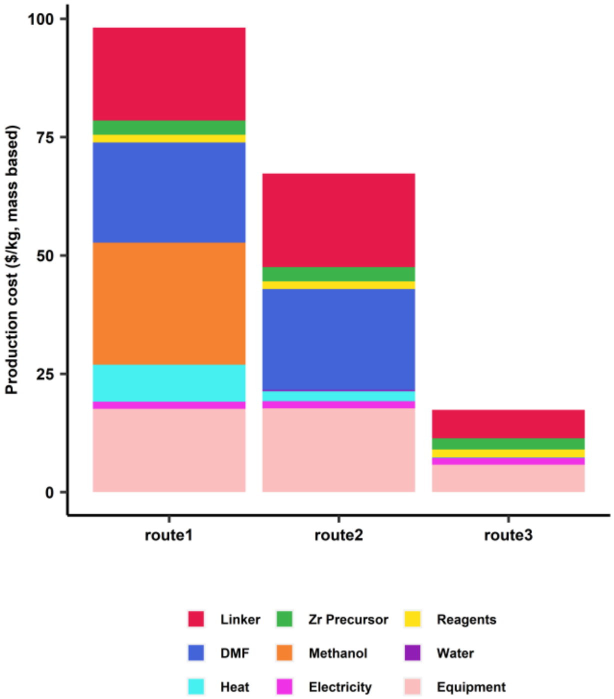

Figure 6. 10. Breakdown of the UiO-66-NH_2 production cost (mass-based FU). The definition of "Reagents" can be found in Figure 6.7.

Finally, a sensitivity analysis was conducted to investigate the variability of key variables (Table E.14) on the production cost, and the top four variables for each route were presented in Figure 6.11. For the solvothermal system, the organic solvent recycle rate is the most sensitive parameter, leading to large changes in production costs. Besides the solvent recycle rate, the market price of organic solvents (i.e., DMF and methanol) is also impactful. This is not surprising, as both solvents recycle rate and market price could directly translate into the solvent costs, which are found to be crucial for the production cost (Figure 6.10). Finally, the MOF yield is also an important variable for solvothermal systems, suggesting that future improvement in the synthesis method might reduce the production cost. As for the aqueous solution-based system, the linker yield and the market price of Pd/C are the most sensitive parameters. Such observation is consistent with the production costs distribution (Figure 6.10), as the cost associated with linker production contributes to 36% of the total cost. The equipment capital costs and equipment lifetime also have appreciable impacts on the production costs, demonstrating that extension of the equipment lifetime and reduction of the capital costs will be effective methods to reduce the production costs of the aqueous system.

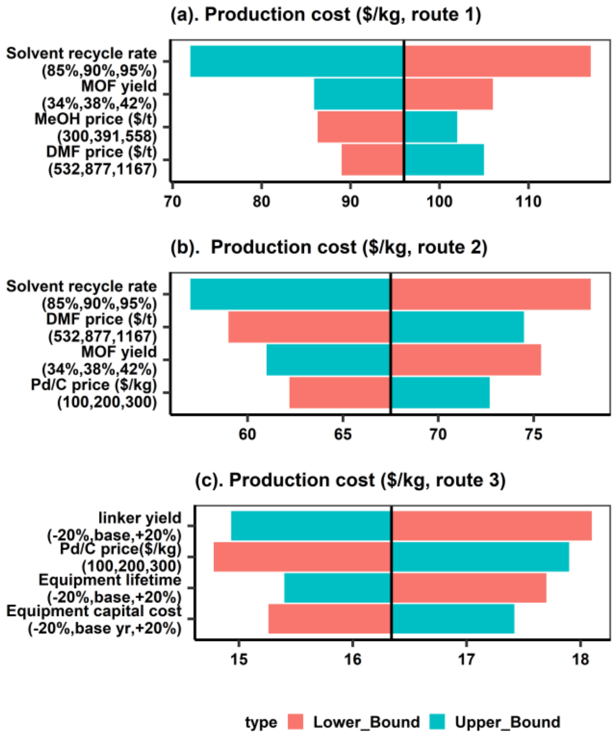

Figure 6. 11. Sensitivity analysis of production costs (mass-based FU).

Our TEA results highlight the high economic favorability of the aqueous solution-based system in the production of UiO-66-NH_2, and these results might extend to the aqueous solution-based production of other MOFs. Together with the LCA results in the previous section, we conclude that the aqueous solution-based production is the most environmentally friendly and economically favorable method of UiO-66-NH_2. In the next section, we will discuss some implications behind the sustainability-related applications of UiO-66-NH_2 based on our LCA-TEA results.

6.3.3 Environmental implications

Recently, UiO-66-NH_2 and other UiO-66 derivatives have attracted a lot of research interests in terms of CO_2 capture and storage, which is a promising route to achieve significant CO_2 reduction in the near term [60]. Both the UiO-66-NH_2 and other UiO-66 derivatives have good stability and moderate CO_2 uptakes, ranging from 60 g/kg to 260 g/kg, therefore previous literature studies have regarded them as a promising tool to mitigate the greenhouse gas [39-43, 54-58]. Such a conclusion might be true if we only look at the gate-to-grave part of the UiO-66-NH_2 life cycle. However, if the cradle-to-gate part of UiO-66-NH_2 life cycle is also included, i.e., if we consider the full life cycle of UiO-66-NH_2, the previous conclusion, that UiO-66-NH_2 is a promising tool to mitigate the GHG emissions, might be subverted, depending on how UiO-66-NH_2 is used in the CO_2 capture and separation. In the following discussions, we will assume the UiO-66-NH_2 is made from the most environmentally friendly route, the aqueous solution-based system, at the base yield (96%). Under this assumption, the GWP value of UiO-66-NH_2 is 43 kg CO_2 eq/kg.

In the simplest case, UiO-66-NH_2 is applied in a single-use manner, and the CO_2 saturated UiO-66-NH_2 is buried such that the adsorbed CO_2 is fixed. In this case, the life-cycle environmental benefit of UiO-66-NH_2 is -0.06 to -0.26 kg CO_2 eq/kg, and is negligible compared to its upstream life-cycle environmental burdens. Hence, if UiO-66-NH_2 is used in this manner, it is not a good candidate to mitigate GHG emissions, especially when comparing to other single-use negative emission technologies (e.g., biochar for carbon sequestration) [82, 83]. Alternatively, UiO-66-NH_2 could be used as an intermediate storage medium for CO_2 capture, i.e., UiO-66-NH_2

is used to concentrate CO_2, in post-combustion CO_2 capture and storage (CCS). In this case, UiO-66-NH_2 could be regenerated and reused, and its life-cycle environmental benefit might exceed its life-cycle environmental burdens. However, regenerating and reusing UiO-66-NH_2 does not guarantee that UiO-66-NH_2 is a better alternative than the current benchmark CCS medium, monoethanolamine (MEA) [84-86], because MEA has a higher CO_2 uptake (364-400 g/kg) [87, 88] and a much lower cradle-to-gate GWP (3.46 kg CO_2 eq/kg) [63]. Indeed, the solvent loss (0.0032 kg MEA/kg CO_2 captured) [60] and energy consumption (3.54 MJ/kg CO_2 captured) [75] associated with MEA regeneration can be concerning factors. It is possibly true that less energy demand and material loss can be achieved to regenerate UiO-66-NH_2 than MEA [89], yet further quantitative analysis is required to determine if the emission reduction in sorbent regeneration could overcome the higher emissions associated with upstream production before claiming UiO-66-NH_2 as a more sustainable alternative for MEA in CCS.

Hence, we computed the cradle to grave life cycle analysis on conventional PC-fired power plant, PC coupled with MEA based CCS, as well as the UiO-66-NH_2 based CCS. The technical summary of three configurations and resulting data were demonstrated in Table 6.3. To reiterate, the life cycle GWP accounts for the direct CO_2 emissions from coal as well as the cradle to gate GWP associated with MEA/UiO-66-NH_2 production, while the solvent/sorbent disposal was not accounted due to the lack of accessible data. Based on the results from Table 6.3, CCS can significantly reduce the direct CO_2 emissions from the power plant. The upstream GHG emissions associated with coal mining, washing, and transportation, on the other hand, are not affected by CCS. As a result, for the MEA-based CCS plant, the upstream GWP associated coal accounts for 38% of the total GWP.

Table 6. 3. Key energy and material flows, and life cycle GWP associated with coal and solvent/sorbent

Parameters	**Base**	**Amine-based CCS**	**MOF based CCS**
Coal input (tonne/h)	210	210	210
CO_2 in the flue gas (tonne/h)	490	490	490
Material loss during CCS (tonne/tonne captured CO_2)	0	0.0032	x (unknown)
Net power output (MW)	608	406	540
Direct CO_2 emissions from coal combustion (tonne CO_2/h)	490	49	49
Upstream GWP associated with coal processing (tonne CO_2 eq/h)	32.4	32.4	32.4
GWP of solvent/sorbent initial loading (tonne CO_2 eq/h)	0	0.02	0.58
GWP of solvent/sorbent losses (tonne CO_2 eq/h)	0	4.87	17647x
Life cycle GWP (tonne CO_2/MWh)	**0.858**	**0.212**	**(49+32.4+0.58+17647x)/540**

Due to the lower heat requirement for sorbent regeneration, the net power output from power plant coupled with MOF-based CCS appears to be higher than that of conventional MEA based CCS. However, the GWP of the two systems remains a challenge to be determined, owing to the lack of data on MOF losses due to the degradation or decomposition. Existing data on MOF degradation was mostly on a lab-scale, and only 4-6 cycles were performed [57, 90], while long-term experimental work on MOF degradation was not yet carried. According to current studies on the reversibility/recyclability of UiO-66-NH_2 and/or other UiO-66 derivatives, the adsorption capacity decreased by 3.6% after 4 cycles [90], and 4% after 6 cycles [55]. Due to the lack of data availability on long-term experimental work, it is not clear if the adsorption capacity will decrease linearly as more adsorption/desorption cycles are performed or remain relatively steady after certain cycles. Here we assumed the MOFs mass loss for capturing 1 tonne CO_2 as an unknown value, and the GWP of electricity from UiO-66-NH_2 based CCS plant was plotted against the material losses and compared to the reference plant without CCS, and MEA-based CCS plant. The corresponding results are shown in Figure 6.12. When the MOF loss is less 0.0017 tonne/tonne captured CO_2, the life cycle GWP of electricity from MOF based CCS plant is lower than GWP of power produced by MEA based CCS plant. As the sorbent loss increases, the environmental burdens associated with UiO-66-NH_2 based CCS increases. When sorbent loss is higher than 0.02 tonne/tonne CO_2 captured, the environmental impacts of UiO-66-NH_2 based CCS system is even higher than the reference power plant without CCS.

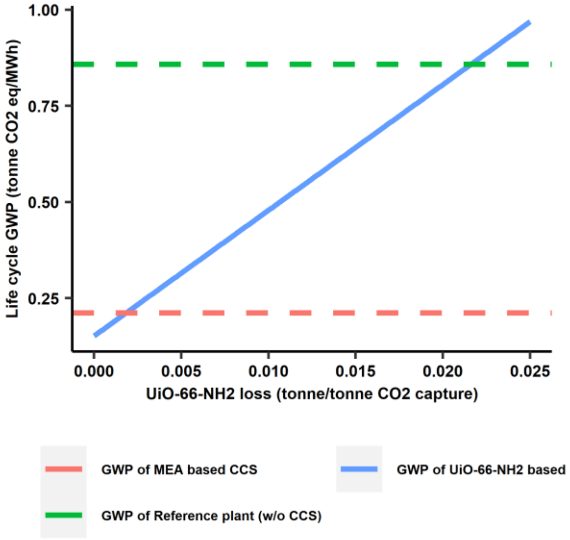

Figure 6. 12. Comparison between the performance of electricity produced from coal-fired plant w/o CCS (green), MEA (red), and UiO-66-NH_2 (blue) based post-combustion CCS plants. For MEA, the upstream GWP is 3.46 kg CO_2 eq/kg, the CO_2 uptake is 0.38 kg CO_2/kg solvent (average of 0.36-0.4) [87, 88], the heat of regeneration is 3.54 MJ/kg CO_2 captured [75], and the solvent loss is 0.0032 kg MEA/kg CO_2 captured [60]. For UiO-66-NH_2, the upstream GWP is 43 kg CO_2 eq/kg, the CO_2 uptake is 0.16 kg CO_2/kg sorbent (average of 0.06-0.26) [39-43, 54-58], the heat of regeneration is assumed to be 30 kJ/mol CO_2 (i.e., 681MJ/tonne CO_2) captured (identical to the heat of sorption) [91]

The discussions above emphasized the importance of considering the cradle-to-gate impacts of UiO-66-NH_2 when it is used in sustainability-related applications. Also, the long-term experimental works on the reversibility/recyclability of MOFs are crucial to determine cradle to grave environmental impacts when it comes to sustainability-related applications. To date, a large variety of materials has been created and used for sustainable purposes, while most research efforts have been focused on gate-to-grave environmental impacts. For those materials, the cradle-to-gate LCA could be implemented to comprehensively evaluate the full life-cycle sustainability.

6.4. Conclusions

In this paper, process-based cradle-to-gate LCA and TEA were carried out to evaluate the life cycle environmental impacts and production costs associated with UiO-66-NH_2 production via the conventional solvothermal system and the aqueous solution-based system on the pilot-scale. The LCA results demonstrate that the aqueous solution-based system has much lower environmental impacts compared to the conventional solvothermal system. The aqueous solution-based system differs from the conventional solvothermal system by using water as the solvent and the cleaning agent. In this regard, the significant environmental burdens associated with organic solvents production and heat required for solvent recovery could be avoided. Furthermore, higher product yield is achieved in the aqueous solution-based system such that less material is consumed and the environmental burdens are lower. Compared with the solvothermal system, the aqueous solution-based system reduces the environmental impacts to up to 91%. A similar trend was observed in the TEA. The production cost of UiO-66-NH_2 from the aqueous solution-based system (14.2 $/kg to 17.5 $/kg) is much lower compared to that from the solvothermal system (56 $/kg to 117 $/kg) due to the significant reduction of operating costs.

Our results reveal UiO-66-NH_2 production from the aqueous solution-based system is significantly more environmentally and economically feasible than the solvothermal system, and we believe this conclusion holds true for other MOFs given the high contributions of organic solvent usage to TEA and LCA metrics. Despite the environment and economic favorability of aqueous system, if UiO-66-NH_2 is applied in sustainability-related areas (e.g., CO_2 capture and storage), further research should be done to investigate if UiO-66-NH_2 could be a better alternative to the existing benchmark (i.e., MEA) via comprehensive cradle-to-grave LCA. Our results demonstrate retrofitting existing coal-fired power plant with CCS can lead to a significant reduction in life cycle GWP. If the material loss of UiO-66-NH_2 is less than 0.0017tonne/captured CO_2, UiO-66-NH_2 based CCS system could be more environmentally friendly than the MEA-based CCS system. However, due to the lack of long-term experimental work on MOF degradation and decomposition, as well as the high production costs, it is apparent there are remaining technical challenges for MOFs to be deployed at scale as an optimal material for CCS.

To the best of our knowledge, this work is the first LCA and TEA study on UiO-66-NH_2 production via different synthesis systems. The findings of this article help identify the most promising approaches for MOFs synthesis at scale. In particular, using aqueous synthesis approaches seems to be eco-friendlier and more cost-effective if possible. Further investigations on UiO-66-NH_2 losses during the CO_2 capture and regeneration processes are encouraged to be done to facilitate the accurate evaluation of using UiO-66-NH_2 for CCS.

6.5 Reference:

1. H. Furukawa, K.E. Cordova, M. O'Keeffe, and O.M. Yaghi, The chemistry and applications of metal-organic frameworks. Science, 2013. **341**(6149). DOI: http://doi.org/10.1126/science.1230444.
2. J.L. Rowsell and O.M. Yaghi, Metal–organic frameworks: a new class of porous materials. Microporous and mesoporous materials, 2004. **73**(1-2): p. 3-14. DOI: https://doi.org/10.1016/j.micromeso.2004.03.034.
3. H.-C. Zhou, J.R. Long, and O.M. Yaghi, Introduction to Metal–Organic Frameworks. Chemical Reviews, 2012. **112**(2): p. 673-674. DOI: https://doi.org/10.1021/cr300014x.
4. F.X.L. i Xamena, A. Abad, A. Corma, and H. Garcia, MOFs as catalysts: Activity, reusability and shape-selectivity of a Pd-containing MOF. Journal of Catalysis, 2007. **250**(2): p. 294-298. DOI: https://doi.org/10.1016/j.jcat.2007.06.004.
5. J. Lee, O.K. Farha, J. Roberts, K.A. Scheidt, S.T. Nguyen, and J.T. Hupp, Metal–organic framework materials as catalysts. Chemical Society Reviews, 2009. **38**(5): p. 1450-1459. DOI: https://doi.org/10.1039/B807080F.

6. X. Wang, J. Zhou, H. Fu, W. Li, X. Fan, G. Xin, J. Zheng, and X. Li, MOF derived catalysts for electrochemical oxygen reduction. Journal of Materials Chemistry A, 2014. **2**(34): p. 14064-14070. DOI: https://doi.org/10.1039/C9CS00906J.
7. E.A. Dolgopolova, A.M. Rice, C.R. Martin, and N.B. Shustova, Photochemistry and photophysics of MOFs: steps towards MOF-based sensing enhancements. Chemical Society Reviews, 2018. **47**(13): p. 4710-4728. DOI: https://doi.org/10.1039/C7CS00861A.
8. L.E. Kreno, K. Leong, O.K. Farha, M. Allendorf, R.P. Van Duyne, and J.T. Hupp, Metal–organic framework materials as chemical sensors. Chemical reviews, 2012. **112**(2): p. 1105-1125. DOI: https://doi.org/10.1021/cr200324t.
9. B. Liu, W.-P. Wu, L. Hou, and Y.-Y. Wang, Four uncommon nanocage-based Ln-MOFs: highly selective luminescent sensing for Cu2+ ions and selective CO2 capture. Chemical Communications, 2014. **50**(63): p. 8731-8734. DOI: https://doi.org/10.1039/C4CC03049D.
10. A. Legrand, A. Pastushenko, V. Lysenko, A. Geloen, E.A. Quadrelli, J. Canivet, and D. Farrusseng, Enhanced Ligand-Based Luminescence in Metal–Organic Framework Sensor. ChemNanoMat, 2016. **2**(9): p. 866-872. DOI: https://doi.org/10.1002/cnma.201600124.
11. M. Dincă and J.R. Long, Hydrogen storage in microporous metal–organic frameworks with exposed metal sites. Angewandte Chemie International Edition, 2008. **47**(36): p. 6766-6779. DOI: https://doi.org/10.1002/anie.200801163.
12. M. Eddaoudi, J. Kim, N. Rosi, D. Vodak, J. Wachter, M. O'Keeffe, and O.M. Yaghi, Systematic design of pore size and functionality in isoreticular MOFs and their application in methane storage. Science, 2002. **295**(5554): p. 469-472. DOI: https://doi.org/10.1126/science.1067208.
13. H. Furukawa and O.M. Yaghi, Storage of hydrogen, methane, and carbon dioxide in highly porous covalent organic frameworks for clean energy applications. Journal of the American Chemical Society, 2009. **131**(25): p. 8875-8883. DOI: https://doi.org/10.1021/ja9015765.
14. B. Panella, M. Hirscher, H. Pütter, and U. Müller, Hydrogen adsorption in metal–organic frameworks: Cu-MOFs and Zn-MOFs compared. Advanced Functional Materials, 2006. **16**(4): p. 520-524. DOI: https://doi.org/10.1002/adfm.200500561.
15. J.L. Rowsell, E.C. Spencer, J. Eckert, J.A. Howard, and O.M. Yaghi, Gas adsorption sites in a large-pore metal-organic framework. Science, 2005. **309**(5739): p. 1350-1354. DOI: https://doi.org/10.1126/science.1113247.
16. N.L. Rosi, J. Eckert, M. Eddaoudi, D.T. Vodak, J. Kim, M. O'Keeffe, and O.M. Yaghi, Hydrogen storage in microporous metal-organic frameworks. Science, 2003. **300**(5622): p. 1127-1129. DOI: https://doi.org/10.1126/science.1083440
17. Z. Zhang, Y. Zhao, Q. Gong, Z. Li, and J. Li, MOFs for CO 2 capture and separation from flue gas mixtures: the effect of multifunctional sites on their adsorption capacity and selectivity. Chemical Communications, 2013. **49**(7): p. 653-661. DOI: https://doi.org/10.1039/C2CC35561B.
18. J.-R. Li, R.J. Kuppler, and H.-C. Zhou, Selective gas adsorption and separation in metal–organic frameworks. Chemical Society Reviews, 2009. **38**(5): p. 1477-1504. DOI: https://doi.org/10.1039/B802426J.
19. T.H. Bae, J.S. Lee, W. Qiu, W.J. Koros, C.W. Jones, and S. Nair, A high-performance gas-separation membrane containing submicrometer-sized metal–organic framework crystals. Angewandte Chemie, 2010. **122**(51): p. 10059-10062. DOI: https://doi.org/10.1002/anie.201006141.

20. R.-B. Lin, S. Xiang, H. Xing, W. Zhou, and B. Chen, Exploration of porous metal–organic frameworks for gas separation and purification. Coordination Chemistry Reviews, 2019. **378**: p. 87-103. DOI: https://doi.org/10.1016/j.ccr.2017.09.027.

21. H. Zhang, J. Hou, Y. Hu, P. Wang, R. Ou, L. Jiang, J.Z. Liu, B.D. Freeman, A.J. Hill, and H. Wang, Ultrafast selective transport of alkali metal ions in metal organic frameworks with subnanometer pores. Science advances, 2018. **4**(2): p. eaaq0066. DOI: http://doi.org/10.1126/sciadv.aaq0066.

22. Y. Guo, Y. Ying, Y. Mao, X. Peng, and B. Chen, Polystyrene sulfonate threaded through a metal–organic framework membrane for fast and selective lithium-ion separation. Angewandte Chemie, 2016. **128**(48): p. 15344-15348. DOI: https://doi.org/10.1002/anie.201607329.

23. X. Li, H. Zhang, P. Wang, J. Hou, J. Lu, C.D. Easton, X. Zhang, M.R. Hill, A.W. Thornton, and J.Z. Liu, Fast and selective fluoride ion conduction in sub-1-nanometer metal-organic framework channels. Nature communications, 2019. **10**(1): p. 1-12. DOI: https://doi.org/10.1038/s41467-019-10420-9.

24. M. Kadhom and B. Deng, Metal-organic frameworks (MOFs) in water filtration membranes for desalination and other applications. Applied Materials Today, 2018. **11**: p. 219-230. DOI: https://doi.org/10.1016/j.apmt.2018.02.008.

25. E. Elsayed, A.-D. Raya, S. Mahmoud, P.A. Anderson, A. Elsayed, and P.G. Youssef, CPO-27 (Ni), aluminium fumarate and MIL-101 (Cr) MOF materials for adsorption water desalination. Desalination, 2017. **406**: p. 25-36. DOI: https://doi.org/10.1016/j.desal.2016.07.030.

26. X. Liu, N.K. Demir, Z. Wu, and K. Li, Highly water-stable zirconium metal–organic framework UiO-66 membranes supported on alumina hollow fibers for desalination. Journal of the American Chemical Society, 2015. **137**(22): p. 6999-7002. DOI: https://doi.org/10.1021/jacs.5b02276.

27. Z. Hu, Y. Chen, and J. Jiang, Zeolitic imidazolate framework-8 as a reverse osmosis membrane for water desalination: insight from molecular simulation. The Journal of chemical physics, 2011. **134**(13): p. 134705. DOI: https://doi.org/10.1063/1.3573902.

28. A. Dhakshinamoorthy, Z. Li, and H. Garcia, Catalysis and photocatalysis by metal organic frameworks. Chemical Society Reviews, 2018. **47**(22): p. 8134-8172. DOI: https://doi.org/10.1039/C8CS00256H.

29. J.-R. Li, J. Sculley, and H.-C. Zhou, Metal–organic frameworks for separations. Chemical reviews, 2012. **112**(2): p. 869-932. DOI: https://doi.org/10.1021/cr200190s.

30. M. Rubio-Martinez, C. Avci-Camur, A.W. Thornton, I. Imaz, D. Maspoch, and M.R. Hill, New synthetic routes towards MOF production at scale. Chemical Society Reviews, 2017. **46**(11): p. 3453-3480. DOI: https://doi.org/10.1039/C7CS00109F.

31. H. Reinsch, S. Waitschat, S.M. Chavan, K.P. Lillerud, and N. Stock, A facile “green” route for scalable batch production and continuous synthesis of zirconium MOFs. European Journal of Inorganic Chemistry, 2016. **2016**(27): p. 4490-4498. DOI: https://doi.org/10.1002/ejic.201600295.

32. A.U. Czaja, N. Trukhan, and U. Müller, Industrial applications of metal–organic frameworks. Chemical Society Reviews, 2009. **38**(5): p. 1284-1293. DOI: https://doi.org/10.1039/B804680H.

33. L. Huelsenbeck, H. Luo, P. Verma, J. Dane, R. Ho, E. Beyer, H. Hall, G.M. Geise, and G. Giri, Generalized Approach for Rapid Aqueous MOF Synthesis by Controlling Solution pH. Crystal Growth & Design, 2020. **20**(10): p. 6787-6795. DOI: https://doi.org/10.1021/acs.cgd.0c00895.

34. A. Polyzoidis, T. Altenburg, M. Schwarzer, S. Loebbecke, and S. Kaskel, Continuous microreactor synthesis of ZIF-8 with high space–time-yield and tunable particle size. Chemical Engineering Journal, 2016. **283**: p. 971-977. DOI: https://doi.org/10.1016/j.cej.2015.08.071.

35. F. Li, C. Duan, H. Zhang, X. Yan, J. Li, and H. Xi, Hierarchically porous metal–organic frameworks: green synthesis and high space-time yield. Industrial & Engineering Chemistry Research, 2018. **57**(28): p. 9136-9143. DOI: https://doi.org/10.1021/acs.iecr.8b00470.

36. R.U. Ayres, Life cycle analysis: A critique. Resources, conservation and recycling, 1995. **14**(3-4): p. 199-223. DOI: https://doi.org/10.1016/0921-3449(95)00017-D.

37. D.F. Ciambrone, *Environmental life cycle analysis*. 1997: CRC Press.

38. A.F. Clarens, E.P. Resurreccion, M.A. White, and L.M. Colosi, Environmental life cycle comparison of algae to other bioenergy feedstocks. Environmental science & technology, 2010. **44**(5): p. 1813-1819. DOI: https://doi.org/10.1021/es902838n.

39. H.R. Abid, H. Tian, H.-M. Ang, M.O. Tade, C.E. Buckley, and S. Wang, Nanosize Zr-metal organic framework (UiO-66) for hydrogen and carbon dioxide storage. Chemical Engineering Journal, 2012. **187**: p. 415-420. DOI: https://doi.org/10.1016/j.cej.2012.01.104.

40. Q. Huang, J. Ding, X. Huang, X. Wei, and W. Wang, Experimental and computational investigation of CO2 capture on mix-ligand metal-organic framework UiO-66. Energy Procedia, 2017. **105**: p. 4395-4401.

41. A. Huang, L. Wan, and J. Caro, Microwave-assisted synthesis of well-shaped UiO-66-NH2 with high CO2 adsorption capacity. Materials Research Bulletin, 2018. **98**: p. 308-313.

42. Y. Jiang, C. Liu, J. Caro, and A. Huang, A new UiO-66-NH2 based mixed-matrix membranes with high CO2/CH4 separation performance. Microporous and Mesoporous Materials, 2019. **274**: p. 203-211.

43. Z. Li, W. Sun, C. Chen, Q. Guo, X. Li, M. Gu, N. Feng, J. Ding, H. Wan, and G. Guan, Deep eutectic solvents appended to UiO-66 type metal organic frameworks: Preserved open metal sites and extra adsorption sites for CO2 capture. Applied Surface Science, 2019. **480**: p. 770-778. DOI: https://doi.org/10.1016/j.apsusc.2019.03.030.

44. D. DeSantis, J.A. Mason, B.D. James, C. Houchins, J.R. Long, and M. Veenstra, Techno-economic analysis of metal–organic frameworks for hydrogen and natural gas storage. Energy & Fuels, 2017. **31**(2): p. 2024-2032. DOI: https://doi.org/10.1021/acs.energyfuels.6b02510.

45. V. Chiodo, G. Zafarana, S. Maisano, S. Freni, and F. Urbani, Pyrolysis of different biomass: Direct comparison among Posidonia Oceanica, Lacustrine Alga and White-Pine. Fuel, 2016. **164**: p. 220-227. DOI: https://doi.org/10.1016/j.fuel.2015.09.093.

46. I. Pakamorė, J. Rousseau, C. Rousseau, E. Monflier, and P.Á. Szilágyi, An ambient-temperature aqueous synthesis of zirconium-based metal–organic frameworks. Green Chemistry, 2018. **20**(23): p. 5292-5298. DOI: https://doi.org/10.1039/C8GC02312C.

47. Y. Pan, Y. Liu, G. Zeng, L. Zhao, and Z. Lai, Rapid synthesis of zeolitic imidazolate framework-8 (ZIF-8) nanocrystals in an aqueous system. Chemical Communications, 2011. **47**(7): p. 2071-2073. DOI: https://doi.org/10.1039/C0CC05002D.

48. Q. Bao, Y. Lou, T. Xing, and J. Chen, Rapid synthesis of zeolitic imidazolate framework-8 (ZIF-8) in aqueous solution via microwave irradiation. Inorganic Chemistry Communications, 2013. **37**: p. 170-173. DOI: https://doi.org/10.1016/j.inoche.2013.09.061.

49. C. Avci-Camur, J. Troyano, J. Pérez-Carvajal, A. Legrand, D. Farrusseng, I. Imaz, and D. Maspoch, Aqueous production of spherical Zr-MOF beads via continuous-flow spray-drying. Green chemistry, 2018. **20**(4): p. 873-878. DOI: https://doi.org/10.1039/C7GC03132G.

50. S. Cadot, L. Veyre, D. Luneau, D. Farrusseng, and E.A. Quadrelli, A water-based and high space-time yield synthetic route to MOF Ni2(dhtp) and its linker 2, 5-dihydroxyterephthalic acid. Journal

of Materials Chemistry A, 2014. **2**(42): p. 17757-17763. DOI: https://doi.org/10.1039/C4TA03066D.

51. C.A. Grande, R. Blom, A. Spjelkavik, V. Moreau, and J. Payet, Life-cycle assessment as a tool for eco-design of metal-organic frameworks (MOFs). Sustainable Materials and Technologies, 2017. **14**: p. 11-18. DOI: https://doi.org/10.1016/j.susmat.2017.10.002.

52. S.G. Subraveti, S. Roussanaly, R. Anantharaman, L. Riboldi, and A. Rajendran, Techno-economic assessment of optimised vacuum swing adsorption for post-combustion CO2 capture from steam-methane reformer flue gas. Separation and Purification Technology, 2021. **256**: p. 117832. DOI: https://doi.org/10.1016/j.seppur.2020.117832.

53. S.M. Moosavi, K.M. Jablonka, and B. Smit, The Role of Machine Learning in the Understanding and Design of Materials. Journal of the American Chemical Society, 2020. **142**(48): p. 20273-20287. DOI: https://doi.org/10.1021/jacs.0c09105.

54. S. Biswas and P. Van Der Voort, A general strategy for the synthesis of functionalised UiO-66 frameworks: characterisation, stability and CO2 adsorption properties. European Journal of Inorganic Chemistry, 2013. **2013**(12): p. 2154-2160. DOI: https://doi.org/10.1002/ejic.201201228.

55. Y. Cao, Y. Zhao, Z. Lv, F. Song, and Q. Zhong, Preparation and enhanced CO2 adsorption capacity of UiO-66/graphene oxide composites. Journal of Industrial and Engineering Chemistry, 2015. **27**: p. 102-107. DOI: https://doi.org/10.1016/j.jiec.2014.12.021.

56. H. Molavi, A. Eskandari, A. Shojaei, and S.A. Mousavi, Enhancing CO2/N2 adsorption selectivity via post-synthetic modification of NH2-UiO-66 (Zr). Microporous and Mesoporous Materials, 2018. **257**: p. 193-201. DOI: https://doi.org/10.1016/j.micromeso.2017.08.043.

57. Y. Cao, H. Zhang, F. Song, T. Huang, J. Ji, Q. Zhong, W. Chu, and Q. Xu, UiO-66-NH2/GO composite: synthesis, characterization and CO2 adsorption performance. Materials, 2018. **11**(4): p. 589. DOI: https://doi.org/10.3390/ma11040589.

58. L. Liu, J. Zhang, H. Fang, L. Chen, and C.Y. Su, Metal–Organic Gel Material Based on UiO-66-NH2 Nanoparticles for Improved Adsorption and Conversion of Carbon Dioxide. Chemistry–An Asian Journal, 2016. **11**(16): p. 2278-2283. DOI: https://doi.org/10.1002/asia.201600698.

59. Z. Guo, H. Li, Y. Li, and F. Dong, *Method for production of high-purity zirconium oxychloride and coproduction of silicon tetrachloride by zircon sand fluidizing chlorination*. 2015, Peop. Rep. China . p. 16pp.

60. N. MacDowell, N. Florin, A. Buchard, J. Hallett, A. Galindo, G. Jackson, C.S. Adjiman, C.K. Williams, N. Shah, and P. Fennell, An overview of CO 2 capture technologies. Energy & Environmental Science, 2010. **3**(11): p. 1645-1669.

61. G. Towler and R. Sinnott, *Chemical engineering design: principles, practice and economics of plant and process design*. 2012: Elsevier.

62. R. Sinnott, *Chemical engineering design*. Vol. 6. 2014: Elsevier.

63. G. Wernet, C. Bauer, B. Steubing, J. Reinhard, E. Moreno-Ruiz, and B. Weidema, The ecoinvent database version 3 (part I): overview and methodology. The International Journal of Life Cycle Assessment, 2016. **21**(9): p. 1218-1230.

64. J. Aguilera-Sigalat and D. Bradshaw, A colloidal water-stable MOF as a broad-range fluorescent pH sensor via post-synthetic modification. Chemical Communications, 2014. **50**(36): p. 4711-4713. DOI: https://doi.org/10.1039/C4CC00659C.

65. B. Yin, B. Huang, X. Fan, Y. Sun, X. Liu, L. He, and Z. Wu, *Zirconium tetrachloride and zirconia preparation process by secondary chlorination*. 2018, Xinjiang Jingshuo New Materials Co., Ltd., Peop. Rep. China . p. 10pp.

66. Y. Sun, C. Chen, J. Wu, Z. Yi, and Y. Zuo, *Crystallization process and device for preparation of zirconyl chloride*. 2003, Guangdong Orient Zirconic Ind Sci and Tech Co., Ltd., Peop. Rep. China . p. 9 pp.

67. J. Chen, C. Shen, L. Fu, and F. Li, *Production method of zirconium oxychloride using membrane treatment technology*. 2018, Longmang Billions Group Co., Ltd., Peop. Rep. China . p. 4pp.

68. M. Li, M. Ge, T. Yu, and Y. Huang, *Method for preparing diazonium salt by depolymerizing waste polyester fibers using ethylene glycol*. 2014, Jiangnan University, Peop. Rep. China . p. 9pp.

69. E.B. Skibo and J.H. Gilchrist, Synthesis and electrochemistry of pyrimidoquinazoline-5, 10-diones. Design of hydrolytically stable high potential quinones and new reductive alkylation systems. The Journal of Organic Chemistry, 1988. **53**(18): p. 4209-4218. DOI: https://doi.org/10.1021/jo00253a010.

70. J.B. Guinée and E. Lindeijer, *Handbook on life cycle assessment: operational guide to the ISO standards*. Vol. 7. 2002: Springer Science & Business Media.

71. F. Wu, Z. Zhou, and A.L. Hicks, Life cycle impact of titanium dioxide nanoparticle synthesis through physical, chemical, and biological routes. Environmental science & technology, 2019. **53**(8): p. 4078-4087.

72. K. Lokesh, A.S. Matharu, I.K. Kookos, D. Ladakis, A. Koutinas, P. Morone, and J. Clark, Hybridised sustainability metrics for use in life cycle assessment of bio-based products: resource efficiency and circularity. Green Chemistry, 2020. **22**(3): p. 803-813. DOI: https://doi.org/10.1039/C9GC02992C.

73. M.A. Huijbregts, Z.J. Steinmann, P.M. Elshout, G. Stam, F. Verones, M. Vieira, M. Zijp, A. Hollander, and R. van Zelm, ReCiPe2016: a harmonised life cycle impact assessment method at midpoint and endpoint level. The International Journal of Life Cycle Assessment, 2017. **22**(2): p. 138-147. DOI: https://doi.org/10.1007/s11367-016-1246-y.

74. R. White, F. Segundo Navarro-Pineda, T. Cockerill, V. Dupont, and J. César Sacramento Rivero, Techno-Economic and Life Cycle Impacts Analysis of Direct Methanation of Glycerol to Bio-Synthetic Natural Gas at a Biodiesel Refinery. Energies, 2019. **12**(4): p. 678. DOI: https://doi.org/10.3390/en12040678.

75. H.C. Mantripragada, H. Zhai, and E.S. Rubin, Boundary Dam or Petra Nova – Which is a better model for CCS energy supply? International Journal of Greenhouse Gas Control, 2019. **82**: p. 59-68. DOI: https://doi.org/10.1016/j.ijggc.2019.01.004.

76. A. Venkatesh, P. Jaramillo, W.M. Griffin, and H.S. Matthews, Uncertainty in Life Cycle Greenhouse Gas Emissions from United States Coal. Energy & Fuels, 2012. **26**(8): p. 4917-4923. DOI: 10.1021/ef300693x.

77. T.A. Adams II, L. Hoseinzade, P.B. Madabhushi, and I.J. Okeke, Comparison of CO2 capture approaches for fossil-based power generation: review and meta-study. Processes, 2017. **5**(3): p. 44. DOI: https://doi.org/10.3390/pr5030044.

78. H. Zhai, Y. Ou, and E.S. Rubin, Opportunities for Decarbonizing Existing U.S. Coal-Fired Power Plants via CO2 Capture, Utilization and Storage. Environmental Science & Technology, 2015. **49**(13): p. 7571-7579. DOI: https://doi.org/10.1021/acs.est.5b01120.

79. J. Koornneef, T. van Keulen, A. Faaij, and W. Turkenburg, Life cycle assessment of a pulverized coal power plant with post-combustion capture, transport and storage of CO2. International Journal of Greenhouse Gas Control, 2008. **2**(4): p. 448-467. DOI: https://doi.org/10.1016/j.ijggc.2008.06.008.

80. P. Caramazana-Gonzalez, P.W. Dunne, M. Gimeno-Fabra, M. Zilka, M. Ticha, B. Stieberova, F. Freiberg, J. McKechnie, and E. Lester, Assessing the life cycle environmental impacts of titania nanoparticle production by continuous flow solvo/hydrothermal syntheses. Green Chemistry, 2017. **19**(6): p. 1536-1547.

81. P. Küsgens, M. Rose, I. Senkovska, H. Fröde, A. Henschel, S. Siegle, and S. Kaskel, Characterization of metal-organic frameworks by water adsorption. Microporous and Mesoporous Materials, 2009. **120**(3): p. 325-330. DOI: https://doi.org/10.1016/j.micromeso.2008.11.020.

82. F. Cheng, H. Luo, and L.M. Colosi, Slow pyrolysis as a platform for negative emissions technology: An integration of machine learning models, life cycle assessment, and economic analysis. Energy Conversion and Management, 2020. **223**: p. 113258. DOI: https://doi.org/10.1016/j.enconman.2020.113258.

83. F. Cheng, M.D. Porter, and L.M. Colosi, Is hydrothermal treatment coupled with carbon capture and storage an energy-producing negative emissions technology? Energy Conversion and Management, 2020. **203**: p. 112252. DOI: https://doi.org/10.1016/j.enconman.2019.112252.

84. R. Idem, M. Wilson, P. Tontiwachwuthikul, A. Chakma, A. Veawab, A. Aroonwilas, and D. Gelowitz, Pilot plant studies of the CO2 capture performance of aqueous MEA and mixed MEA/MDEA solvents at the University of Regina CO2 capture technology development plant and the boundary dam CO2 capture demonstration plant. Industrial & engineering chemistry research, 2006. **45**(8): p. 2414-2420. DOI: https://doi.org/10.1021/ie050569e.

85. D. Singh, E. Croiset, P.L. Douglas, and M.A. Douglas, Techno-economic study of CO2 capture from an existing coal-fired power plant: MEA scrubbing vs. O2/CO2 recycle combustion. Energy conversion and Management, 2003. **44**(19): p. 3073-3091. DOI: https://doi.org/10.1016/S0196-8904(03)00040-2.

86. C. Alie, L. Backham, E. Croiset, and P.L. Douglas, Simulation of CO2 capture using MEA scrubbing: a flowsheet decomposition method. Energy conversion and management, 2005. **46**(3): p. 475-487. DOI: https://doi.org/10.1016/j.enconman.2004.03.003.

87. A.C. Yeh and H. Bai, Comparison of ammonia and monoethanolamine solvents to reduce CO2 greenhouse gas emissions. Science of the Total Environment, 1999. **228**(2-3): p. 121-133.

88. D. Zhu, M. Fang, Z. Lv, Z. Wang, and Z. Luo, Selection of blended solvents for CO2 absorption from coal-fired flue gas. Part 1: Monoethanolamine (MEA)-based solvents. Energy & fuels, 2012. **26**(1): p. 147-153. DOI: https://doi.org/10.1021/ef2011113.

89. C.A. Trickett, A. Helal, B.A. Al-Maythalony, Z.H. Yamani, K.E. Cordova, and O.M. Yaghi, The chemistry of metal–organic frameworks for CO 2 capture, regeneration and conversion. Nature Reviews Materials, 2017. **2**(8): p. 1-16. DOI: https://doi.org/10.1038/natrevmats.2017.45.

90. J. Zhu, L. Wu, Z. Bu, S. Jie, and B.-G. Li, Polyethyleneimine-Modified UiO-66-NH2(Zr) Metal–Organic Frameworks: Preparation and Enhanced CO2 Selective Adsorption. ACS Omega, 2019. **4**(2): p. 3188-3197. DOI: 10.1021/acsomega.8b02319.

91. Y. Huang, W. Qin, Z. Li, and Y. Li, Enhanced stability and CO 2 affinity of a UiO-66 type metal–organic framework decorated with dimethyl groups. Dalton Transactions, 2012. **41**(31): p. 9283-9285. DOI: https://doi.org/10.1039/C2DT30950E.

Chapter 7. Aqueous Solution-based Synthesis of UiO-66-NH_2/Poly(L-DOPA)@PVDF Mixed Matrix Membranes and Their Ion Transport Properties

7.1 General Motivations

Metal-organic frameworks (MOFs) are a new class of materials, consisting of metal ions or clusters coordinated with organic linkers. MOFs are known for their high porosity and high degree of chemical/structural tunability.[1–3] An attractive feature of MOFs is their uniform and tunable pore size, which can be utilized for selective size-based small molecule separation.[4] For example, ZIF-8 [5] has a nominal pore radius lager than water molecule radius and smaller than hydrated ion (e.g., Na^+ and Cl^-) radius and is therefore a promising material for desalination applications.[6,7] Moreover, UiO-66-R (R= - H, -NH_2, -OH, etc.) has a tunable pore radius (based on the R group) [8,9] that is generally similar to the radius of some hydrate alkali/alkali earth metal ions (e.g., Li^+, Na^+, Mg^{2+}). [10] As such, UiO-66-R is suitable for selective ion separations and will be the MOFs used in the proposed work.

The particulate nature of UiO-66-R hinders its ability to form free-standing self-supporting films for separation applications, so therefore, porous membrane supports are required to fabricate UiO-66-R containing mixed matrix membranes (MMMs).[11–13] In the typical solvothermal fabrication of MMMs, porous Al_2O_3 membranes are heated in a DMF precursor solution of UiO-66-R (e.g., $ZrCl_4$ and terephthalic acid) for 24 to 48 h in an autoclave, and UiO-66-R attaches to the membrane surface by heterogeneous nucleation.[10,14,15] The resulting MMMs have high surface coverage of UiO-66-R, and good morphology control over the UiO-66-R crystals are achieved in this process. [10,14,15] This Al_2O_3-DMF solvothermal system, although widely used, has several drawbacks that limit its application for large scale fabrication of UiO-66-R containing MMMs. First, the porous Al_2O_3 membranes are brittle, and any uneven force encountered could potentially result in membrane failure (i.e., small cracks can lead to 100% loss of selectivity). Second, using DMF limits the options for replacing brittle Al_2O_3 with porous polymeric membranes (e.g., polysulfone (PSf), polyethersulfone (PES) and polyvinylidene fluoride (PVDF)), because many membrane materials are soluble in DMF. Finally, this solvothermal synthesis is not suitable for continuous large-scale fabrication of MMMs because it is usually carried out in sealed pressurized containers (i.e., the synthesis has a batch nature). Therefore, developing alternative synthesis conditions for facile UiO-66-R containing MMMs fabrication is a pressing engineering challenge that must be resolved before these MMMs can be commercialized and further adapted in separations.

Recently, Huelsenbeck *et al.* developed an aqueous solution-based system for rapid UiO-66-R (R= -H, $-NH_2$) synthesis.[16] Uniquely in this system, the zirconium oxo cluster [8,9] (the secondary building units (SBUs) for UiO-66-R) formation and the linker deprotonation are performed in separate aqueous solutions, and the UiO-66-R forms instantaneously after mixing the two solutions together. Compared to the DMF solvothermal synthesis, the new synthesis method can be applied to more polymeric membranes as the membranes used for ion separations are fully compatible with water. Nevertheless, the instantaneous formation of UiO-66-R has the potential to be developed into a continuous MMMs fabrication process. As such, this system is chosen to be the platform of the proposed work.

7.2 Transport Scenario Analysis

Although the aqueous solution-based system for rapid UiO-66 derivatives synthesis is favorable from the commercialization aspect and the environmental impact aspect, this synthesis technique still faces some challenges in achieving good ion selectivity. In the traditional DMF solvothermal synthesis, the reactions rate is slow enough so the SBUs have enough time to adhere to the membrane surface even in the absence of specific binding sites.[10,14,15] However, in the novel rapid synthesis, the reaction often completes in few seconds, so the adhesion of UiO-66 derivatives to the membrane surface will be poor in the absence of specific binding sites. The difference in adhesion results in different packing of UiO-66 derivatives on the membrane surface and/or in the membrane pores, and such packing differences lead to different transport scenarios. Four representative transport scenarios (Figure 7.1) are discussed below.

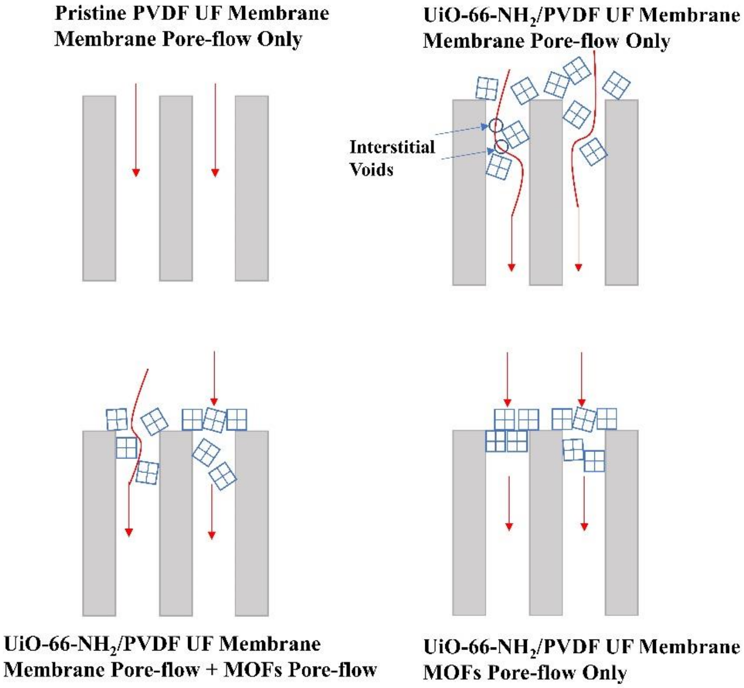

Figure 7. 1. Possible ion transport mechanisms in the UiO-66-NH2/PVDF MMMs. In pristine PVDF UF membranes (top-left case), the transport is achieved by membrane pore-flow. In UiO-66-NH$_2$/PVDF UF membranes (top-right case through bottom right case), the transport could be achieved by membrane pore-flow (top-right case), membrane pore-flow and MOFs pore-flow (bottom-left case) or MOFs pore-flow. The exact transport mechanism in UiO-66-NH$_2$/PVDF UF membranes depends on the packing of UiO-66-NH$_2$ particles in the membrane pores and/or on the membrane surface.

In the pure PVDF ultrafiltration (UF) membranes, the ion transport occurs through the interconnected membrane pores (Figure 7.1 top-left case). The surface chemistry of the PVDF membrane pores is not expected to affect ion selectivity, and indeed, the PVDF UF K^+/Li^+ membrane selectivity, measured to be 1.45, is identical to the bulk solution diffusivity selectivity.[17] In the UiO-66-NH_2/PVDF MMMs, the ion transport mechanism is highly related to the packing of UiO-66-NH_2 particles on the membrane surface and/or inside the membrane pores. If the UiO-66-NH_2 particles are poorly packed (Figure 7.1 top-right case), the particle-particle and/or particle-polymer interstitial space size is much greater than the UiO-66-NH_2 pore size. In this case, the UiO-66-NH_2 particles are present in the MMMs, but mass transport through the interstitial space dominates over transport through the MOF, so the MOF primarily takes up space relative to the no MOF case. If the UiO-66-NH2 are closely packed (Figure 7.1 bottom-left case), the particle-particle and/or particle-polymer interstitial space size is comparable to the UiO-66-NH_2 pore size). In this case, the UiO-66-NH_2 particles in the MMMs starts to provide additional size-based selectivity because the ion transport occurs through both interstitial space and UiO-66-NH_2 pores. Finally, if the UiO-66-NH_2 particles occupy all the membrane pores or cover the membrane surface (Figure 7.1 bottom-right case), the ion transport is achieved solely by diffusion through the UiO-66-NH_2 pores, and the highest ion selectivity could be achieved. This selectivity is equivalent to the intrinsic ion selectivity of the UiO-66-NH_2. It should be noted that analysis above did not consider the defects in UiO-66-NH2 particles. If defects are formed in the UiO-66-NH_2 particles, the ion selectivity will be compromised. For example, in the Figure 7.1 bottom-right case, if the UiO-66-NH_2 particles are defective, the ion transport situation might fall between the Figure 7.1. bottom-left case and the Figure 7.1. bottom-right case depending on the defect size and concentration.

The ion selectivity of the MMMs could be improved by enhancing the MOFs-polymer interactions (i.e., the membrane surface and or the pore surface could be functionalized to bind strongly with the MOFs). In a recent study, porous polyethylene terephthalate (PET) membranes were treated with NaOH solution to create carboxylic acid terminated membrane pore surface.[18] These carboxylic acid groups bound favorably to the zirconium oxo clusters to create growth sites for UiO-66-NH_2 on the pore surface, which caused the membrane pores to be completely filled with UiO-66-NH_2 particles. As such, the ion transport in these UiO-66-NH_2@PET MMMs occurred through the UiO-66-NH_2 pores, and high anion selectivity was reported. Similar design criteria will be introduced to the proposed work, where the commercially available PVDF UF membranes will be modified with levodopa (L-DOPA) to make poly(L-DOPA)@PVDF membranes.

7.3 Experimental Methods

7.3.1 Functionalization of the PVDF Membrane by poly(L-DOPA) Deposition

In the previous transport mechanism analysis, it is expected that the highest selectivity to be achieved when UiO-66-NH_2 crystals could fully cover the membrane surface or fill the membrane pores. Therefore, it is desired to initiate the nucleation and growth of UiO-66-NH_2 from the membrane surface or the membrane pore surface so the UiO-66-NH_2 crystals would adhere tightly to the membrane/membrane pore surface. However, the surface chemistry of the pristine PVDF UF membranes is considered as inert to both the zirconium-oxo cluster and the 2-aminoterephalitic acid linker, so therefore, initiating nucleation and growth from the membrane surface or the membrane pore surface is difficult. Hence, the surface of the pristine PVDF UF membranes need to be modified to create carboxylic acid groups as anchoring sites for the nucleation and growth of UiO-66-NH_2.

The typical experimental procedures are summarized as follows. A 15 mM Tris buffer solution was prepared by dissolving 0.03 g of NaOH and 1 mL 1.5 M Tris-HCl solution (pH = 8.8) in 99 mL DI water. The L-DOPA coating solution was then prepared by dissolving 200 mg of L-DOPA powder in the 15 mM Tris buffer solution (2 mg L-DOPA/mL solution). A 9 cm × 9 cm piece of PVDF membrane was cut from the membrane roll and soaked in DI water overnight to get fully hydrated. The hydrated membrane piece was then sandwiched between two 12 cm × 12 cm silicone pads, and the silicone pad on the top has an 8 cm × 8 cm opening. The sandwiched sample was further sandwiched between two 12 cm × 12 cm PTFE plates, and the PTFE plate on the top also has an 8 cm × 8 cm opening. This custom PTFE mold was tightened by 8 set of screws (Figure 7.2). The L-DOPA coating solution will then be poured onto the PVDF membrane in the custom Teflon mold, and the mold subsequently placed on an orbital shaker (shaking speeding = 20 rpm). After 12 h of coating at 26±1 °C , the poly(L-DOPA) solution was drained by a pipette. The membrane was washed by both water and ethanol to remove any residual L-DOPA and weakly attached poly(L-DOPA) and was stored in DI water till further modifications and/or characterizations. It should be noted that, during the coating process, the coating solution turned from light orange to black, and the membrane surface turned from white to dark brown. An illustration of the coating process is presented in Figure 7.3.

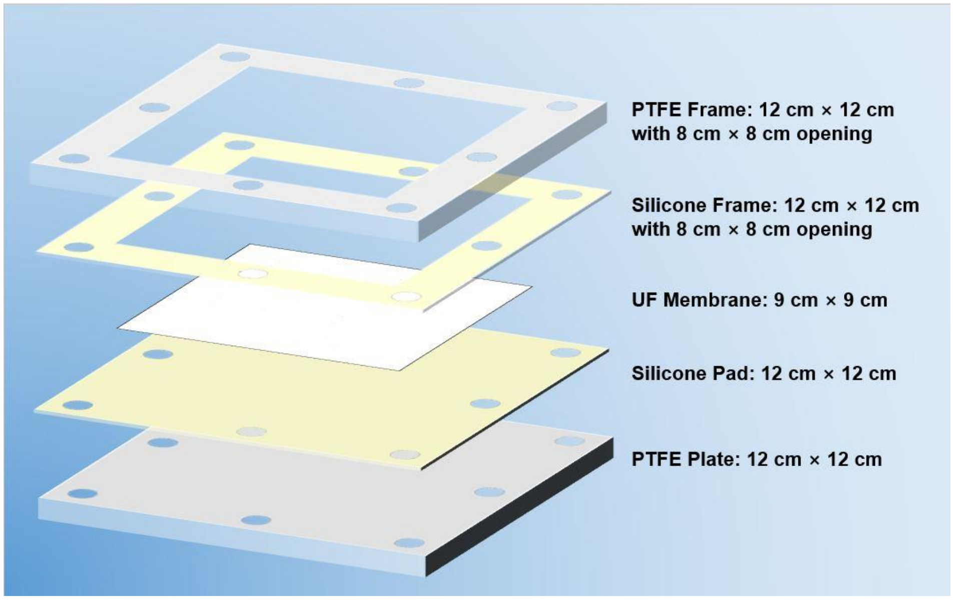

Figure 7. 2 Structure of the custom PTFE mold for reactions. The reaction area of the membrane is 64 cm^2.

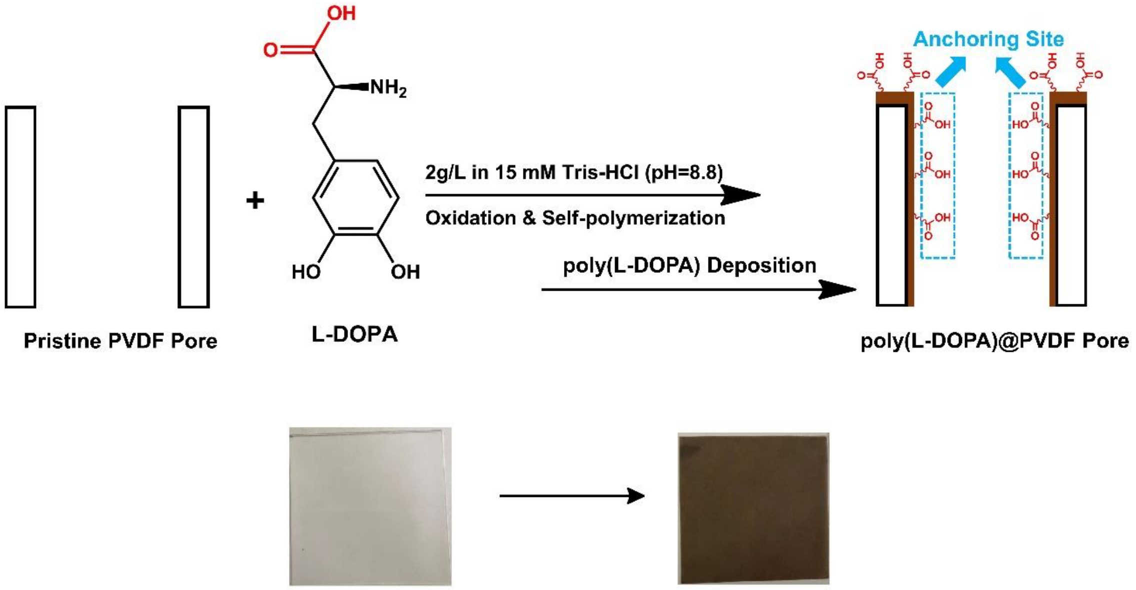

Figure 7. 3 Modification of the PVDF UF membrane by poly(L-DOPA) deposition. In a basic solution, the presence of dissolved oxygen initiated the oxidation and self-polymerization of DOPA, and the product poly(L-DOPA) slowly deposited onto the membrane surface. At the end of the coating process, both the membrane surface and the membrane pore surface were terminated in carboxylic acid groups, and these groups would serve as anchoring sites for the nucleation and growth of UiO-66-NH_2 in the subsequent modifications.

7.3.2 Synthesis of the UiO-66-NH_2/poly(L-DOPA)@PVDF Mixed Matrix Membranes

In a recent work by Huelsenbeck *et al.*, an aqueous solution-based reaction system was developed for rapid synthesis of UiO-66 derivatives.[16] In this reaction system, a metal (node) solution and a linker solution were prepared separately, and the two solutions were subsequently mixed to produce UiO-66 derivatives. Huelsenbeck *et al.* further combined this synthesis technique with sequential dip coating (SQD) to fabricate UiO-66 derivative on different fiber substrates. Based on their experience, a layer-by-layer (LbL) synthesis method will be used in this project.

The typical synthesis conditions are summarized below. To prepare the metal node (e.g., zirconium oxo cluster) solution, 2.576 g zirconyl chloride octahydrate ($ZrOCl_2{\cdot}8H_2O$), 10 mL acetic acid (AcOH) and 24 mL DI water were first mixed in a 100 mL glass beaker to form a transparent solution. This solution was autoclaved at 70 °C in a convection oven for 2 h. After the solution cooled down to room temperature, the solution was transferred into another glass beaker, and Na_2CO_3 was slowly added to the solution till the solution pH reaches 4.5.[19] To prepare the linker solution, 1.448 g 2-aminoterephthalic acid (2-ATA) and 0.64 g NaOH were co-dissolved in 40 mL DI water. A 9 cm × 9 cm piece of poly(L-DOPA) modified PVDF membrane was placed in the PTFE mold described earlier, and the residual water on the membrane surface will be gently removed using a laboratory wipe. The membrane was then rinsed with the metal solution for 1 min, rinsed with DI water for 30 s and rinsed with the linker solution for another 1 min. After one metal solution rinse and one linker solution rinse, the membrane surface was washed with DI water to remove any unattached particles. The process of one metal solution rinse, one linker solution rinse is referred to as one cycle. The LbL synthesis will be repeated up to 10 cycles (1, 3, 5, 7, 9 and 10 cycles), and the final UiO-66-NH_2 loaded poly(L-DOPA) modified PVDF membranes were be labelled by the number of growth cycles. For example, if the growth was repeated for 3 cycles for a membrane, then this membrane was named as “Cycle 3”. When the LbL synthesis was done, the membranes were stored in DI water till further characterizations.

7.3.3 Salt Permeance Measurements

Salt permeance, *B*, was measured from direct permeation experiment on a custom dual chamber permeation cell (Figure 7.4).[20] The general experimental procedures are summarized below. Prior to the experiment, the membrane samples were taken out from DI water and cut into 3 cm ×3 cm squares, and the residual water on sample surface was gently removed using a laboratory wipe. This sample was then sandwiched between two silicone pads with pre-defined 2 cm diameter openings, and the sandwiched sample was carefully placed in between the donating-cell and the receiving-cell such that the openings on the silicone pads and on the cells were perfectly aligned. In all experiments, the functionalized PVDF surface was facing the donating-solution and the PET backing was facing the receiving solution. At the beginning of the experiment, the donating-cell was charged with 150 mL of 0.1 M salt solution, and the receiving-cell was charged with 150 mL DI water. The solution in both cells was stirred at 420 rpm using overhead mechanical stirrers to homogenize the solution. A DDSJ 308F conductivity meter was inserted into the receiving solution to keep track of the change in solution conductivity over time, and the solution conductivity was translated into the solution salt concentration at the end of each experiment using the corresponding calibration curves. Finally, B was calculated as:

$$\ln\left[1 - 2\frac{C_R(t)}{C_D(0)}\right]\left[-\frac{V}{2A}\right] = Bt \qquad (1)$$

where $C_R(t)$ is the receiving-cell salt concentration at time t, $C_D(0)$ is the initial donating-cell salt concentration (0.1 M), V is the solution volume in each cell (150 mL), and A is the effective transport area (3.14 cm^2). Under the pseudo-steady-state analysis, a linear line was obtained by plotting $\ln\left[1 - 2\frac{C_R(t)}{C_D(0)}\right]\left[-\frac{V}{2A}\right]$ against t, and the slope for this line is B (Eqn. (1)).

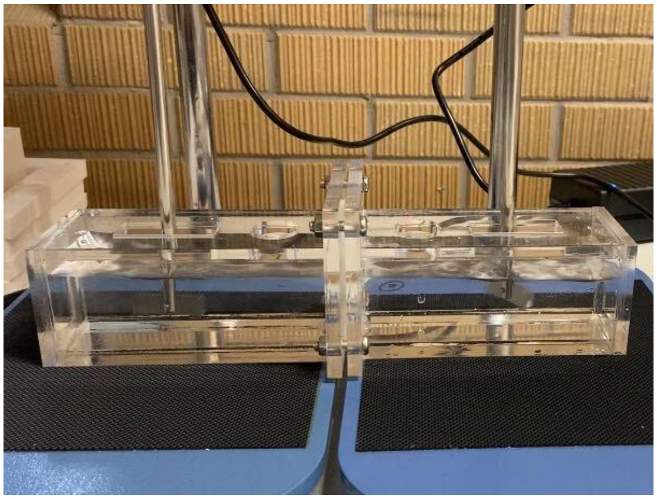

Figure 7. 4 General setups for direct permeation experiments. The donating-cell is on the left side, and the receiving-cell in on the right side. The conductivity meter (not pictured) is inserted into the receiving-cell to track the change in solution conductivity during the experiments.

7.3.4 Instrumental Analysis

Fourier Transform-Infrared Spectroscopy (FTIR) and X-ray Diffraction (XRD) were used to verify the presence of UiO-66-NH_2 on the membranes. Thermalgravimetric Analysis (TGA) and Surface Analysis (SA) were used to investigate the quality of the obtained UiO-66-NH_2 phase. Scanning Electron Microscope (SEM) was used to study the morphology of the UiO-66-NH_2 phase.

7.4 Results and Discussions

7.4.1 Salt Permeance and Salt Selectivity

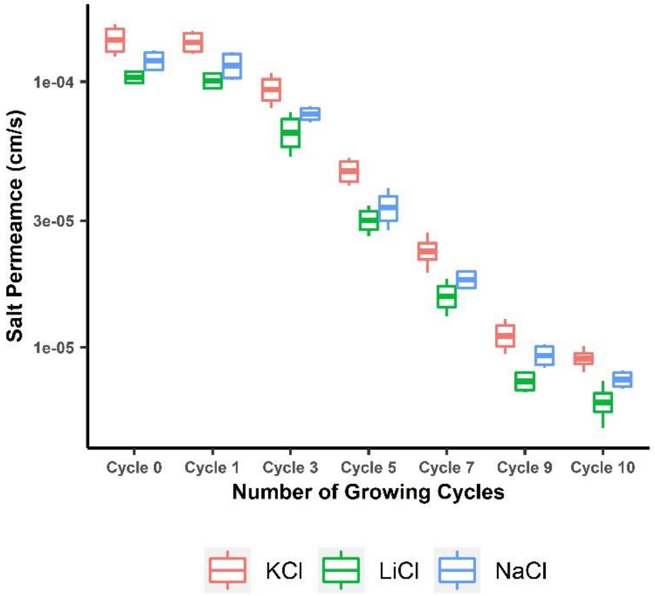

Figure 7. 5 Membrane salt permeance results as a function of the number of UiO-66-NH_2 growing cycles. For each membrane-salt pair, six direct permeation tests were conducted to maximize the statistical confidence of the results. All the tests were carried out at 299±1 K, using 0.5 M salt solutions as the donors.

As shown in Figure 7.5, the membrane salt permeance decreased monotonically as more UiO-66-NH_2 particles were loaded, for all salt tested, and the salt permeance reduction was as high as 94% when the UiO-66-NH_2 growth was repeated for 10 cycles. The salt permeance reduction could be explained with the serial-resistance model for mass transfer. [21] When the membrane is covered by a layer of less permeable materials, i.e., UiO-66-NH_2 in this work, the overall mass transfer resistance is largely determined by the covering layer, and the overall salt permeance decreased as the layer gets thicker, i.e., more growing cycles performed. Furthermore, the salt permeance reduction did not vary linearly with the increase in the number of growing cycles, and an initial lag (cycle 0 to cycle 1) and a possible final plateau (cycle 9 to cycle 10) were observed. Such observations were related to the growing manner of UiO-66-NH_2 on the membrane. When the cycle number was low, i.e., below 3 cycles, the UiO-66-NH_2 might not be able to cover the whole membrane surface, so the membrane salt permeance did not change dramatically. When the cycle number was high, i.e., above 9 cycles, the adhesion of newly formed UiO-66-NH_2 particles to the existing layer might be weak, thus the increase in mass transfer resistance is minimal and the membrane salt permeance did not decrease further. In dense polymeric membranes, the decrease in membrane salt permeability is often correlated with the increase in the membrane salt selectivity.[22,23] However, for the membrane composites considered in this work, the conclusion above might not be true. For example, if the UiO-66-NH_2 layer has defects (e.g., 4 nm voids compared to the 1 nm UiO-66-NH_2 pores), the transport of ions is more preferable through the non-selective defects than through the selective pores due to the lower mass transfer resistance. Hence, the membrane salt selectivity values were calculated by normalizing the membrane salt permeance over membrane LiCl permeance, and the results were presented in Figure 7.6.

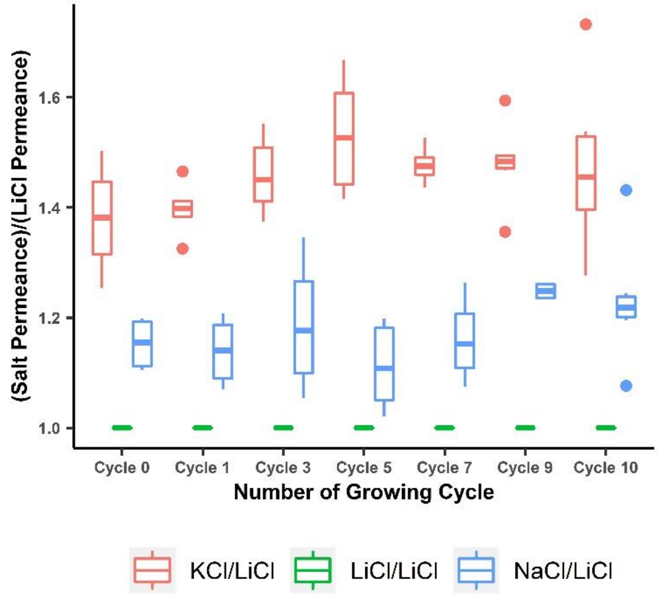

Figure 7. 6 Membrane salt selectivity as a function of the number of UiO-66-NH_2 growing cycles.

As shown in Figure 7.6, the control membrane (Cycle 0 sample) has a KCl/LiCl selectivity of 1.38 and a NaCl/LiCl selectivity of 1.17, and these two salt selectivity values are close to the corresponding solution diffusivity selectivity values. Therefore, the control membrane did not provide additional salt selectivity for the salt pairs analyzed in this work. The UiO-66-NH_2 loaded membranes, from Cycle 1 to Cycle 10, did not show statistical difference in their salt selectivity values when compared to the control membrane (i.e., Cycle 0). Hence, the active layer of UiO-66-NH_2 is defective, according to the analysis in the previous section, and the defects could originate from two sources, the defects within UiO-66-NH_2 particles and/or the voids between adjacent UiO-66-NH_2 particles. In Section 2, comprehensive instrumental analysis results will be presented and interpreted to identify which type(s) of defects existed in the UiO-66-NH_2 active layer.

7.4.2 Instrumental Analysis Results

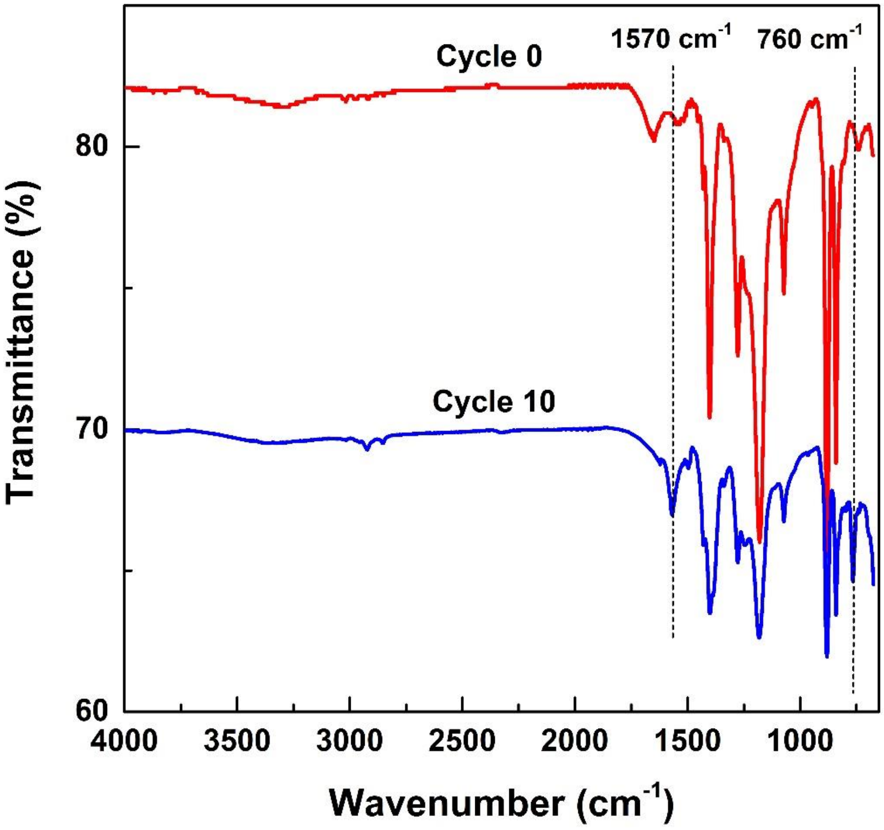

Figure 7. 7 FTIR spectra for the Cycle 0 sample and the Cycle 10 sample. The measurement resolution was fixed at 4 cm^{-1}.

As shown in Figure 7.7, two major peaks, locating at 1570 cm^{-1} and 760 cm^{-1}, were found in the spectrum for the Cycle 10 sample. Hence, after 10 cycles of repeated growth, the bonding pattern that exists in the UiO-66-NH_2 was found on the membrane, which indicates that UiO-66-NH_2 might form successfully.[24,25] However, it is still possible that the obtained phase was an amorphous zirconium-carboxylate coordination polymer, so further XRD characterization was carried out.

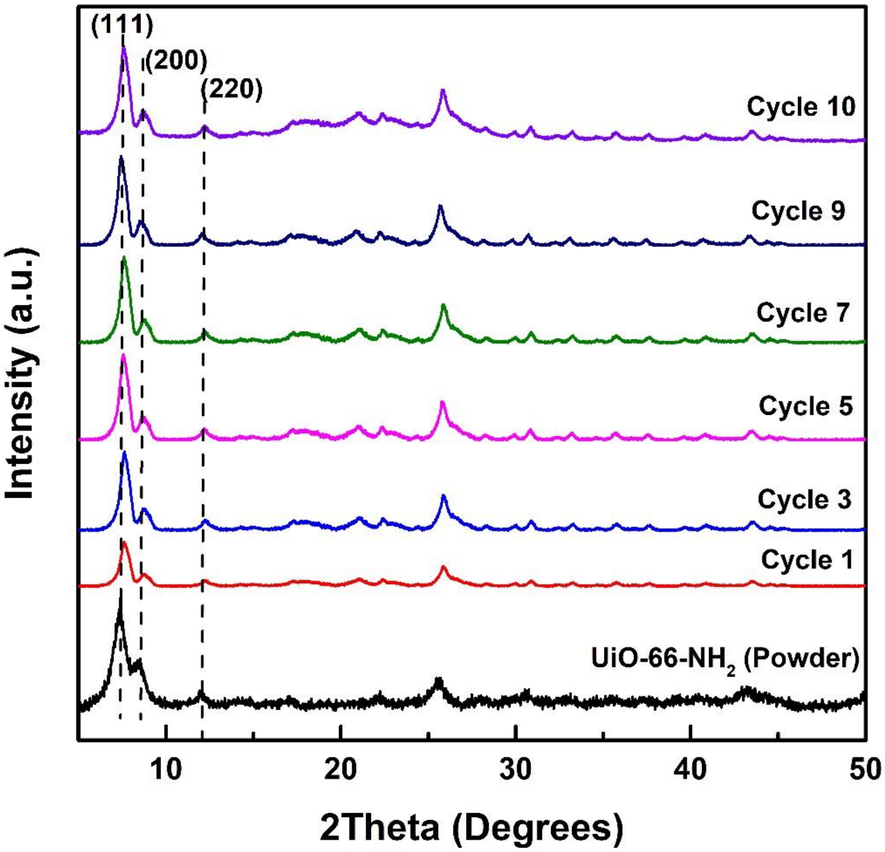

Figure 7. 8 XRD patterns for the UiO-66-NH_2 powder and the Cycle samples. The measurement resolution was fixed at 0.02°.

In the above XRD patterns, three major peaks for UiO-66-NH_2, locating at 7.5°, 9°, and 12.5°, were found in all samples. These peaks correspond to the 111, 200, and 220 planes of UiO-66-NH_2, respectively.[16,26,27] For all samples investigated, the diffraction peaks were not sharp or intense, which indicates that small particles were presented in the UiO-66-NH_2 phase. Furthermore, the peak intensity for the Cycle 1 sample was even lower compared to that for any other sample analyzed, and such low peak intensity is due to the low surface coverage of UiO-66-NH_2 in the Cycle 1 sample, which was also confirmed by the ion transport tests in the previous section. The XRD results confirmed the obtained phase was UiO-66-NH_2, yet it could not provide more insights on the defects in/between UiO-66-NH_2 particles. Therefore, TGA, SA and SEM were conducted.

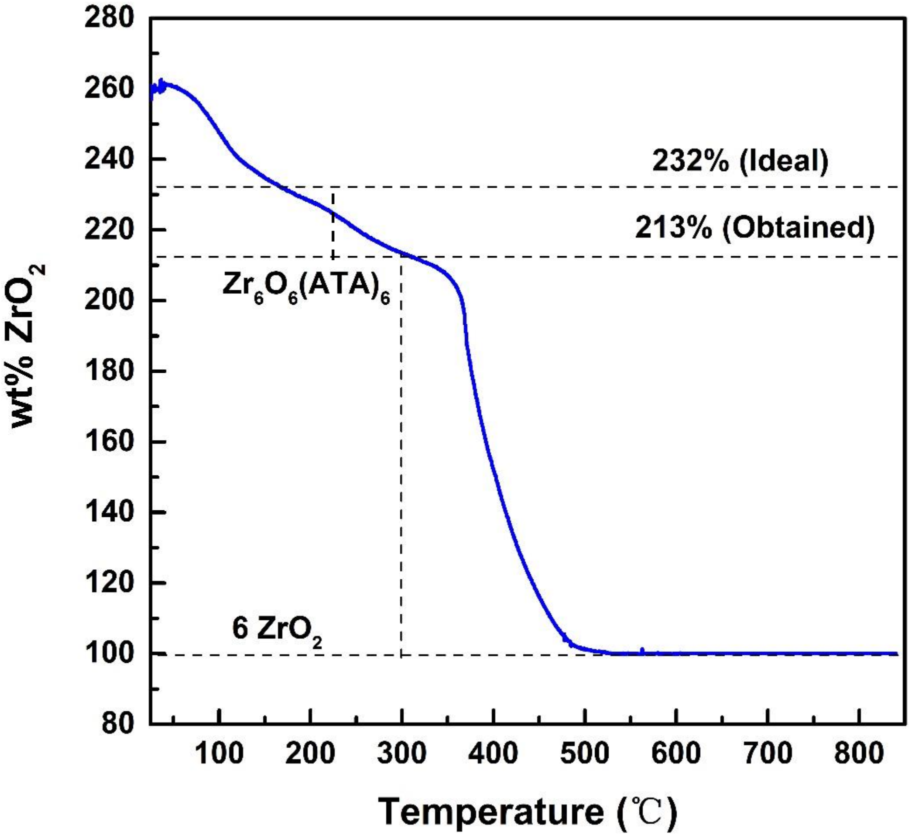

Figure 7. 9 TGA curve of the UiO-66-NH_2 powder obtained from the repeated growth method. The TGA test was carried out in air, and the heating rate was fixed at 10 °C/min.

The decomposition of UiO-66-NH_2 in air is a three-stage process.[16] First, the trapped solvent, i.e., H_2O in this work, was evacuated from the pores at low temperature, i.e., below 150 °C. Next, dehyroxylation occurred at moderate temperature, i.e., between 150 and 300 °C, and UiO-66-NH_2 was converted into $Zr_6O_6(ATA)_6$ at 300 °C. Finally, complete oxidation-decomposition took place at high temperature, i.e., above 300 °C, and $Zr_6O_6(ATA)_6$ was fully oxidized into ZrO_2, N_2, CO_2 and H_2O at 600 °C. The TGA curve in Figure 7.5 was generated by setting the ZrO_2 weight (ash weight) to 100% and normalizing the sample mass with this value. If the UiO-66-NH_2 is defect free, then the normalized sample weight at 300 °C should be 232%.[16,27] However, the normalized sample weight for the obtained UiO-66-NH_2 was 213% at the same temperature, so the obtained sample has missing linker defects. The number of missing linkers was further calculated, and on average 1.6 linkers (out of the 12 linkers) were missing per metal cluster. The TGA results indicate that the UiO-66-NH_2 obtained from the repeated growth method was slightly defective,[16] so SA was conducted to study the potential influence of the defects on the sample surface area.

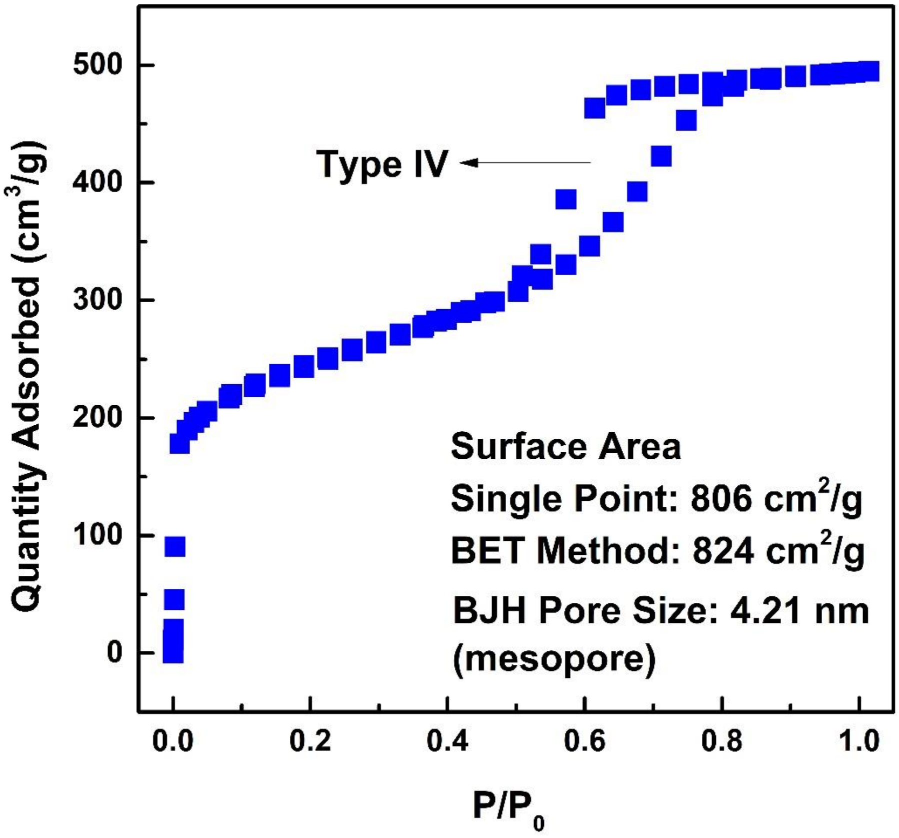

Figure 7. 10 N_2 adsorption-desorption isotherms of the UiO-66-NH_2 powder obtained from the repeated growth method. The isotherms were measured at 77 K.

The N_2 adsorption-desorption isotherms of the UiO-66-NH_2 were generated by plotting the amount of N_2 adsorbed as a function of the relative pressure, P/P_0. The specific surface area of UiO-66-NH_2 was calculated using both the single point method and the BET method, and the calculated values are 806 cm^2/g and 824 cm^2/g, respectively. The specific surface area of UiO-66-NH_2 in this work is comparable to the values reported by our previous paper.[16] Therefore, the missing linker detected by TGA did not significantly change the UiO-66-HN_2 crystal structure, otherwise the specific surface area of UiO-66-NH_2 would be much lower. Interestingly, a hysteresis loop was found on the isotherms, thus indicating the UiO-66-NH_2 obtained in this work is mesoporous.[25,26] Further BJH pore size calculation yielded an average pore size of 4.21 nm. The origin of the mesopore could come from two sources. On the one hand, a large single crystal could have a decent amount of internal cavity, i.e., both metal clusters and linkers are missing (so the linker to metal cluster ratio is relatively unchanged). On the other hand, the mesopores could form when a large number of small crystals form an aggregate.[25,26] The origin of the mesopores needs to be further elucidated by SEM images, yet the presence of mesopores is sufficient to explain why the UiO-66-NH_2 layer provided no size-based ion selectivity.

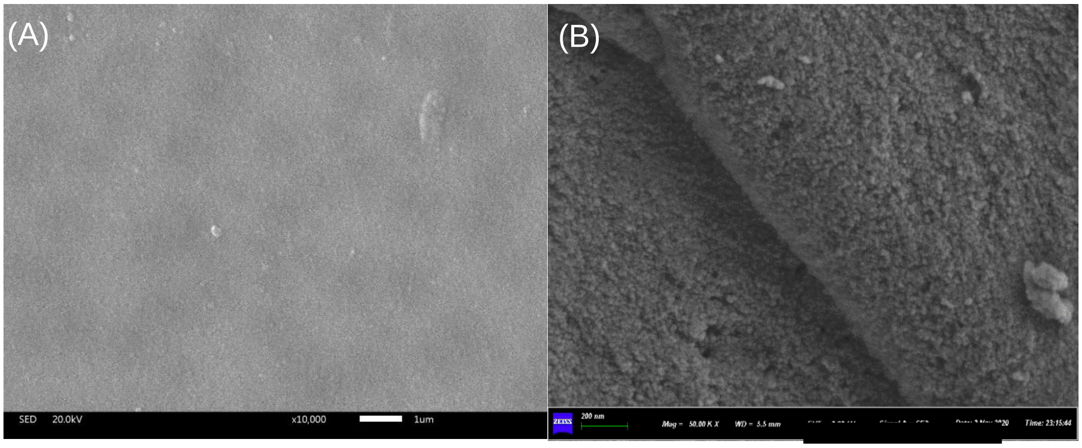

Figure 7. 11 SEM images of the Cycle 10 membrane at (A) low resolution and (B) high resolution.

The SEM images of the Cycle 10 membrane were taken at different resolutions. In Figure 7.11(A), no particles or cracks could be observed, which suggests the particles are small and are densely packed. In Figure 7.11(B), small particles with diameter between 10 to 20 nm were observed, and these particles aggregated into a dense layer. Hence, the mesopores detected in SA were more likely the result of small particle aggregation. These mesopores need to be eliminated or filled before the UiO-66-NH_2 layer provides size-based ion selectivity.

7.5 Conclusion and Perspectives

Applying the rapid aqueous solution-based synthesis of UiO-66-NH_2 on the L-(DOPA) modified PVDF membranes did not yield improvement in the membrane ion selectivity as expected, due to the formation of the mesopores between UiO-66-NH_2 particles. Two possible routes could be taken to solve the problem, and both of them require the presence of a polymer. First, a water-soluble polymer, e.g., PVA, could be dissolved in both the metal solution and the linker solution to create an inter-penetrating network during the UiO-66-NH_2 formation. Alternatively, the UiO-66-NH_2 could be dispersed in a PVA solution, and the PVA-UiO-66-NH_2 mixture could be filtered onto an UF membrane to create a selective layer. The results from this work is intended to serve as a start point for further research efforts on the synthesis of ion selective MMMs from aqueous solutions.

7.6 References

[1] S.L. James, Metal-organic frameworks, Chem. Soc. Rev. 32 (2003) 276–288.

[2] J.R. Long, O.M. Yaghi, The pervasive chemistry of metal–organic frameworks, Chem. Soc. Rev. 38 (2009) 1213–1214.

[3] H.-C. Zhou, J.R. Long, O.M. Yaghi, Introduction to metal–organic frameworks, (2012).

[4] J.-R. Li, J. Sculley, H.-C. Zhou, Metal–organic frameworks for separations, Chem. Rev. 112 (2012) 869–932.

[5] Y. Pan, Y. Liu, G. Zeng, L. Zhao, Z. Lai, Rapid synthesis of zeolitic imidazolate framework-8 (ZIF-8) nanocrystals in an aqueous system, Chem. Commun. 47 (2011) 2071–2073.

[6] Z. Hu, Y. Chen, J. Jiang, Zeolitic imidazolate framework-8 as a reverse osmosis membrane for water desalination: Insight from molecular simulation, J. Chem. Phys. 134 (2011) 134705.

[7] Z. Wang, Z. Wang, S. Lin, H. Jin, S. Gao, Y. Zhu, J. Jin, Nanoparticle-templated nanofiltration membranes for ultrahigh performance desalination, Nat. Commun. 9 (2018) 1–9.

[8] M. Kandiah, M.H. Nilsen, S. Usseglio, S. Jakobsen, U. Olsbye, M. Tilset, C. Larabi, E.A. Quadrelli, F. Bonino, K.P. Lillerud, Synthesis and stability of tagged UiO-66 Zr-MOFs, Chem. Mater. 22 (2010) 6632–6640.

[9] L. Valenzano, B. Civalleri, S. Chavan, S. Bordiga, M.H. Nilsen, S. Jakobsen, K.P. Lillerud, C. Lamberti, Disclosing the complex structure of UiO-66 metal organic framework: a synergic combination of experiment and theory, Chem. Mater. 23 (2011) 1700–1718.

[10] T. Xu, M.A. Shehzad, D. Yu, Q. Li, B. Wu, X. Ren, L. Ge, T. Xu, Highly Cation Permselective Metal–Organic Framework Membranes with Leaf-Like Morphology, ChemSusChem. 12 (2019) 2593–2597.

[11] M.W. Anjum, F. Vermoortele, A.L. Khan, B. Bueken, D.E. De Vos, I.F.J. Vankelecom, Modulated UiO-66-based mixed-matrix membranes for CO2 separation, ACS Appl. Mater. Interfaces. 7 (2015) 25193–25201.

[12] M.S. Denny Jr, S.M. Cohen, In situ modification of metal–organic frameworks in mixed-matrix membranes, Angew. Chemie Int. Ed. 54 (2015) 9029–9032.

[13] J. Shen, G. Liu, K. Huang, Q. Li, K. Guan, Y. Li, W. Jin, UiO-66-polyether block amide mixed matrix membranes for CO2 separation, J. Memb. Sci. 513 (2016) 155–165.

[14] D.T. Lee, J. Zhao, C.J. Oldham, G.W. Peterson, G.N. Parsons, UiO-66-NH2 Metal–Organic Framework (MOF) Nucleation on TiO2, ZnO, and Al2O3 Atomic Layer Deposition-Treated Polymer Fibers: Role of Metal Oxide on MOF Growth and Catalytic Hydrolysis of Chemical Warfare Agent Simulants, ACS Appl. Mater. Interfaces. 9 (2017) 44847–44855.

[15] X. Liu, N.K. Demir, Z. Wu, K. Li, Highly water-stable zirconium metal–organic framework UiO-66 membranes supported on alumina hollow fibers for desalination, J. Am. Chem. Soc. 137 (2015) 6999–7002.

[16] L. Huelsenbeck, H. Luo, P. Verma, J. Dane, R. Ho, E. Beyer, H. Hall, G.M. Geise, G. Giri, Generalized Approach for Rapid Aqueous MOF Synthesis by Controlling Solution pH, Cryst. Growth Des. (2020). https://doi.org/10.1021/acs.cgd.0c00895.

[17] H. Vinh-Thang, S. Kaliaguine, Predictive models for mixed-matrix membrane performance: a review, Chem. Rev. 113 (2013) 4980–5028.

[18] H. Zhang, J. Hou, Y. Hu, P. Wang, R. Ou, L. Jiang, J.Z. Liu, B.D. Freeman, A.J. Hill, H. Wang, Ultrafast selective transport of alkali metal ions in metal organic frameworks with subnanometer pores, Sci. Adv. 4 (2018) eaaq0066.

[19] H. Luo, F. Cheng, L. Huelsenbeck, N. Smith, Comparison between conventional solvothermal and aqueous solution-based production of UiO-66-NH2: Life cycle assessment, techno-economic assessment, and implications for CO2 capture and storage, J. Environ. Chem. Eng. 9 (2021) 105159. https://doi.org/10.1016/j.jece.2021.105159.

[20] H. Luo, J. Aboki, Y. Ji, R. Guo, G.M. Geise, Water and Salt Transport Properties of Triptycene-Containing Sulfonated Polysulfone Materials for Desalination Membrane Applications, ACS Appl. Mater. Interfaces. (2018). https://doi.org/10.1021/acsami.7b17225.

[21] E.L. Cussler, Diffusion: Mass Transfer in Fluid Systems, 2nd edition, 1997.

[22] G.M. Geise, H.B. Park, A.C. Sagle, B.D. Freeman, J.E. McGrath, Water permeability and water/salt selectivity tradeoff in polymers for desalination, J. Memb. Sci. (2011). https://doi.org/10.1016/j.memsci.2010.11.054.

[23] J.G. Wijmans, R.W. Baker, The solution-diffusion model: a review, J. Memb. Sci. (1995). https://doi.org/10.1016/0376-7388(95)00102-I.

[24] A. Schaate, P. Roy, A. Godt, J. Lippke, F. Waltz, M. Wiebcke, P. Behrens, Modulated synthesis of Zr-based metal-organic frameworks: From nano to single crystals, Chem. - A Eur. J. (2011). https://doi.org/10.1002/chem.201003211.

[25] Y. Zhang, Q. Ruan, Y. Peng, G. Han, H. Huang, C. Zhong, Synthesis of hierarchical-pore metal-organic framework on liter scale for large organic pollutants capture in wastewater, J. Colloid Interface Sci. (2018). https://doi.org/10.1016/j.jcis.2018.04.063.

[26] Z. Li, H. Chen, C. Chen, Q. Guo, X. Li, Y. He, H. Wang, N. Feng, H. Wan, G. Guan, High dispersion of polyethyleneimine within mesoporous UiO-66s through pore size engineering for selective CO2 capture, Chem. Eng. J. (2019). https://doi.org/10.1016/j.cej.2019.121962.

[27] M.J. Katz, Z.J. Brown, Y.J. Colón, P.W. Siu, K.A. Scheidt, R.Q. Snurr, J.T. Hupp, O.K. Farha, A facile synthesis of UiO-66, UiO-67 and their derivatives, Chem. Commun. (2013). https://doi.org/10.1039/c3cc46105j.

8. Conclusion

For dense ion exchange membranes used in electric field-driven specific ion separation applications, their performance is often evaluated by the ion separation factor. The ion separation factor is related to two selectivity, the sorption selectivity and the diffusivity selectivity. The ion sorption selectivity can be determined from either ion exchange isotherm or ionic conductivity measurements. When ion exchange isotherm measurements are used to determine the sorption selectivity, a dimensionless ion exchange affinity is often used to correlate the membrane phase ion concentration to its fixed charge concentration, for a given solution phase composition. Alternatively, conductivity measurements can be used to determine the sorption selectivity when the counter-ion form of the membrane is not dominated by a single counter-ion when ion specific interactions with the polymer are negligible. As for the diffusivity selectivity, it could be either predicted theoretically or measured experimentally. The free volume theory may be useful for connecting membrane water/salt selectivity, a type of selectivity that is important for desalination membranes, to the counter-ion/counter-ion selectivity that is critical for ion separation. When the counter-ion diffusivity selectivity is measured using ionic conductivity experiments, the influence of co-ion transport should be carefully considered, as neglecting the co-ion transport is sometime inappropriate.

The water and salt transport properties of desalination membranes are often influenced by the presenting functional groups. These functional groups could be further classified into two categories, the non-interactive functional groups and the interactive functional groups. The non-interactive functional groups have negligible interactions with water or ions in the membranes, while the interactive functional groups have specific interactions with water or ions.

Water and salt transport properties of a series triptycene-containing sulfonated polysulfones were studied, and the water/salt selectivity properties of the materials suggest that incorporating triptycene groups (non-interactive) into sulfonated polysulfone materials may increase modestly water/salt permeability selectivity. The triptycene-containing sulfonated polysulfones sorb more water than sulfonated polysulfones without triptycene (at comparable degrees of sulfonation), but the dry polymer density is not greatly affected by incorporation of triptycene in the polymer possibly due to strong hydrogen bond interactions between sulfonate groups in the dry polymers. No significant difference in salt sorption was observed between the TRP-BP materials and other sulfonated polysulfone materials as a function of water content. Both water and salt diffusion coefficients in the TRP-BP materials were suppressed compared to those values measured for BPS(H) and BisAS materials (at comparable water content). These observations may result from the influence of triptycene on polymer chain packing and/or on the distribution of free volume in the polymer, which could result in more tortuous transport pathways in the triptycene-containing polymers. Water/salt permeability selectivity was analyzed by considering both diffusion selectivity and sorption selectivity. The observed increase in water/salt permeability selectivity for some of the TRP-BP sulfonated polysulfone materials compared to the other materials that do not contain triptycene, suggests that incorporating bulky functional groups, such as triptycene, in polymers may be a strategy to increase the selectivity of desalination membrane materials.

Water and salt transport properties of a series hydroxyl group-containing methacrylate membranes (HEMA:GMA:GMAOH) were studied, and the water/salt selectivity properties of the materials suggest that shifting the hydroxyl group configuration from a vicinal diol-rich configuration (GMAOH-rich) to an evenly-distributed configuration (HEMA-rich) lead to an increase in water/salt permeability selectivity. In these methacrylate membranes with equivalent water content, configuring the hydroxyl group in an even-distribution manner leads to a reduction in salt sorption and permeability coefficients, which is favorable for desalination membrane applications. The observed reduction in salt sorption as the HEMA content of the co-polymer increases is consistent with the reduction in the freezable water content of the hydrated co-polymer. A reduction in the apparent salt diffusion coefficient as the HEMA content of the co-polymer increases is also consistent with a hydrogen bonding environment where water molecules interact to a greater extent with the polymer backbone, and both of these conditions are consistent with the observed reduction in freezable water content as the HEMA content of the co-polymer increased. . The results suggest that a more distributed functional group configuration may facilitate low rates of salt transport, which could be a viable strategy for preparing water/salt selective polymers for desalination membrane applications.

Process-based cradle-to-gate LCA and TEA were carried out to evaluate the life cycle environmental impacts and production costs associated with UiO-66-NH_2 production via the conventional solvothermal system and the aqueous solution-based system on the pilot-scale. The LCA results demonstrate that the aqueous solution-based system has much lower environmental impacts compared to the conventional solvothermal system. The aqueous solution-based system differs from the conventional solvothermal system by using water as the solvent and the cleaning agent. In this regard, the significant environmental burdens associated with organic solvents production and heat required for solvent recovery could be avoided. Furthermore, higher product yield is achieved in the aqueous solution-based system such that less material is consumed and the environmental burdens are lower. Compared with the solvothermal system, the aqueous solution-based system reduces the environmental impacts to up to 91%. A similar trend was observed in the TEA. The production cost of UiO-66-NH_2 from the aqueous solution-based system (14.2 \$/kg to 17.5 \$/kg) is much lower compared to that from the solvothermal system (56 \$/kg to 117 \$/kg) due to the significant reduction of operating costs. If UiO-66-NH_2 is applied CCS, our results demonstrate retrofitting existing coal-fired power plant with CCS can lead to a significant reduction in life cycle GWP. If the material loss of UiO-66-NH_2 is less than 0.0017tonne/captured CO2, UiO-66-NH2 based CCS system could be more environmentally friendly than the MEA-based CCS system. If UiO-66-NH_2 was to be applied in specific ion separation, the aqueous solution-based production should be used, and the gate-to-grave LCA is necessary to compare the performance of UiO-66-NH_2 to the existing membrane materials.

Applying the rapid aqueous solution-based synthesis of UiO-66-NH_2 on the L-(DOPA) modified PVDF membranes did not yield improvement in the membrane ion selectivity as expected, due to the formation of the mesopores between UiO-66-NH_2 particles. Two possible routes could be taken to solve the problem, and both of them require the presence of a polymer. First, a water-soluble polymer, e.g., PVA, could be dissolved in both the metal solution and the linker solution to create an inter-penetrating network during the UiO-66-NH_2 formation. Alternatively, the UiO-66-NH_2 could be dispersed in a PVA solution, and the PVA-UiO-66-NH2 mixture could be filtered onto an UF membrane to create a selective layer. The results from this work are intended to serve as a start point for further research efforts on the synthesis of ion selective MMMs from aqueous solutions.

Appendix

Appendix A: List of Symbols

Table A. 1 List of Symbols

A	polymer related constant
A	membrane mass in the auxiliary liquid
A_{PS}	effective area of the sample available for saltpermeation
A_{PW}	effective area of the sample available for water permeation
B	membrane mass in air
b	adjustable parameter related to the size of the penetrant
C_0	(equivalents of charge per volume) concentration of cations in the solution phase
C_0	initial soaking solution concentration
C_A^m	concentration of fixed charge group in the membrane phase
$C_D(0)$	initial donor chamber salt concentration
C_f	desorption solution concentration
C_i^m	concentration of *i* in the membrane phase
C_i^s	concentration of ion *i* in the upstream solution
C_M^m	concentration of counter-ion in the membrane phase
$C_R(t)$	receiver chamber salt concentration at time *t*
C_W^m	membrane water concentration
C_W^S	water concentration in the external solution
C_X^m	concentration of co-ion in the membrane phase
D_i^m	average diffusion coefficient of ion *i* in the membrane phase
D_i^s	average diffusion coefficient of ion *i* in the solution phase
D_M^m	average diffusion coefficient of counter ion in the membrane phase
D_S	average salt diffusion coefficient
D_W	average water diffusion coefficient
D_X^m	average diffusion coefficient of co-ion in the membrane phase
e	elementary charge
F	Faraday’s constant
H	hydration
I	current density
J_i	average flux of ion *i*
J_W	permeate water flux
k	Boltzmann’s constant
K_i	ion sorption coefficient
K_{iex}	ion exchange equilibrium constant
K_j^i	membrane sorption selectivity of counter-ion *i* relative to counter-ion *j*
$K_{M,i}$	counter-ion sorption coefficient
K_W	membrane water sorption coefficient
P_i	permeability of ion *i*

P_W^D	diffusive water permeability
P_W^H	hydraulic water permeability
L	membrane thickness
l	membrane thickness
m_{dry}	dry membrane mass
m_f	freezable water mass in the co-polymer
$m_{hydrated}$	hydrated membrane mass
M_W	molecular weight of water
R	gas constant
SF	separation factor
T	absolute temperature
t_i	transport number of *i*
$t_{M,min}^m$	minimum counter-ion transport number
u_i^m	membrane phase mobility of ion *i*
V	solution volume in each salt permeation chamber
V^*	minimum free volume size required by a penetrant
V_F^H	average free volume element size in the hydrated polymer
V_f	total free volume of the membrane
V_f	desorption solution volume
$V_{f,P}$	polymer free volume
$V_{f,W}$	free volume of water
V_m	hydrated membrane volume
$\bar{V}_W$	partial molar volume of water
w_f	freezable water
w_{nf}	non-freezable water
$W.U$	water uptake
x_j	dimensionless composition of counter-ion *j* in the solution phase
y_j	dimensionless composition of counter-ion *j* in the membrane phase
z_i	valence of ion *i*
z_M	valence of counter-ion
z_X	valence of co-ion
α_i^j	dimensionless ion exchange affinity
γ	correction factor to prevent double counting the free volume elements
$\gamma_\pm^m$	mean ionic activity coefficient in the membrane
$\gamma_\pm^s$	mean ionic activity coefficient in the solution
δ	thermodynamic non-ideality
$\Delta H_{polymer}$	enthalpy of melting in the co-polymer
$\Delta H_{m,H_2O}^{\circ}$	enthalpy of melting for water
Δp	pressure difference across the membrane
$\Delta\pi$	osmotic pressure difference across the membrane
ε	relative dielectric permittivity
ε_0	permittivity of free space

κ	ionic conductivity of the membrane
λ_B	Bjerrum length
ξ	Manning parameter
ρ_{aux}	density of the auxiliary liquid
ρ_{dry}	dry membrane density
ϕ_W	membrane water volume fraction

Appendix B: Supporting information for Chapter 3

B.1. Diffusive Water Permeability and Water Diffusion Coefficient Calculations and Analysis using Flory-Huggins Theory

The conversion of measured hydraulic permeability, P_W^H, to diffusive permeability, P_W^D, requires information about water sorption and thermodynamic non-ideality:

$$P_W^D = P_W^H \frac{RT}{\bar{V}_W} \frac{1-K_W}{\delta} \tag{B.1}$$

where K_W is the water sorption coefficient (effectively the volume fraction of water sorbed by the polymer at equilibrium, c.f., Eq. (3.6) in the main text), R is the gas constant, T is the absolute temperature, and $\bar{V}_W$ is the partial molar volume of water in the polymer (taken to be the molar volume of water, 18 cm^3/mol),[1] and δ is a thermodynamic factor that describes the relationship between the volume fraction of water sorbed by the polymer, ϕ_W, and the thermodynamic activity of water in the polymer, a_W^m, at equilibrium.[2] The thermodynamic factor is defined as:[2]

$$\delta \equiv \left. \frac{\partial \ln \phi_W}{\partial \ln a_W^m} \right|_{a_{W0}^m} \tag{B.2}$$

where a_{W0}^m is the activity of water in the polymer at the upstream (or high pressure) polymer-solution interface. In many studies, the thermodynamic factor and the convective frame of reference term, $1 - K_W$, in Eq. (B.1) are set equal to unity, which is a reasonable assumption if $K_W \ll 1$ and mixing between water and polymer can be considered thermodynamically ideal.[2]

Evaluating δ can be accomplished by either measuring water sorption isotherms as a function of water activity or by using a suitable equation of state. One approach reported in the literature is to use Flory-Huggins theory to evaluate δ.[1, 2] Flory-Huggins theory describes the relationship between the activity of water and the volume fraction of water sorbed in the polymer using an interaction parameter, χ:[3, 4]

$$\ln a_W^m = \ln \phi_W + (1 - \phi_W) + \chi(1 - \phi_W)^2 \tag{B.3}$$

The water sorption coefficient, K_W, is effectively equivalent to ϕ_W,[5] so δ can be evaluated using Flory-Huggins theory as:[2]

$$\delta = \frac{1}{(1-K_W)(1-2\chi K_W)} \tag{B.4}$$

Thus, if the Flory-Huggins interaction parameter for water and a polymer of interest is known, the diffusive water permeability can be calculated from the measured hydraulic water permeability and sorption coefficient as:[6, 7]

$$P_W^D = P_W^H \frac{RT}{\bar{V}_W}\left[(1-K_W)^2(1-2\chi K_W)\right] \tag{B.5}$$

The water diffusion coefficient, D_W, can then be calculated as:[2, 6, 8]

$$D_W = \frac{P_W^D}{K_W} \tag{B.6}$$

As discussed in the main text, the use of Eq. (B.5) to calculate the diffusive water permeability will only be accurate if Flory-Huggins theory accurately describes the relationship between water sorption and the activity of water.

Water sorption isotherms as a function of water activity are not available for many polymers of interest, and this lack of experimental data prevents the direct calculation of δ using Eq. (B.2) or validation of whether Flory-Huggins theory is an appropriate model for the system. As such, attempts have been made to estimate the Flory-Huggins interaction parameter using a single point fit of the Flory-Huggins model (typically made using the pure water sorption data for the polymer).[1, 2] While this approach yields a value of δ for use in Eq. (B.5), it is possible that the approach could introduce an artifact if the Flory-Huggins model does not accurately describe water sorption in the polymer.

In the main text, the analysis was performed by setting the interaction parameter in Eq. (B1) equal to unity. Here, the diffusive water permeability is calculated using two alternate cases: 1) the single point fit using Flory-Huggins theory and Eq. (B.5) and 2) the low water content approximation where the convective frame of reference term, $1-K_W$, is neglected and δ is taken as unity:[2, 9]

$$P_W^D = P_W^H \frac{RT}{\bar{V}_W} \tag{B.7}$$

Interaction parameters, diffusive water permeability values, and water diffusion coefficients calculated using the single point Flory-Huggins fit and Eqs. (B.5) and (B.6) are provided in Table B.1 for the polymers discussed in this study. Water sorption isotherms presently are not available for the TRP-BP, BPS(H), or BisAS polymers discussed in this study, so the applicability of Flory-Huggins theory (or the single point fit) to these materials is not currently known.

Table B. 1. Water transport properties and Flory-Huggins interaction parameters for the polymers discussed in this study. Previously reported data for the BPS(H) polymers and the BisAS polymers are included for comparison. Experimentally measured (using a dead-end cell pressurized to 400 psig at room temperature) hydraulic water permeability data are also provided.

Material	**P_W^H (L•µm/m^2•h•bar)**	**χ [a]**	**D_W [b] (×10^{-6} cm^2/s)**	**P_W^D [c] (× 10^{-7} cm^2/s)**
TRP-BP 1:1-35-acid	2.8±0.2	0.81	1.7±0.1	8.0±0.6
TRP-BP 1:1-35-salt	0.55±0.07	0.9	0.7±0.1	2.5±0.3
TRP-BP 2:1-35-acid	2.9±0.1	0.79	1.5±0.1	7.2±0.3
TRP-BP 2:1-35-salt	0.75±0.07	0.93	1±0.1	3.8±0.4
TRP-BP 1:1-50-salt	3.8±0.23	0.79	1.9±0.1	9.3±0.6
BPS-35[1]	0.39	1.1	1.3	3.5
BPS-40[1]	0.65	1.05	1.7	5
BPSH-35[1]	2.1	0.88	2.1	8.7
BPSH-40[1]	4.4	0.79	2.3	11
BisAS-30[10]	0.46±0.02	1.15	1.9±0.1	4.5±0.2
BisAS-40[10]	1.53±0.23	0.96	2.6±0.2	8.9±1.3

[a] Calculated via a single point fit using pure water sorption data and Eq. (B.3)

[b] Calculated using Eqs. (B.5) and (B.6)

[c] Calculated using Eq. (B.5)

Figs. 3.2, 3.6, 3.7, and 3.9 from the main text were adjusted using the values reported in Table B.1 to prepare Figs. B.1, B.2, B.3, and B.4, respectively. Comparing Fig. B.1 to Fig. B.2 (main text) and Fig. B.2 to Fig. B.6 (main text) reveals qualitative similarity between the data. This similarity suggests that the method of analysis does not appreciably affect the qualitative results that water diffusivity in the TRP-BP materials is suppressed at a given water content compared to the BPS(H) and BisAS materials (Fig. B.1 and Fig. B.5) and that salt diffusivity is more sensitive to water content compared to water diffusivity in the TRP-BP materials (Fig. B.2 and Fig. B.6).

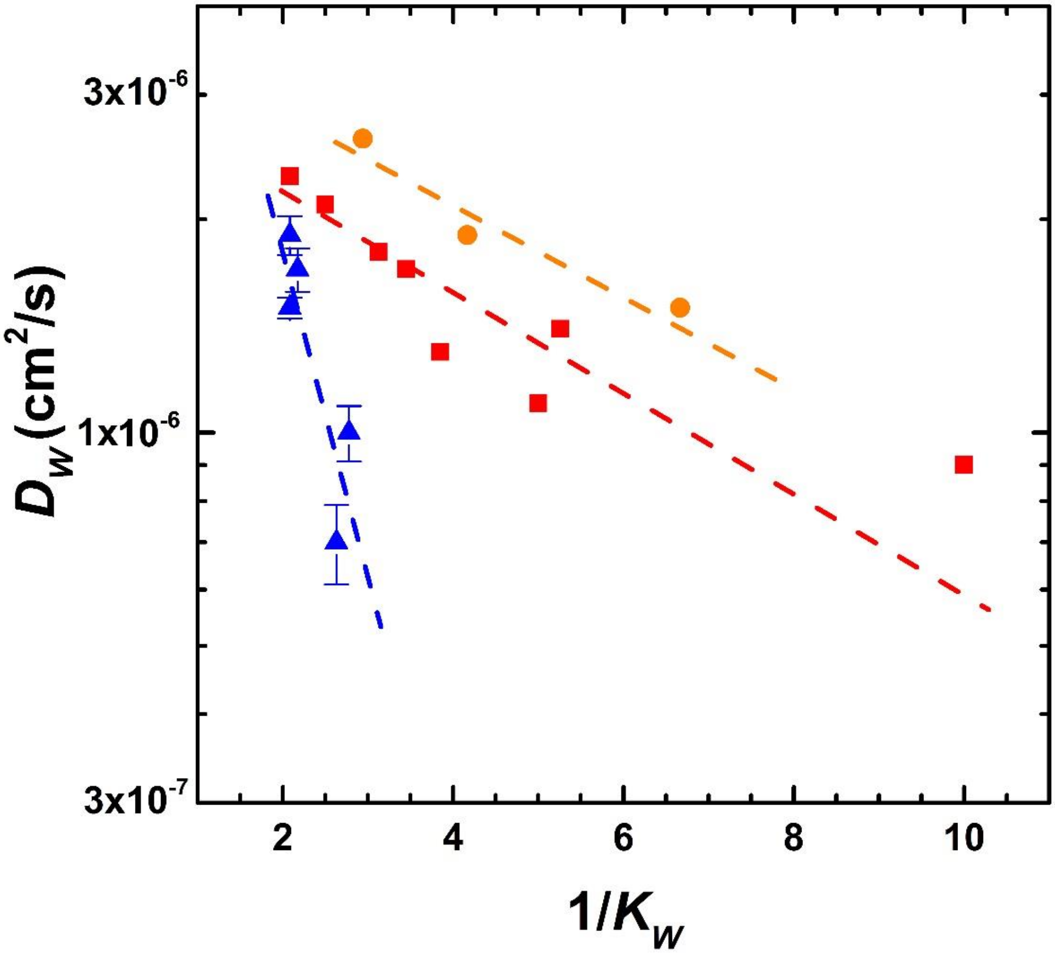

Figure B. 1. Water diffusivity, D_W, as a function of $1/K_W$ for the TRP-BP (▲), BPS(H) (■)[1], and BisAS (●)[10] materials. The D_W values (Table B.1) were calculated using Eqs. (B.5) and (B.6).

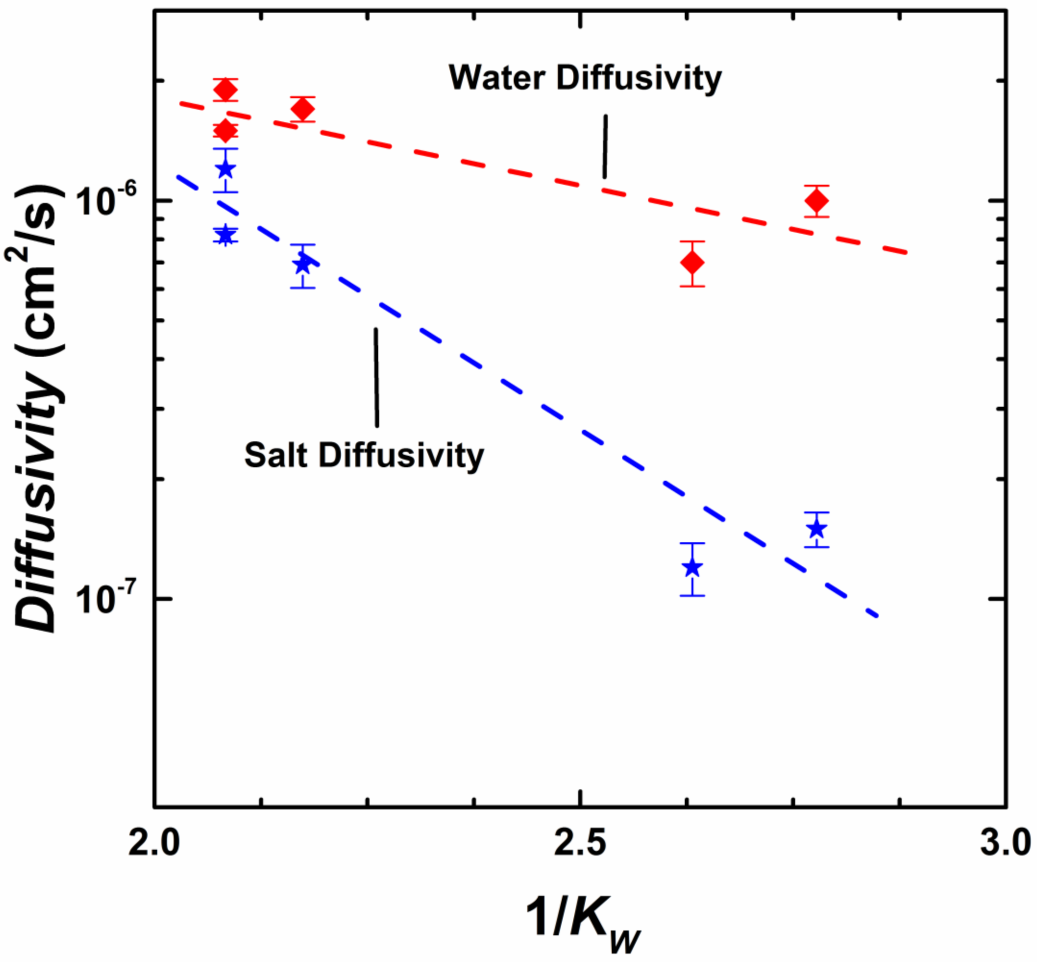

Figure B. 2. TRP-BP water diffusivity (D_W, ◆, from Table B.1 – calculated using Eqs. (S5) and (S6)) and salt diffusivity (D_S, ★, calculated from P_S and K_S values using Eq. (3.14) from the main text) as a function of 1/K_W.

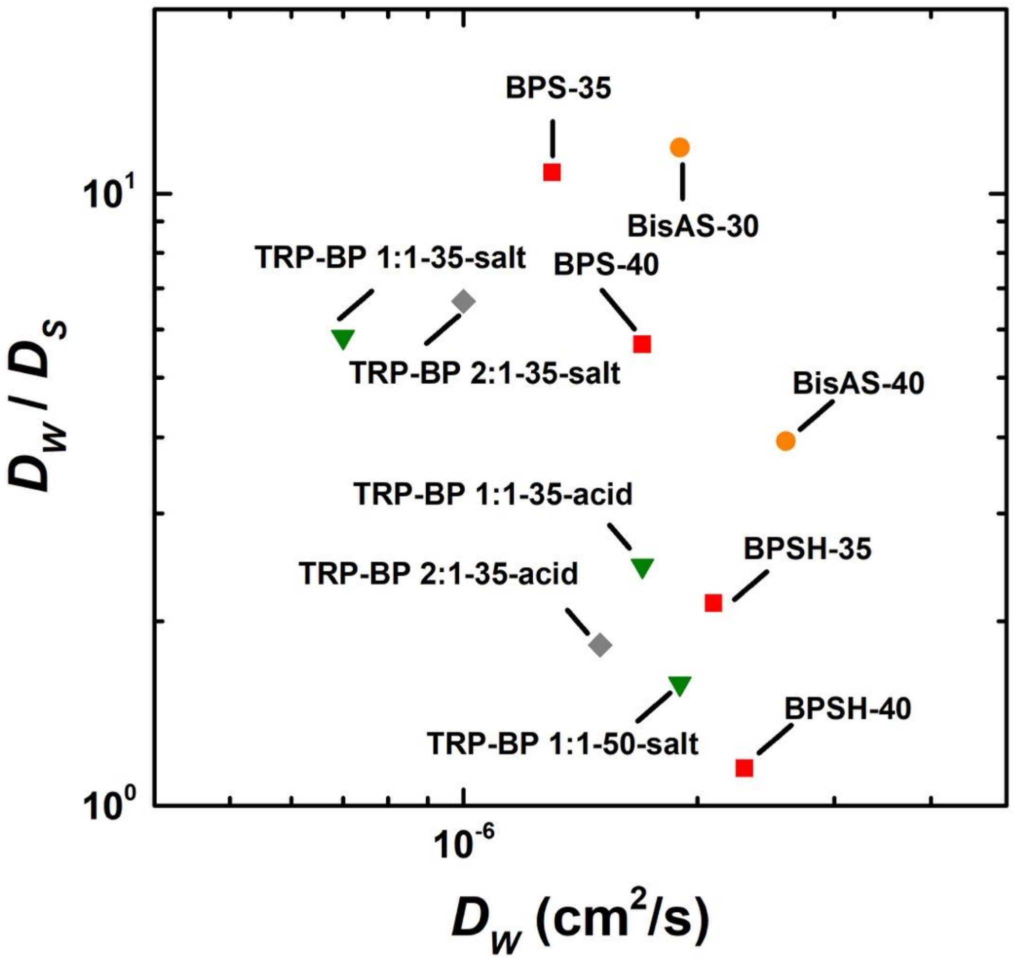

Figure B. 3. Diffusion selectivity, D_W/D_S, as a function of D_W for the TRP-BP 1:1 (▼), TRP-BP 2:1 (◆), BPS(H) (■)[1], and BisAS (●)[10] materials. The D_W values (Table B.1) were calculated using Eqs. (B.5) and (B.6).

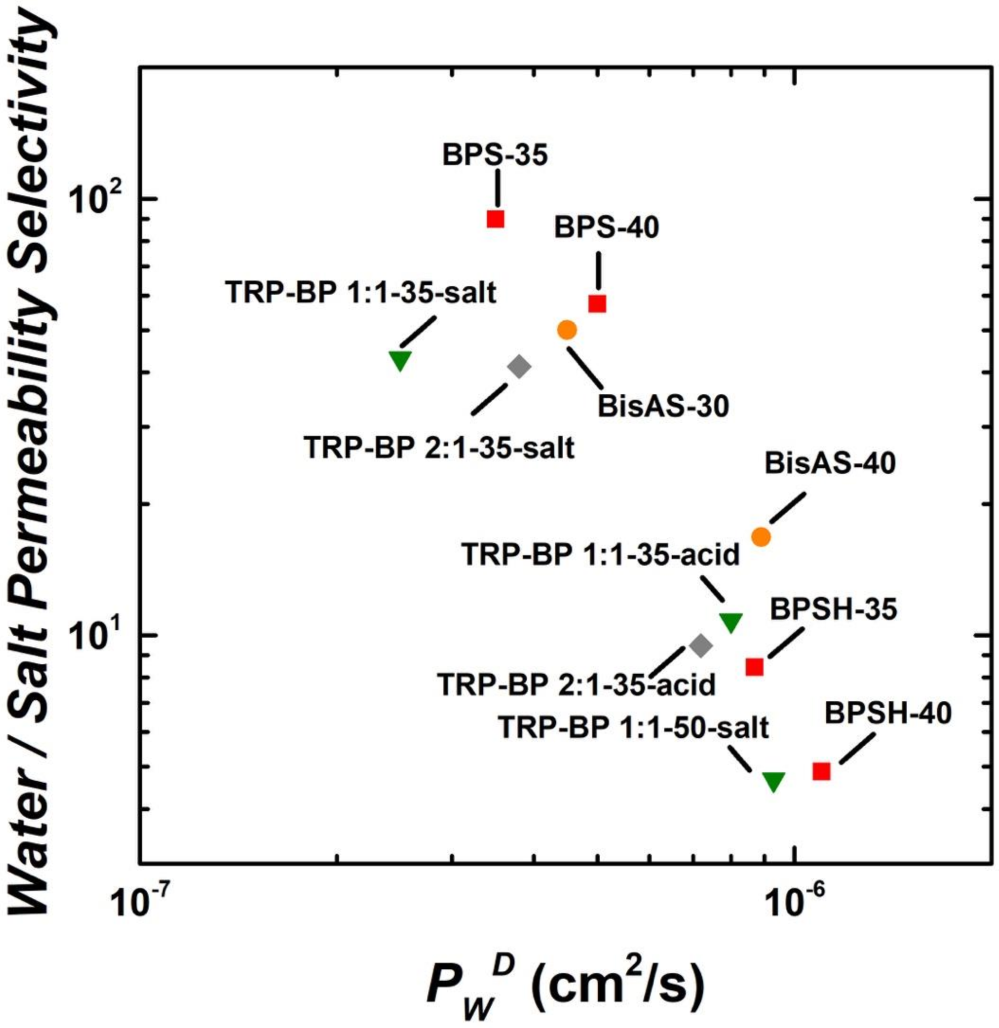

Figure B. 4. Trade-off between water/salt permeability selectivity, P_W^D/P_S, and diffusive water permeability, P_W^D, for the TRP-BP 1:1 (▼), TRP-BP 2:1 (◆), BPS(H) (■)[1], and BisAS (●)[10] materials. P_W^D values were calculated using Eq. (B.5).

As observed in Figs. B.3 and B.4, using the single point Flory-Huggins fit to calculate values of the diffusive water permeability and water diffusion coefficients gives a qualitatively different picture of the material selectivity properties compared to the discussion in the main text. The water/salt diffusivity selectivity of the TRP-BP materials is suppressed relative to the other sulfonated polysulfones (Fig. B.3), and the acid-form TRP-BP materials have water/salt permeability selectivity values that are comparable to those values for the other sulfonated polysulfones (Fig. B.4). Since the sulfonated polysulfone materials are glassy polymers, it is not clear whether the single point fit Flory-Huggins theory-based analysis of the diffusive water permeability and water diffusion coefficient introduces an artifact due to the way that the thermodynamics of the system are handled. This alternate analysis, though, is provided in contrast to the main text results to provide a comparison that is similar to other approaches that have been described in the literature.[1, 11, 12]

When the diffusive water permeability and water diffusion coefficient are calculated using Eqs. (B.7) and (B.6), i.e., neglecting both the convective frame of reference and thermodynamic correction terms, the water/salt diffusivity and permeability selectivity plots can be updated accordingly (Figs. B.5 and B.6). This method of analysis suggests that the water/salt diffusivity (Fig. B.5) and permeability (Fig. B.6) selectivity properties of the TRP-BP materials are higher or comparable to that of the other sulfonated polysulfones. This analysis also is provided as other reports in the literature have taken this approach to analyze water transport data.[13] The three different approaches (one in the main text and 2 presented here) yield different quantitative results, and are provided in the interest of completeness.

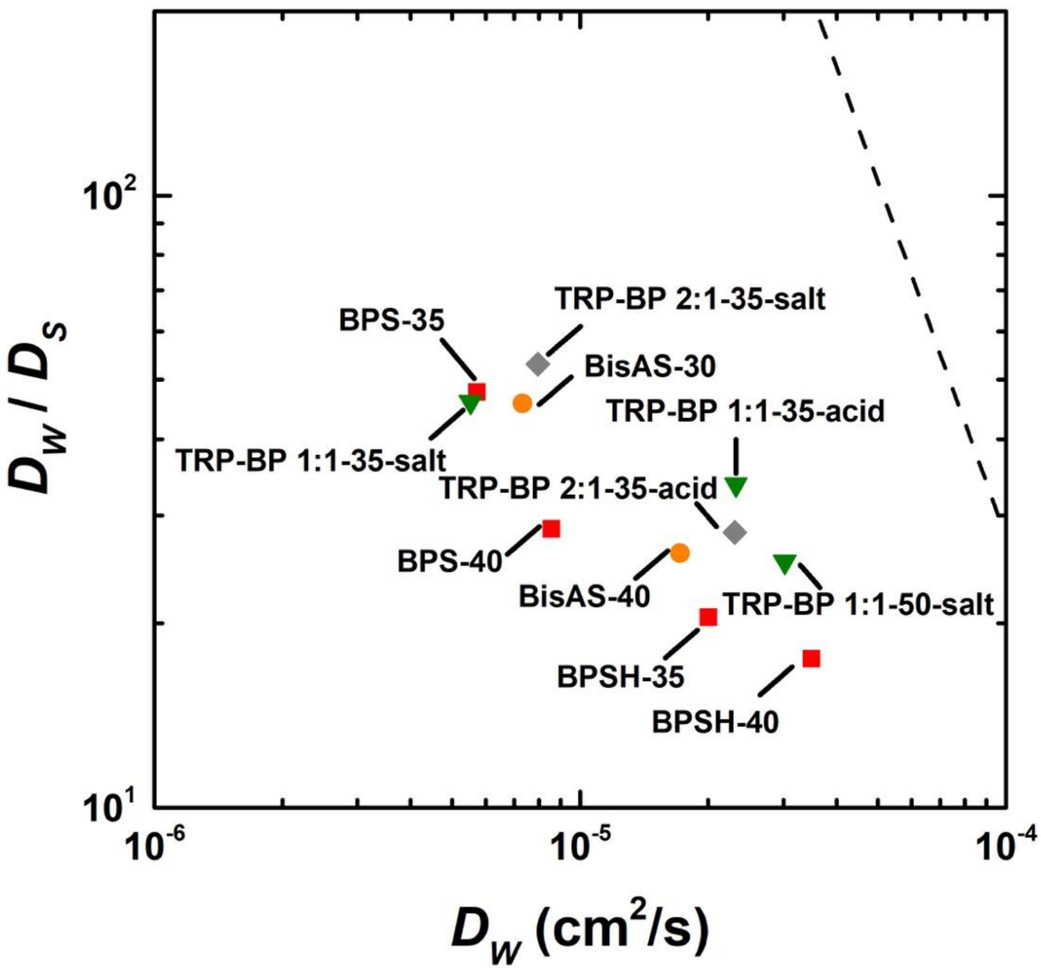

Figure B. 5. Diffusion selectivity, D_W/D_S, as a function of D_W for the TRP-BP 1:1 (▼), TRP-BP 2:1 (◆), BPS(H) (■)[1], and BisAS (●)[10] materials. The D_W values were calculated using Eqs. (B.7) and (B.6). The dashed line represents an empirical tradeoff frontier reported for desalination membranes.[13]

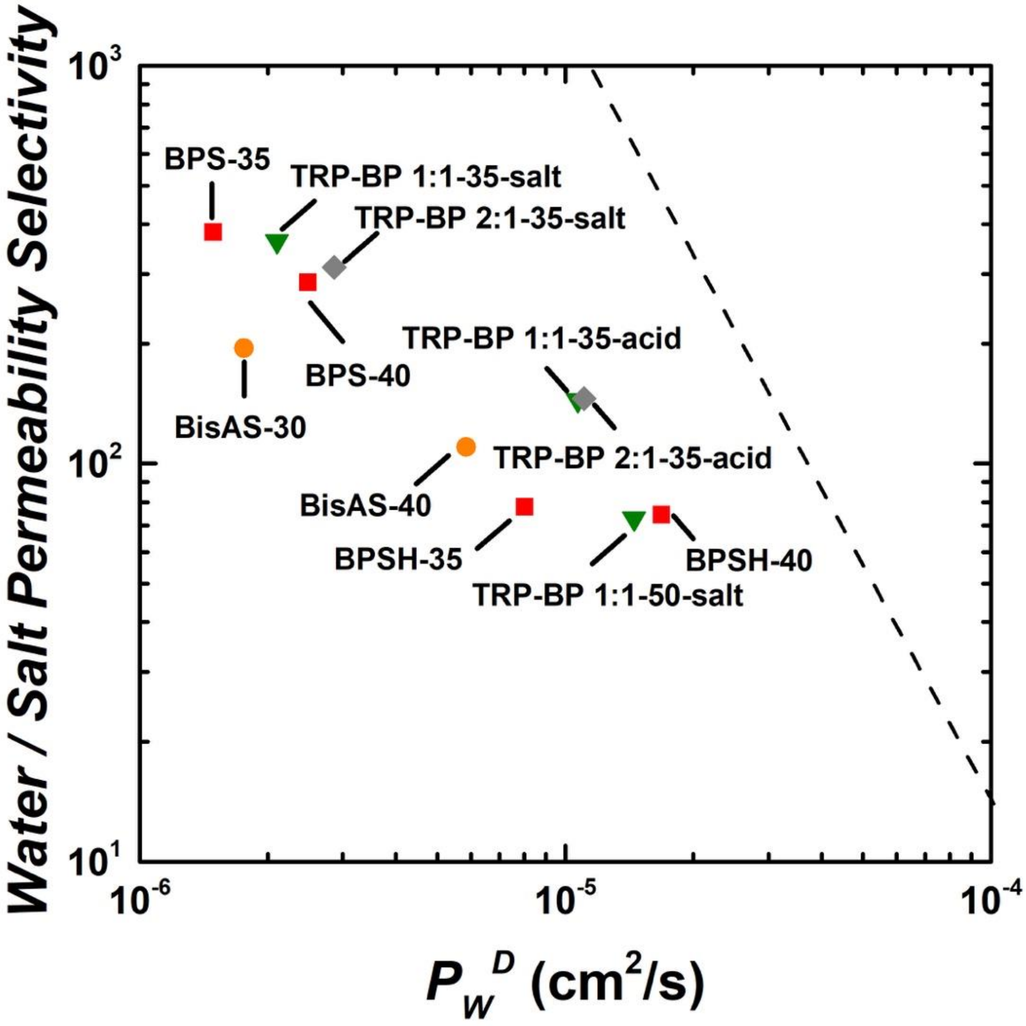

Figure B. 6. Trade-off between water/salt permeability selectivity, P_W^D/P_S, and diffusive water permeability, P_W^D, for the TRP-BP 1:1 (▼), TRP-BP 2:1 (◆), BPS(H) (🟥)[1], and BisAS (●)[10] materials. P_W^D values were calculated using Eq. (B.7). The dashed line represents an empirical tradeoff frontier reported for desalination membranes.[13]

B.2. Further Discussion Related to the Supression of Water and Salt Diffusion Coefficients upon Incorporation of Triptycene into Sulfonated Polysulfone

The main text suggests that the TRP moieties in the TRP-BP polymers may affect the distribution of free volume in the TRP-BP polymers compared to the other sulfonated polysulfones in a manner that could be consistent with the idea of increasing the effective tortuosity of the transport pathways in the TRP-BP polymers. To further support the suggestion that triptycene incorporation in sulfonated polysulfone might effectively introduce more transport pathway tortuosity compared to the other sulfonated polysulfones, the salt transport properties of two set of sulfonated styrenic pentablock copolymers (sPBC)[14, 15] are compared to the sulfonated polysulfone data (Figs. B.7 and B.8); Figs. B.7 and B.8 correspond to Figs. 3.3 and 3.4 in the main text, respectively.

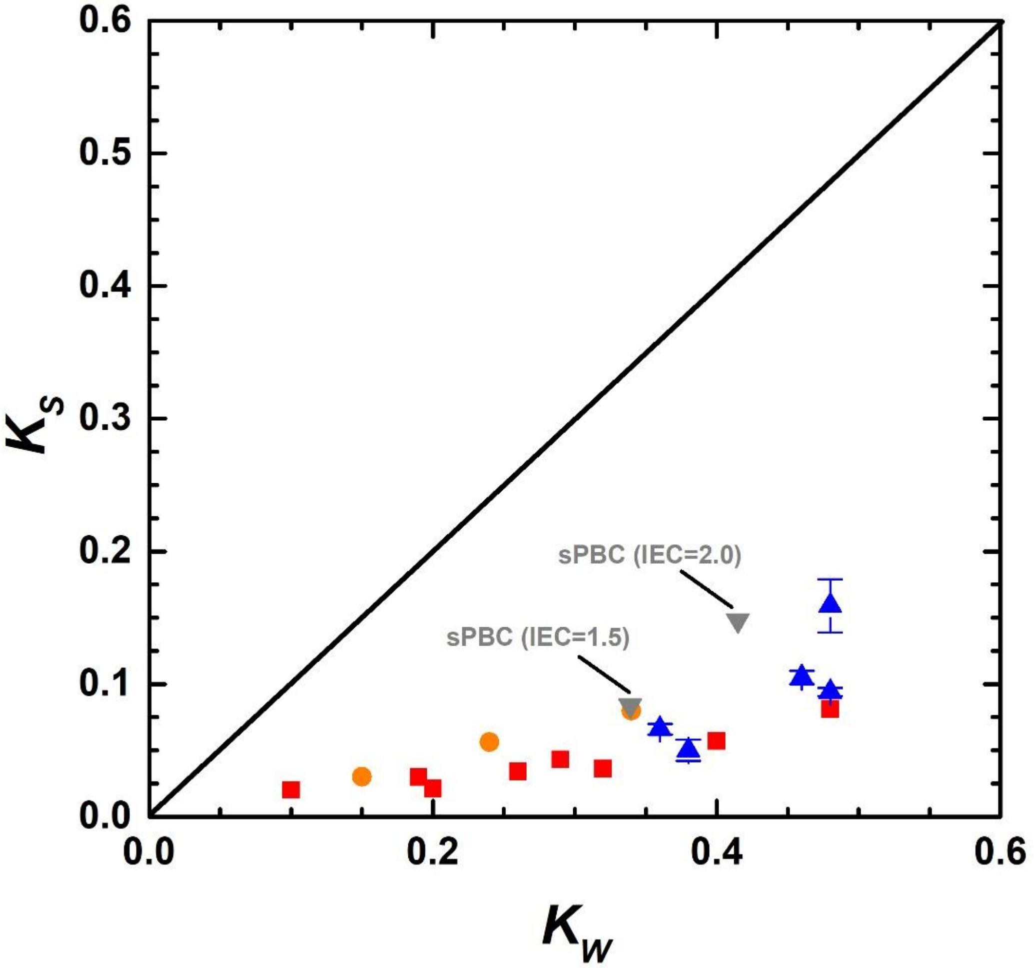

Figure B. 7. Salt sorption coefficient, K_S, values as a function of the water sorption coefficient, K_W, for the TRP-BP (▲), BPS(H) (■)[1], BisAS (●)[10], and sPBC (▼)[14] materials.

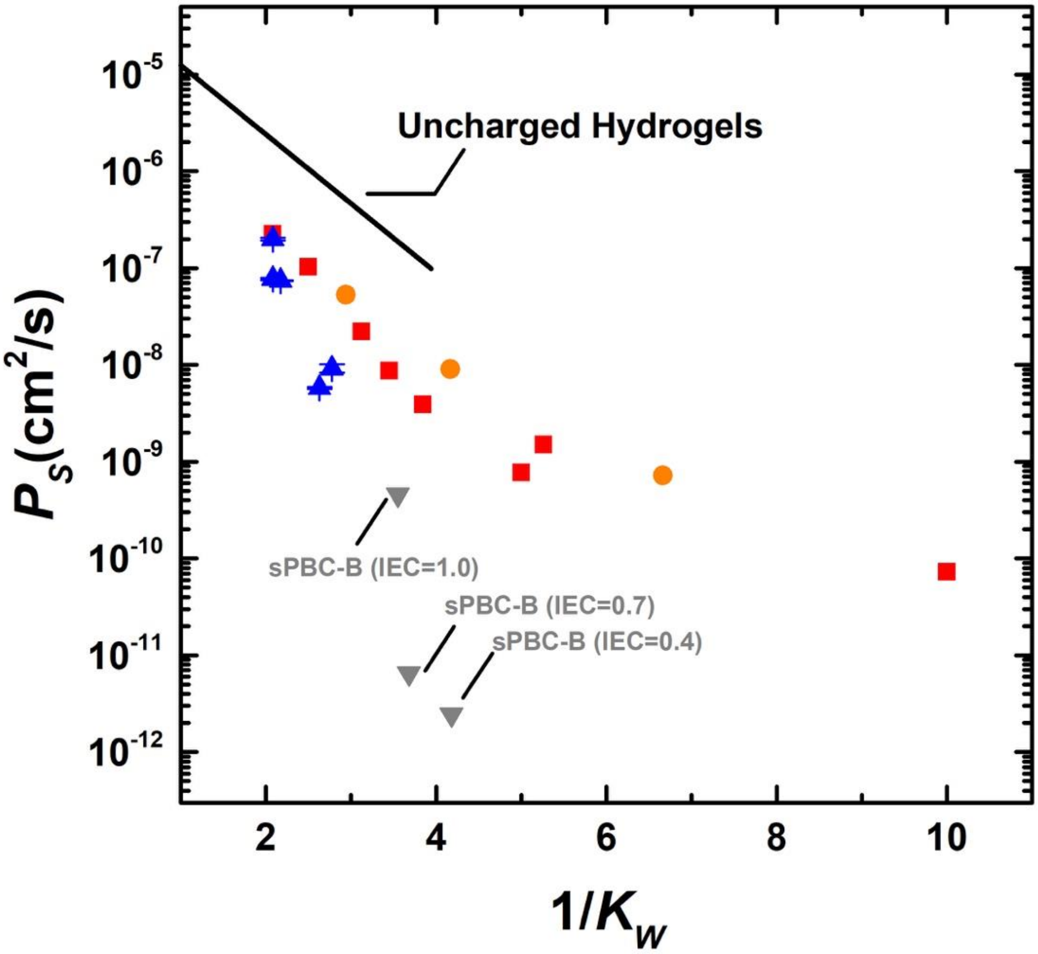

Figure B. 8. Salt permeability, P_S, as a function of $1/K_W$ for the TRP-BP (▲), BPS (H) (■)[1], BisAS (●)[10], and sPBC-B (▼)[15] materials. The data are compared to a general representation (solid line) of uncharged hydrogel data reported by Yasuda et al.[16]

This comparison was made due to the lack of random copolymer data where the tortuosity of the transport pathways was systematically varied. The pentablock copolymers micro-phase separate into hydrophilic and hydrophobic micro-domains.[17] Therefore, the pentablock copolymers have some element of transport pathway tortuosity.

The salt sorption properties of the sPBC materials are similar to the sulfonated polysulfones as a function of polymer water content (Fig. B.7). Salt sorption data are not available for the sPBC-B materials discussed here, so further analysis is focused in terms of salt permeability as opposed to salt diffusion coefficients. If the salt sorption coefficient properties of the sPBC-B materials are similar to the sPBC materials, which may be a reasonable assumption given the chemical similarity between the materials, then discussion of salt permeability would be analogous to a discussion of salt diffusion coefficients.

In Fig. B.8, the TRP-BP materials appear to establish a functional relationship between P_S and $1/K_W$ that appears to be largely coincident with the sPBC-B materials. While this observation does not confirm that triptycene affects the structure of the TRP-BP materials in a manner that is consistent with micro-phase separation in a block copolymer, the observation does suggest that micro-phase separation and tortuous transport pathways also tend to suppress salt permeation properties of micro-phase separated materials relative to non-micro-phase separated materials at comparable water content.

This discussion is presented in terms of salt permeability due to the availability of published data for comparison. A similar situation and discussion might be expected for water transport properties as both water and salt transport in the materials are described by the solution-diffusion model. Therefore, the incorporation of triptycene into sulfonated polysulfone may influence the polymer chain configurations (and/or the free volume distribution) in the materials in a manner that suppresses rates of water and salt permeability and diffusion.

B.3. References

1. W. Xie, J. Cook, H.B. Park, B.D. Freeman, C.H. Lee, and J.E. McGrath, Fundamental salt and water transport properties in directly copolymerized disulfonated poly(arylene ether sulfone) random copolymers. Polymer, 2011. **52**(9): p. 2032-2043.
2. G.M. Geise, D.R. Paul, and B.D. Freeman, Fundamental water and salt transport properties of polymeric materials. Progress in Polymer Science, 2014. **39**: p. 1-42.
3. P.J. Flory, Thermodynamics of high polymer solutions. The Journal of Chemical Physics, 1941. **9**(8): p. 660-660.
4. M.L. Huggins, Solutions of long chain compounds. The Journal of Chemical Physics, 1941. **9**(5): p. 440-440.
5. G.M. Geise, B.D. Freeman, and D.R. Paul, Sodium chloride diffusion in sulfonated polymers for membrane applications. Journal of Membrane Science, 2013. **427**: p. 186-196.
6. J.G. Wijmans and R.W. Baker, The solution-diffusion model: a review. Journal of Membrane Science, 1995. **107**(1): p. 1-21.
7. D.R. Paul, Relation between hydraulic permeability and diffusion in homogeneous swollen membranes. Journal of Polymer Science: Polymer Physics Edition, 1973. **11**(2): p. 289-296.
8. D.R. Paul, Reformulation of the solution-diffusion theory of reverse osmosis. Journal of Membrane Science, 2004. **241**(2): p. 371-386.
9. H.K. Lonsdale, U. Merten, and R.L. Riley, Transport properties of cellulose acetate osmotic membranes. Journal of Applied Polymer Science, 1965. **9**: p. 1341-1362.
10. J. Cook, *Fundamental water and ion transport characterization of sulfonated polysulfone desalination materials*. 2014, Ph.D. Thesis, The University of Texas at Austin.
11. A.C. Sagle, H. Ju, B.D. Freeman, and M.M. Sharma, PEG-based hydrogel membrane coatings. Polymer, 2009. **50**: p. 756-766.
12. H. Ju, A.C. Sagle, B.D. Freeman, J.I. Mardel, and A.J. Hill, Characterization of sodium chloride and water transport in poly(ethylene oxide) hydrogels. Journal of Membrane Science, 2010. **358**: p. 131-141.
13. G.M. Geise, H.B. Park, A.C. Sagle, B.D. Freeman, and J.E. McGrath, Water permeability and water/salt selectivity tradeoff in polymers for desalination. Journal of Membrane Science, 2011. **369**(1-2): p. 130-138.
14. G.M. Geise, L.P. Falcon, B.D. Freeman, and D.R. Paul, Sodium chloride sorption in sulfonated polymers for membrane applications. Journal of membrane science, 2012. **423**: p. 195-208.
15. G.M. Geise, B.D. Freeman, and D.R. Paul, Characterization of a sulfonated pentablock copolymer for desalination applications. Polymer, 2010. **51**(24): p. 5815-5822.
16. H. Yasuda, C.E. Lamaze, and L.D. Ikenberry, Permeability of solutes through hydrated polymer membranes. Part I. Diffusion of sodium chloride. Die Makromolekulare Chemie, 1968. **118**(1): p. 19-35.
17. J.-H. Choi, C.L. Willis, and K.I. Winey, Structure-property relationship in sulfonated pentablock copolymers. Journal of Membrane Science, 2012. **394-395**: p. 169-174.

Appendix C: Supporting information for Chapter 4

C.1 Fourier-transform infrared (FT-IR) spectroscopy

The FT-IR spectra of the hydrated HEMA:GMA:GMAOH film samples are shown in Figure C.1. All peak intensities were normalized to the C–O peak (for ester and ether functional groups) located at approximately 1160 cm^{-1} [1]. The location and intensity of most of the major peaks in the spectra are very similar, which is in good agreement with the structural similarity and equivalent water content nature of the materials.

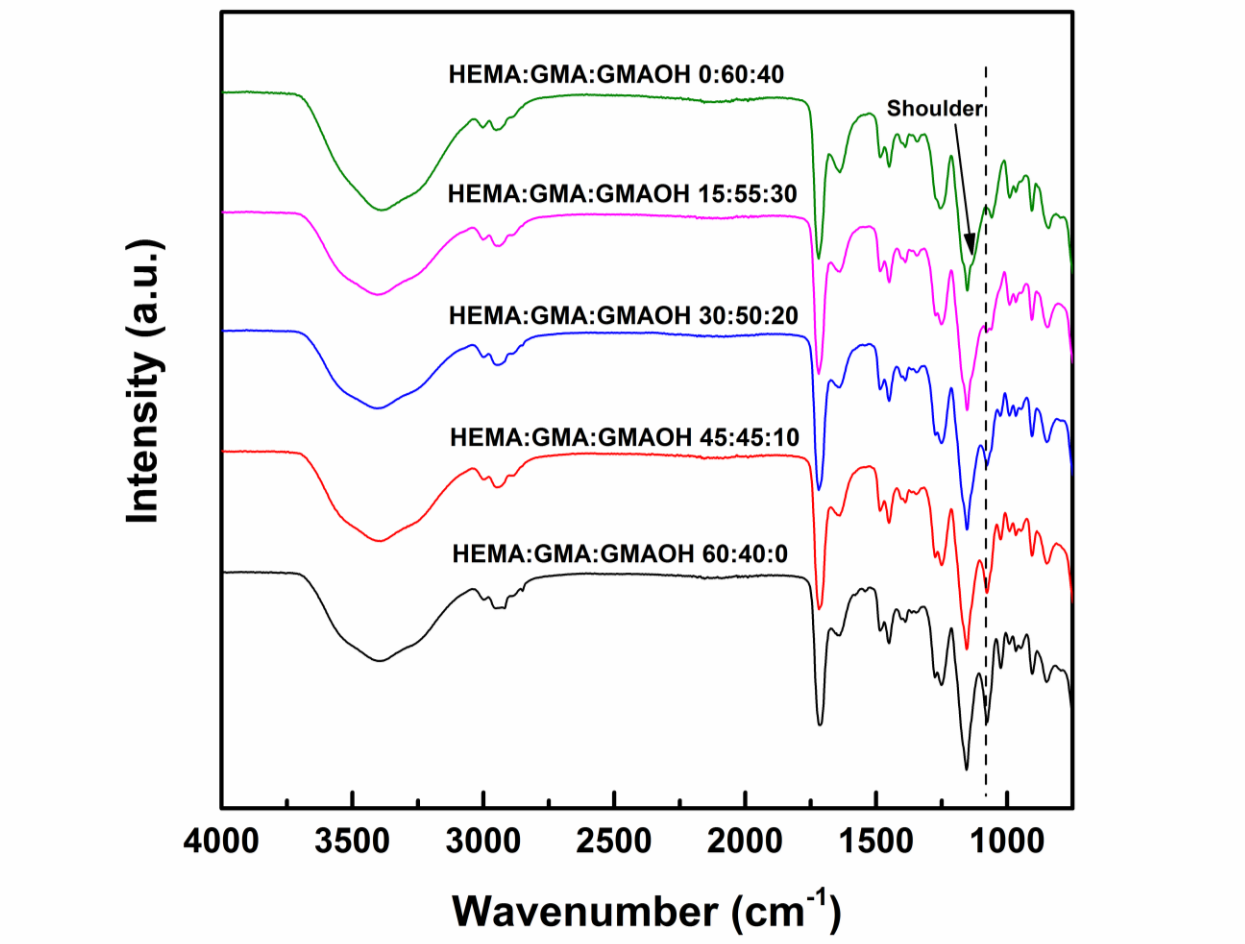

Figure C. 1. FT-IR spectra of hydrated HEMA:GMA:GMAOH film samples measured using an attenuated total reflectance (ATR) cell. The composition of the pre-polymerization solution used to prepare each co-polymer is listed for each spectrum. The dashed line indicates the position of the primary alcohol stretching peak (approximately 1070 cm^{-1}) for the HEMA:GMA:GMAOH 60:40:0 material to illustrate the shift that occurs as GMAOH content increases. Additionally, the shoulder on the 1160 cm^{-1} peak is identified.

The C–O stretching peak, attributed to primary alcohol functionality (-CH$_2$**CH$_2$OH**) and located at approximately 1070 cm^{-1} [1], shifts to a lower wavenumber as the GMAOH composition of the pre-polymerization solution (used to prepare the co-polymers) increases. We attribute this peak shift to an increase in the vicinal diol content (-*CHOH***CH$_2$OH**) of the material that lowers the bond stretching energy for the primary alcohol moiety in GMAOH [1]. Furthermore, the presence of the secondary alcohol group in GMAOH (-**CHOH**CH$_2$OH) could lead to multiple peaks in the range of 1150–1075 cm^{-1} due to coupling, and these peaks could overlap with the aforementioned C-O peak at 1160 cm^{-1} to yield the observed broad absorbance and a peak shoulder [1]. Hence, the FT-IR results support the qualitative increase in the GMAOH content of the co-polymer as the GMAOH content in the pre-polymerization solution increases.

C.2 Freezable water content per equivalent of hydroxyl group functionality

To further explore the formation of freezable (i.e., bulk-like) water in the co-polymers, we calculated the number of moles of freezable water sorbed in the co-polymer per equivalent of hydroxyl group functionality in the material (Table C.1). This quantity provides additional insight into the distribution of water within the co-polymer. The vicinal diol-rich materials (i.e., the low HEMA-content co-polymers) have more freezable water compared to the HEMA-rich co-polymers, and each hydroxyl group in the GMAOH-rich materials contributes more to the formation of freezable or bulk-like water. In other words, distributing the hydroxyl groups more evenly throughout the co-polymer (as in the HEMA-rich materials) results in a situation where each hydroxyl group creates less freezable water.

Table C. 1. The freezable water content, non-freezable water content, and the number of moles of freezable water per equivalent of hydroxyl group in the hydrated HEMA:GMA:GMAOH co-polymers.

HEMA:GMA:GMAOH Composition (by mass)	W_f (%)	W_{nf} (%)	mol(freezable water) / eq(hydroxyl group)
0:60:40	2.3	21.2	0.26
15:55:30	1.9	22.3	0.22
30:50:20	1.8	21.7	0.21
45:45:10	1.2	22.3	0.14
60:40:0	0.9	22.4	0.11

A sample calculation is provided for the HEMA:GMA:GMAOH 15:55:30 co-polymer. First, a dry polymer mass (m_{dry}) basis was taken to be 1 g(dry polymer). The number of moles of freezable water in 1 g(dry polymer), n_{fw}, was calculated as:

$$n_{fw} = \frac{m_{dry} \times W_f}{MW(water)} = \frac{1\,g \times 0.019}{18\,g/mol} = 0.00106\,mol \qquad (C.1)$$

where W_f is the mass of freezable water in the polymer per gram of dry polymer expressed as a decimal. The number of equivalents of hydroxyl functional groups in 1 g(dry polymer) was calculated using the theoretical composition of the co-polymer:

$$n_{OH} = m_{dry}\left(\frac{wt\,\%(GMAOH) \times 2}{MW(GMAOH)} + \frac{wt\,\%(HEMA)}{MW(HEMA)}\right) = 1\,g\left(\frac{30\% \times 2}{160\,g/eq} + \frac{15\%}{130\,g/eq}\right) = 0.0049\,eq \qquad (C.2)$$

Therefore, n_{fw} / n_{OH} = 0.22 mol(freezable water) per equivalent of hydroxyl group in the hydrated co-polymer.

C.3 References

[1] G. Socrates, Infrared and raman characteristic group frequencies: Tables and charts, 3rd ed., John Wiley & Sons, West Sussex, England, 2004.

Appendix D: Supporting information for Chapter 5

D.1. Additional Material Properties and Characterization

D.1.1 Chemical Structure and Composition

The chemical structure of the cross-linked HEMA:GMA:GMAOH co-polymer is shown as Figure D.1. The pre-polymerization solutions used to prepare the co-polymers for this study were prepared to contain a x:y:z, by mass, ratio of the HEMA:GMA:GMAOH co-monomers. While the sample nomenclature is based on this mass composition of the co-monomers in the pre-polymerization solution, the pre-polymerization solution co-monomer and cross-linker mole fractions are provided in Table D.1 along with the theoretical hydroxyl group content of the materials, which was calculated under the assumption that the compositions of the pre-polymerization solution and the resulting co-polymer are identical.

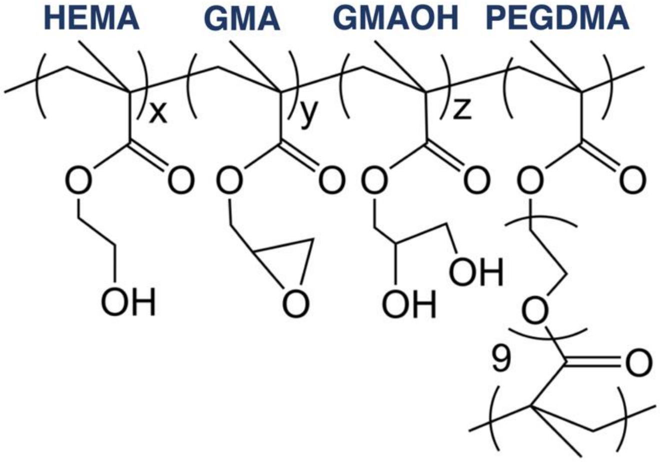

Figure D. 1. Chemical structure of the HEMA:GMA:GMAOH co-polymer along with labels for the co-monomers (i.e., HEMA, GMA, and GMAOH) and cross-linker (i.e., PEGDMA).

Table D. 1. Pre-polymerization solution co-monomer and cross-linker mole fractions and the theoretical hydroxyl group content of the materials.

Co-Polymer Sample	Pre-Polymerization Solution Co-Monomer and Cross-Linker Mole Fractions				Hydroxyl Group Content (meq –OH/ g dry polymer)
	HEMA	GMA	GMAOH	PEGDMA	
0:60:40	0	0.612	0.362	0.026	4.5
15:55:30	0.163	0.547	0.265	0.026	4.5
30:50:20	0.318	0.485	0.172	0.025	4.4
45:45:10	0.465	0.426	0.084	0.024	4.3
60:40:0	0.606	0.370	0	0.024	4.2

The data in Table D.1 suggest that the extent of cross-linking and the hydroxyl group content of the co-polymer decrease slightly (by 8% and 7%, respectively) across the range of materials considered. Extent of cross-linking is known to affect water and salt transport properties,[1-4] and the hydroxyl group content may influence transport properties as well. The compositions chosen for this study yielded co-polymers with equivalent water content (as discussed in more detail in the main text), and this result may be due to the simultaneous 8% reduction in cross-link density, which would be expected to cause an increase in water content,[1] and 7% decrease in hydroxyl group content, which would be expected to cause a decrease in water content (due to the reduction in the concentration of hydrophilic moieties in the material). It is possible that these factors may influence the water and salt transport properties of the materials considered in this study, but due to the significant influence of polymer water content on water and salt transport properties,[5-7] the water content was held constant in this study to minimize the influence of water content changes on water and salt transport properties.

D.1.2 Fourier-Transform Infrared (FT-IR) Spectroscopy

The co-polymers were analyzed using Fourier-transform infrared (FT-IR) spectroscopy. The spectra (Figure D.2) are very similar for the five materials considered, which is expected given the structural similarity of the co-polymers. The peak located at approximately 1050 cm^{-1} broadened as the content of GMAOH in the pre-polymerization solution increased, and peaks in this range of the spectrum can be attributed to the C–O stretch associated with the hydroxyl groups on the side chains.[8] The broadening of this peak is consistent with a shift toward a higher vicinal diol content of the co-polymer due to the presence of the second hydroxyl group on the GMAOH side chain.[8] Thus, these results suggest a qualitative increase in the co-polymer GMAOH content as the pre-polymerization solution GMAOH content increased.

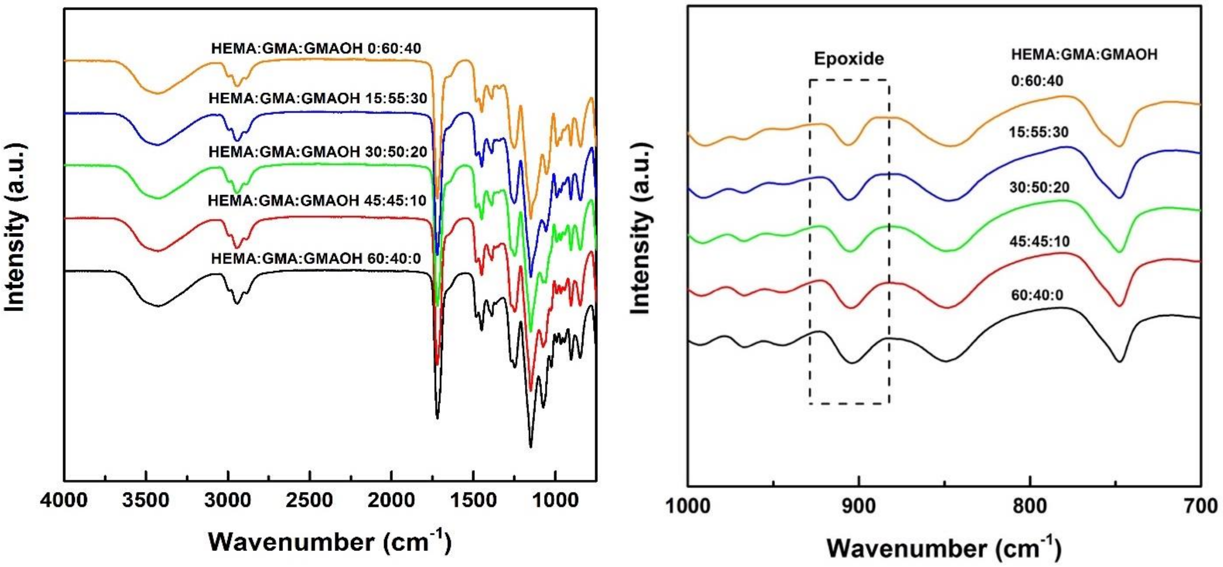

Figure D. 2. Fourier-transform infrared (FT-IR) spectra for dry HEMA:GMA:GMAOH co-polymers. The spectra were obtained in attenuated total reflectance mode using co-polymers that had been dried under vacuum for 24 hours after an approximately 2 month long period where the films were soaked in de-ionized (DI) water. The figure on the right highlights the 700 to 1000 cm^{-1} region of the spectra shown on the left.

Additionally, the FT-IR data suggest that the potentially reactive epoxide on the GMA side chain may be uniformly stable across the series of materials considered. The peak slightly above 900 cm^{-1} can be attributed to the epoxide on the GMA co-monomer.[8] This peak is similar for all of the materials. Furthermore, the FT-IR analysis was performed on co-polymers that had been soaked in de-ionized (DI) water for approximately 2 months (before being dried in advance of the FT-IR measurement). As such, the FT-IR results suggest that the epoxide functionality in the co-polymers remains after 2 months of soaking in DI water.

D.1.3 Thermal Properties

In the main text, the difference between the water/salt diffusivity selectivity properties of the HEMA:GMA:GMAOH and PEG materials is suggested to be due to the glassy nature of the HEMA:GMA:GMAOH co-polymers compared to the rubbery nature of the PEG materials. The glass transition temperatures of the materials can be used to further support this explanation. The PEG materials reported in Figures 5.1 and 5.2 in the main text[9] are cross-linked poly(ethylene glycol) diacrylate hydrogels, and these materials have reported glass transition temperatures that are all below 0°C.[10] As a result, the PEG materials referenced in the main text were all rubbery polymers at the room temperature measurement conditions.

The glass transition temperatures of the hydrated HEMA:GMA:GMAOH materials can be estimated using the Fox equation.[11, 12] While this approach is only a first approximation, it provides an estimate of the glass transition temperature of hydrated materials, such as HEMA:GMA:GMAOH, where the glass transition may be obscured by vaporization of some of the water sorbed in the polymer. Additionally, reasonable agreement between Fox equation calculated and measured glass transition temperatures has been reported for co-polymers containing HEMA.[13] The Fox equation suggests that the glass transition temperature of the hydrated HEMA:GMA:GMAOH co-polymers increases in the order of 108°C, 113°C, 116°C, 121°C, and 126°C as the pre-polymerization solution HEMA composition increases from 0 to 60% (by mass). As such, these materials can be assumed to be glassy materials at room temperature as the glass transition temperatures of the materials are expected to be well above room temperature.

Because segmental dynamics are significantly slower in glassy polymers compared to rubbery polymers,[14, 15] the segmental dynamics of the glassy HEMA:GMA:GMAOH co-polymers are likely much slower compared to the segmental dynamics in the rubbery PEG materials.

D.2. Experimental Methods

D.2.1 Water Uptake

Water uptake was measured gravimetrically by first equilibrating film samples in de-ionized (DI) water (18.2 MΩ cm) and subsequently drying the films under vacuum.[16-18] The dry polymer density was measured using an Archimedes principle method[16, 18] with cyclohexane, which was not sorbed to an appreciable extent by the co-polymers over the measurement timescale, as the auxiliary solvent. The water sorption coefficient, K_w, (or effectively the volume fraction of water in the co-polymer[19]) was calculated using a common volume additivity assumption.[5, 16, 17, 20-23] Samples were discarded and not characterized further after either the water uptake or density measurement process (i.e., all subsequent characterization was performed on separate samples that had not been dried following initial hydration).

D.2.2 Salt Sorption

Salt sorption was measured using a desorption procedure.[17, 24] Samples were initially equilibrated in an excess of 0.5 mol/L aqueous sodium chloride to allow salt to partition into the samples. The volume of the salt solution-equilibrated sample was determined by measuring the thickness and diameter of the circular coupons, and the sorbed salt was extracted from the sample by soaking the film in an excess of initially DI water.[17, 24] The salt sorption coefficient, K_s, was determined as the concentration of salt sorbed in the co-polymer relative to the concentration of salt in the solution used to initially equilibrate the sample.[24]

D.2.3 Pure Water Permeability

Hydraulic water permeability was measured using a dead-end cell apparatus.[16] DI water was pressurized on the upstream side of the sample at 200 psi (13.8 bar), and permeate was collected over time to determine the steady state water flux, which was converted to hydraulic water permeability by normalizing the water flux by film thickness and the applied pressure difference.[5] The hydraulic permeability was converted into the diffusive water permeability, P_w, using the convective frame of reference correction factor and assuming that mixing of polymer and water was thermodynamically ideal.[5, 16]

D.2.4 Salt Permeability

Salt permeability was measured using a diffusion cell apparatus.[16] The upstream side of the diffusion cell was charged with 100 mL of 0.5 mol/L aqueous sodium chloride, and the concentration of salt in the downstream side of the diffusion cell (initially charged with 100 mL DI water) was measured as a function of time using a conductivity probe. The salt permeability measurement was maintained at 25^{o}C by circulating water through the jacketed cell using a temperature-controlled circulator, and osmotic water transport was negligible over the approximately 1 hr long experiment. The concentration versus time data were combined with the measured film thickness to calculate the salt permeability of the sample.[16, 25]

D.2.5 Hydrated Polymer Dielectric Property Characterization

Dielectric permittivity properties were characterized from 0.45 to 20 GHz using a vector network analyzer (VNA) to study dipole relaxation dynamics of water sorbed in the materials. The measurement, described elsewhere,[17] was made on hydrated film samples that were wrapped around the center conductor of a 3.5 mm diameter coaxial transmission line. To improve the resolution of the dielectric loss spectra,[26] the annular space of the 5 cm long transmission line was filled with either 1 cm (for frequencies between 0.45 and 4 GHz) or 0.5 cm (for frequencies between 1 and 20 GHz) of sample. The remaining space in the transmission line was filled with air, which was accounted for during data analysis. The data measured between 1 and 4 GHz for the two different sample lengths overlapped, as expected. The calibrated VNA measured S-parameters were then related to the complex dielectric permittivity.[17, 27] The real part of the complex dielectric permittivity is the relative permittivity, ε', (often referred to as the dielectric constant) of the sample, and the imaginary part of the relative complex permittivity is the dielectric loss, ε'', of the sample.[28]

D.3. Microwave Dielectric Spectroscopy

We measured the microwave frequency dielectric loss spectra for the hydrated co-polymers to probe dipole relaxation dynamics of water sorbed in the materials. The dielectric loss spectra for the hydrated HEMA:GMA:GMAOH co-polymers have features similar to that of pure water.[17, 26, 29] This similarity is reasonable given that water dipoles relax in the microwave frequency range (as opposed to polymer segmental dynamics that relax at lower frequencies).[30]

As the HEMA content of the pre-polymerization solution used to prepare the co-polymer increased, the magnitude of the dielectric loss decreased, across the entire spectrum, but the shape of each spectrum remained similar (Figure D.3). This result suggests that, as the HEMA content of the pre-polymerization solution used to prepare the co-polymer increased, both energy dissipation and orientation polarizability for sorbed water molecules in the co-polymers decreased. This result may be due to a suppression of water motions caused by increased water interactions with the hydrophilic hydroxyl groups as the hydroxyl groups are more evenly distributed throughout the co-polymer.

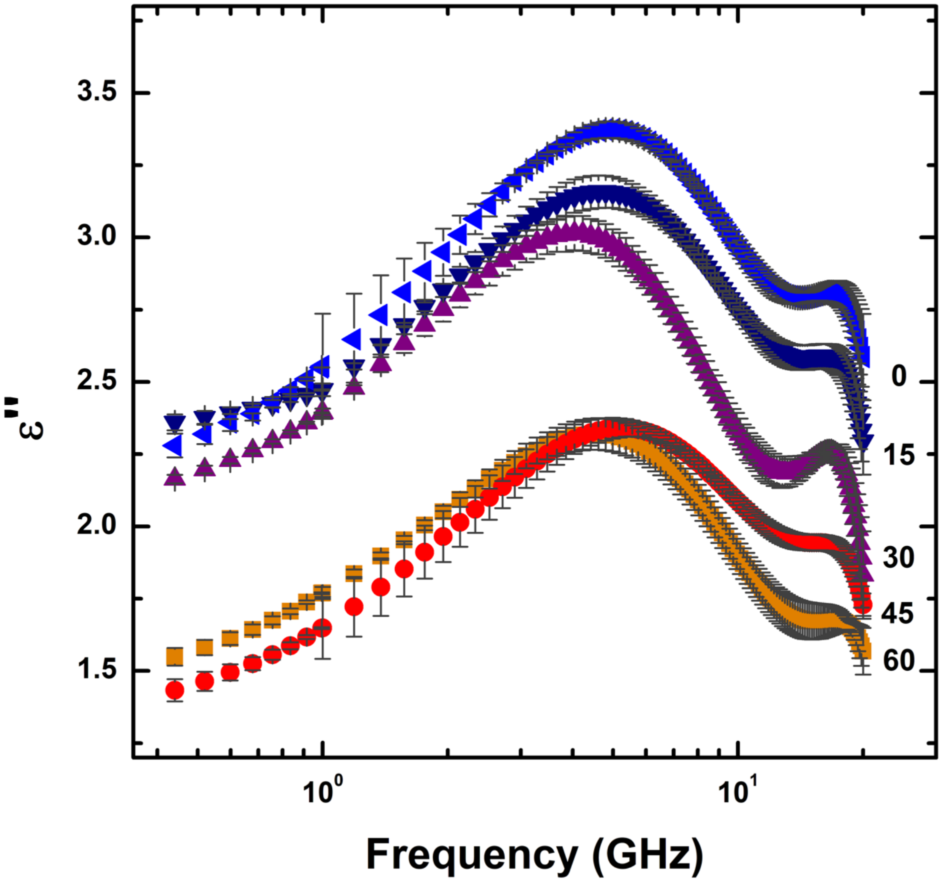

Figure D. 3. Frequency-dependent dielectric loss spectra, ε'', for the hydrated HEMA:GMA:GMAOH co-polymers. The spectra are labeled with the composition of the HEMA content of the pre-polymerization solution used to prepare the co-polymer. All measurements were made at 22 ± 1 ºC, and the uncertainty was taken as one standard deviation from the mean of three measurements.

To further analyze the water-polymer interactions in hydrated HEMA:GMA:GMAOH, we fit the dielectric loss data to a model containing three Debye relaxation processes that we attributed to three different water relaxation modes: highly restricted (HR) motion, less restricted (LR) motion, and non-restricted (NR) (i.e., bulk water) motion.[31-33] This approach is consistent with reports[26, 31, 34] suggesting that multiple Debye relaxation processes can be observed in hydrated polymers and that the necessary number of Debye relaxation processes depends on the polymer water content.[26, 34] The dielectric loss can be expressed as a summation over all relaxation processes, i, as:

$$\varepsilon'' = \sum_i \frac{\Delta\varepsilon_i \omega \tau_i}{1 + (\omega\tau_i)^2} \tag{S1}$$

We used a three relaxation model, so *i* represented the different relaxation modes (i.e., HR, LR, and NR). The dielectric strength, $\Delta\varepsilon_i$, is a measure of relative amount of water that contributes to a particular relaxation mode.[26] The frequency of the microwave radiation used in the measurement, *f*, was expressed as the angular frequency, $\omega = 2\pi f$, and the relaxation time constant of a particular relaxation mode, τ_i, is related to the frequency where maximum dielectric loss occurs, f_{max}, as $\tau_i = 1/2\pi f_{max}$.

In the three Debye relaxation model, six parameters ($\Delta\varepsilon_i$ and τ_i for i = HR, LR, and NR) are needed to describe the dielectric loss spectra (Figure D.3). Because the non-restricted relaxation mode was taken as that of bulk water, the value of τ_{NR} was fixed at a measured value of 8.8 ps.[17] The remaining five parameters (Table D.2) were regressed, for each of the co-polymers, using Equation S1 and a generalized reduced gradient, GRG, nonlinear method in Microsoft Excel. Regressions were performed separately on three spectra for each co-polymer, and the regressed parameters were averaged. The uncertainty in the regressed parameters was taken as one standard deviation from the average value.

Table D. 2. Relaxation time constants and dielectric strengths determined by fitting the dielectric loss spectra (Figure D.3) to a three Debye relaxation process model (Equation S1). The uncertainty was taken as one standard deviation from the mean of three parameters regressed from three distinct dielectric loss spectra.

Co-Polymer Sample	τ_{HR} (ps)	$\Delta\varepsilon_{HR}$	τ_{LR} (ps)	$\Delta\varepsilon_{LR}$	τ_{NR}[a] (ps)	$\Delta\varepsilon_{NR}$
0:60:40	401 ± 78	3.3 ± 0.2	46 ± 2	4.6 ± 0.1	8.8	3.5 ± 0.1
15:55:30	433 ± 8	3.5 ± 0.1	46 ± 1	4.4 ± 0.2	8.8	3.1 ± 0.2
30:50:20	485 ± 80	3.1 ± 0.1	51 ± 4	4.5 ± 0.2	8.8	2.5 ± 0.1
45:45:10	379 ± 29	2.0 ± 0.1	42 ± 2	3.2 ± 0.2	8.8	2.3 ± 0.1
60:40:0	377 ± 13	2.2 ± 0.1	43 ± 2	3.5 ± 0.1	8.8	1.7 ± 0.1

[a]The time constant for the non-restricted (i.e. bulk water) relaxation mode was fixed at a measured value of 8.8 ps.[17]

The results of the regression (Table D.2) suggest that the relaxation time constants for the three relaxation modes span two orders of magnitude. Additionally, the dielectric strength (and, thus, relative amount of water) associated with all three relaxation modes decreases as the HEMA content of the pre-polymerization solution used to prepare the materials increases. These results suggest that polymer chemistry influences the distribution of sorbed water across the different relaxation modes in water content equivalent materials. Preparing polymers with distributed hydrophilic groups (e.g., higher HEMA content in this study) may promote stronger water-polymer interactions.

D.4. Hydration of Hydroxyl Groups in HEMA and GMAOH

As discussed in the main text and Section S3, the microwave dielectric spectroscopy data suggest that water may hydrate the hydroxyl group on the HEMA side chain to a greater extent compared to the hydroxyl groups on the GMAOH side chain. In addition to the steric explanation discussed in the main text, an enthalpy of mixing analysis can be considered. In lieu of enthalpy of mixing data for the water:HEMA and water:GMAOH systems, enthalpy of mixing data were considered for the water:ethanol[35] and water:1,2-propanediol[36] systems, as the side chains of the HEMA and GMAOH co-monomers contain ethanol and 1,2-propanediol moieties, respectively.

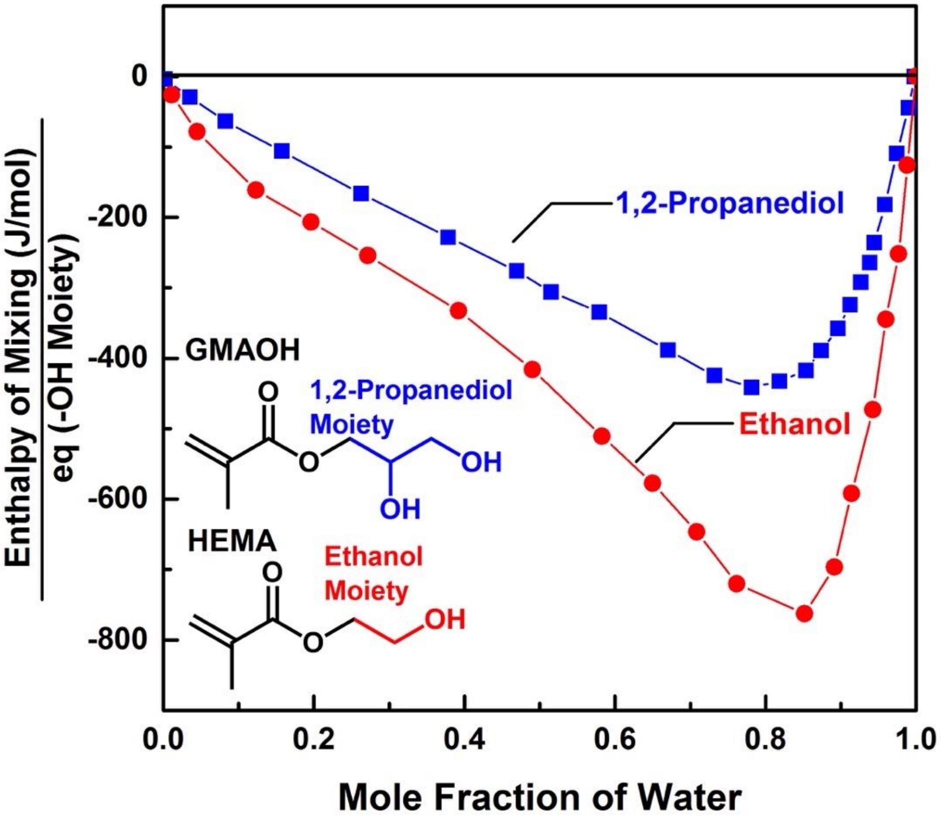

Figure D. 4. Enthalpy of mixing data as a function of mole fraction of water for mixtures of water and either ethanol[35] or 1,2-propanediol[36] at 25ºC. Ethanol and 1,2-propanediol were chosen because of their similarity to the side chain moieties on the HEMA and GMAOH co-monomers. The enthalpy of mixing data were normalized by the equivalents of –OH moieties in the organic molecule (i.e., 1 eq(–OH) for ethanol and 2 eq(–OH) for 1,2-propanediol).

The enthalpy of mixing data in Figure D.4 are normalized by the equivalents of –OH moieties in the organic molecule (i.e., 1 eq(–OH) for ethanol and 2 eq(–OH) for 1,2-propanediol). On this per eq(–OH) basis, the enthalpy of mixing data for water and ethanol are more negative (i.e., more thermodynamically favored) compared to the situation for water and 1,2-propanediol over the entire range of composition. Thus, the enthalpy of mixing data for representative small molecules and water further support the microwave dielectric data by suggesting that water may interact more strongly with the hydroxyl group on the HEMA side chain compared to the hydroxyl groups on the GMAOH side chain.

D.5. References

1. B.J. Sundell, E.-S. Jang, J.R. Cook, B.D. Freeman, J.S. Riffle, and J.E. McGrath, Cross-Linked Disulfonated Poly(arylene ether sulfone) Telechelic Oligomers. 2. Elevated Transport Performance with Increasing Hydrophilicity. Industrial & Engineering Chemistry Research, 2016. 55(5): p. 1419-1426.
2. M. Paul, H.B. Park, B.D. Freeman, A. Roy, J.E. McGrath, and J.S. Riffle, Synthesis and crosslinking of partially disulfonated poly(arylene ether sulfone) random copolymers as candidates for chlorine resistant reverse osmosis membranes. Polymer, 2008. 49: p. 2243-2252.
3. Y. Song, P. Sun, L.L. Henry, and B. Sun, Mechanisms of structure and performance controlled thin film composite membrane formation via interfacial polymerization process. Journal of Membrane Science, 2005. 251(1): p. 67-79.
4. R.J. Petersen, Composite reverse osmosis and nanofiltration membranes. Journal of Membrane Science, 1993. 83: p. 81-150.
5. G.M. Geise, D.R. Paul, and B.D. Freeman, Fundamental water and salt transport properties of polymeric materials. Progress in Polymer Science, 2014. 39(1): p. 1-42.
6. H. Yasuda, C.E. Lamaze, and L.D. Ikenberry, Permeability of solutes through hydrated polymer membranes Part I. Diffusion of sodium chloride. Die Makromolekulare Chemie, 1968. 118: p. 19-35.
7. P. Meares, The mechanism of water transport in membranes. Philosophical Transactions of the Royal Society of London B, 1977. 278: p. 113-150.
8. G. Socrates, *Infrared and raman characteristic group frequencies: Tables and charts*. 3rd ed. 2004, Hoboken, NJ: John Wiley & Sons.
9. H. Ju, A.C. Sagle, B.D. Freeman, J.I. Mardel, and A.J. Hill, Characterization of sodium chloride and water transport in poly(ethylene oxide) hydrogels. Journal of Membrane Science, 2010. 358: p. 131-141.
10. H. Ju, B.D. McCloskey, A.C. Sagle, V.A. Kusuma, and B.D. Freeman, Preparation and characterization of crosslinked poly(ethylene glycol) diacrylate hydrogels as fouling-resistant membrane coating materials. Journal of Membrane Science, 2009. 330(1): p. 180-188.
11. T.G.J. Fox and P.J. Flory, Second-order transition temperatures and related properties of polystyrene. I. Influence of molecular weight. Journal of Applied Physics, 1950. 21(6): p. 581-591.
12. P.C. Hiemenz and T.P. Lodge, *Polymer chemistry*. 2nd ed. 2007, Boca Raton, FL: CRC Press LLC.
13. K. Chang, A. Korovich, T. Xue, W.A. Morris, L.A. Madsen, and G.M. Geise, Influence of Rubbery versus Glassy Backbone Dynamics on Multiscale Transport in Polymer Membranes. Macromolecules, 2018. 51(22): p. 9222-9233.
14. D.W. Van Krevelen, *Properties of Polymers*. 3rd ed. 1997, Amsterdam: Elsevier.
15. I.M. Hodge, Physical aging in polymer glasses. Science, 1995. 267: p. 1945-1947.

16. H. Luo, J. Aboki, Y. Ji, R. Guo, and G.M. Geise, Water and Salt Transport Properties of Triptycene-Containing Sulfonated Polysulfone Materials for Desalination Membrane Applications. ACS Applied Materials & Interfaces, 2018. 10(4): p. 4102-4112.

17. K. Chang, H. Luo, and G.M. Geise, Water content, relative permittivity, and ion sorption properties of polymers for membrane desalination. Journal of Membrane Science, 2019. 574: p. 24-32.

18. Y. Ji, H. Luo, and G.M. Geise, Specific co-ion sorption and diffusion properties influence membrane permselectivity. Journal of Membrane Science, 2018. 563: p. 492-504.

19. G.M. Geise, B.D. Freeman, and D.R. Paul, Sodium chloride diffusion in sulfonated polymers for membrane applications. Journal of Membrane Science, 2013. 427: p. 186-196.

20. G.M. Geise, C.L. Willis, C.M. Doherty, A.J. Hill, T.J. Bastow, J. Ford, K.I. Winey, B.D. Freeman, and D.R. Paul, Characterization of aluminum-neutralized sulfonated styrenic pentablock copolymer films. Industrial & Engineering Chemistry Research, 2013. 52(3): p. 1056-1068.

21. A.C. Sagle, H. Ju, B.D. Freeman, and M.M. Sharma, PEG-based hydrogel membrane coatings. Polymer, 2009. 50: p. 756-766.

22. W. Xie, J. Cook, H.B. Park, B.D. Freeman, C.H. Lee, and J.E. McGrath, Fundamental salt and water transport properties in directly copolymerized disulfonated poly(arylene ether sulfone) random copolymers. Polymer, 2011. 52: p. 2032-2043.

23. H. Ju, A.C. Sagle, B.D. Freeman, J.I. Mardel, and A.J. Hill, Characterization of sodium chloride and water transport in crosslinked poly(ethylene oxide) hydrogels. Journal of Membrane Science, 2010. 358(1): p. 131-141.

24. G.M. Geise, L.P. Falcon, B.D. Freeman, and D.R. Paul, Sodium chloride sorption in sulfonated polymers for membrane applications. Journal of Membrane Science, 2012. 423-424: p. 195-208.

25. G.M. Geise, B.D. Freeman, and D.R. Paul, Characterization of a novel sulfonated pentablock copolymer for desalination applications. Polymer, 2010. 51(24): p. 5815-5822.

26. Z. Lu, G. Polizos, D.D. Macdonald, and E. Manias, State of water in perfluorosulfonic ionomer (Nafion® 117) proton exchange membranes. Journal of The Electrochemical Society, 2008. 155(2): p. B163-B171.

27. P.G. Bartley and S.B. Begley, A new technique for the determination of the complex permittivity and permeability of materials. IEEE Instrumentation & Measurement Technology Conference Proceedings, 2010: p. 54-57.

28. L.F. Chen, *Microwave Electronics: Measurement and Materials Characterization*. 2004, Hoboken, New Jersey: Wiley. xiii, 537 p. : ill. ; 26 cm.

29. W.J. Ellison, K. Lamkaouchi, and J.M. Moreau, Water: A dielectric reference. Journal of Molecular Liquids, 1996. 68(2): p. 171-279.

30. J.P. Runt and J.J. Fitzgerald, *Dielectric Spectroscopy of Polymeric Materials: Fundamentals and Applications*. 1997, Washington, DC: American Chemical Society.

31. Z. Lu, State of water in perfluorosulfonic acid membranes studied by microwave dielectric relaxation spectroscopy. 2006. Ph.D. Thesis, Department of Materials Science and Engineering, The Pennsylvania State University, University Park, Pennsylvania.

32. P. Debye, *Polar Molecules*. 1929, New York: Dover. 172 p. : ill. ; 23 cm.

33. G. Smith, A.P. Duffy, J. Shen, and C.J. Olliff, Dielectric relaxation spectroscopy and some applications in the pharmaceutical sciences. Journal of Pharmaceutical Sciences, 1995. 84(9): p. 1029-1044.

34. Z. Lu, M. Lanagan, E. Manias, and D.D. Macdonald, Two-Port Transmission Line Technique for Dielectric Property Characterization of Polymer Electrolyte Membranes. The Journal of Physical Chemistry B, 2009. 113(41): p. 13551-13559.

35. R.F. Lama and B.C.Y. Lu, Excess thermodynamic properties of aqueous alcohol solutions. Journal of Chemical & Engineering Data, 1965. 10(3): p. 216-219.

36. D.V. Batov, A.M. Zaichikov, V.P. Slyusar, and V.P. Korolev, Enthalpies of mixing and state of components in aqueous-organic mixtures with nets of hydrogen bonds. Russian Journal of General Chemistry, 2001. 71(8): p. 1208-1214.

Appendix E: Supporting information for Chapter 6

E.1. Descriptions of the Chemical Processes

Synthesis of zirconium tetrachloride ($ZrCl_4$) from zircon ($ZrSiO_4$)

The zirconium precursor for the solvothermal synthesis of UiO-66-NH_2, zirconium tetrachloride ($ZrCl_4$), is obtained from chlorination reaction of zircon ($ZrSiO_4$) at high temperature.[1] In a typical reaction, 30 kg of $ZrSiO_4$, 4 kg of char (C) and 75 kg of chlorine (Cl_2) are fed to a reactor at 1200 °C, and the chlorination reaction occurs in the following manner:

$$ZrSiO_4 + 2C + 4Cl_2 \rightarrow ZrCl_4 + SiCl_4 + 2CO_2 \tag{E.1}$$

At the reaction temperature, both the target product, $ZrCl_4$, and the byproduct, silicone tetrachloride ($SiCl_4$), are in the vapor phase, so therefore further separation is necessary. The post-reaction vapor mixture is cooled down to 200 to 300 °C to allow for the desublimation of $ZrCl_4$. Finally, $ZrCl_4$ is collected as a white powder, and its purity is enough for the synthesis of UiO-66-NH_2. The typical yield of $ZrCl_4$ was reported to be ~90%. It should be note that the vapor mixture after $ZrCl_4$ separation still contains $SiCl_4$, which could be condensed at even lower temperature. However, in this work, we decided not to include the production of $SiCl_4$ when we estimate the life cycle impact data of $ZrCl_4$ since $SiCl_4$ is usually produced from other processes. If the production of $SiCl_4$ were to be considered in the process above, then the environmental burdens associated with $ZrCl_4$ production will be lower.

Synthesis of zirconyl chloride octahydrate ($ZrOCl_2 \cdot 8H_2O$) from $ZrCl_4$

The zirconium precursor for the aqueous solution-based synthesis of UiO-66-NH_2, zirconyl chloride octahydrate ($ZrOCl_2 \cdot 8H_2O$), is obtained from the direct hydrolysis reaction of $ZrCl_4$.[2]

In a typical reaction, 0.95 kg of $ZrCl_4$, 2.4 kg of DI water and 0.75 kg 20% hydrochloric acid (HCl) solution are fed to a reactor at 50 ℃, and the hydrolysis reaction occurs in the following manner:

$$ZrCl_4 + H_2O \rightarrow ZrOCl_2 + 2HC \tag{E.2}$$

The post reaction solution is further concentrated at 90 ℃ under vacuum, such that the equivalent concentration of ZrO_2 in the solution reaches 190±10 g/L. The concentrated solution is sent to a crystallizer to allow for the crystallization of $ZrOCl_2\cdot 8H_2O$, and the primary mother liquor is concentrated again for secondary crystallization. The typical yield of $ZrOCl_2\cdot 8H_2O$ was reported to be ~90%. It should be noted that $ZrOCl_2\cdot 8H_2O$ could also be produced from other processes, but the process described above was reported to be more cost-effective and energy-saving.[2-4]

Synthesis of 2-amino terephthalic acid from terephthalic acid

The 2-amino terephthalic acid (2-ATA) could be synthesized from terephthalic acid (TPA) *via* nitration and hydrogenation, and the typical synthesis conditions from literature are summarized below.[5, 6]

Nitration of TPA: In a cooling water bath, 2 g of TPA was slowly added to 10 g of 98% sulfuric acid (H_2SO_4) under continuous stirring. The resulting viscous mixture was stirred for 10 min, and then 3 g of 68% nitric acid (HNO_3) was added dropwisely. When the HNO_3 addition was done, the cooling water bath was removed, and the mixture was heated to 353 K and stirred at this temperature for 10 hours. Upon the completion of the nitration reaction, the mixture was cooled down to room temperature, and the product, 2-nitro terephthalic acid (2-NTA), was separated from the mixture by vacuum filtration. The crude 2-NTA, collected as the filter cake, still contained acids and needed to be further purified. Hence, cold de-ionized water (DI water) was filtered through the filter cake, and the washing process was repeated until the filtrate pH reached 6. The use of cold DI water in the washing step could minimize the dissolution of 2-NTA. Finally, the purified 2-NTA was dried at room temperature under vacuum. The typical yield for this nitration reaction is 72%±10%.

Hydrogenation of 2-NTA: In a stainless steel hydrogenator, 4.223 g of 2-NTA, 1.6 g of sodium hydroxide and 0.5 g 5% palladium-on-carbon (Pd/C) catalyst was added to 100 mL DI water. This step would produce a suspension of Pd/C catalyst in disodium 2-NTA (2-NTA-Na_2) solution. The hydrogenator was first flushed with nitrogen to remove oxygen and then flushed with hydrogen to replace nitrogen. The hydrogenation reaction was then allowed to proceed at 50 psi and at room temperature for a designated time (e.g., 12 h). Upon the completion of the hydrogenation reaction, the solution was filtered to recover the Pd/C catalyst, and he filtrate, disodium 2-ATA (2-ATA-Na_2) solution, was acidified with 4 g of 36.5% hydrochloric acid (HCl). The acidification process would protonate 2-ATA-Na_2 into 2-ATA, which is insoluble in water and would crush out from the solution as a yellow powder. The crude 2-ATA was separated from the slurry by vacuum filtration, and was washed with DI water in the same manner as 2-NTA. Finally, the purified 2-ATA was dried at room temperature under vacuum. The typical yield for the hydrogenation reaction is 60%±10%.

Synthesis of UiO-66-NH_2

The UiO-66-NH_2 could be synthesized from a zirconium source (e.g., zirconium chloride ($ZrCl_4$) and zirconyl chloride octahydrate ($ZrOCl_2 \cdot 8H_2O$)) and the 2-ATA using both the solvothermal synthesis and the aqueous solution-based synthesis, and the typical synthesis conditions are summarized below.[7, 8]

Conventional solvothermal synthesis: Solvothermal approach is the most commonly used method for UiO-66-NH_2 synthesis. In a typical experiment, 0.125 g of $ZrCl_4$ and 0.134 g of 2-ATA were first dissolved in 15 mL N,N-dimethylformamide (DMF), and this DMF solution was further acidified by adding 1 mL 36.5% HCl. The precursor solution was transferred into a 30 mL Teflon lined stainless steel autoclave, and the autoclave was kept in a convection oven at 393 K for 24 hours, during which the UiO-66-NH_2 nanocrystals were formed by nucleation and growth. Upon the completion of the solvothermal synthesis, the autoclave was cooled down to room temperature and disassembled, and the UiO-66-NH_2 nanocrystals were separated from the post-reaction mixture, washed with 15 mL of an appropriate solvent (e.g., methanol or water) for three times and dried at the normal boiling temperature for the washing solvent (e.g., 338 K for methanol) for 24 hours.

Aqueous solution-based synthesis of UiO-66-NH_2: In this synthesis method, the zirconium-oxo-cluster solution and the 2-ATA-Na_2 solution were prepared separately. To prepare the zirconium-oxo-cluster solution, 1.288 g of $ZrOCl_2 \cdot 8H_2O$, 5 mL acetic acid (AcOH) and 12 mL DI water were first mixed in a 50 mL round bottom flask to form a transparent solution. This solution was heated in an oil bath at 343 K for 2 hours under continuous stirring. After the solution cooled down to room temperature, 1.325 g of sodium carbonate (Na_2CO_3) was slowly added to the solution, to partially neutralize the acid. To prepare the linker solution, 0.724 g 2-ATA and 0.32 g sodium hydroxide (NaOH) were dissolved in 20 mL DI water. The zirconium-oxo-cluster solution and the 2-ATA-Na_2 solution were simultaneously poured into a 100 mL glass beaker, and the resulting yellow slurry was further stirred vigorously for 5 min, during which the UiO-66-NH_2 nanocrystals were formed. Upon the completion of the reaction, the UiO-66-NH_2 crystals were separated from the post-reaction mixture, washed with 20 mL 0.1% NaOH solution for three times and 20 mL DI water for 3 times, and dried at 373 K for 24 hours.

E.2. Assumptions in the process scaling-up

Producing UiO-66-NH_2 at the lab scale could be very different than producing UiO-66-NH_2 at the pilot scale, even though the batch-to-batch production feature is preserved. For example, the solvent or the reaction medium might be recycled or reused in a pilot-scale plant to minimize the environmental impacts and maximize the economic impacts of the production process, whereas the solvent or reaction medium is often considered for single-use in a lab. Hence, we made several assumptions in the process scaling-up to capture/mimic the features of the hypothetical pilot scale production of UiO-66-NH_2. These assumptions are likely to be incomprehensive since no information on the large-scale production of UiO-66-NH_2 (e.g., a plant that produces ~10 t of UiO-66-NH_2 per year) is available, yet we hope our assumptions could help with further process design/development/refinement by other researchers.

Assumptions for the nitration reaction: In the nitration reaction, HNO_3 reacts with PTA to form 2-NTA and water, and water is absorbed by concentrated H_2SO_4 to maintain a forward reaction (i.e., forming 2-NTA). If we assume the conversion of the limiting reactant, TPA, is 100% and the loss of both HNO_3 and H_2SO_4 during filtration is negligible (e.g., < 5%), then the net change to the nitration medium (i.e., HNO_3 and H_2SO_4) is the net consumption of HNO_3 and the net introduction of water. If the concentration of the concentrated H_2SO_4 does not drop significantly, this concentrated H_2SO_4 could be reused as water trap for another nitration reaction. Li *et al*. used an 82% H_2SO_4 for the nitration reaction, so therefore we assume that 82% is the minimum required concentration for the concentrated H_2SO_4 at the beginning of the nitration reaction.[5] Meanwhile, the consumed HNO_3 is replenished at the beginning of the next nitration reaction. Based on these assumptions and the nitration reaction description, we did the following calculations to determine the maximum reuse number of the nitration medium as well as the required mass of HNO_3 for each replenishment:

$$Net\ consumption\ of\ dry\ HNO_3\ in\ one\ reaction = \frac{m_{TPA}}{MW_{TPA}} \times MW_{HNO_3} = \left(\frac{2}{166.13} \times 63.01\right)\ g \qquad \text{(E.3)}$$

$$= 0.759\ g$$

$$Net\ replenishment\ of\ 68\%\ HNO_3\ for\ one\ reaction = \frac{m_{HNO_3,dry}}{0.68} = \left(\frac{0.759}{0.68}\right)\ g = 1.116\ g \qquad \text{(E.4)}$$

$$Net\ introduction\ of\ water\ in\ one\ reaction = \frac{m_{TPA}}{MW_{TPA}} \times MW_{H_2O} + m_{HNO_3,68\%} \times \omega_{H_2O}$$

$$= \left(\frac{2}{166.13} \times 18.02 + 3 \times 0.32(\text{first reaction})\ or\ 1.116 \times 0.32(\text{from the 2nd reaction})\right)\ g \qquad \text{(E.5)}$$

$$= 1.177\ g\ (\text{first reaction})\ or\ \ 0.574\ g\ (\text{from the 2nd reaction})$$

$$Concentration\ of\ H_2SO_4\ after\ nth\ reuse = \frac{m_{H_2SO_4,dry}}{m_{H_2SO_4,dry} + m_{H_2O}} \qquad \text{(E.6)}$$

$$= \frac{10 \times 0.98}{10 \times 0.98 + 10 \times 0.02 + 1.177 + n \times 0.574} \times 100\%$$

$$= 87.7\%\ (n = 0)\ or\ 83.4\%\ (n = 1) or\ 79.5\%\ (n = 2)$$

The calculations above suggest the concentration of H_2SO_4 is above 82% after the first reuse and below 82% after the second reuse. Therefore, the maximum reuse number of the nitration medium is 2. Now, we can integrate the nitration medium reuse into the description of the single loop nitration reaction and calculate the materials input for 3 nitration reactions:

$$Net\ consumption\ of\ TPA\ in\ three\ reactions = 2\ g \times 3 = 6\ g \tag{E.7}$$

$$Net\ use\ of\ 98\%\ H_2SO_4\ in\ three\ reactions = 10\ g$$ (E.8

$$Net\ use\ of\ 68\%\ HNO_3\ in\ three\ reactions = 3 + 1.116 \times 2 = 5.232\ g \tag{E.9}$$

By reusing the nitration medium, the net use of H_2SO_4 and HNO_3 dropped by 66.7%, and 41.9%, respectively. The drop in the net acid use makes the process more favorable both from the environmental impact aspect and the economic impact aspect. First, the less the acid is used, the lower the environmental burdens (e.g., terrestrial acidification)[9] the process creates. Nevertheless, when less acid is used, the cost associated with purchasing and treating acid is also reduced. The same criteria will be adapted in the following sections when we consider the necessity of recycling other chemicals.

Assumptions for the hydrogenation reaction: In the hydrogenation reaction, the nitro group in the 2-NTA is reduced to the amino group by hydrogen in the presence of the Pd/C catalyst.[6] The supply of hydrogen to the reaction system could be achieved in several manners. For example, hydrogen could be continuously bubbled through the solution at a constant flowrate and pressure, or it could be added in small portions to maintain the desired pressure (e.g., 50 psi) of the reaction system.[10] The latter manner usually requires the minimum consumption of hydrogen, i.e., the hydrogen consumed by the reaction and the hydrogen required to pressurize the hydrogenator to the desired pressure, so therefore we will assume the supply of hydrogen to the reaction system is achieved in this manner. If we assume the fill rate of the hydrogenator is 50%, i.e., a 200 mL hydrogenator is used for the reaction described previously, then the net use of hydrogen in one hydrogenation reaction is:

$$Net\ use\ of\ hydrogen\ in\ 1\ reaction = \frac{m_{2-NTA}}{MW_{2-NTA}} \times MW_{H_2} \times 2 + \rho_{H_2} V_{H_2} \tag{E.10}$$

$$= \frac{4.223}{211.13} \times 2 \times 2 + 0.285 \times 0.1 = 0.109\ g$$

Also, unlike the nitration reaction, where the reaction medium is an acid mixture, the hydrogenation reaction is carried out in water, and the final solution (i.e., after acidification and 2-ATA separation) is a NaCl solution, which does not create huge environmental burdens or significant economic interests. Therefore, reuse of the hydrogenation medium is unnecessary. However, in the hydrogenation reaction, the Pd/C catalyst is rather expensive, so the recovery (and perhaps the reactivation) of the catalyst is necessary. Here, we assume the Pd/C recovery rate is 95% after each hydrogenation reaction and the average lifetime of Pd/C is 20 reactions. The net use of the Pd/C catalyst over 10 hydrogenation reactions is:

$$Net\ use\ of\ Pd/C\ catalyst\ in\ 20\ reactions = 0.5 + 0.5 \times 0.05 \times 20 = 1\ \ g \tag{E.11}$$

Assumptions for the conventional solvothermal synthesis: In the conventional solvothermal synthesis of UiO-66-NH_2, the UiO-66-NH_2 is obtained from the reaction between $ZrCl_4$ and 2-ATA in DMF, and is further washed methanol.[7] In this synthesis process, both DMF and methanol are presented in large excess, have significant economic interests (i.e., both solvents are much more expensive than water) and could create huge environmental burdens. Therefore, the recycle of both DMF and methanol from the synthesis process is necessary, and we assume the recycle rate for both of them is 90%, which is a value commonly used in industry and other LCA works.[11] However, DMF and methanol have very different normal boiling points, i.e., 426 K for DMF vs. 337 K for methanol, so different recycle processes will be adapted. More specifically, the methanol is recycled by ambient pressure distillation (e.g., 1 bar, 337 K), while DMF is recycled by vacuum distillation (e.g., 0.15 bar, 373 K). By integrating the solvent recycle into the conventional solvothermal synthesis, the net use of solvent for one synthesis is:

$$Net\ use\ of\ DMF\ in\ 1\ synthesis = 15\ mL \times 0.1 \times 0.944\ g/mL = 1.416\ \ g \tag{E.12}$$

$$Net\ use\ of\ methanol\ in\ 1\ synthesis = 15\ mL \times 0.1 \times 3 \times 0.792\ g/mL = 3.564\ \ g \tag{E.13}$$

Assumptions on the UiO-66-NH₂ yield: Traditionally, researchers assume the percentage yield of MOFs is identical to the percentage conversion of the limiting reactant, regardless of the percentage crystallinity of the obtained MOFs.[8] Such an assumption might work well if the percentage crystallinity of the MOFs is close to 100%, or the percentage crystallinity has no impact on the performance of the MOFs in certain applications. Alternatively, the percentage yield could be taken as the product of the percentage conversion of the limiting reactant and the percentage crystallinity of the MOFs.[8] This alternative definition is more conservative as it assumes the crystalline MOFs are the desired product. These two definitions lead to different choices of the functional unit (FU). If the first definition is used, i.e., the percentage yield is simply the conversion of the limiting reactant, then we set the FU to be 1 kg of UiO-66-NH_2. If the alternative definition is used, i.e., the crystallinity of the UiO-66-NH_2 is considered, then we set the FU to be 1 kg of *crystalline* UiO-66-NH_2.

In this work, both FUs will be used in the process scaling up, and we will consider three different cases (e.g., case 1, 2 and 3). First, in case 1, we will scale up process the using assumption that both the limiting reactant-to-product conversion and the product percentage crystallinity is 100%, i.e., the overall yield is 100%. Next, in case 2, we will scale up the process by setting the FU to be 1 kg of UiO-66-NH_2, i.e., the limiting reactant-to-product conversion will be considered. Finally, in case 3, we will scale up the process using by setting the FU to be 1 kg of *crystalline* UiO-66-NH_2, i.e., both the limiting reactant-to-product conversion and the product percentage crystallinity will be considered. By comparing the three cases, it is not difficult to find that case 1 and case 3 are the global limiting cases as they represent the minimum/maximum environmental burdens and costs of the process.

Assumptions for the process heating/drying: In the production of UiO-66-NH_2, heat is required to bring a mixture to its desired reaction temperature or evaporate the solvent from an intermediate/the final product. In lab-scale synthesis, such heat is usually supplied by an oil bath or a convection oven, so consequently a large excess amount of heat is wasted. Therefore, in the process scaling up, we assume the heat is supplied by natural gas combustion, and the heat loss factor is 25%.[12, 13] Additionally, we assume that, for all solutions/reaction mixtures, the amount of heat required is calculated based on the mass of the solvent and the heat capacity of the solvent. In other words, the contribution of the dissolved solids to the total heat is neglected. Furthermore, unless otherwise specified, we assume the residual solvent content in a wet product is 50% (by mass), and the residual solvent is brought up to its normal boiling point (e.g., 338 K for methanol and 373 K for water) for evaporation. The heat required for solvent distillation is calculated in the same manner as the heat required for drying. The following equations are used to calculate the heat associated with heating and drying:

$$H_{heating} = (m_{solvent} \times C_{p,solvent} \times (T - 25)^\circ C))/0.75 \tag{E.14}$$

$$H_{drying} = [(m_{solvent} \times C_{p,solvent} \times (T_b - 25)^\circ C) + m_{solvent} \times \Delta \mathrm{H}_{\mathrm{vap}}(T_b)]/0.75 \tag{E.15}$$

The following tables summarize the materials and heat input for the production of UiO-66-NH_2 before and after scaling up. As mentioned in the main text, the FU is 1 kg of UiO-66-NH_2 so we set the mass of the UiO-66-NH_2 to 1 kg after scaling up. The values in Table E.1 are directly summarized from the previous process descriptions. The values in Table E.2 are obtained by modifying the values in Table E.1 with the pilot plant scaling assumptions, so therefore the values in Table E.2 are used as the basis for direct scaling up. The values in Table E.3 through Table E.8 are the final scaled-up values.

E.3. Mass and Energy Inputs for Life-cycle Analysis

Table E. 1. Summary of the materials and energy input for the production of UiO-66-NH_2 before scaling up. For solutions, solvents and other liquid form chemicals that have a usage reported in volume, their mass is calculated as the product of the volume (*V*), the density (ρ) and the mass fraction (ω), i.e., $m = V\rho\omega$. The typical density values (g/mL) for the solutions, solvents and other liquid form chemicals used in this work are 1.19 for 36% HCl solution, 0.944 for DMF, 0.792 for MeOH, 1 for H_2O, 1.05 for AcOH, respectively.[14]

	Input Chemical Name	***Mass (g)***	***Output Product Name***	***Mass (g)*** [e f g]	***Heat (kJ)*** [h i]
Nitration of TPA	TPA H_2SO_4 [a] HNO_3 [a]	2.000 9.800 2.040	2-NTA	1.830	7.727

	Water	1.160			
Hydrogenation of 2-NTA	2-NTA	4.223	2-ATA	2.173	7.075
	NaOH	1.600			
	H_2	0.109			
	Pd/C	0.500			
	HCl [a]	1.460			
	Water	102.540			
Conventional solvothermal synthesis	$ZrCl_4$ [b]	0.125	UiO-66-NH_2	0.153	4.424-4.703
	2-ATA	0.134			
	HCl [a]	0.4284			
	Water [d]	0.7616/45.7616			
	DMF	14.160			
	MeOH	35.640/0			
Aqueous solution-based synthesis	$ZrOCl_2 \cdot 8H_2O$ [c]	1.288	UiO-66-NH_2	1.141	7.608
	2-ATA [c]	0.724			
	AcOH	5.25			
	NaOH	0.38			
	Na_2CO_3	1.325			
	Water [d]	152.000			

[a] Dry-base mass.

[b] $ZrCl_4$ is the limiting reactant in the solvothermal synthesis.

[c] Either $ZrOCl_2 \cdot 8H_2O$ or 2-ATA could be considered as the limiting reactant because they were fed in stoimetric ratio.

[d] The amount of water presented may contain water used for washing. In the conventional solvothermal synthesis, either MeOH or water is used as the washing solvent.

[e] The mass of 2-NTA and 2-ATA is calculated using the average yield.

[f] The limiting reactant-to-product yield is assumed to be 100% for UiO-66-NH_2.

[g] The formula for UiO-66-NH_2 is $Zr_{24}O_{120}C_{192}H_{96}N_{24}$, which has a formula weight of 6848.10 g/mol.[15]

[h] The heat in the third entree is reported as a range due to the use of different washing solvent.

[i] The heat capacity values (J/g°C) used for the calculations are 1.41 for pure H_2SO_4,[16] 1.746 for pure HNO_3,[17] 4.184 for water,[18] 2.21 for DMF-water mixture (DMF wt% =95%),[19] 2.53 for methanol,[20] and 3.62 for AcOH-water mixture (water wt% = 69.5%),[21] respectively. The latent heat of vaporization (kJ/g) used for the calculation is 2.26 for water at 373 K,[22] 2.44 for water at 298 K,[22] and 1.11 for methanol at 338 K.[23]

Table E. 2. Summary of the *modified* materials and energy input for the production of UiO-66-NH_2 before scaling up. The pilot plant scaling assumptions are adapted in this table.

	Input Chemical Name	***Mass (g)***	***Output Product Name***	***Mass (g)***	***Heat (kJ)***
Nitration of TPA [a]	TPA	6.000	2-NTA	5.490	22.923
	H_2SO_4	9.800			
	HNO_3	3.558			

	Water	2.525			
Hydrogenation of 2-NTA [b]	2-NTA	84.460	2-ATA	43.460	141.488
	NaOH	32.000			
	H_2	2.180			
	Pd/C	1.000			
	HCl	29.200			
	Water	2050.800			
Conventional solvothermal synthesis [c]	$ZrCl_4$	0.125	UiO-66-NH_2	0.153	17.212-68.735 [d]
	2-ATA	0.134			
	HCl	0.4284			
	Water	0.7616/45.7616			
	DMF	1.146			
	MeOH	3.564/0			
Aqueous solution-based synthesis	$ZrOCl_2 \cdot 8H_2O$	1.288	UiO-66-NH_2	1.141	7.608
	2-ATA	0.724			
	AcOH	5.250			
	NaOH	0.380			
	Na_2CO_3	1.325			
	Water	152.000			

[a] Values are based on 3 reactions (i.e., lifetime of the nitration medium)

[b] Values are based on 20 reactions (i.e., lifetime of the Pd/C catalyst)

[c] Both DMF and methanol have a recovery rate of 90%

[d] The heat capacity values (J/g°C) used for the calculations are 2.06 for pure DMF,[19] and 2.53 for methanol,[20] respectively. The latent heat of vaporization (kJ/g) used for the calculation is 2.26 for water at 373 K,[22] 0.581 for DMF at 373 K,[24] and 1.11 for methanol at 338 K.[23]

Table E. 3. Summary of the materials and energy input for the conventional solvothermal production of UiO-66-NH_2 after scaling up. The limiting reactant-to-product yield is assumed to be 100%. (case 1)

	Input Chemical Name	***Mass (kg)***	***Output Product Name***	***Mass (kg)***	***Heat (MJ)***
Nitration of TPA	TPA	1.860	2-NTA	1.702	7.107
	H_2SO_4	3.038			
	HNO_3	1.103			
	Water	0.783			
Hydrogenation of 2-NTA	2-NTA	1.702	2-ATA	0.876	2.851
	NaOH	0.645			
	H_2	0.044			
	Pd/C	0.020			

	HCl	0.588			
	Water	41.328			
Conventional solvothermal synthesis	$ZrCl_4$	0.817	UiO-66-NH_2	1.000	112.497-448.979
	2-ATA	0.876			
	HCl	2.800			
	Water	4.978/299.095			
	DMF	9.255			
	MeOH	23.294/0			

Table E. 4. Summary of the materials and energy input for the aqueous-solution based production of UiO-66-NH_2 after scaling up. The limiting reactant-to-product yield is assumed to be 100%. (case 1)

	Input Chemical Name	***Mass (kg)***	***Output Product Name***	***Mass (kg)***	***Heat (MJ)***
Nitration of TPA	TPA	1.348	2-NTA	1.233	5.149
	H_2SO_4	2.201			
	HNO_3	0.799			
	Water	0.567			
Hydrogenation of 2-NTA	2-NTA	1.233	2-ATA	0.635	2.065
	NaOH	0.467			
	H_2	0.032			
	Pd/C	0.015			
	HCl	0.426			
	Water	29.942			
Aqueous solution-based synthesis	$ZrOCl_2 \cdot 8H_2O$	1.128	UiO-66-NH_2	1.000	6.668
	2-ATA	0.635			
	AcOH	4.601			
	NaOH	0.333			
	Na_2CO_3	1.161			
	Water	133.216			

Table E. 5. Summary of the materials and energy input for the conventional solvothermal production of UiO-66-NH_2 after scaling up. The limiting reactant-to-product yield is assumed to be 38% (experimentally determined from our previous work).[8] (case 2)

	Input Chemical Name	***Mass (kg)***	***Output Product Name***	***Mass (kg)***	***Heat (MJ)***
Nitration of TPA	TPA	4.895	2-NTA	4.479	18.702
	H_2SO_4	7.995			
	HNO_3	2.092			

	Water	2.060			
Hydrogenation of 2-NTA	2-NTA	4.479	2-ATA	2.305	7.503
	NaOH	1.697			
	H_2	0.116			
	Pd/C	0.053			
	HCl	1.549			
	Water	108.758			
Conventional solvothermal synthesis	$ZrCl_4$	2.150	UiO-66-NH_2	1.000	296.044-1182.227
	2-ATA	2.305			
	HCl	7.368			
	Water	13.099/787.093			
	DMF	24.355			
	MeOH	61.300/0			

Table E. 6. Summary of the materials and energy input for the aqueous-solution based production of UiO-66-NH_2 after scaling up. The limiting reactant-to-product yield is assumed to be 96% (experimentally determined from our previous work).[8] (case 2)

	Input Chemical Name	*Mass (kg)*	*Output Product Name*	*Mass (kg)*	*Heat (MJ)*
Nitration of TPA	TPA	1.404	2-NTA	1.285	5.363
	H_2SO_4	2.293			
	HNO_3	0.832			
	Water	0.591			
Hydrogenation of 2-NTA	2-NTA	1.285	2-ATA	0.661	2.152
	NaOH	0.487			
	H_2	0.033			
	Pd/C	0.015			
	HCl	0.444			
	Water	31.190			
Aqueous solution-based synthesis	$ZrOCl_2 \cdot 8H_2O$	1.176	UiO-66-NH_2	1.000	6.946
	2-ATA	0.661			
	AcOH	4.793			
	NaOH	0.347			
	Na_2CO_3	1.210			
	Water	138.767			

Table E. 7. Summary of the materials and energy input for the conventional solvothermal production of UiO-66-NH_2 after scaling up. The limiting reactant-to-product yield is 18% (experimentally determined from our previous work, 38% conversion and 47% crystallinity).[8] (case 3)

	Input Chemical Name	*Mass (kg)*	*Output Product Name*	*Mass (kg)*	*Heat (MJ)*
Nitration of TPA	TPA	10.334	2-NTA	9.456	39.481
	H_2SO_4	16.879			
	HNO_3	6.128			
	Water	4.349			
Hydrogenation of 2-NTA	2-NTA	9.456	2-ATA	4.866	15.840
	NaOH	3.583			
	H_2	0.244			
	Pd/C	0.112			
	HCl	3.269			
	Water	229.601			
Conventional solvothermal synthesis	$ZrCl_4$	4.539	UiO-66-NH_2	1.000	624.981-2495.812
	2-ATA	4.866			
	HCl	15.556			
	Water	27.654/1661.641			
	DMF	51.416			
	MeOH	129.412/0			

Table E. 8. Summary of the materials and energy input for the aqueous-solution based production of UiO-66-NH_2 after scaling up. The limiting reactant-to-product yield is 36% (experimentally determined from our previous work, 96% conversion and 38% crystallinity).[8] (case 3)

	Input Chemical Name	*Mass (kg)*	*Output Product Name*	*Mass (kg)*	*Heat (MJ)*
Nitration of TPA	TPA	3.744	2-NTA	3.425	14.303
	H_2SO_4	6.115			
	HNO_3	2.220			
	Water	1.575			
Hydrogenation of 2-NTA	2-NTA	3.425	2-ATA	1.763	5.739
	NaOH	1.289			
	H_2	0.088			
	Pd/C	0.041			
	HCl	1.184			
	Water	83.173			
Aqueous solution-based synthesis	$ZrOCl_2 \cdot 8H_2O$	3.136	UiO-66-NH_2	1.000	18.521
	2-ATA	1.763			
	AcOH	12.781			
	NaOH	0.925			
	Na_2CO_3	3.226			

	Water	370.046

E.4. Assumptions in the techno-economic analysis (TEA)

In the previous sections, we discussed how the UiO-66-NH_2 production process at the pilot scale is different from that at the lab scale, and several assumptions were made in the process scaling up. Similarly, the economic aspects of pilot-scale production are also different from those of lab-scale production. For example, the chemicals are usually purchased in bulk in pilot-scale production whereas they are often purchased in small quantities in lab-scale production. Additionally, equipment with large capacity is used in pilot-scale production. Both purchasing the chemicals in bulk and using larger equipment lead to lower production costs and make the product UiO-66-NH_2 more economically attractive. Therefore, we made several assumptions on the purchase of the chemicals and the selection of the equipment. Again, these assumptions only represent the best of our knowledge, and their validity may vary depending on the location of the hypothetical pilot-scale plant (i.e., the pricing data in China might be significantly different from those in the United States).

Assumptions for the chemical purchases: Among the chemicals required for the production of UiO-66-NH_2, 2-ATA is the only one that we decided to produce on-site, so therefore all other chemicals would be purchased from the commercial vendors in bulk. In the bulk purchases, the price of H_2 and Pd/C is determined on the kilogram base due to its availability, while the price of all other chemicals is determined on the metric-ton base. Furthermore, the real price of Pd/C is different from the listed price, because Pd/C will be purchased back and regenerated by the vendors at the end of its lifetime. Therefore, in the TEA, we assume the real price of Pd/C is 20% of the listed price, and this real price could be regarded as the “rental fee” of Pd/C. The price of all chemicals used in the production is listed in Table E.9.

Assumptions for the productions: For both the conventional solvothermal production and the aqueous solution-based production, we assume 1 FU, i.e., 1 kg of UiO-66-NH_2, is produced per batch, and the production of 1 FU/batch will be used in equipment selection and pricing (i.e., one set of equipment is capable for producing 1 FU/batch). For the conventional solvothermal production, we assume the production rate is 1 batch/day in the hypothetical pilot-scale plant. For the aqueous solution-based production, we assume the production rate is 3 batches/day due to its high space-time-yield (STY) feature.

Assumption for the equipment selection: The selection of the equipment depends on the size and the material of the equipment. The size of the equipment is determined from the volume of the reaction mixture and the loading coefficient. We assume the loading coefficient is 40% to 60%, which is commonly used in chemical/pharmaceutical productions.[25, 26] A loading coefficient below 40% might cause ineffective stirring, while a loading coefficient above 60% could create potential safety hazard.[25, 26] For the hydrogenation reaction, the loading coefficient is fixed at 50% since the net consumption of hydrogen is calculated based on this value. The volume of the reaction mixture and the corresponding volume for the reactors are listed in Table E.10. The material of the equipment is determined from the nature of the reaction mixture (e.g., corrosive acids) and the reaction conditions (e.g., high temperature or high pressure). For non-hydrogenation reactions, we assume the reactions are carried out in (a series of) glass reactors. For the hydrogenation reaction, we assume the reaction is carried out in (a series of) high-pressure stainless steel reactors. For all processes, we assume the filtration, washing and drying steps are carried out by the same 3-in-1 equipment. For all major pieces of equipment used in the production, their price and key specifications are is listed in Table E.11.

E.5. Operating Cost and Capital Cost Inputs for Techno-economic Assessment

Table E. 9. Summary of the price of all chemicals. Other than the concentrated acids, all other chemicals have purities above 98%. Unless otherwise specified, the price values were gathered from Alibaba.com or Molbase.com on Aug/21/2020. The specific vendor names are omitted to avoid any conflict of interests.

	Minimum ($)	**Base ($)**	**Maximum ($)**
98% H_2SO_4 (t)	240	260	300
68% HNO_3 (t)	100	343	680
5% Pd/C (kg)	100	200	300
H_2 (kg)	1	2	3
TPA	500	903	1500

$ZrCl_4$ (t) [2],[a]	868	1295	1937
36% HCl (t)	100	204	350
DMF (t)	532	578	1167
MeOH (t)	300	392	558
$ZrOCl_2 \cdot 8H_2O$ (t)	1200	1791	2678
AcOH (t)	228	467	622
NaOH (t)	100	407	720
Na_2CO_3 (t)	180	204	350
DI Water (t)	-	0.4	-
Natural gas (MJ)[27]	0.0021	0.004	0.011
Electricity (kWh)[28]	-	0.0683	-

[a] The price of $ZrCl_4$ is converted from the price of $ZrOCl_2 \cdot 8H_2O$ since the former is used to produce the latter.

Table E. 10. Summary of the reaction mixture volume and the required reactor volume.

Process in Table E.3

	Reaction Mixture Volume (L)	***Reactor Volume (L) Loading Coefficient = 40%***	***Reactor Volume (L) Loading Coefficient = 50%***	***Reactor Volume (L) Loading Coefficient = 60%***
Nitration [a]	8.166	20.415	16.332	13.610
Hydrogenation	41.328		82.656	
Solvothermal	104.433	261.083	208.866	174.055

Process in Table E.4

	Reaction Mixture Volume (L)	***Reactor Volume (L) Loading Coefficient = 40%***	***Reactor Volume (L) Loading Coefficient = 50%***	***Reactor Volume (L) Loading Coefficient = 60%***
Nitration	6.296	15.740	12.592	10.493
Hydrogenation	29.942		59.884	
Aqueous (metal solution)	14.898	37.245	29.796	24.830
Aqueous (linker Solution)	17.541	43.853	35.082	29.235

Process in Table E.5

	Reaction Mixture Volume (L)	*Reactor Volume (L) Loading Coefficient = 40%*	*Reactor Volume (L) Loading Coefficient = 50%*	*Reactor Volume (L) Loading Coefficient = 60%*
Nitration	19.263	48.158	38.526	32.105
Hydrogenation	108.758		217.516	
Solvothermal	274.820	687.050	549.640	458.033

Process in Table E.6

	Reaction Mixture Volume (L)	*Reactor Volume (L) Loading Coefficient = 40%*	*Reactor Volume (L) Loading Coefficient = 50%*	*Reactor Volume (L) Loading Coefficient = 60%*
Nitration	6.499	16.248	12.998	10.832
Hydrogenation	31.190		62.380	
Aqueous (metal solution)	15.520	38.800	31.040	25.867
Aqueous (linker Solution)	18.260	45.650	36.520	30.433

Process in Table E.7

	Reaction Mixture Volume (L)	*Reactor Volume (L) Loading Coefficient = 40%*	*Reactor Volume (L) Loading Coefficient = 50%*	*Reactor Volume (L) Loading Coefficient = 60%*
Nitration	39.150	97.875	78.300	65.250
Hydrogenation	229.601		459.202	
Solvothermal	580.177	1450.443	1160.354	966.962

Process in Table E.8

	Reaction Mixture Volume (L)	*Reactor Volume (L) Loading Coefficient = 40%*	*Reactor Volume (L) Loading Coefficient = 50%*	*Reactor Volume (L) Loading Coefficient = 60%*
Nitration	15.055	37.638	30.110	25.092
Hydrogenation	83.173		166.346	
Aqueous (metal solution)	41.386	103.465	82.772	68.977
Aqueous (linker Solution)	48.702	121.755	97.404	81.170

[a] The reaction mixture volume increases with the number of reuse of the nitration medium. The volume listed in the table is the maximum volume, i.e., the volume when the nitration medium is reused twice.

Table E. 11. Summary of the price and key specifications of all major pieces of equipment. The equipment price was quoted from vendors in China on Aug/21/2020. The specific vendor names are omitted to avoid any conflict of interests.

Type	*Materials*	*Operating Pressure (MPa)*	*Nominal Stirring Power/Working Power (kW)*	*Maximum Temp (°C)*	*Lifetime (Year)*
Glass Reactor	GG-17 Borosilicate Glass	0.002-0.2	0.250 (10-50 L)/0.400 (50-100 L)	400	10~15
Stainless Steel Reactor	316L Stainless Steel	≤9.8	0.250/0.400	350	10~15
Filtration-Washing-Drying 3-in-1	N/A	0.4	4.0	130	10~15

Process in Table E.3

Reaction Type	*Reactor Type*	*Reactor Size (L)* [b]	*Number of Reactors*	*Reactor Price (CNY)*	*Total Price (CNY)* [c]	*Total Price (USD)* [d]
Nitration	Glass	20	1	7500	64500	9334.298
Hydrogenation	Stainless Steel Reactor	80	1	57000		
Solvothermal [a]	Glass	100	2	14000	42000	6078.148

Solvent Recovery	Glass	100	1	14000		

Process in Table E.4

Reaction Type	***Reactor Type***	***Reactor Size (L)***	***Number of Reactors***	***Reactor Price (CNY)***	***Total Price (CNY)***	***Total Price (USD)***
Nitration	Glass	15	1	7300	59300	8581.766
Hydrogenation	Stainless Steel Reactor	60	1	52000		
Aqueous [e]	Glass	30	3	8500	25500	3690.304
Solvent Recovery	Glass	N/A	0	N/A		

Process in Table E.5

Reaction Type	***Reactor Type***	***Reactor Size (L)***	***Number of Reactors***	***Reactor Price (CNY)***	***Total Price (CNY)***	***Total Price (USD)***
Nitration	Glass	40	1	9000	133000	19247.47
Hydrogenation	Stainless Steel Reactor	100	2	62000		
Solvothermal	Glass	100	5	14000	98000	14182.34
Solvent Recovery	Glass	100	2	14000		

Process in Table E.6

Reaction Type	***Reactor Type***	***Reactor Size (L)***	***Number of Reactors***	***Reactor Price (CNY)***	***Total Price (CNY)***	***Total Price (USD)***
Nitration	Glass	15	1	7300	59300	8581.766
Hydrogenation	Stainless Steel Reactor	60	1	52000		
Aqueous	Glass	30	3	8500	25500	3690.304
Solvent Recovery	Glass	N/A	0	N/A		

Process in Table E.7

Reaction Type	***Reactor Type***	***Reactor Size (L)***	***Number of Reactors***	***Reactor Price (CNY)***	***Total Price (CNY)***	***Total Price (USD)***

Nitration	Glass	80	1	12500	322500	46671.49
Hydrogenation	Stainless Steel Reactor	100	5	62000		
Solvothermal	Glass	100	10	14000	196000	28364.69
Solvent Recovery	Glass	100	4	14000		
Process in Table E.8						
Reaction Type	***Reactor Type***	***Reactor Size (L)***	***Number of Reactors***	***Reactor Price (CNY)***	***Total Price (CNY)***	***Total Price (USD)***
Nitration	Glass	30	1	8500	124500	18017.37
Hydrogenation	Stainless Steel Reactor	80	2	58000		
Aqueous	Glass	100	3	14000	42000	6078.148
Solvent Recovery	Glass	N/A	0	N/A		
All Processes						
Process Type	***Equipment Type***	***Equipment Size***	***Number of Equipment***	***Equipment Price (CNY)***	***Total Price (CNY)***	***Total Price (USD)***
Filtration-Washing-Drying	3-in-1	0.78 m^2 (filtration area) /0.86 m^3 (capacity)	1 [f]	205000	205000	29667.149

[a] Some papers suggest large reactors might have effects on the nucleation and growth of the UiO-66-NH_2 in solvothermal production,[29] but such effects are not taken into considerations in this work. If those effects do occur and smaller reactors must be used, the equipment price would be higher.

[b] Price for reactors larger than 100 L is less available.

[c] The price on the top is for the equipment used in the 2-ATA production, and this price is eventually reflected in the price of 2-ATA. The price on the bottom is for the equipment directly used in the UiO-66-NH_2 production.

[d] Based on the exchange rate on 08/21/2020.

[e] One additional reactor is used for the reaction between the metal solution and the linker solution (i.e., the reaction that produces UiO-66-NH_2). The volume of this additional reactor is chosen to be the same as the volume of the reactors used for preparing the metal solution and the linker solution. Hence, the reaction that produces UiO-66-NH_2 needs to be carried out twice to get 1 FU. Given the high STY of the aqueous solution-based method, we assume that running the reaction for an additional time does not affect the number of FU this set of equipment could produce per day.

[f] According to the manufacturer, this equipment could be used for different processes/products.

Total process energy consumption

The total process energy consumption is consisted of two parts, the process heat consumption and the process electricity consumptions. The process heat consumption is calculated using Equation (E.14) and (E.15), and the values were listed in Table E.3 through Table E.8. The process electricity consumption for stirring is calculated using the suggested stirring power per volume mixture,[30] listed in Table E.12, the mixture volume, listed in Table E.10, and the equipment working time, described in the chemical synthesis descriptions, via the following equation:

$$
\begin{aligned}
&Electricity\ (Sitrring) \\
&\quad = Suggested\ stirring\ power\ per\ volume\ mixture \times Mixture\ volume \\
&\quad \times Working\ time
\end{aligned}
\tag{E.16}
$$

The process electricity consumption of filtration/washing/drying is calculated by the following equation:

$$Electricity\ (Filtration/Washing/Drying) = Nominal\ Power \times 80\% \times Working\ time$$

The power adjusting coefficient, 80%, is applied in the above equation since the actual motor power in production is usually 80% to 90% of the nominal motor power.[30] The process heat and electricity consumption are listed in Table E.13. (17)

Table E. 12. Summary of the suggested stirring power per volume mixture.[30]

Stirring Type	Power per volume mixture (kW/m^3)
Liquid mixing	0.067
Solid suspending	0.197-0.295 [a]
Organic solid dissolution	0.295-0.394 [a]
Inorganic solid dissolution	0.984

[a] The larger value will be used in the calculations.

Table E. 13. Summary of the process heat and electricity consumption.

Process in Table E.3		
	Heat (MJ)	***Electricity (kWh)***
Nitration of TPA [a]	7.107	6.406
Hydrogenation of 2-NTA [a]	2.851	6.527
Conventional Solvothermal Synthesis [a]	112.497-448.979	7.157

Process in Table E.4		
	Heat (MJ)	***Electricity (kWh)***
Nitration of TPA	5.149	6.405
Hydrogenation of 2-NTA	2.065	6.492
Aqueous solution-based synthesis [a]	6.668	6.411

Process in Table E.5		
	Heat (MJ)	***Electricity (kWh)***
Nitration of TPA	18.702	6.414
Hydrogenation of 2-NTA	7.503	6.733
Conventional Solvothermal Synthesis	296.044-1182.227	8.939

Process in Table E.6		
	Heat (MJ)	***Electricity (kWh)***
Nitration of TPA	5.363	6.405
Hydrogenation of 2-NTA	2.152	6.496
Aqueous solution-based synthesis	6.946	6.411

Process in Table E.7		
	Heat (MJ)	***Electricity (kWh)***
Nitration of TPA	39.481	6.429
Hydrogenation of 2-NTA	15.84	7.104
Conventional Solvothermal Synthesis	624.981-2495.812	10.608

Process in Table E.8	*Heat (MJ)*	*Electricity (kWh)*
Nitration of TPA	14.303	6.411
Hydrogenation of 2-NTA	5.739	6.655
Aqueous solution-based synthesis	18.521	6.429

[a] Assuming stirring is on during the entire synthesis.

Table E. 14. Uncertainty associated with UiO-66-NH_2 production

	Minimum	**Base**	**Maximum**	**Reference**
Uio-66-NH_2 yield (mass based)- Solvothermal	0.34	0.38	0.42	[8]
Uio-66-NH_2 yield (mass based)- Aqueous	0.95	0.96	0.97	[8]
Uio-66-NH_2 yield (crystallinity based)- Solvothermal	0.15	0.18	0.21	[8]
Uio-66-NH_2 yield (crystallinity based)- Aqueous	0.33	0.36	0.39	[8]
Solvent recycle rate	0.85	0.9	0.95	Industrial setting
Linker yield	-20%	0.432	+20%	This study
Equipment life time	-20%	10 yr	+20%	This study
Equipment costs	-20%	Scenario-specific	+20%	This study
Market price	Table E.9	Table E.9	Table E.9	

E.6. Supplementary Figures

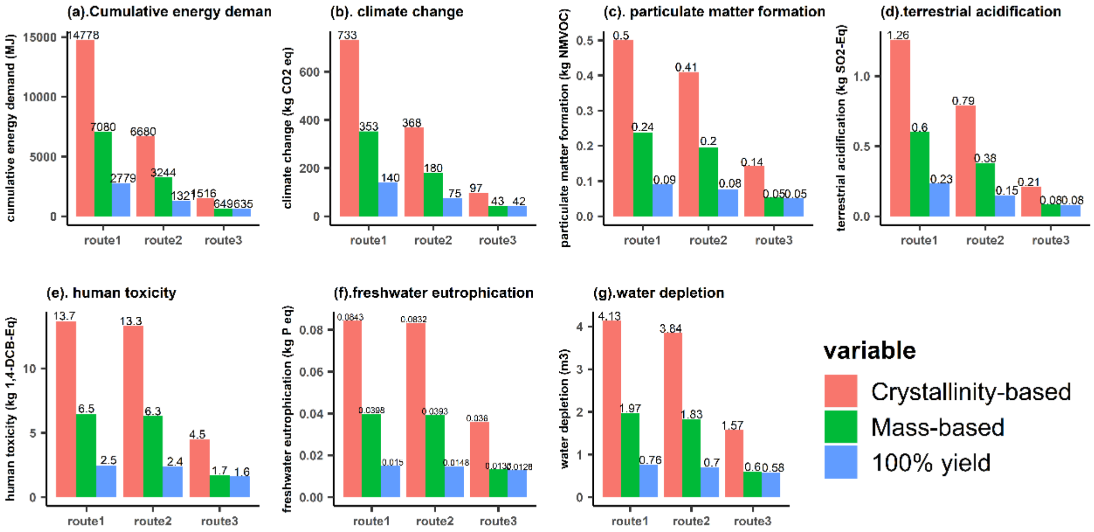

Figure E. 1. Life cycle impacts for route 1, 2, and 3 based on mass-based FU, crystallinity-based FU, and ideal case (100% yield).

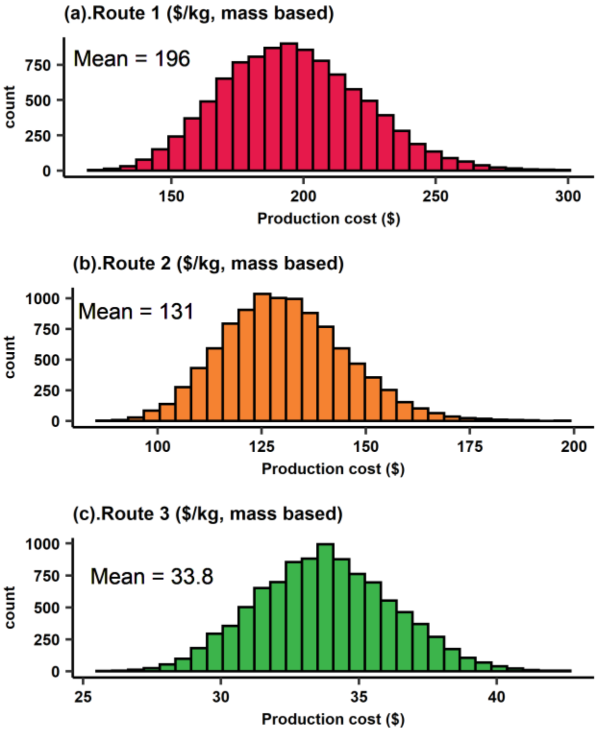

Figure E. 2. Production costs for route 1, 2, and 3 based on crystallinity-based FU

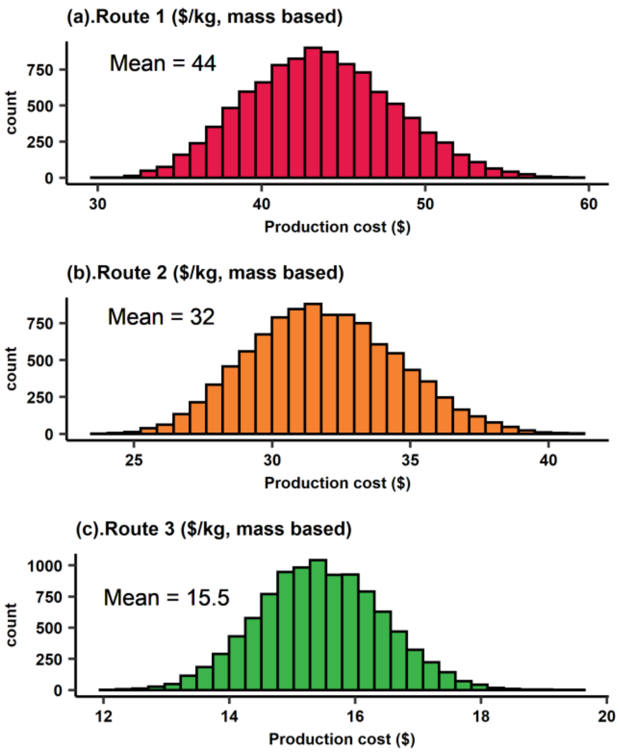

Figure E. 3. Production costs for route 1, 2, and 3 based on ideal case (100% yield)

E.7 References:

1. B. Yin, B. Huang, X. Fan, Y. Sun, X. Liu, L. He, and Z. Wu, Zirconium tetrachloride and zirconia preparation process by secondary chlorination. 2018, Xinjiang Jingshuo New Materials Co., Ltd., Peop. Rep. China . p. 10pp.
2. Z. Guo, H. Li, Y. Li, and F. Dong, Method for production of high-purity zirconium oxychloride and coproduction of silicon tetrachloride by zircon sand fluidizing chlorination. 2015, Peop. Rep. China . p. 16pp.
3. J. Chen, C. Shen, L. Fu, and F. Li, Production method of zirconium oxychloride using membrane treatment technology. 2018, Longmang Billions Group Co., Ltd., Peop. Rep. China . p. 4pp.
4. Y. Sun, C. Chen, J. Wu, Z. Yi, and Y. Zuo, Crystallization process and device for preparation of zirconyl chloride. 2003, Guangdong Orient Zirconic Ind Sci and Tech Co., Ltd., Peop. Rep. China . p. 9 pp.
5. M. Li, M. Ge, T. Yu, and Y. Huang, Method for preparing diazonium salt by depolymerizing waste polyester fibers using ethylene glycol. 2014, Jiangnan University, Peop. Rep. China . p. 9pp.
6. E.B. Skibo and J.H. Gilchrist, Synthesis and electrochemistry of pyrimidoquinazoline-5, 10-diones. Design of hydrolytically stable high potential quinones and new reductive alkylation systems. The Journal of Organic Chemistry, 1988. **53**(18): p. 4209-4218.
7. J. Aguilera-Sigalat and D. Bradshaw, A colloidal water-stable MOF as a broad-range fluorescent pH sensor via post-synthetic modification. Chemical Communications, 2014. **50**(36): p. 4711-4713.

8. L. Huelsenbeck, H. Luo, P. Verma, J. Dane, R. Ho, E. Beyer, H. Hall, G.M. Geise, and G. Giri, A Generalized Approach for Rapid Aqueous MOF Synthesis by Controlling Solution pH. Crystal Growth & Design, 2020.

9. K. Lokesh, A.S. Matharu, I.K. Kookos, D. Ladakis, A. Koutinas, P. Morone, and J. Clark, Hybridised sustainability metrics for use in life cycle assessment of bio-based products: resource efficiency and circularity. Green Chemistry, 2020. **22**(3): p. 803-813.

10. Y. Li and C. Gao, Hydrogenation Reaction in the Pharmaceutical Industry. 2020.

11. D. DeSantis, J.A. Mason, B.D. James, C. Houchins, J.R. Long, and M. Veenstra, Techno-economic analysis of metal–organic frameworks for hydrogen and natural gas storage. Energy & Fuels, 2017. **31**(2): p. 2024-2032.

12. F. Cheng, H. Luo, and L.M. Colosi, Slow pyrolysis as a platform for negative emissions technology: An integration of machine learning models, life cycle assessment, and economic analysis. Energy Conversion and Management, 2020. **223**: p. 113258.

13. F. Cheng, M.D. Porter, and L.M. Colosi, Is hydrothermal treatment coupled with carbon capture and storage an energy-producing negative emissions technology? Energy Conversion and Management, 2020. **203**: p. 112252.

14. D.R. Lide, CRC handbook of chemistry and physics. Vol. 85. 2004: CRC press.

15. J. Long, S. Wang, Z. Ding, S. Wang, Y. Zhou, L. Huang, and X. Wang, Amine-functionalized zirconium metal–organic framework as efficient visible-light photocatalyst for aerobic organic transformations. Chemical Communications, 2012. **48**(95): p. 11656-11658.

16. J. Kunzler and W. Giauque, Aqueous Sulfuric Acid. Heat Capacity. Partial Specific Heat Content of Water at 25 and-20. Journal of the American Chemical Society, 1952. **74**(14): p. 3472-3476.

17. S.A. Stern, J. Mullhaupt, and W.B. Kay, The Physicochemical Properties of Pure Nitric Acid. Chemical Reviews, 1960. **60**(2): p. 185-207.

18. Y.-F. Huang and S.-L. Lo, Predicting heating value of lignocellulosic biomass based on elemental analysis. Energy, 2020. **191**: p. 116501.

19. C. De Visser, G. Perron, J.E. Desnoyers, W.J. Heuvelsland, and G. Somsen, Volumes and heat capacities of mixtures of N, N-dimethylformamide and water at 298.15 K. Journal of Chemical and Engineering Data, 1977. **22**(1): p. 74-79.

20. Methanol - Specific Heat. [cited 2020 Aug 21]; Available from: https://www.engineeringtoolbox.com/methanol-CH3OH-specific-heat-capacity-Cp-Cv-isobaric-isochoric-d_2103.html.

21. A. Campbell and J. Gieskes, Heats of mixing and heat capacities in the system: acetic acid–chloroform–water, at 25. Canadian Journal of Chemistry, 1965. **43**(5): p. 1004-1011.

22. Water - Heat of Vaporization. [cited 2020 Aug 21]; Available from: https://www.engineeringtoolbox.com/water-properties-d_1573.html.

23. Methyl Alcohol. [cited 2020 Aug 22]; Available from: https://webbook.nist.gov/cgi/cbook.cgi?ID=C67561&Mask=4.

24. H. Luo, J. Aboki, Y. Ji, R. Guo, and G.M. Geise, Water and Salt Transport Properties of Triptycene-Containing Sulfonated Polysulfone Materials for Desalination Membrane Applications. ACS Applied Materials & Interfaces, 2018. **10**(4): p. 4102-4112.

25. R. Sinnott, Chemical engineering design. Vol. 6. 2014: Elsevier.

26. G. Towler and R. Sinnott, Chemical engineering design: principles, practice and economics of plant and process design. 2012: Elsevier.

27. R. White, F. Segundo Navarro-Pineda, T. Cockerill, V. Dupont, and J. César Sacramento Rivero, Techno-Economic and Life Cycle Impacts Analysis of Direct Methanation of Glycerol to Bio-Synthetic Natural Gas at a Biodiesel Refinery. Energies, 2019. **12**(4): p. 678.

28. V. Chiodo, G. Zafarana, S. Maisano, S. Freni, and F. Urbani, Pyrolysis of different biomass: Direct comparison among Posidonia Oceanica, Lacustrine Alga and White-Pine. Fuel, 2016. **164**: p. 220-227.

29. M. Rubio-Martinez, C. Avci-Camur, A.W. Thornton, I. Imaz, D. Maspoch, and M.R. Hill, New synthetic routes towards MOF production at scale. Chemical Society Reviews, 2017. **46**(11): p. 3453-3480.

30. Y. Chen and J. Yi, Chemical Equipment Design Book: Mixing Equipment Design. 1985: Shanghai Scientific and Technical Publishers.